

Supplementary Information for

The role of ancient genetic selection and climatic factors in the dispersal of anatomically modern humans out of Africa

Raymond Tobler^{*‡}, Yassine Souilmi^{*‡}, Christian D. Huber^{*}, Nigel Bean, Chris S.M. Turney, Shane T. Grey^{†‡}, Alan Cooper^{†‡}

* These authors contributed equally to this work

† These authors contributed equally to this work

‡ Corresponding authors: R.T.: ray.tobler@anu.edu.au; Y.S.: yassine.souilmi@adelaide.edu.au; S.T.G.: s.grey@garvan.org.au; A.C.: alanjcooper42@gmail.com

This document includes:

Supplemental Materials 1-4

Supplemental Figures S1-S13

Supplemental Tables S1-S10

Links to additional Datasets:

Datasets S1-S56: <https://doi.org/10.25909/22359865>

Dataset S57: <https://doi.org/10.25909/22359874>

Table of Contents

Supplemental Materials 1. Data processing and sweep detection pipeline	4
1.1 Population designation	4
1.2 Selection terminology and evidence of selection in human history	4
1.3 Data collection and processing	4
1.4 Sweep scans	5
1.5 Outlier gene detection	6
1.6 Candidate sweep classification	7
1.7 Impact of SNP missingness on sweep detection	8
1.8 Comparison with SweepFinder2 scans in modern African populations	8
Supplemental Materials 2. Inferring selection onset and sweep dynamics	10
2.1 Determining marker alleles for sweep haplotypes	10
2.2 Sweep haplotype detection methods and datasets	11
2.3 Estimating sweep haplotype dynamics	13
2.4. Estimating the onset of selection and genetic isolation of OoA migrants	14
2.5 Statistical properties of the sweep haplotype detection method	16
2.6 Recalibration of age of Neandertal admixture	17
2.7 Location of Neandertal admixture event and Main Eurasian dispersal	20
2.8 Using sweep haplotype presence to reconstruct Paleolithic Eurasian population history	24
2.9 Potential implications of the reconstructed model of Eurasian dispersals 51ka onwards	29
2.10 'Out of Arabia': Climate changes in the Arabian Peninsula and wider region	29
Supplemental Materials 3. Functional classification and analyses of candidate genes	32
3.1 Refining the targets of selection	32
3.2 Comparative candidate gene sets	32
3.3 Sweeps are enriched with genes intolerant of deletion in present day populations	34
3.4 Functional characterization of ancient Eurasian candidate genes	35
3.5 Candidate genes form coordinated functional pathways	36
3.6 Neurological function as an underappreciated adaptive target in humans	37
3.7 Confirming functional concordance through analyses of protein-protein interactions	38

3.8 Quantitative evaluation of functional annotations	40
3.9 Generality of functional annotations beyond hard sweeps	40
3.10 Arctic human candidate genes likely had local selection pressures	41
Supplemental Materials 4. Evaluating the hominin source of sweep driver alleles	44
Supplemental Figures	47
Supplemental Tables	64
References	161

Supplemental Materials 1. Data processing and sweep detection pipeline

Information on genomic population genomic sequence processing and selection scans are outlined in ref. (1), which examines the masking effects of Holocene admixture on the 57 historical hard sweep signals. Key aspects are summarized in this section for convenience.

1.1 Population designation

The assignment of individuals to 18 distinct populations was governed by minimizing temporal and spatial variability among samples previously defined in the ancient DNA literature as sharing genetic affinities, while also preserving the archaeological context and retaining enough individuals to ensure that our analyses were sufficiently powerful to detect selection. The population assignments in this study produce reasonably distinct genetic clusters in principal component analysis (PCA) space (Fig. S1) that align with previously reported PCA results (2–4). We use a population nomenclature that follows the guidelines recently proposed for ancient DNA research (5).

1.2 Selection terminology and evidence of selection in human history

The classical definition of a hard sweep is based on the fixation of a new beneficial allele and linked neutral variants (6). In contrast, soft sweeps capture scenarios where either the beneficial allele is present prior to the onset of selection, such that the allele is present on multiple haplotypes that can potentially be picked up by selection, or where the mutation rate is sufficiently high at the beneficial locus that no single version of the allele is likely to become fixed. In the current study, a ‘hard sweep’ refers to a locus that has produced a specific distortion of the site frequency spectrum that is detectable by SweepFinder2 (see [section 1.4](#)). This pattern is the characteristic genetic signal produced by a classical hard sweep, but such signals can also be created in cases where selection has driven an initially rare haplotype to high frequencies (7). Formal evaluation of this issue is provided in ref. (1).

Another form of selection, known as polygenic selection, involves simultaneous changes across multiple genomic loci that all contribute to the beneficial trait. This mode of selection tends to result in numerous subtle allele frequency shifts that are subsequently unlikely to produce distinctive sweep signals at individual beneficial loci (8, 9) and be detected in our analyses.

1.3 Data collection and processing

To produce a robust dataset and avoid potential bioinformatic batch effects, the raw sequence read data for 1,162 ancient genomic datasets (Table S1) was retrieved from the Short Read Archive (SRP029640, SRP057056) or the European Nucleotide Archive (ERP003900, PRJEB6622, PRJEB6272,

PRJNA230689, PRJEB7618, PRJEB609, PRJEB9021, PRJEB8987, PRJEB9783, PRJEB11364, PRJEB11450, PRJEB1418, PRJEB13123, PRJEB11848, PRJEB14455, PRJEB22629, PRJEB12155, PRJEB22652, PRJEB23635, PRJEB24794, PRJEB29603) and processed through a standardized pipeline. To minimize the risk of modern contamination, the forward and reverse reads of the paired-end reads were merged (collapsed) using fastp (10), and only merged reads were retained (modern data is more likely to comprise large DNA fragments that do not collapse). All collapsed reads were filtered for potential residual adaptor sequences and chimeras using Poly-X with fastp (10). The retained filtered set of sequence reads were aligned to the human reference genome (h37d) using the Burrows-Wheeler Aligner v0.7.15 (11). All mapped reads were sorted using SAMtools v1.3 (12) and then realigned around insertions and deletions and potential PCR duplicate reads marked and removed using the Genome Analysis ToolKit (GATK) v3.5 (13).

Prior to variant calling, all remaining aligned reads were screened and base-calls recalibrated for aDNA postmortem damage using mapDamage2 (14). To further limit the impact of postmortem damage on variant calling (15), bamUtil (16) was used to trim 3 base-pairs from each of the 5' and 3' ends of each mapped read. From the resulting set of reads, pseudohaploid variants were called at the set of 1240k capture SNPs (3) across the 22 autosomes, using a combination of SAMtools mpileup (17) and sequenceTools (<https://github.com/stschiff/sequenceTools>). The 1240k capture was developed to minimize ascertainment in non-African populations and was used to generate data for most samples used in the study, whereby concentrating on the 1240k variants ensured a common and robust set of variants for the subsequent analyses. Pseudohaplodization of read data is a standard strategy in aDNA analyses, whereby a single read is randomly sampled at each prespecified SNP position (3) in order to mitigate potential biases introduced by differences in coverage or post-mortem damage between samples (2). The pseudohaploid variant calls were converted from EIGENSOFT format (18, 19) to binary Plink format using EIGENSOFT. Plink v1.9 (20, 21) was used to assign samples to the predefined populations (Table S2) and convert the variants to reference polarized VCF files, with correct polarization being checked using BCFtools (17). Finally, a custom Python script was used to generate the site frequency spectrum (SFS) input files for SweepFinder2 analysis (<https://gist.github.com/yassineS/fe2712ad52d76460b927e3f391ea51f6>).

1.4 Sweep scans

We computed the SweepFinder2 CLR (composite likelihood ratio) statistic (22, 23) across the genome in successive 1kb intervals for all 18 ancient, along with five modern human populations from the 1,000 Genomes Project (i.e. Utah residents with Northern and Western European ancestry (CEU); Finnish in Finland (FIN); Toscani in Italy (TSI); Han Chinese in Beijing (CHB); Yoruba in Ibadan, Nigeria (YRI); ref. (24)). Allele frequency data and SweepFinder2 results for individual ancient populations can be accessed at <https://doi.org/10.25909/6324956ee6ba6>.

The CLR statistic evaluates evidence for hard sweeps in dynamically sized windows, by comparing the distribution of allele frequencies expected under a mathematical model of a hard sweep with the expectation under neutral evolution (larger CLR scores indicate more evidence for selection). The

expected site frequency spectrum (SFS) under the hard selective sweep model is computed conditional on the neutral SFS, assuming a certain selection coefficient and recombination rate. The neutral SFS is based on the background SFS calculated from the whole genome, assuming that the influence of sweeps on the SFS on a genome-wide scale is negligible.

SweepFinder2 is robust to genome-wide effects such as ascertainment bias and demography (25) by allowing these processes to affect the expected SFS under neutrality (i.e. the background SFS). Further, unlike many other selection methods, the assumptions on the input data for SweepFinder2 are suitable for the low coverage and ascertained nature of ancient DNA datasets. Since it is only based on the spatial (genomic) pattern of allele frequencies but not on haplotype homozygosity or population differentiation, it is possible to detect selection without reference to a second population, calling genotypes, or phasing haplotypes. The reliance on an empirically estimated null model (i.e. the background SFS) and the model-based alternative hypothesis makes it both more powerful and more robust compared to alternate test statistics that are based on deviations of the SFS from expectations under the standard neutral model (e.g. Tajima's D , Fay and Wu's H).

While SweepFinder2 also has an option to detect sweeps based on local genomic reductions in diversity, we did not calculate this diversity-based metric since accurate and unbiased estimation of diversity requires full genome data, whereas our dataset consists of a set of ascertained SNPs.

1.5 Outlier gene detection

Human gene annotations were obtained from ENSEMBL database (26) (genome reference version GRCh37), which was accessed using the R bioMart package (27, 28) (version 2.36.1). Of the 24,554 annotated 'genes' on the bioMart database, we removed any that were not annotated in the NCBI database (ftp.ncbi.nih.gov/gene/DATA/GENE_INFO/Mammalia/Homo_sapiens.gene_info.gz) and also excluded those that lacked specific protein and RNA based annotations (in the bioMart transcript_biotype field). This resulted in a list of 19,603 genes, from which we removed 26 that did not contain any polymorphic sites in our datasets (all such genes being situated in the most terminal areas of chromosomes), leaving 19,577 genes that were used in the subsequent analyses. For each population, all SweepFinder2 CLR scores were \log_{10} transformed and assigned to each of 19,577 genes by binning the transformed scores within the genomic boundaries of each gene. The gene boundaries were extended by 50kb on either side to also capture *cis*-regulatory regions. Because this typically resulted in several scores per gene, we took the maximum score to represent the evidence for a sweep involving that gene. Each gene score was corrected for gene-length using a non-parametric standardization algorithm (29, 30), resulting in the gene scores having an approximately standard normal distribution. Finally, p values were calculated for all genes and a q value correction (27) applied for each population. The q value is a Bayesian posterior estimate of the p value that accounts for the expected inflation of false positives due to multiple testing (27), whereby a q value of 0.01 implies a false discovery rate of 1% per population.

1.6 Candidate sweep classification

Sweeps were identified by determining a set of outlier genes across all populations (above), which were classified into sweep regions according to 1) the distance between the mid-point of neighboring pairs of outlier genes (i.e. inter-gene distance) and 2) overlapping sweep regions between populations. Step 1 was performed independently for each population, whereby all outlier genes with midpoints that were less than a specific distance apart from the midpoint of a neighboring outlier gene were collapsed into a single category. After generating the collapsed categories for each population, step 2 was applied to ensure that the sweep categories sharing at least one gene across different populations were considered as a single historical sweep.

We ran our sweep quantification pipeline at three q value thresholds (i.e. $q < 0.01$, 0.05 or 0.10 , which imply false discovery rates of 1%, 5% and 10% per population, respectively) and the three different inter-gene distances (midpoint distances less than 250kb, 500kb or 1Mb). As expected, changing the q value had a large impact on the number of sweeps (ranging from ~50 for $q < 0.01$ to ~500 for $q < 0.1$), whereas changing the inter-gene midpoint distance had comparatively little impact overall, particularly at more stringent q value cutoffs (see ref. (1)). Based on these results, we decided to use the most stringent q value cutoff and the most liberal inter-gene distance to define a robust set of candidate sweeps for all further analysis. However, because this stringent cutoff might lead to the removal of potentially causal genes in a sweep (which could have values slightly above 0.01), we first defined our sweeps based on the more permissive $q < 0.1$ threshold, and then removed all sweeps that did not have at least one gene with $q < 0.01$.

To further improve sweep determination, we removed populations with small sample sizes from the sweep determination process, as previous results of modern genomes suggest that SweepFinder2 has poor power to detect sweeps when less than 10 haploid genome copies are being analyzed (31). Specifically, we removed populations with an effective sample size, n_{eff} , less than 10, as these populations had poor power and exhibited notable distorted gene score distributions in both empirical data and under neutral simulations of population history (see ref. (1) for a full description of the simulation framework and statistical properties of the analytical pipeline). The n_{eff} metric captures the composite effect of sample size, ploidy and data missingness in a paleogenomic context, and is defined as $n_{\text{eff}} = k \times n \times (1 - M)$, i.e. the product of the ploidy of each sample (k) with the sample size (n) and the average proportion of non-missing sites (M) (also see ref. (1)).

Finally, to ensure that the sweeps being defined were all relevant to western Eurasian history, the two modern populations from East Asia (CHB) and Africa (YRI) were also excluded from the sweep classification process. This strategy resulted in a total of 57 candidate sweeps that were used in subsequent analyses. Plots showing the distribution of SweepFinder2 CLR scores and the transformed gene scores within each candidate sweep are provided as Datasets S1-S56 (<https://doi.org/10.25909/22359865>).

1.7 Impact of SNP missingness on sweep detection

We examined if SNP missingness (i.e. the proportion of samples that lack a pseudohaploid allele call at a given SNP) was impacting sweep detection in the ancient populations by regressing gene scores against the average level of SNP missingness observed in each gene (extending gene boundaries by 50kb to make gene definitions compatible with our analytical pipeline). This regression analysis was performed separately for each ancient population used in the sweep detection assay (i.e. populations with $n_{\text{eff}} \geq 10$; see [section 1.6](#) and ref. (1)).

For all ancient populations, gene scores tended to decrease gradually as the mean SNP missingness increased (Fig. S2). These results likely reflect a loss of power to detect selection in regions with reduced genetic information and suggest that SNP missingness is unlikely to have inflated the number of false positives in our study.

1.8 Comparison with SweepFinder2 scans in modern African populations

The 57 sweep signals observed in ancient Eurasian populations were absent in modern Yorubans from West Africa (i.e. YRI), consistent with the underlying selection pressure most likely arising after the separation of African and non-African human lineages. To explore the origin of the sweeps in more detail, we examined if any of our 57 sweep regions overlapped with positively selected regions identified in a recent study of high coverage genomes from multiple African populations (32). We compared our 57 sweeps to the 492 reported candidate loci identified in six different African populations, finding nine unique African candidate loci that overlap four of our sweeps (namely, *DOCK3*, *GABBR1*, *PNLIPRP3*, *MIR662*). To test if the four selected regions found in our study and also ref. (32) were consistent with random expectations, we used the R package *regioneR* (33) to randomly sample 57 genomic windows from across the genome that matched the sizes of our sweeps, then counted the number of sweeps that overlapped at least one of the 492 candidate regions from ref. (32). We obtained an empirical *p* value by repeating this sampling process 10,000 times and calculating the proportion of random samples that had an equal or larger number of sweeps overlapping African candidate regions than we observe (i.e. four unique sweeps).

We also repeated this process to account for the possibility that both our hard sweep signals and the reported outlier windows were more likely to be detected regions with low recombination rates (which may have more power in genome-wide selection scans), by sampling from a modified genome that had been rescaled according to the local recombination rate. Specifically, we used the sex-averaged recombination rates measured across 10kb genomic intervals (34) to rescale the length of each interval (l_i) according to $l_i = 1/(1+r_i)$, where r_i is the recombination rate for the i th genomic interval. We also rescaled each sweep window through linear interpolation to the recombination-rescaled genome and used *regioneR* (33) to randomly sample 10,000 sets of 57 genomic windows matching these lengths from the rescaled genome. The sampled windows were then converted back to a standard physical length by interpolating to the original (unscaled) genome, and the overlap with outlier regions tested in the standard way.

Both the standard permutation test and the recombination rate adjusted test returned non-significant results (Standard test: expected number of overlapping sweeps ~ 2.92 , $p = 0.33$; Recombination rate adjusted test: expected number of overlapping sweeps ~ 3.32 , $p = 0.3986$), consistent with the number of overlaps between the two studies matching chance expectations. Thus, our results are consistent with the 57 sweeps observed in this study arising after the separation of ancestors of modern Eurasians from African lineages.

Supplemental Materials 2. Inferring selection onset and sweep dynamics

2.1 Determining marker alleles for sweep haplotypes

Our analyses suggest that the underlying selection pressure driving the 57 sweeps most likely arose following the separation of the ancestors of non-African populations with ancestral African AMH lineages (see [section 1.8](#)). The deep antiquity of this separation (~100ka; (35)) should mean that SNPs linked to the 57 sweep haplotypes have become highly diverged when contrasting Eurasian populations with contemporary African populations. Accordingly, we sought to identify a set of up to 30 marker SNPs in each sweep that were highly divergent in all pairwise comparisons between modern Yorubans (i.e. *YRI*) and the tested Eurasian populations.

To calculate population divergence, we used Hudson's F_{st} estimator (specifically, equation 10 from ref. (36)) to calculate pairwise F_{st} in each Yoruban-Eurasian pair across all ~1M SNPs in the genome. For each pairwise test, we excluded SNPs that did not have at least 10 copies in each population (this condition was always satisfied for the Yoruban population, so was dependent on the number of samples and SNP missingness in the relevant Eurasian population). For each sweep, we then averaged the F_{st} values after omitting values from Eurasian populations that did not show evidence for the sweep signal (i.e. populations that had no gene with $q < 0.2$ across the specific sweep region). In addition to estimating the mean F_{st} for SNPs within sweep regions, we also computed this statistic for all SNPs occurring in regions of the genome lying outside of the 57 sweep regions. These SNPs provide a conservative 'neutral' background (conservative because it will also include SNPs from regions impacted by positive selection that are not detected by our selection scan), which we used to calculate thresholds to identify the most strongly differentiated SNPs in each sweep region. Accordingly, we excluded all SNPs in sweep regions with mean F_{st} values below the 80th percentile of 'neutral' mean F_{st} values (the threshold mean F_{st} value ranged from ~0.2 to 0.27 across all sweeps and tended to increase as an inverse function of the number of Eurasian populations used to compute the mean). The remaining SNPs were ranked according to the mean F_{st} and up to 30 with the lowest ranks (i.e. highest mean F_{st}) were chosen as marker SNPs.

After identifying the set of marker SNPs for each sweep region, for each marker SNP we determined the putative allele linked to the sweep haplotype as the most common (major) allele across the same subset of European populations that were used to calculate the mean F_{st} . To ensure that the major allele was robust to our choice of frequency estimator, we calculated the mean SNP frequency in two ways – either by 1) calculating the average across the raw population frequencies or 2) weighting the population frequencies by the number of samples in each population – and only kept SNPs that produced the same major allele with both estimators. Applying this procedure to each sweep resulted in a unique set of up to 30 marker alleles. The position of the marker SNPs in the sweep is shown in Datasets S1-S56 (<https://doi.org/10.25909/22359865>). To ensure that sweep haplotype estimation was robust to SNP missingness, only samples with at least 50% of marker SNPs in a particular sweep were evaluated. Note that one sweep (*LINC01153*) was excluded from further marker-based analyses as it

only had 3 SNPs that passed all marker filtering criteria, whereas all other sweeps had ≥ 6 marker SNPs and the majority (46/57; ~81%) had 30 or more marker SNPs.

2.2 Sweep haplotype detection methods and datasets

Sweep haplotypes were defined as present in the genome of a particular ancient sample if a certain minimum proportion of marker alleles were observed at all called pseudohaploid sites within a sweep region. Specifically, to determine sweep presence, we tested different combinations of the number of marker SNPs and the minimum proportion of marker alleles observed – i.e. either 90% or 95% of the top 10, 20, or 30 ranked marker alleles – creating six categories overall. For each sample, we determined sweep presence based on the aggregate signal across all six categories, requiring the sweep to be present in at least three of the six categories. We chose this intermediate value as it provides a reasonable balance of the false positive and false negative rate (see [section 2.5](#) for details). For samples where diploid calls were available (i.e. all modern samples and high coverage ancient samples such as Ust'-Ishim), we randomly selected a single allele at all SNPs to mimic pseudohaploidy prior to making haplotype calls. The statistical consequences of the pseudohaplodization process on our sweep haplotype inferences are discussed in [section 2.5](#).

Sweep haplotype presence was quantified in ancient and modern genomic data to perform three complementary sets of analyses: (1) model-based inference of sweep haplotype dynamics in Eurasian history ([section 2.3](#)) (2) regression and population genetic models to estimate the approximate onset of the underlying selection pressures ([section 2.4](#)), and (3) a heuristic approach to reconstruct migratory movements subsequent to AMH dispersal into Eurasia ([section 2.8](#)).

For all three analyses, we created a set of 39 ancient Eurasian samples, which comprised recently published samples from the Eurasian Upper Paleolithic – namely, Zlaty kun (37) in Czechia and six specimens from Bacho Kiro (38) in Bulgaria – and 32 high quality ancient samples curated in the Allen Ancient DNA Resource (AADR; version 42.4), a collection of ancient, archaic, and modern human genomes curated by the Reich Laboratory in Harvard University (<https://reich.hms.harvard.edu/allen-ancient-dna-resource-aadr-downloadable-genotypes-present-day-and-ancient-dna-data>). These AADR samples were all at least 10,000 years old and had a valid pseudohaploid call for more than 600k of the ~1.1M capture probe SNPs. Alignment (i.e. BAM; (12)) files for the Zlaty kun and six Bacho Kiro specimens were downloaded from links provided in each paper and pseudohaploidized according to the protocols outlined in [section 1.3](#) of the Methods. Two of the Bacho Kiro samples (BachoKiro_AA7-738 and BachoKiro_CC7-2289) had too few sites for robust haplotype detection and were removed from all subsequent analyses.

In addition to the 32 ancient samples, for the haplotype dynamics model ([section 2.3](#)) we included an additional 424 Holocene-era (<10ka) European individuals from the AADR with reasonable SNP coverage ($\geq 600k$ SNPs), focusing on samples from three distinct geographical regions with reasonable temporal coverage over the Holocene period (sample numbers indicated in square brackets, see Table S3 for the full sample list):

- 1) The British Isles: Great Britain [110], Ireland [7]
- 2) Central Europe: Germany [50], Czech Republic [52], Hungary [75], Poland [43]
- 3) the Iberian Peninsula: Portugal [15], Spain [72].

The broad temporal coverage within each of these three regions allowed us to discriminate the impacts of Holocene admixture events within geographically bounded regions and to ascertain whether any spatiotemporal variation in the sweep haplotype frequencies conformed with reported shifts in genetic ancestry observed across Europe (4, 39).

For the heuristic analysis of AMH migratory movements ([section 2.8](#)) we complemented the 32 Paleolithic Eurasian samples with 50 samples from the European Holocene (i.e. < 10,000 years old) that had at least 1 million SNPs with valid pseudohaploid calls. High quality genomes were prioritized for this analysis as initial evidence for sweep haplotype presence was important for inferring possible migratory routes, and higher sample availability and better DNA preservation for the Holocene period permitted more stringent selection criteria for samples from this period (see Table S2). To provide a broad representation of human populations outside of continental Eurasia, we also included historic and ancient samples from Africa (12 samples), the Americas (26 samples), and Oceania and the Andamans (5 samples; collectively referred to as the ‘Oceanic’ group) that had at least 600k marker SNPs present, along with all 2,504 samples from phase 3 of the 1,000 Genomes Project (24) (all available in the AADR v42.4). Finally, to provide additional representation for the ancient migrations that brought modern humans into Island Southeast Asia and Sahul, we also included 28 Papuan samples from the recent Human Genome Diversity Panel (HGDP; (40)). Improved estimates of sample age were obtained for several ancient Eurasian samples (Table S10) using the recent IntCal20 calibration curve (41).

For the onset time analyses ([section 2.4](#)) we reused a subset of 22 ancient and modern genomes that we had used in our heuristic analysis of AMH movements (Fig. S11). This set includes Western Hunter Gatherers (WHG) and moderate- to high-coverage specimens from the early period of the Upper Paleolithic, along with several Oceanic samples that our haplotype dynamics analyses (Figs. 1, S3, S4) suggest should provide a reasonable proxy for sweep presence around the separation time of these lineages from the Main Eurasian branch (~54-51ka; see [section 2.6](#)).

Finally, we noticed a strong male bias in the available genomic sequences older than the Holocene that are of sufficient coverage for analysis (20 of 23 samples [87%]; Table S2, Fig. S13). Male sex biases have been detected in Pleistocene megafaunal remains and have been related to behavioral and ranging differences between male and female individuals, particularly young males, and resulting changes in the probabilities of preservation and discovery in the environment (42). However, the vast majority of the 23 pre-Holocene AMH samples were found in human occupation sites (caves, rock shelters, camps) and range widely in geographic location (from western Europe to Beijing) and temporal age (across 35,000 years). This broad range helps provide a reasonable survey despite the small sample size. The high frequency of male specimens with genomic data raises the possibility that there has been a sex-bias in burials, at least for sites likely to be sampled for ancient DNA. In contrast, there are nine available hominin genomic datasets that pass our quality filtering criteria for sufficient genomic coverage (one Denisovan, one hybrid Denisovan-Neandertal, seven Neandertal), and of these only one

Neandertal specimen is known to be male, although more are known (43). While potentially important from an anthropological perspective, it is not obvious that there are any reasons that a pronounced male bias in the older part of our AMH dataset should noticeably influence our analyses or conclusions.

2.3 Estimating sweep haplotype dynamics

To infer the collective sweep dynamics, we enumerated the number of sweeps present in each sample and regressed this against the reported sample age, using local (LOESS) regression to allow for non-linear changes in sweep haplotype frequencies (using the loess function from the base R programming language (44)). Instances of sweeps missing at least 50% of the total marker SNPs for a particular sample were not evaluated, such that we used the proportion of total sweeps (i.e. the number of sweeps present in a sample relative to all evaluated sweeps) as the explanatory variable to account for missing sweep information in some samples. Separate LOESS regressions were performed for each of the three Holocene groups combined with 32 Paleolithic Eurasian samples, and also using three different values for the span parameter (i.e. 0.35, 0.5, 0.65, which determines the proportion of neighboring samples used to fit the local regression). These span values were based on the range of optimal spans obtained across all three geographically bounded regions and also the three haplotype detection criteria used in this study (see [section 2.2](#)), which were estimated using generalized cross validation (loess.as function from the fANOVA R package v. 0.6-1 (45)).

The LOESS regression trends reveal that the hard sweeps accumulate steadily across the Eurasian Upper Paleolithic before undergoing a marked decrease in all three regional European groups from the late Glacial/early Holocene (Figs. 1, S3). While the lack of British Isle samples dated prior to 6ka preclude obtaining more nuanced patterns of events during the early Holocene period, several trends are evident among the Iberian and Central European samples that corroborate previous work showing admixture to be an effective means of masking historical hard sweep signals (1). First, the sweep haplotype counts exhibit two broadly synchronous periods of marked decline around 8ka and 4.5ka in both Iberian and Central European populations, which coincide with the documented introduction of Anatolian and Steepe related ancestry into these regions, respectively (2, 39, 46). Second, the sweep haplotype counts rebound strongly in between these two admixture events, a period coincident with the re-emergence of local hunter gatherer ancestry reported across much of Europe (2, 4, 39, 46–48). Finally, the sweep counts appear to have undergone a further decline within the past thousand years in Iberian populations before recovering again in contemporary populations from this region (Figs. 2, S4). This trend aligns with previous reports of an influx of North African, sub-Saharan African, and Levantine related ancestries during the Moorish conquest of Iberia from ~700 CE and the subsequent resurgence in local European ancestry following the expulsion of Moor-related descendant communities over the ensuing centuries (39).

Importantly, all observed relationships between sweep presence and sample age were almost identical after accounting for the SNP missingness among the samples (i.e. redoing the LOESS analysis using residuals from a linear regression of sweep presence against SNP presence for all 456 samples; Fig. S4), indicating missing data was not a confounding factor in our analyses. Overall, our results closely

corroborate the temporal patterns of sweep signal degradation documented in ref. (1) and confirm that previously reported admixture events (2, 39) most likely caused the dilution of historic hard sweeps signals in European Holocene populations.

2.4. Estimating the onset of selection and genetic isolation of OoA migrants

Our LOESS analyses of the aggregate sweep patterns ([section 2.3](#)) suggest that sweep presence increased at a relatively linear rate in the ancestors of modern Europeans throughout the Upper Paleolithic period. To investigate this pattern further, we used the *lm* function in R v3.6.3 (49) to regress the total number of sweeps as a linear function of sample date. Notably, the linear function provided an excellent fit to the 22 ancient and modern samples (see [section 2.2](#) for sample list), with an adjusted-R² of 0.7048 (Fig. S11A). Under the assumption that sweeps have aggregated in an approximately linear fashion since humans first left Africa, we explored the age when this linear model would indicate the date estimate for zero sweeps (i.e. the predicted x-intercept in the regression model), as this provides a rough estimate for the initial isolation of the OoA population. To account for the uncertainty in the specimen age, for each specimen we sampled ages from a Gaussian distribution that was parameterized by the reported mean and standard deviation estimates (Table S10). For each set of sampled ages, we used the bootstrap *boot* package v1.3-24 in R (44) to resample the residuals and refit a linear model, to determine 1,000 samples for the x-intercept. We aggregated the x-intercept samples from each of the 1,000 sets of sampled dates and then determined the mean x-intercept to be 83,141 yBP and the associated empirical 95% confidence interval to be between 72,369 and 97,284 yBP.

Since the linear regression model assumes that hard sweeps will accumulate linearly through time – an assumption that may be unrealistic given the complexities of Western Eurasian evolutionary history – we also performed a more extensive analysis that explicitly models key aspects of Eurasian demography and evolutionary history, drawing the relevant parameters from recent population genetic studies of Eurasian history. Specifically, we simulated a demographic scenario where novel beneficial mutations arise at random in a single panmictic population over the last 200,000 years, with the mutation frequency depending on the current effective population size (i.e. beneficial mutations are more[less] likely to occur as N_e gets larger[smaller]). The population size dynamics are based on N_e estimates leading up to Early European Farmers (EEF) from ref. (50), which included ancient Eurasian samples in their inference procedure. For simplicity, we ignore other historical events in our model, such as the separation of Main Eurasian and Basal Eurasian lineages and also the Neandertal admixture event. Using the coalescent simulator msms (51), we simulated 5,000 selected allele frequency trajectories under this evolutionary model. For each selected locus, we also simulated linked neutral genetic variation data across a 5Mb region for the hypothetical EEF population from ~8ka (i.e. LBK branch in ref. (50)) and ran these sequences through SweepFinder2 to filter out selected loci that did not leave a significant sweep signal in this population. To ensure that the simulated data match the statistical properties of the ancient data used in the present study, we replicated the empirical SNP ascertainment scheme by conditioning on SNP presence in a simulated African population and also generated the same number of simulated 5Mb sequences as observed for the Neolithic Anatolian

population in the present study. Similarly, selection coefficients were sampled from an exponential distribution with a mean selection coefficient of $s = 1\%$, which leads to selection coefficients that broadly match those estimated from our sweeps (s ranging between ~ 1 to $\sim 11\%$; see ref. (1)). More details of our simulation approach, including command line parameters and estimation of selection coefficients, are available in ref. (1).

To infer the earliest time for the onset of selection that best fits the data under our evolutionary model, we removed all simulated loci with a significant SFS signal that started prior to time point x , and then averaged the frequency trajectories of remaining loci to estimate the aggregate probability of observing a sweep haplotype across time. This is equivalent to estimating the proportion of all sweeps that are observable at each time point, conditional on the sweep arising after time point x and being detected by SweepFinder2 in the EEF population 8,000 years ago. Additionally, to incorporate the statistical properties introduced by missing data and sample pseudohaploidization (see [section 2.5](#)) in our estimation, we modeled the probability of detecting a particular sweep haplotype in an individual as $p_x = (1-f_x)^2 \times 0.061 + 2f_x(1-f_x) \times 0.256 + f_x^2$, where f_x is the frequency of the sweep at time point x . In other words, we are estimating the expected weighted frequency of the beneficial haplotype at a given time, where the genotype frequencies (assuming Hardy-Weinberg equilibrium) are weighted by the estimated probability of detecting a sweep haplotype given that genotype (see [section 2.5](#)). The subsequent estimates of p_x are then averaged over all selected loci to obtain the probability for detecting a sweep haplotype at time x .

To compare the simulated results to our empirical estimates, we used maximum likelihood (ML) to measure the fit of key ancient and modern samples to the predicted p_x value, varying the earliest onset of selection over successive 1,000-year intervals between 25ka to 150ka. Because our simulations were based on a single panmictic population, we only estimated the ML function for ancient Eurasian specimens >30 ky old, as more recent specimens are likely to be affected by the substantial structuring observed in West Eurasian populations that arose during the Last Glacial Maximum ~ 30 -15ka (52), and consequently are only expected to contain a subset of all sweeps that occurred along the ancestral lineage that leads to the EEF population. Using the same samples that were used for the linear regression analysis reported above (other than samples dated within the past 30ka), we inferred the probable onset of selection to be 79ka, with a 95% confidence interval spanning between 74 and 91ka (Fig. S11B). Thus, the linear regression and model-based approach arrive at very similar point estimates, ca. 80ka, and concordant confidence intervals (97-72ka and 91-74ka, respectively) for the earliest starting time of selection for the hard sweeps we have detected.

Notably, samples from the Mesolithic (which were not included in the model) have $>30\%$ fewer sweeps than expected assuming sweeps aggregate at the constant rate across time. This may result from our model conditioning on the presence of sweep signatures in a hypothetical single panmictic Mainland Eurasian population during the Neolithic, whereas the sampled individuals come from structured Mesolithic West Eurasian populations. Each population is expected to accumulate local sweeps, increasing the number of sweeps overall but depressing the proportion of observed sweep haplotypes in any single subpopulation below what is expected under a panmictic model.

Taken together, the two approaches suggest that following the early initial isolation of the OoA migrants from other African populations (e.g. around ~100ka based on genomic data (35)), the Main Eurasians became genetically isolated from other contemporaneous populations and started to accumulate hard sweeps from around 80ka (~74-91ka). The resulting prolonged period of genetic isolation of ~20 to 30 thousand years is far more compatible with the large number of hard sweeps observed in the earliest Oceanic and Eurasian groups than the commonly used 50-60ka estimate for the OoA movement, which is largely based on the mean time of Neandertal gene flow into Main Eurasians. The estimated ~80ka origin for the period of genetic isolation and selection in the ancestral Main Eurasian group also closely coincides with archaeological evidence for the widespread dispersal of AMH populations throughout the Arabian Peninsula area (including the southern Iranian coast) during the final MIS 5 moist phase ~80ka (Fig. 5). Paleoenvironmental reconstructions indicate AMH populations would have been rapidly fragmented and isolated by the return of cold arid conditions shortly thereafter, especially during MIS 4 (~71-57ka), which is consistent with the absence of archaeological evidence for AMH populations in the Arabian Peninsula during this time (53, 54). The population fragmentation caused by these movements may also have initiated the separation of the Main and Basal Eurasian populations within the Arabian Peninsula area, which genetic estimates indicate occurred around this time (35). The above events are shown in Fig. 4, as part of the Arabian Standstill model, while the relationship to the moist phases, and timing of major global drying and cooling events following the onset of MIS 4 (~71ka) are indicated in Fig. 5.

2.5 Statistical properties of the sweep haplotype detection method

An important consequence of the pseudohaploidization process for our sweep haplotype detection method is that samples that are heterozygous for a specific sweep haplotype may be more likely to be classified as non-sweep carriers, leading to underestimates of the true sweep haplotype frequency in populations where the sweep is at intermediate frequencies. To quantify the impact of pseudohaploidy on our estimation procedure, we measured the presence of each sweep using the phased 1KGP modern datasets, and again after randomly sampling a single allele at each marker SNP to mimic the pseudohaploidy of ancient samples. As expected, the frequency of the sweep haplotype was consistently underestimated for pseudohaploid samples, and underestimates were proportionate to the level of heterozygosity of the sweep haplotype in that population (underestimating the sweep frequency by as much as 20% when the true frequency is around 50%; Fig. S09).

For individual samples, pseudohaploidization will not affect sweep detection in samples that are homozygous for the sweep haplotype (i.e. sweep homozygotes), even in ancient samples where information from some of the marker SNPs may be missing. While errors in allele calling or recombination could potentially result in other alleles appearing at the marker SNPs, the potential impact of these factors will be diminished to some extent because our detection method does not require all SNPs to be present. Thus, we expect that false negatives will be rare and interpret the patchy sweep detection patterns observed across ancient samples to imply that no sweep was fixed prior to the

colonization of Eurasia ~55-50 thousand years ago, although *DOK5* and *LIN28B* appear to have been in very high frequency in the Oceanic and IUP samples.

Ancient samples that carry two non-sweep haplotypes, i.e. non-sweep homozygotes, can still be falsely called as sweep carriers. Such false positive sweeps are expected to largely depend upon the number and informativeness of missing marker SNPs and the similarity of the alleles on non-sweep and sweep haplotypes. Further, our previous results suggest that ancient samples that carry one sweep haplotype and one non-sweep haplotype (i.e. sweep heterozygotes) will tend to be called as non-sweep carriers, but this will be ameliorated to some extent by the factors that impact false positive calls (i.e. the patterns of SNP missingness and allelic similarities between sweep and non-sweep haplotypes).

Accordingly, we quantified the impact of pseudohaploidization on the sweep haplotype calling rate for non-sweep homozygotes (i.e. the false positive rate; FPR) and for sweep heterozygotes in ancient samples. To estimate the FPR, for each sweep we randomly sampled 2,000 non-sweep haplotypes from the 1KGP phased samples. We then randomly paired these haplotypes to create 1,000 diploid genomes and sampled a single allele for each marker SNP to generate pseudohaploids. Finally, we set specific marker SNPs to missing, according to the SNP missingness observed in the ancient samples and modern samples that were used to infer the timing of the onset of the selection pressure for each sweep (see [section 2.2](#)). To measure the calling rate for sweep heterozygotes, we repeated the process outlined above after randomly replacing one of the non-sweep haplotypes with a sweep haplotype.

Applying the same test criteria used to detect sweep haplotypes – i.e. the sweep is called in at least three of the six possible tested categories (i.e. combinations of 90% or 95% of the top 10, 20, or 30 marker SNPs) – we found that the FPR was generally below 10% for all combinations of sweeps and samples (Fig. S10). As expected, the sweep detection rate is systematically elevated in sweep heterozygotes (i.e. when replacing one of the non-sweep haplotypes with a sweep haplotype), and this is strongly positively correlated with the FPR (Fig. S10). This positive correlation appears to be largely the result of non-sweep haplotypes being more like the sweep haplotype, as this increases the probability that alleles on the non-sweep haplotype will match the homologous sweep marker allele.

Taken together, our results indicate that our sweep detection method will tend to underestimate sweep presence in ancient samples. Based on the criteria used in the study (i.e. the sweep is called in at least three of the six possible tested categories), only around 26% of sweep heterozygotes will be called as sweep carriers on average (Fig. S10). Because the FPR is comparatively lower under the same criteria (~6%; Fig. S10), on balance we are more likely to miss sweep haplotypes in heterozygotes rather than to falsely call them in non-sweep homozygotes.

2.6 Recalibration of age of Neandertal admixture

Genomic data reveals that Neandertal admixture with AMH has been occurring for some time. For example, a limited early admixture event between Neandertals and an early human lineage related to modern AMH (possibly between 270-370 ka, although this is unclear) appears to have resulted in the replacement of the Neandertal Y and mitochondrial genomes by early modern human variants (43).

This admixture event may have potentially involved the late-surviving Middle Pleistocene fossil *Homo* group recently identified in the Levant (55), or *Homo heidelbergensis* in other areas. However, modern global non-African populations contain Neandertal DNA resulting from a much more recent admixture event between Main Eurasians and Neandertals around 50-60ka, thought to have occurred in the Near East immediately prior to the dispersal of AMH across Eurasia. The timing of this admixture has been studied using the size of the Neandertal genomic fragments in the Ust'-Ishim AMH specimen from western Siberia, whose age and high-quality genomic data provide a useful calibration point close in time to the events. The Ust'-Ishim femur has been radiocarbon dated at (41,410 +/- 960 BP), calibrated via IntCal20 at 42.9-46.0ka cal BP (68% CI) (41) (Table S10). The original calibration via IntCal13 was 44-45.8 (68% CI), or 43.2-46.8ka cal BP (95% CI) (52, 56). A recombination clock suggested that 232-430 generations would be required to produce the size distribution of introgressed Neandertal fragments in the Ust'-Ishim genome, under a simple model of a single pulse of Neandertal admixture. This would give an admixture date of 50-60ka using the standard generation time of around 29 years (52, 56). This temporal range was constrained by more detailed modeling which indicated the credible range of peak Neandertal gene flow was 7,521 +/- 854y (260 +/- 30 generations) earlier than Ust'-Ishim (equating to 50-54ka with the IntCal20 calibration), again under a single pulse model (52, 56). However, two distinct size classes of Neandertal fragments were identified in the Ust'-Ishim genome, such that a model of two admixture pulses was much more strongly supported (52, 56). The two-pulse model indicated the Ust'-Ishim genome Neandertal content resulted from a major early admixture event (estimated at 6,660 +/- 218y, or ~228 +/- 21 generations before Ust'-Ishim, or 49-53ka), along with a minor secondary event that occurred considerably later (1,258 +/- 113y, or ~43 +/- 4 generations before Ust'-Ishim, or 44-47ka). The latter event was potentially restricted to just the Ust'-Ishim lineage and took place several millennia after the dispersal of AMH groups across Eurasia.

Recent modeling suggests that the admixture date estimates may be sensitive to inhomogeneous recombination rates and have difficulty discerning a single pulse of admixture from ongoing gene flow over potentially hundreds of generations (57). As a result, the 50-54ka estimate should be regarded as a credible range for the mean time of Neandertal gene flow rather than an absolute range, as this may have started earlier. Similarly, recent analyses using different recombination clocks have suggested a smaller number of generations between Ust'-Ishim and the main Neandertal introgression event, potentially as few as 119 generations, or ~3500y (37). This would suggest the credible range for the main Neandertal introgression event as recently as 46.5-49.5ka, slightly younger than current dates of confirmed AMH presence in Eurasia.

Given the uncertainty around these estimates, we adopt a conservative date estimate of ~50-54ka for the main Neandertal gene flow. Importantly, this window aligns closely with a prolonged period of northern hemisphere warmer temperatures recorded in ice core records between the intense cold periods of Marine Isotope Stage (MIS) 4 beforehand (71-57ka), and Heinrich 5 afterwards (49-47ka), shown in Fig. 5. As a result, this period is likely to have seen a rapid increase in size and movement of AMH populations, increasing the likelihood of interactions with neighboring Neandertal populations.

The younger bound for the timeframe of the estimated Neandertal gene flow (50ka) agrees with, and is presumably also constrained by, the AMH settlement of Australia given that Indigenous Australian and

New Guinea populations appear to possess the standard Main Eurasian ~2% Neandertal signal, and show no signs of genetic input after their initial settlement of the Sahul continent (mainland Australia, Tasmania, New Guinea and related islands) (58–60). AMH settlement of Australia has been estimated by several genetic and archaeological studies at being close to 50 ka or slightly earlier, with a range of dated archaeological sites rapidly appearing across Australia between 50–47 ka. In contrast, the few dates earlier than 52 ka have been widely questioned (58–60). Similarly, the notable lack of clear archaeological evidence for AMH presence in southeast Asia prior to this period has been highlighted (61, 62).

The presence of Neandertal genomic content in Aboriginal and New Guinea populations at comparable levels to other Out of African AMH populations suggests that their ancestral lineage diverged from other Main Eurasians after the majority of Neandertal admixture had occurred. Hence, while it is possible that Neandertal admixture with the Main Eurasian lineage may have been ongoing (potentially for many thousands of years) prior to the 54–50 ka estimates for the geneflow (57), it seems likely that the Main Eurasian dispersal (including Ust'-Ishim and the Oceanic group) had not occurred prior to this date. In contrast, the dates associated with AMH settlement of Australia indicates it had definitely occurred by 50 ka.

The movement from the Arabian Peninsula area to Australia/New Guinea would presumably take some time as this represents an overland distance of around 18,000 km, and required major marine voyages through eastern ISEA, even with increased land exposure due to ~50 m lower sea levels (62, 63). If one millennia is allowed for this movement as a relatively conservative estimate (*i.e.* an average of 18 km/yr, which is lower than some suggestions for hunter-gatherer movement through new territory (64)) this would mean that the Neandertal genomic content of the Sahul populations probably constrains the main Neandertal admixture to being older than ~51 ka. As a result of the above lines of evidence, we assume a date of ~54–51 ka for the Main Eurasian dispersal as our best estimate and use this in the main text and Fig. 4. Importantly however, a more conservative ~50–54 ka date (or even 50–60 ka) would not change our conclusions.

One interesting implication of an inferred dispersal of AMH populations from the Arabian Peninsula to New Guinea before 50 ka is the rapid nature of the movement, which has been noted previously and has raised questions about the apparent speed of progress through ISEA given that over-the-horizon marine voyaging for hundreds to thousands of individuals was required (65, 66). While archaeological evidence during the Arabian Standstill phase is limited as noted above, the potentially prolonged restriction (*e.g.* from >71–57 ka) of main Eurasian populations to coastal sites, such as the southern end of the Euphrates river valley created by lowered sea levels in the Arabian Gulf, has been used to suggest a potential development of nascent marine technology (67). Alternatively, analyses of southern African deep mitochondrial branches have been used to suggest early AMH origins in paleo-wetland areas, and that nascent watercraft technology may have been developed early in our history (68). Either of these scenarios could provide a potential explanation of the apparent lack of noticeable delay for the development of marine technology during the ISEA migration, addressing debates about the extent to which purposeful voyaging and boat construction was possible during this event (65). Interestingly, while recent reports place an initial, potentially short-lived, presence of AMH in southern Europe at

54ka (69), the successful settlement of Europe appears to have been comparatively delayed until ~47ka (70, 71) possibly due to the cold conditions of Greenland Stadial 13/Heinrich Event 5 (Fig. 5), and the requirement for further genetic adaptation to cold conditions, first seen as the sweeps appearing in the IUP specimens (Figs. 1, 4, Tables S2, S9). Genetic studies of the Zlaty kun specimen from Czechia have suggested that it might represent the earliest member of the OoA population in Europe (37), but unfortunately partial genomic coverage, a lack of accurate dating and phylogenetic results confound interpretation. As a result, for the moment we have conservatively regarded it as being an early part of the initial IUP invasion of Europe depicted in Figure 4, potentially around 45-47ka.

2.7 Location of Neandertal admixture event and Main Eurasian dispersal

While the geographic location of the inferred Neandertal-Main Eurasian admixture remains unclear, it is likely this took place in the Arabian Peninsula area as essentially all modern and ancient non-African individuals outside of this area appear to carry introgressed Neandertal DNA from this admixture. (Lineages descended from the extinct sister Basal Eurasian group, such as the Bedouin, are thought to have occupied the same area (Fig. 4) but have lower amounts of Neandertal DNA.) The long-term presence of adjacent AMH and Neandertal populations in the northern Arabian Peninsula area provides further support. The apparent consistency of the amount and distribution of introgressed Neandertal DNA in modern non-African human populations suggests that the initial admixing Main Eurasian population was both relatively small, and also stayed together for some time either during or after the admixture phase to allow for the homogenization of the Neandertal genetic contribution across the population prior to the subsequent dispersal across Eurasia. Indeed, some studies have estimated the starting Neandertal genomic content in the admixed AMH population may have been as high as 10% (72) prior to purifying selection removing deleterious alleles, although it has been noted that this value would be influenced by the nature and timing of the Neandertal gene flow (57). Similarly, analyses of long-term selection against the Neandertal genomic ancestry content found that most of the decline occurs quickly within the first few hundred generations (73). Interestingly, a large-scale global genomic analysis indicated that between 2-4 Neandertal individuals would be sufficient to explain the allelic diversity of Neandertal DNA observed in modern AMH populations (40). The strong implication is that the long-term effective population size of the admixing OoA AMH population must have been very small indeed (potentially a few hundreds) if as few as 2-4 Neandertal individual admixture events could produce an initial post-admixture Neandertal genomic content of 2-3%, or potentially even as high as 10% or more. This is further evidence that the ancestral Main Eurasian population existed as a small population in late MIS 4, consistent with the lack of MIS 4 archaeological records in the Arabian Peninsula area, outside of southern Iran (74).

Paleoanthropological studies suggest early dispersals out of Africa (OoA) and throughout the Arabian Peninsula occurred during climatic moist phases as far back as 400ka, although it is currently unclear as to which movements might represent AMH (53, 54, 75). By early MIS 5, around ~130ka, stone tools (75) and footprints (76) indicate AMH presence (Figs. 4, 5) with initial sites ranging from northern Arabia, to coastal sites such as the Levant (Skhul and Qafzeh) and the Arabian Sea (Jebel Faya) (54,

75, 77). Recent fossil discoveries have raised the potential that populations around 140-120ka in the Levant and Negev Desert might have represented a separate, late-surviving, group of Middle Pleistocene *Homo*, which may have interacted with initial AMH populations moving OoA (55). However, no genetic signature of this group has been detected in modern genomes, and archaeological evidence suggests that the MIS 5 Arabian Gulf populations in sites like Jebel Faya resulted from a southern dispersal from north eastern Africa across the Red Sea and southern Arabian Peninsula (Fig. 4) and do not appear to have been connected with northern groups (54, 77). However, as noted above, a late-surviving, group of Middle Pleistocene *Homo* in the Levant area may have provided the early human-like mtDNA and Y variants that introgressed into late surviving Neandertals somewhere between 270-416ka (43). Paleoenvironmental reconstructions also suggest the Levant may have been cut off from AMH populations to the south for much of the past 130ka, or more (53, 75).

AMH occupation throughout the interior of the Arabian Peninsula and potentially the adjacent Iranian plateau was associated with short periods of relatively moist climatic conditions in MIS 5e, 5c, and 5a, around 125, 100, and 80ka (Fig. 5), when paleorivers and lakes were apparent (74, 78). Lowered sea levels during glacial conditions have been proposed to have facilitated AMH movement out of Africa either across the southern margin of the Red Sea and Bab el-Mandeb Strait into the adjacent biodiverse Yemen highlands (southern route; (54, 76, 77, 79)), or northwards alongside the Red Sea or Nile River Valley, and through the Sinai (northern route; (54, 75)). It has been proposed that arid or mountainous conditions to the north, east, and west of the Arabian Peninsula area in combination with periodic cold arid conditions, limited colonization outside this area (53, 54, 75, 77, 78, 80). While archaeological evidence demonstrates AMH presence across the Arabian Peninsula during the wet climatic phases, the lack of continuity in material cultures through time has been interpreted as indicating that the intervening cold arid spells (MIS 5b, 5d) caused population contraction and local abandonment. As a result, the predominantly cold arid conditions between 100-57ka (Fig. 5) could help explain the limited signs of AMH dispersal much further than the Arabian Peninsula during this time, with archaeological data suggesting population isolation and primary occupation of coastal sites during arid phases (81). Important coastal sites include the Arabian Gulf, where lowered sea levels during cold stadial periods would have largely exposed the entire Gulf region potentially creating a site allowing AMH population continuity over long periods of time (54, 67, 77, 81). The exposed Gulf is thought to have been a broad river valley featuring numerous subterranean water sources (submarine freshwater springs exist in the southern and southwestern areas today) and a marshy southern margin, creating a potentially important site for AMH populations in the cold arid MIS 4 conditions between ~71 and 57ka (54, 67, 77), although currently the archaeological evidence for MIS 4 occupation in the area is limited to southern Iranian sites such as Boof Cave (74) that borders the northern Gulf. The long-term AMH occupation of this area though different periods of human history has been described as the Arabian Gulf Oasis model (54, 67), and recent genetic studies suggest that Basal Eurasian populations may have also occupied this area (82). The Arabian Gulf would have remained a potentially stable occupation area until the early Holocene rise in global sea levels to -40m (~10,000ya) which would have flooded much of the low-lying areas, potentially concealing many archaeological records of earlier occupation. The timing of this inundation is consistent with inferred dispersals of Basal Eurasian populations out of this area in the early Holocene (82), and the subsequent decrease in apparent sweep frequencies observed across central/southern Europe (Fig. 1; (1)).

Apart from potential MIS 4 southern Iranian sites (74), the current lack of archaeological evidence for AMH presence in the Arabian Peninsula during MIS 4 has been interpreted as indicating a local abandonment of the area due to the cold arid conditions (54, 75, 81). Consequently, it is important to consider that the extended phase of isolation and strong genetic selection indicated by the hard sweeps may have occurred in a location somewhere outside the Arabian Peninsula area. However, the requirement for genetic isolation from other African populations over the extended 30,000 year period suggests that it is unlikely to be a location on mainland Africa, such as in northern Africa (e.g. Egypt or Morocco). This is another relatively isolated area where archaeological evidence indicates a long AMH presence (54), but also has extensive potential connection routes for AMH populations (83). Since there is little to no evidence during MIS 5-4 for long-term AMH presence outside of either Africa or the Arabian Peninsula area to act as an alternative, the genetic patterns would appear to suggest that despite the relative lack of archaeological records in the greater Arabian Peninsula area, at least a single AMH population (and potentially two – the Main and Basal Eurasians) survived from the end of MIS 5 through MIS 4 somewhere. Potential locations include poorly dated or explored sites on the Iranian plateau, where Middle Paleolithic sites such as Boof Cave on the northern coast of the Arabian Gulf contain MIS 4 archaeological dates (74), although it is not certain that they are AMH in origin. Alternatively, other potential cryptic refugia in the Arabian Peninsula area include the southern Arabian coast of the Yemen highlands, and the southern areas of both the Red Sea and Arabian Gulf (54). Both latter sites include significant areas now under water, which may explain the apparent lack of archaeological records, especially if the ancestral AMH populations (e.g. Main and Basal Eurasians) remained small, or geographically constrained during the harsh conditions of MIS 4. Overall, the Arabian Gulf is a good match to the genetic, archaeological, paleoenvironmental and geographic patterns and as a result is depicted in Fig. 4 as a potential location for a long-term population refugium. However, while we have used the term Arabian Standstill to refer to this event, we acknowledge that further evidence will be required to confirm the exact locations where the ancestral OoA population(s) underwent isolation (from ~100ka), and subsequent strong genetic selection (from ~80ka).

The genetic data suggest the following model for the Arabian Standstill. The ancestral OoA population moved into the Arabian Peninsula area during either the MIS 5c moist phase ~100ka, or potentially the subsequent moist phase starting ~85ka (MIS 5a) after having separated from other African groups earlier. Previous AMH populations in the Arabian Peninsula area during MIS 5e (~125ka) had abandoned the area during the cold MIS 5d phase and did not contribute genetically to subsequent groups. The MIS 5a moist phase caused AMH population expansion and movements throughout the area but was quickly followed by the return of severe cold arid conditions during MIS 4, which caused a phase of population contraction and isolation that explains the separation of the Main and Basal Eurasian AMH populations ~80ka. The Main Eurasian population subsequently remained genetically isolated for a long period between ~80ka (the estimated origin date for the hard sweeps), through MIS 4 and until warming conditions ~54-51ka when the Main Eurasian group dispersed across Eurasia. During MIS 4 the average temperatures consistently declined, potentially creating an environmental trap around refugial areas (Fig 5) (53, 75), where small populations might leave little archaeological record. As noted above, the genetic signals indicate the AS population(s) were of small size, and the Main Eurasian population appears to have contained just two African L3 haplogroup mitochondrial sub-branch lineages, which are ancestral to the N and M haplogroups that gave rise to all mitochondrial

lineages outside of Africa. This scenario is shown in simplistic fashion in Figure 4, with the Arabian Gulf depicted as the location of the Arabian Standstill population(s). While the geographic source of the Neandertal admixture is unknown, the location depicted in Figure 4 corresponds to the Zagros Mountains of Iran, which had a concentration of Neandertal individuals geographically close to the inferred location of the Arabian Standstill population. Other potential areas include the Levant and the Caucasus regions. It is possible that the more cold-adapted Neandertal populations in these regions expanded further southwards during cold periods, and retreated northwards during warmer periods while the warm-adapted AS population potentially mirrored these movements. In this way, effective contact between the populations may have been minimized despite the close geographic proximity and availability of corridors such as the Euphrates River valley between them. The timing of peak Neandertal gene flow into the Main Eurasian population is estimated to have been around 54-51ka (see above) during an extended period of wetter climatic conditions when AMH populations may have expanded northwards into Neandertal territory (Fig. 5), although it possibly had been ongoing at lower rates over a much longer time prior to this period (57). It is notable that while northern hemisphere conditions were warming during the 54-51ka period, the temperatures in the Arabian area continued to fall (Fig. 5), potentially creating a push-pull factor encouraging AMH population movement northwards and into the rest of Eurasia.

The migration routes indicated in Figure 4 are a synthesis of current archaeological and genetic data but involve considerable amounts of inference and had to be simplified for visual clarity. This simplification includes the initial movements OoA and across the Arabian Peninsula ~130ka towards Jebel Faya in the UAE, shown as either the southern (via Yemen) or northern (via the Sinai) routes. This initial MIS 5e phase is combined visually with the subsequent movements throughout the interior during wet phases including around 80ka, which is shown as resulting in the separation of the Main and Basal Eurasian populations (Figs. 4, 5). The latter split has been shown towards the lower Arabian Gulf area due to Basal Eurasian genetic ancestry exhibiting an east to west gradient in the area (82), and high levels present today in groups such as the Bedouin. While Basal Eurasian ancestry is currently most common in northern Iran, a movement into this area is not shown in Figure 4 purely for visual simplicity. For similar reasons, the settlement of Europe is simplified and shown as three pulses (as there is no genetic evidence from the earlier temporary presence prior to Heinrich 5 (69), unless this is represented by the Zlaty kun individual (37, 38)), with the Initial Upper Paleolithic (IUP) and (Proto)Aurignacian entering via the southeast near Bulgaria, and the Gravettian diverging from the Aurignacian within Europe. Tools at IUP and Proto-Aurignacian sites appear to represent dispersals from at least two cultural phases related to the Levant area (Emiran and Ahmarian), consistent with their divergent genetic backgrounds including the hard sweep signals. Based on the shared hard sweep heritage, the Gravettian is shown as diverging from the Proto-Aurignacian lineage and crossing the exposed Black Sea shelf before appearing for the first time in the Sunghir specimens, shortly after 35ka. While the earliest Gravettian sites currently appear in the mid-upper Danube and Crimea, it was not possible to depict this detail.

Similarly, the movement into eastern Eurasia has been simplified to show a likely northern IUP route resulting in the Tianyuan lineage, and separate southern routes into Southeast Asia and Oceania. The

initial phase of the southern route might be considered more likely to have followed the Arabian Gulf but has been depicted further east simply for presentation clarity.

The proposed route through lower southeastern Asia (Thailand, Vietnam, southern China) follows river courses through the savannah habitat thought to exist in the area at the time (63). Similarly, early AMH movement throughout the broader Southeast Asian area has been proposed to track savannah habitat which presumably was somewhat familiar to the African ancestral ecosystems to which these groups had originated. Inferred areas of hominid genetic introgression (63) are depicted but are likely underestimates of the true number of events. While these movements on Figure 4 are necessarily simplistic depictions of far more complex processes, they are designed to highlight key points of the model.

2.8 Using sweep haplotype presence to reconstruct Paleolithic Eurasian population history

The spatiotemporal patterns of the hard sweeps provide a view on the timing and location of selective pressures, and potentially also carry information about broadscale historical migration patterns during the Upper Paleolithic, which remain poorly understood. Because the combination of pseudohaplodity and missing SNP data will make detection of sweep haplotype presence in single ancient samples less reliable, we combined sweep calling results from multiple ancient and modern samples to create temporally consistent consensus signals. To identify the earliest group of sweeps we examined isolated populations thought to be formed from the initial Main Eurasian population movement that colonized ISEA and Sahul (i.e. the former landmass comprising modern Australia and New Guinea) by ~50ka (which we term the Oceanic group), shortly after the main Neandertal gene flow ~54-51ka ([section 2.7](#)). We searched for the presence of sweeps within genomic data from ancient and modern individuals of the Andaman Islands (ref. (84); $n = 1$), Australia (ref. (85); $n = 2$), Vanuatu (refs. (85, 86); $n = 4$) and Papua New Guinea (ref. (40); $n = 28$; comprising individuals from the Highlands, Sepik, and Bougainville populations, using a 35% frequency of the sweep loci within any of these three groups as the cut-off for detection). While the number of individuals surveyed in several of the Oceanic groups was small, the combination of the relative genetic isolation of these groups following the initial AMH colonization, and the four distinct sampling areas across a broad geographic region, is expected to provide a reasonable estimate of the hard sweep haplotypes that were present at moderate frequencies in the initial colonizing population. (If any earlier AMH groups were present in the southeast Asia area they do not appear to have contributed genetically to modern populations, as the latter all feature the standard Main Eurasian ~2% Neandertal genome content, along with additional proportions of Denisovan genomic DNA (62, 63). In this regard, a number of recent studies have questioned stone tool or fragmentary fossil sites in Asia used to support the much earlier presence of AMH as opposed to earlier Homo species (e.g. *H. heidelbergensis*) or archaic hominid groups such as Denisovans (62, 87).)

We identified the presence of 31 of the hard sweeps (Table S2) within the five samples from the Oceanic group, with 28 being detected in multiple groups or multiple individuals (90%), and just three detected in only one individual (1 each in Vanuatu, Australia, and the Andaman Island specimen). The number of sweeps detected in Australia ($n = 21$), Papua New Guinea ($n = 20$), and Vanuatu ($n = 22$)

was highly consistent (i.e. around two thirds of the 31 sweep loci) despite the very different number of samples in each area (from two in Australia versus 28 in PNG), in contrast to 12 within the Andaman Island sample. The latter may relate to the high false negative rate for heterozygote loci in the single sample available for this area, and/or the very small long-term population size of the Andaman Islands leading to higher rates of genetic drift. The number of shared sweeps between each Oceanic area is consistent with their known phylogenetic relationships, with the greatest similarity between Papua New Guinea and Vanuatu (16 shared out of 26 total, or 62%), followed by Australia and Vanuatu (16/27, 59%) and Australia and Papua New Guinea (13/28, 46%), with the most distant being Andaman Islands versus the others (Vanuatu 9/25, Papua New Guinea 9/23, Australia 8/25, average 35%) (Tables S2).

These patterns suggest that while relatively few of the sweeps were fixed within the initial AMH population moving into ISEA (potentially *DOK5*, *LIN28B* and *GTSE1*), many were at high frequency and as a result 23 (74%) have ended up in more than one geographic area. Due to the 31 sweeps being present immediately after the Main Eurasian dispersal, but not being of Neandertal origin (see [section 4](#)), we designated them as originating during the AS and therefore likely arising somewhere between ~80-55ka (Fig. 5, see also Fig. S11).

The oldest group of AMH samples are those of the Eurasian Initial Upper Paleolithic (IUP) groups which were broadly distributed from eastern Europe, across eastern Eurasia to Mongolia. The origin of these groups appears to be within the Levant Emiran culture (88). The four available IUP genomic sequences were from Bacho Kiro, Bulgaria ($n = 3$, CC7-335, BB7-240, F6-620, dated 45-43ka), and Zlaty kun, Czechia ($n = 1$, with poor genomic coverage and an approximate date of 45ka). The Bacho Kiro genomic studies demonstrated a close relationship between the eastern Chinese Tianyuan specimen (40ka) and the European IUP specimens (38), and this is consistent with the pattern of shared hard sweeps. While the three Bacho Kiro specimens shared an average of 17% of their hard sweep signals with each other (reflecting the small number of samples, and lack of fixed loci in the Main Eurasian dispersal), the Tianyuan specimen shared an average of 19% with each individual, and 11 of the 32 (34%) hard sweeps observed across all the Bacho Kiro specimens. This pattern suggests a much more diverse origin for the IUP samples than those from the Oceanic group, and potentially relates to additional local Neandertal admixture events detected in the recent ancestry of many IUP samples (38), or potential population bottlenecks involved in AMH settlement of Oceania.

While the other very old specimen, Ust'-Ishim (45ka), had no associated archaeological evidence so could not be positively associated with the IUP, genomic data suggests it diverged from the IUP genetic lineage or perhaps separated from the Main Eurasians shortly before the IUP group (38). In this regard, while the Ust'-Ishim specimen only had eight hard sweeps, seven were shared with the IUP or Tianyuan specimens, and seven with the Oceanic group samples. However, Ust'-Ishim possessed only one of the IUP-Tianyuan specific sweeps (*LINC00293*), suggesting a separate origin. As a result, it has been depicted with a dashed line on Figure 4 indicating these uncertain origins. The Czechia Zlaty kun specimen has similarly uncertain origins and placement (37).

Interestingly, one hard sweep (*DOK5*) was fixed across all Oceanic and IUP samples (including Tianyuan) and the Ust'-Ishim specimen. This appears to be the closest to a fixed loci in the AS/Main

Eurasian dispersal detected in the study, although it was subsequently absent in some of the younger European samples.

The four IUP samples at Bacho Kiro and Zlaty kun (37, 38) were published after the first phase of analyses in this paper had been completed. As a result of their early age within the Main Eurasian dispersal, they effectively provide an independent test of the approach of using the Oceanic group samples to define the sweeps occurring within the AS. The IUP samples (including Tianyuan) contained 24 of the 30 (80%) AS hard sweeps defined by the Oceanic group samples, which is consistent with the small number of samples in both datasets, and elevated false negative detection rate. The remaining six AS hard sweeps absent from the IUP were detected in the next youngest Eurasian samples, suggesting they were indeed present in Europe/Eurasia but simply remained undetected in the IUP dataset.

In total, the IUP/Tianyuan/Ust'-Ishim specimens (45-40ka) contained eight hard sweeps that were not detected in the Oceanic group samples (*CCDC7*, *DHODH*, *DOCK3*, *LINC00293*, *METTL6*, *PAX1*, *WWOX*, *ZMYM6*) and so we assume these originated on the Levant (Emiran)/West Eurasian/IUP lineage somewhere between ~51ka and 45ka (or potentially as late as 40ka for *WWOX* and *CCDC7*, which are first detected in the Tianyuan specimen). Alternatively, it is possible that some of these hard sweeps may have been present in the Arabian Standstill population but simply were not present in the founders of the southern dispersal into ISEA and Sahul or were lost by drift early in the process.

Following the IUP/Tianyuan/Ust'-Ishim group, a distinct group of nine new hard sweeps are observed for the first time in two slightly younger western European samples, the 38ka Kostenki14 specimen in western Russia (*ANKS6*, *BAIAP2L1*, *DNAH7*, *FANCD2*, *TBC1D7*) and 35ka Goyet 116 specimen from Belgium (*BAIAP2L1*, *DNAH7*, *ELMO1*, *ENAM*, *FANCD2*, *OIT3*, *MARS*). These individuals are associated with the Aurignacian Upper Paleolithic culture (~43/42-35ka; (89)), one of the earliest pan-European technocomplexes which evolved out of the widely distributed Proto-Aurignacian AMH groups, who were the successors to the IUP populations on the landscape (38). Both European Early Upper Paleolithic populations appear to result from distinct dispersal waves stemming from the Levant area. The initial IUP (ca. 47-43ka, expressed as localized cultures e.g. Bohunician in Ukraine) are thought to have descended from the Levant Emiran culture, while the following more widespread Proto-Aurignacian cultures (ca ~43-41k; (90)) descended from a separate movement related to the Levant Ahmarian culture (88). The initial movements into Europe are observed around 54ka, immediately before the extended severe cold periods of GS13/Heinrich Event 5 (Fig. 4), but successful settlement of Europe by the IUP was delayed until 47ka following this intense cold period and appears to have entered through southeastern Europe, where the earliest archaeological evidence in Bulgaria and Romania suggests a point of entry (69). The simplistic pattern shown in Figure 4 depicts two separate movements descended in some fashion from the stem lineage of western Main Eurasians originating from around the Levant area.

Only two samples with sufficient genomic coverage are available for the Aurignacian culture, although the geographic sampling is broad (Belgium and western Russia; Fig. 4). Given the small number of samples, it is perhaps surprising to see nine sweeps appear for the first time in this group. However, we can be reasonably sure this is accurate due to the widespread sampling of the period immediately after

the AS, comprising more than 41 samples (i.e. IUP/Tianyuan/Ust'-Ishim, Oceanic group samples) in which these nine sweeps are not detected. The distinct pattern of Aurignacian hard sweeps is consistent with genomic studies that indicate a near-complete population replacement between the IUP and Aurignacian (71). Therefore, we assume that the above nine sweeps occurred somewhere in the period ~51-38ka in the Levant (Ahmiran) or Western Eurasian Proto-Aurignacian populations during the movement into southeastern Europe. This is marked by the number 3 box in Figure 4.

Genomic analyses suggest the European Aurignacian technocomplex was relatively rapidly replaced ~35ka by the Gravettian technocomplex (which spanned from 35ka to ~25ka (89, 91, 92)), and which is suggested to have originated around the Danube River Valley and initially spread across eastern Europe. There are several ancient AMH samples during the Gravettian with sufficient genomic coverage for analysis, notably Sunghir 1-4 ($n = 4$) and Vestonice 16 ($n = 1$), along with other specimens in the Gravettian period from northern Siberia (e.g. Yana, $n = 2$). The potential route for this group is shown in Figure 4 and reflects the location of Sunghir (and Crimea) in western Russia as the earliest sampling points. While only one hard sweep (*SMCO2*) is detected for the first time in the Gravettian individuals (in the oldest Sunghir specimen, 34.6ka), the Gravettian specimens have a distinct pattern of hard sweeps that appears to be a unique combination of those seen earlier in the IUP and Aurignacian individuals (Tables S2, S9). For example, four of the eight IUP-unique hard sweeps, and five of the nine Aurignacian hard sweeps appear within the Gravettians. This pattern is consistent with genomic analyses that have suggested that Sunghir individuals and Vestonice-16 share a significant amount of ancestry with the Aurignacian Kostenki14 and Goyet 116 lineages (93). The pattern of hard sweeps is similar to that seen in the Yana individuals, although the latter have been identified as a local regional culture.

The sweep signals suggest that while the Gravettian represented a significant new genetic input, the source lineage was related to that of the Aurignacian lineage and the two had perhaps not been diverged for long as only one new hard sweep (*SMCO2*) is detected (Fig. 4, Tables S2, S9). An alternative model is that a large degree of genetic admixture occurred between the early Gravettian and late surviving Aurignacian individuals, and that on-going selective pressure was sufficient to return the Aurignacian sweeps to a high enough frequency in the Sunghir individuals for detection in our tests. However, given the very short time period between the end of the Aurignacian (~35k) and the early Sunghir 2 and 3 specimens (~34.6ka and ~34.5ka) there does not appear to be sufficient time or generations for selection to act across all the loci as required for the latter model, and an abrupt population replacement seems much more consistent with the results, and matches existing genomic analyses (89, 91, 92).

Interestingly, the Gravettian hard sweep patterns suggest that a younger specimen recovered from excavations in the 1970's at Bacho Kiro (BK-1653, 35.3-34.6ka) is potentially also Gravettian (Tables S2, S9). This specimen was found in layers with sparse artifacts, which were attributed to be Aurignacian and hence the specimen was as well (38, 71). However, the hard sweep pattern in BK-1653 shows the characteristic combination of IUP and Aurignacian hard sweeps seen in the other Gravettian samples. The age of the specimen is exactly at the transition from the Aurignacian to the

Gravettian, although like other Upper Paleolithic replacements the process is spatiotemporally complex.

It has been pointed out that the end of the IUP and onset of the Aurignacian (or Proto-Aurignacian at some sites), occurs around the time of major environmental changes that have been attributed to atmospheric effects associated with the Laschamps Geomagnetic Event around 42-41ka (90). Similarly, the end of the Aurignacian and onset of the Gravettian (~35ka) also occurs at the next largest geomagnetic excursion - Mono Lake at 35ka (90). Lastly, genetic and some archaeological estimates place the end of the Gravettian close to a further geomagnetic excursion, Rockall at ~26ka (94). While neither the end of the Gravettian or the Rockall excursion are well defined in time, the overall pattern of correlations raises the possibility that climatic shifts or other changes associated with major geomagnetic events have negative impacts on Upper Paleolithic European human cultures (90). Recent studies on three European small mammal species have identified similar major genetic transitions also occur at these three points in time, suggesting environmentally widespread impacts (95).

The last Upper Paleolithic sweep we detect is *FBXO15*, which appears in the Magdalenian culture El Miron specimen (19ka), towards the end of the Last Glacial Maximum (LGM). The El Miron genetic group (52) has been shown to be genetically related to the Goyet-116 lineage and indeed they share 13/34, or 38%, of their combined sweeps. The Magdalenian culture is a western European culture at the end of the LGM, which was superseded by the Azilian culture in western Europe during the Epipaleolithic period (represented by the 13.7ka Bichon specimen from Switzerland).

After the LGM (i.e. <18ka), three sweeps (*CCDC138*, *FBNI*, *PPARD*) appear in European populations of eastern hunter gatherers, of which *PPARD* was also detected in the older 24.3ka Mal'ta specimen (Irkutsk, eastern Russia). As a result of this observation and known gene flow from eastern areas at this time, we have designated these sweeps as likely originating in eastern Eurasia, and largely outside of our sampling area. This makes it difficult to ascertain the actual age of first appearance, although the oldest observation of any sweep in this group is 24.3ka with the Mal'ta specimen.

The last group of three sweeps (*GABBRI*, *MIR662*, *SLC7A1*) all appear in a 15.4ka Anatolian Hunter Gatherer specimen (96) known to have ~25% genomic ancestry from the Basal Eurasians (who diverged from the Main Eurasians prior to the main phase of Neandertal admixture). Given the long separate evolutionary history of the Basal Eurasian lineage, we designate these sweeps as potentially Basal Eurasian in origin, having presumably originated at some point after the divergence from the Main Eurasians. However, they could also represent adaptation in a local Anatolian population or nearby area. It is also interesting that both *GABBRI*, *MIR662* have been detected in modern African populations, raising the question of gene flow between Basal Eurasians and African populations at some point. Again, it is difficult to determine the origin date for these sweeps.

2.9 Potential implications of the reconstructed model of Eurasian dispersals 51ka onwards

It is worth noting that the use of Andaman and Oceanian (Aboriginal, Papuan, Vanuatu) genomes as the closest modern proxy to the AMH population dispersing across Eurasia at ~51-54 ka implies that the shared physiological features distributed across these modern groups may also comprise the best approximation of the initial western European populations of the Early Upper Paleolithic. The latter possibility is consistent with the rapid and widespread appearance of similar detailed figurative art cave art from 45-40ka across the breadth of the area covered in the initial Eurasian dispersal (90, 97) from southern Europe, to ISEA and Australia, where common themes involve red ochre handprints (negatives and positives), series of red ochre dots, as well as figurative depictions (e.g. animals). The fact that the Andaman and Oceanian populations have remained isolated since the initial dispersal means that the characteristics shared across these groups may provide a useful starting point to conceptualize traits (such as genetic, physiological, and behavioral) of the EUP western Eurasian groups prior to the selection imposed by the cold western Eurasian environment.

Recent studies of early Sri Lankan sites dated as early as ~48ka (98) have suggested the use of bows and arrows, nets, and advanced symbolism such as ochre bead necklaces. It seems likely that the AMH groups from this site were descendants of the original dispersal through Southeast Asia including the ancestors of the Oceanians, who clearly used advanced deep sea marine voyaging capabilities to cross to Sahul. Similarly, potential arrowhead formation has been recorded in southern France at 54ka (69). As a result, the implied combined set of technological and symbolic skills held by the dispersing Eurasian groups appears to be much further advanced than is often conceived. Nets in particular would be consistent with a prolonged occupation of the aquatic lower Arabian Gulf environment.

2.10 ‘Out of Arabia’: Climate changes in the Arabian Peninsula and wider region

In contrast to late Pleistocene climate changes recorded in Greenland (99), hydroclimate and temperatures over northeast Africa, the Levant and Arabia did not mirror the stadial-interstadial cycles of the North Atlantic (the glacial period). Instead, distinctly different regional changes appear to have been driven by orbital variability (most notably precession (78)), Eurasian snow and ice coverage (100), lowered atmospheric greenhouse gas concentrations and/or changes in monsoonal intensity and seasonality (101). To disentangle late Pleistocene hydroclimate and temperature trends, several key reconstructions have been generated from continuous marine records straddling the Gulf of Aden, the upwelling zone of the Arabian Sea and extending towards the southwest Indian Ocean (78, 102). Leaf waxes in the Gulf of Aden core RC09-166 are of particular importance. Aerially derived from the Horn of Africa and Afar regions, leaf wax (ice-volume corrected) δD provides a measure of the isotopic composition of precipitation used by higher plants to create their lipids, a proxy for aridity (78). Along with stalactite records (79, 83, 103), these show that during MIS 6, while there were large swings in aridity, the region experienced relatively high sustained mean annual temperatures (78, 102). Importantly, these relatively warm temperatures persisted through the Last Interglacial (MIS 5) with moist conditions during MIS 5e, 5c and 5a, consistent with relatively high precipitation and lake levels (104, 105), creating ‘green corridors’ across the region (78). These brief moist spells have been related

to signs of AMH presence throughout the Arabian Peninsula, especially around 80 ka (103). Towards the end of MIS 5 (~71 ka), mean annual temperatures dramatically decreased by ~4°C, accompanied by increased aridity into the last glacial period. Potentially importantly, AMH populations effectively trapped in the Arabian Peninsula area would have likely been exposed to considerably colder temperatures than these reconstructions suggest. The quantified estimates from the region are derived for alkenones and represent mean annual temperatures (106), implying the boreal winter was considerably more frigid (*i.e.* this is a conservative estimate of the temperature decline). Under the arid conditions of MIS 4 from 71ka onwards, apart from coastal sites and the Arabian Gulf, the biodiversity-rich mountain ranges >2,000m asl across Arabia (e.g. Shada and Hajar Mountains) (107) would have provided potential food and water resources, albeit at the cost of exposure to still colder temperatures. Population movements into these interior sites and around the Arabian Gulf during the brief moist phase around 80ka may have resulted in population fragmentation, potentially such as that separating the Main and Basal Eurasians depicted in Figure 4.

Importantly, the eruption of the Toba volcano in northern Sumatra around 74ka, immediately before the onset of MIS 4 may have amplified the impacts of this prolonged cooling phase (81). Tephra-fall deposits from Toba have been identified across Indonesia, southern continental Asia, the Indian Ocean and into the Arabian Sea (108–110). The Toba eruption was the largest in the last two million years and the associated injection of large quantities of sulfate into the troposphere and stratosphere has been estimated to be 10-100 times that of the 1991 Mt Pinatubo eruption, and as a result, likely had a substantial impact on incoming solar radiation (111). While contentious, resulting changes in surface albedo have been used to explain shifts in climate and vegetation patterns around the world at this time including aridification and replacement of woodland by open grassland in India (112), cooling in the south Atlantic (113), a weakened Asian Monsoon (114), and even the onset of MIS 4 (115). Analysis of the Greenland ice core records suggest amplified cooling following the eruption (116) although modeling studies suggest the impacts were highly variable globally, with major decreases in European and Asian temperatures and rainfall in the years following the eruption (117). There is considerable debate about the long-term impacts of Toba on AMH populations, with recent studies suggesting minimal changes in Africa, consistent with modeling results of the eruption impacts on African climate and rainfall (117). The same modeling study suggests the Arabian Peninsula may have experienced a significant decrease in rainfall (40%) and temperature (2–8°C) in the years following Toba, but it is unclear how long these impacts may have lasted.

The impacts of the prolonged cold conditions of MIS 4, with or without Toba as an amplifier, have been suggested to have radically changed modern human behavior and cognition by enforcing much greater emphasis of extended social and trading intergroup networks, reflected in changes in stone tool industries in southern Africa (81). The idea that human cognitive ability may have undergone significant selective pressure during MIS 4 is provocative given the large number of neural hard sweeps (9/31 functional genes) observed during the Arabian Standstill, especially since many of the loci are associated with mental developmental variation in modern studies.

From 57-50ka (MIS 3), reconstructions suggest a relatively brief moist period across the region, accompanied by sustained cool conditions, providing a potential green corridor for migration

northwards from the Arabian Peninsula (53, 54, 75, 78), very closely matched to the timing of the subsequent main phase of admixture with Neandertals ~54-50 ka, and estimated movement through the region and subsequent Eurasian dispersal 54-51ka.

Supplemental Materials 3. Functional classification and analyses of candidate genes

3.1 Refining the targets of selection

Because 52 of the 57 detected sweeps contained two or more genes, we attempted to refine the putative target of selection to a single gene in each of the 52 multigene sweeps using the iSAFE method (118). iSAFE quantifies the evidence for selection at each SNP within a predefined window that can be used to identify the underlying causal mutation. Using simulated 5Mb regions, the iSAFE developers showed that the selected SNP was among the top 20 ranked SNPs in 94% of cases (118). Accordingly, the proportion of top 20 ranked iSAFE SNPs carried by a gene provides a coarse estimate of the probability that the gene contains the causal allele somewhere within the annotated gene boundaries. Thus, for all 52 multigene sweeps, we searched for instances where a single gene had a majority ($\geq 50\%$) of the top iSAFE SNPs in phased genomes from five modern European populations and five modern African populations from phase 3 of the 1,000 genomes dataset (which included samples from populations used our SweepFinder2 assays, i.e. CEU, FIN, TSI, and YRI). African samples were included in the iSAFE estimation in order to provide a sample of non-sweep haplotypes, as this has been shown to increase power to identify the causal allele when the sweep haplotype is at high frequencies (118). We also extended the boundaries of each sweep by 250kb on each side, as the inclusion of sweep shoulders and flanking regions also improves the power of iSAFE (118).

Application of the iSAFE method to the 52 multigene sweeps resulted in 25 sweeps where a single gene could be identified that contained at least 50% of the top 20 iSAFE alleles (Table S5). Among these 25 sweeps, three sweep regions had at least one other gene that carried a moderate ($\geq 20\%$) proportion of iSAFE SNPs (i.e. sweeps *CCDC138*, *ARGEF1*, and *COL4A3BP*; Table S5). Because such sweeps provided less convincing evidence for a single focal driver gene overall, these were flagged as edge cases. Three additional sweeps (*PNLIPRP3*, *TP53BP1*, and *FMO2*) were also included as edge cases on the basis that these regions had a single gene with $\geq 30\%$ of the top 20 iSAFE SNPs, but no other gene in the sweep contained any of these top ranked iSAFE SNPs (Table S5). The resulting 28 sweeps were combined with four sweeps containing single genes (*LINCO1153* being omitted due to having too few marker SNPs and lacking functional information in the biomedical literature; Table S6) to create a set of candidate genes that were used in functional analyses described in this section.

3.2 Comparative candidate gene sets

Population migrations and range expansions often place organisms in unique conditions that pose new physiological challenges, like those experienced by contemporary human populations that have recently moved from low to high altitude environments and suffer increased perinatal mortality and morbidity compared to high altitude-adapted populations (119–121). Similarly, the OoA migration by

AMH is thought to have led to a variety of adaptations to the cool arid environments of Pleistocene Eurasia (122). Previous investigations of mammalian adaptation to cold environments have reported a number of putatively adaptive changes to organismal temperature regulation, including neurocranial restructuring (face structure in cold living nonhuman primates (123)), as well as changes to the volume and distribution of fat tissue and modifications in energy expenditure (124–126), and selection for skin traits (127). Cold temperatures are also known to affect respiratory health and sensitivity to infection (128, 129).

To determine if our driver loci were potentially part of an adaptive response to living in cold climates during the AMH occupation of Arabian Peninsula and Eurasia, we compared the functional characteristics of the 32 candidate genes with additional candidate loci identified in five previous studies of positive selection in contemporary Arctic human populations living in Greenland (130), Siberia (131, 132), and North America (133, 134). We obtained a previously curated set of 58 candidate genes from refs. (130) and (131) from a recent meta-analysis of mammalian cold adaptation (135), adding six, three, and 15 candidate genes from refs. (132), (133), and (134), respectively. To reduce potential false positives, candidate loci from ref. (132) that were situated outside of annotated gene regions or contained multiple annotated genes were excluded. Similarly for ref. (134), the reported candidate list of ~80 genes was reduced by first removing all genes that did not contain any non-synonymous, splicing, or UTR-based variants, and then removing any remaining genes that were within 1Mb of another outlier gene. Compiling the candidate genes from all five studies resulted in a set of 82 candidate adaptive genes from modern Arctic human groups that were considered for functional analyses (Table S6).

Additionally, previous studies have demonstrated that historical admixture events involving Neandertal and Denisovan lineages have left a large number of introgressed hominin loci segregating in modern human populations (63, 136–139). While many of these archaic loci are thought to have survived simply due to being in selectively neutral areas of the genome, a small number exhibit signs of positive selection suggesting they have conferred an adaptive advantage in some human populations – e.g. the Denisovan variant of the *EPAS1* gene which confers high-altitude tolerance in modern Tibetans (140) and another introgressed Denisovan region comprising two genes (*WARS2* and *TBX15*) suggested to have a role in human cold adaptation (130, 141). Given the potential advantage of cold-adapted Neandertal and Denisovan genes to the AMH population spreading across Eurasia, we also compiled a set of candidate hominin adaptively introgressed (HAI) genes from three studies that performed explicit tests for HAI loci, namely refs. (142–144). To ensure that the likely driver gene was identified, we restricted our analyses to HAI regions comprising a single gene that did not lie within 1Mb of a neighboring adaptively-introgressed region from the same study. Further, due to the large number of reported HAI loci in ref. (143), we restricted HAI regions from this study to those with an FDR < 0.2. This resulted in a set of 56 HAI loci, which were further supplemented with a five additional loci that had been specifically singled out for further functional examination in a recent genomic study (139), producing in a final set of 61 candidate HAI loci that were considered in further functional analyses (Table S6).

3.3 Sweeps are enriched with genes intolerant of deletion in present day populations

The availability of large genomic datasets across multiple human populations has allowed for rigorous assessment of the ‘essentiality’ of all annotated human genes (145). In contrast to genes with high levels of redundancy, such as olfactory genes, that exhibit large numbers of segregating putative loss of function alleles (pLoF) in the human populations (145, 146), genes with essential functions are expected to be less tolerant of such inactivating mutations and subsequently should carry fewer pLoF alleles on average (145). Following this logic, a recent study used pLoF variants identified among >140,000 worldwide human exomes to develop a measure, LOEUF (for loss-of-function observed/expected upper bound fraction), that quantifies the robustness of human genes to pLoF variants (145). Genes with low LOEUF scores tend to have fewer pLoF variants than expected and also tend to be more likely to be haploinsufficient (i.e. heterozygotes do not produce the wild-type phenotype and tend to be lethal when heterozygous in mice and human cell lines) (145). Additionally, segregating variants are more likely to be deleterious in genes with low LOEUF scores in general, regardless of their population frequency (145), and LOEUF scores are correlated with two codon-based measures of gene conservation in human and vertebrate lineages (called synRVIS and synGREP, respectively (147)). Thus, genes with low LOEUF scores tend to be intolerant of new variants in general, and preservation of their core functionality appears to be a crucial determinant in maintaining human health.

We used the LOEUF scores for ~20,000 annotated human genes to test if any of the candidate gene sets (i.e. HAI, Arctic modern human, and driver genes from the present study) were more essential than expected by chance, by contrasting the LOEUF scores in each candidate set against all non-candidate genes using a Wilcoxon Sign Rank Test. The LOEUF scores were significantly lower for all three candidate gene sets (all $p \leq 0.0009$; Fig. S12), and this result remained significant after removing the six edge cases from the Eurasian candidate genes ($p \leq 0.0009$), indicating that these candidate gene sets tend to be less permissive to pLoF mutations in human lineages than expected by chance.

Notably, it is possible that the observed tendency toward low LOEUF scores for three putative selected gene sets was a result of positive selection removing pLoF variation at these loci. To test this scenario, we compared another pLoF-based metric that is correlated with LOEUF that was also calculated in ref (145) – namely p , the probability that a haplotype carries a pLoF mutation at a particular gene – for genomes from African and non-African populations. Specifically, we computed a modified value of p that captures changes that followed OoA movement out of Africa, by performing a LOESS regression of p_{EUR} (i.e. p derived from individuals with non-Finnish European ancestry) upon p_{AFR} (i.e. p calculated for individuals with African or African American ancestry) using the loess function provided by the R statistical programming language with default parameter settings (49). All p values were logarithmically transformed (base 10), which required adding a small random number uniformly distributed between 10^{-5} and 10^{-6} to account for p values equal to 0. After computing the LOESS model on these log-transformed p values, we obtained corrected values, p_{corr} , for each gene by subtracting the observed p_{EUR} from the predicted value in the LOESS model (i.e. the corrected value is the residual score for each gene, whereby positive p_{corr} values indicate that a gene has fewer LoF mutations than expected following the movement of AMH into Eurasia, and vice versa for negative values). We then

used a one-sided Wilcoxon Signed Rank Test to determine if the mean p_{corr} was significantly inflated across any of the three categories of candidate genes (i.e. HAI, Arctic modern human, and ancient Eurasian genes) relative to the remaining ‘null’ set of genes. The observed mean p_{corr} values did not differ from expectations for any of the three candidate gene sets (HAI genes: $p \leq 0.40$; Arctic modern human genes: $p \leq 0.96$; ancient Eurasian genes: $p \leq 0.16$; Fig. S12). Indeed, the deleterious nature of LoF variants imply that most will have evolutionarily recent origins due to the high probability that new LoF mutants are quickly removed by purifying selection. Our results are consistent with this expectation and indicate that the LOEUF scores for our driver genes are probably only weakly impacted by the positive selection events that largely occurred $>10,000$ years ago, and therefore should still provide a robust measure of the essentiality of genes putatively affected by positive selection following the OoA movements.

3.4 Functional characterization of ancient Eurasian candidate genes

The biological function of the 32 putative ancient Eurasian candidate genes identified within our hard sweeps was assessed by multiple complementary methods. We evaluated gene function through a systematic review of human disease literature, as well as animal and cell knockout phenotypic data sets available on OMIM, PubMed, and GeneCards databases, and through utilization of available online bioinformatic functional annotation tools, e.g. STRING (see [section 3.8](#)). This combined approach, which takes particular advantage of current human genomic and clinical data sets, allowed us to define a biological function and assign a physiological process for 32 ancient Eurasian candidate genes (as well as candidate genes identified in modern Arctic human populations and among adaptively introgressed archaic hominin loci; see [section 3.5](#)). A key component in our functional classification approach that differs from related methods employed in evolutionary studies is that we sought to assign primary gene function based on phenotypic data observed in human carriers of crippling or haploinsufficient alleles, or from animal studies investigating the impact of deletions or loss-of-function mutations in orthologous genes. Most of these animal studies were rodent ‘knock-out’ assays, though zebra fish and *Drosophila* studies were also included in some cases (Table S6). For the 11 ancient Eurasian candidate genes lacking this type of phenotypic information, 10 were assigned functions via genome-wide association trait studies (GWAS) or biochemical and cell-based studies human and/or other animals (Table S6), with one gene, *LINCO1153*, being excluded from all functional analyses due to a lack of suitable classificatory data (see Table S6 and [section 3.1](#)).

Using this approach, 32 Eurasian driver genes could be assigned a clear functional role under a surprisingly small number of higher-level categories: Neurological Processes (31% of total genes); Development Processes (34%); Metabolic Processes (28%); and Reproductive Fitness (6%); while no genes were overtly associated with immune function (Table S6). Further, just over half of all the selected genes (59%) were associated with a major physiological impact in humans and animals when mutated, with phenotypes including premature lethality (e.g. *GTSE1*, *FBNI*), spontaneous neuro-developmental defects (e.g. *ARFGEF1*, *NFASC*), premature aging, skeletal and organ malformations and rearrangements (e.g. *TBC1D7*, *DNAH7*) and other whole body defects (e.g. absence of a vascular

network, *BCAS3*; reduced sperm output and fertility defects *ELMO1*) (Table S6). Further evidence for the biological importance of the driver genes is provided by their significantly reduced LOEUF scores (see [section 3.2](#)) and the observation that 25% are associated with a lethal phenotype when functionally crippled (Tables 1, S6). These properties point to the selected genes having relatively high biological significance and performing non-redundant functions in human physiology.

A second striking observation is that most of the driver genes (~88%) encode intracellular proteins (Table S6), and many of these are involved in related evolutionary conserved processes or gene regulatory networks. For example, *CAND1* and *FBXO15* are both components of the Skp1-cullin-F-box (SCF) complex (148) – a cellular E3 ligase machine conserved across yeast, plants, nematodes, drosophila and humans – which is critical to regulation of cell cycle progression (149). Other highly conserved genes include *TP53BP1* (150, 151), which was first identified in yeast, which together with *GTSE1* (152) and *FANCD2* (153) regulate components of the evolutionarily-ancient DNA damage response and repair pathways. Further, the driver gene *TAF15* is an evolutionary conserved transcription factor (related to the *Drosophila melanogaster* homologue *cabeza/SARFH* associated factor (154)) that cooperates with the RNA polymerase II complex to regulate gene transcription, including regulating the expression of the selected gene *DNAH7* (155) (Fig. 2D). This suggests that recent human evolution has included repeated adaptive modifications of proteins involved in core cellular functions. Notably, cell cycle progression and DNA repair are intertwined processes, implying that our driver genes not only fall within a relatively small set of high-level functional classifications, but also share mechanistic associations at the subcellular functional level.

3.5 Candidate genes form coordinated functional pathways

Adopting the same criteria and analyses that were used to functionally characterize the ancient Eurasian candidate genes identified in this study, we were able to assign a function to 54 of the 61 HAI candidate genes and 58 of the 82 Arctic human candidate genes, resulting in a set of 112 additional loci that were subjected to further functional investigation (Table S6). Intriguingly, the high-order functional classifications identified for the HAI and Arctic human candidate genes closely align with the distribution of functions observed for the ancient Eurasian candidate genes: overall, the three sets of candidate genes group with marked concordance around neurological (31%, 35% and 35%, for ancient Eurasian, HAI, and Arctic human candidates, respectively), developmental (34%, 32% and 28%, respectively) and metabolic (28%, 24% and 22%, respectively) processes (Tables 1, S6). The remaining genes are distributed across two distinct physiological functions – reproductive fitness and immunity – with reproductive fitness genes only found within the ancient Eurasian (6%) and HAI (2%) candidates, whereas immune genes are specific to the HAI (7%) and Arctic human (16%) candidates (Table S6). Moreover, many of the candidate genes within either group were associated with severe physiological phenotypes (i.e. lethality and/or Mendelian disease) when disrupted (60% and 63% of all HAI and Arctic human candidate genes, respectively; Table S6).

Strikingly, several of the Eurasian candidate genes also formed parts of larger integrated molecular networks that included both HAI and Arctic human candidate genes. Comparing the functions across

the three datasets revealed distinct interacting gene networks involved in fat synthesis and adipocyte formation, cilia formation and function, and skin physiology (including melanocyte formation). Notably, each produced a phenotype with a potentially adaptive advantage in cold conditions, which are discussed in the main text and accompanying figure (Fig. 2, Table S6). For instance, *EDAR* is an Arctic human candidate gene that also sits within a large ancient Eurasian sweep in the present study, which results in ectodermal dysplasia when mutated (characterized by primary defects in hair, nails, teeth as well as sweat glands and skin) (156). Two additional Arctic human candidate genes also regulate skin and ectodermal properties: *SREBF2*, which associates with impaired skin wound repair and cataracts (157), and *DSP*, which regulates skin thickness and the ‘woolly-hair’ phenotype in mammals (158). Further cases of functions coordinately regulated by genes from different candidate gene sets are outlined in the main text (also see Fig. 2).

3.6 Neurological function as an underappreciated adaptive target in humans

Around one third of the 32 ancient Eurasian candidate genes that could be assigned a clear physiological role are associated with neurological function (Tables 1, S6). Our temporal analyses indicate that most of those neuronal genes (82%; 9/11) were under selection during the Arabian Standstill period of ~80-50ka, with the remaining two genes (*WWOX* and *DOCK3*) arising immediately afterwards during the Initial Upper Paleolithic (~47-43ka). Neuronal adaptations therefore appear to have been essential components of the selective environment during the Arabian Standstill and during the early phase of AMH dispersal across Eurasia. Again, this is provocative given archaeological suggestions of rapid cognitive development during this period (81).

Selection for neurological function stands in apparent contrast to previous evidence of positive selection in humans where the link between the selective pressure and adaptive response are more readily obvious (e.g. changes in diet resulted in selection for genes controlling lactose tolerance, infectious disease resulted in selection for genes controlling malaria resistance, changes in climate resulted in selection for genes controlling pigmentation (122)). While neurological functions initially appear surprising, it is possible that this observation mostly relates to the critical role the nervous system and brain play in coordinating, integrating, and subsequently regulating diverse physiological processes, which are impacted by cold environments. A key influence of the brain in this context is its ability to synthesize immediate environmental contextual cues and integrate these with the present physiological state. This is exemplified by evidence that the brain plays a central role in adjusting fuel metabolism and appetite to food resource availability (159), regulating blood flow in response to changed external conditions (e.g. cold) for thermal homeostasis (160), directly aids immune defense against infection and injury (161), and ensures the fetus is protected, safely delivered, and cared for to facilitate successful pregnancy (162). Indeed, both cognitive performance (163–166) and multiple aspects of neural physiology (167–170) are sensitive to thermal variation, suggesting that sustained occupation of cold environments by AMH may have required recalibration of many essential neurological processes towards new optimal settings, potentially leading to some of the adaptive changes observed in this study. Thus, the Eurasian candidate genes point to the brain as a central

mechanism facilitating human adaptation to changing environmental conditions where cold temperatures are a stressor, a hypothesis that is further supported by our finding that neurological genes also represent one third of candidate genes observed in modern Arctic human groups and HAI genes from putatively cold-adapted archaic groups.

It is intriguing to speculate that neurological adaptation may have played a key role in facilitating the spread of AMH through the colder Eurasian environments ~54–51ka. Future investigation of this hypothesis will benefit from targeted approaches that directly investigate how human cold response is modulated by candidate neuronal genes identified in ancient Eurasians, Arctic humans, and among HAI loci, by recording their singular and combined physiological activity in response to cold stimuli. Exemplar studies of this type have previously revealed how temperature information is relayed to the brain by synaptic firing in nerves regulated by cold-sensitive voltage-gated membrane channels (171, 172). Model organisms offer a further source of mechanistic insights into the candidate neuronal genes, as demonstrated by gene knock-out studies in mice that have revealed the central role of two nerve receptor genes, *TRPM2* and *TRPM8*, in the sensation of warm (173) and cold temperatures (174, 175) (reviewed in refs. (176, 177)). Notably, *TRPM2* is one of the candidate genes identified in modern Arctic human populations (131), and *TRPM8* is regulated by a variant with a clinal distribution across modern Eurasian populations suggestive of adaptation to cold conditions (178). Further, the Eurasian candidate gene *MPP6* is involved in formation of nerve myelin sheaths (179) and myelination levels display plasticity with respect to environmental stimuli (180), suggesting another possible route for neuronal adaptation in new environments. Accordingly, while the role of metabolic and thermogenic processes are well described components of the adaptive mammalian cold response (181, 182), these studies suggest that neuronal processes are also plausible targets of selection that appear to have played a previously underappreciated role in AMH adaptation.

3.7 Confirming functional concordance through analyses of protein-protein interactions

Functional classification of the 32 candidate genes from our study revealed strong concordance with the inferred functions of candidate genes reported in selection studies of Arctic human populations and introgressed from archaic hominins ([section 3.4](#)). Further, by drawing upon previously published molecular studies we were able to identify several cases where genes from each of these three groups contribute to known molecular networks (Fig. 2). These results suggest that the candidate genes from all three sets may have been targeted by one or more common selection pressures that have acted across much of western Eurasian population history.

To provide independent evidence on the degree of the interrelationships between the ancient Eurasian, HAI, and Arctic human candidate gene sets, we used human protein-protein interaction (PPI) data from the STRING database (version 11.5; ref. (183)) to test if the number of PPIs observed between the three different candidate gene sets exceeded chance expectations. Specifically, we performed a series of permutation tests in which all genes from one of the three groups were replaced with the same number of genes randomly selected from all human genes represented in the STRING database, with the number of PPIs among genes from these randomized gene sets being compared to the observed PPI

count. By repeating this process 10,000 times for each of the three gene sets, we calculated an empirical p value by evaluating the number of random gene sets that had more PPIs than in the observed case. Further, to account for the variable levels of evidence among the STRING PPIs, which are denoted by an associated score (0.15 being the minimum value required for reporting a PPI, with 1 being the maximum possible evidence), we performed separate tests after excluding PPIs with scores falling below specific thresholds (i.e. the score quartiles, or 25th, 50th and 75th percentiles, relating to scores of 0.175, 0.216 and 0.309, respectively).

The PPI analyses provide quantitative support for the strong functional concordance observed among the three different candidate gene sets from our bespoke functional annotations: all pairwise combinations of the three gene sets tend to have more pairwise PPIs than expected (Fig. S6 and Table S7), with Arctic human and HAI genes showing the most significant inflation in PPIs overall ($p < 0.0011$ for all tests; Table S7). Ancient Eurasian candidate genes also have significantly more PPIs with Arctic human genes than expected for several tests, though this signal was comparatively weaker at the most stringent PPI score threshold (i.e. when removing PPIs in the bottom 75% of scores), albeit with the excess of PPIs still being relatively high (~15%; Table S7). The ancient Eurasian candidate genes also do not have significant levels of PPIs among themselves, which contrasts with the significant inflation in PPIs observed within the Arctic human and HAI candidate genes. Notably, when comparing results from the two permutation tests performed for each pair of candidate gene sets, p values were generally lower when replacing genes from the smaller of the two gene sets (Table S7). This result suggests that the ancient Eurasian candidate gene set, which had approximately 50% to 60% fewer genes than the HAI and Arctic human candidates respectively, may have had comparatively less statistical power than the two larger gene sets, which may have been further exacerbated when using more stringent PPI score thresholds.

Intriguingly, each of the ancient Eurasian, Arctic human, and HAI candidate gene sets exhibit a significant excess of PPIs when compared to remaining genes from the STRING database (Wilcoxon sign rank test $p \leq 0.039$ for all three gene sets across all PPI score thresholds; Fig. S8). This result complements findings from a recent study, which showed that genes with high levels of PPIs, also known as ‘hub’ genes, are also significantly more likely to exhibit signals of positive selection in humans (184). Moreover, hub genes were also found to be among the most evolutionary constrained genes in both human and mammalian evolutionary history (184), a result that also broadly aligns with the deficit of loss of function alleles observed for among the three candidate gene sets analyzed in the present study. These results suggest positively selected genes in human history may share a core set of common features that include elevated levels of protein connectivity and a general intolerance to protein altering mutations; though we note that determining the influence of PPI and other potentially causal factors in gene evolution remains a complex and contentious topic (185, 186) and further unraveling these factors is beyond the scope of the current manuscript.

3.8 Quantitative evaluation of functional annotations

To assess the accuracy of our functional annotations across candidate genes identified in ancient Eurasians, Arctic humans, and introgressed from hominins (HAI genes), we examined if any of the functionally distinct sets of genes identified through our annotation protocol (see sections 3.4, 3.5 and 3.6) were enriched for Gene Ontologies (GO) or other biomedical annotations with similar functions. We used the STRING online enrichment tool (v. 11.5; <https://string-db.org/>) to perform separate enrichment tests for candidate genes classified into the four most common broad functional categories – i.e. Neurological, Development, Metabolism, and Immune (Table S6), with additional testing on four functionally distinct subcategories identified in our analyses – i.e. Adipocyte and free fatty acid synthesis, Skin physiology (which combines Skin properties and Melanogenesis; see Fig. 2), Cilia formation, and DNA damage repair (see sections 3.4, 3.5 and 3.6, and Table S6). All tests were limited to functional groups with more than five genes, with non-candidate genes shown in Fig. 2 also being included in the subcategory tests. All enrichment test results are reported in the main text and Table S8.

3.9 Generality of functional annotations beyond hard sweeps

We also investigated the generality of our functional annotations to positively selected loci in ancient Eurasians beyond hard sweeps. We used outFLANK to identify SNPs with elevated divergence between the 12 ancient Eurasian populations (*i.e.* those with $n_{\text{eff}} \geq 10$; see section 1.6) and a modern African population (*i.e.* YRI), and submitted these to enrichment testing using the STRING (183) online GO testing facilities. Specifically, we evaluated frequencies at each ~1.1M ascertained SNPs in the YRI samples and the combined samples from all ancient populations (*i.e.* creating a single ancient Eurasian group), and calculated F_{st} for each SNP using the standard Weir-Cockerham estimator (187). After excluding SNPs with heterozygosity less than 0.1, we then used OutFLANK to estimate the probability that each SNP was more divergent than expected under neutrality (*i.e.* assuming a null χ^2 distribution with parameters estimated from putatively neutral SNPs (188); see Dataset S57 [<https://doi.org/10.25909/22359874>] for results from all evaluated SNPs). This divergence-based method should in principle capture modes of positive selection leaving less distinctive genetic signals than hard sweeps, including soft and partial sweep signals. Further, OutFLANK is robust to non-equilibrium demographic models (188), including rapid range expansions that are thought to have resulted in highly divergent alleles observed in modern human populations (*i.e.* through allele surfing; (189)).

The outFLANK analyses support the authenticity of the 57 hard sweep signals, with 49 sweeps (~86%) having significantly elevated F_{ST} values relative to the remaining background genome ($p < 0.05$, Wilcoxon Rank Sum Test; see ref. (1)). To obtain a complementary set of outFLANK candidate loci for functional classification, we compiled a set of 423 candidate selected genes that contained at least one outlier SNP ($q < 0.05$) within the annotated gene boundaries, excluding all ambiguous genes where outlier SNPs were situated between two or more overlapping genes. We then applied the same candidate selection criteria after extending gene boundaries by 50kb on either side, identifying a further 111 candidate genes with one or more outlier SNP located in proximal flanking regions (and more than

50kb of all other genes), and submitted the final list of 534 unique OutFLANK candidate genes to STRING for functional analysis (Table S8). Notably, around 8% of the OutFLANK candidate genes (44/534) are also found within the 57 sweep regions, suggesting that the OutFLANK candidate set likely captured additional positively selected loci that have left less pronounced genomic signals in ancient Eurasians.

The OutFLANK candidate genes were significantly enriched in more than 100 of biological categories across a range of different ontologies ($FDR < 0.05$) – with neurological, developmental, and cell adhesion/signaling categories being particularly abundant – and also had significantly more PPIs than expected (Table S7). Applying the same STRING enrichment analyses to the complete set of 175 candidate genes from ancient Eurasians, Arctic humans, and HAI loci, also resulted in enriched neurological and cell adhesion categories, suggesting that these broad functions were targeted by multiple modes of positive selection in ancient Eurasians. Further, these results also highlight that statistical analyses of aggregated gene sets that combine functionally diverse genes can overlook signals that were evident in our functional characterization of individual candidate genes. This result emphasizes the value of the gene-centric approach adopted in this study for gaining a more complete understanding of the targets of historical selection.

3.10 Arctic human candidate genes likely had local selection pressures

No genes were shared between the 32 ancient Eurasian candidate genes identified in this study and the combined set of 82 candidate genes from the five studies of modern Arctic human adaptation (though the Arctic human candidate gene *EDAR* sits within an ancient Eurasian sweep), suggesting that selection has utilized different sets of genes to adaptively modify common functional targets (see [section 3.5](#)). However, this lack of overlap was partly by design, as we preferentially chose candidate genes having ‘local’ selection signals – i.e. where the adaptive event most likely arose only after the settlement of Arctic regions – to increase the probability that the underlying selection pressures were a consequence of human occupation of the cold arid Arctic environment.

For instance, ref. (132) applied a combination of haplotype-based analyses (i.e. iHS (190) and XP-EHH (191)) to eight populations from the Russian Arctic region, which could potentially recover adaptive loci resulting from both recent (i.e. XP-EHH with either European [CEU] or East Asian populations [CHB] as contrasts) and older (i.e. XP-EHH with an African population [YRI] contrast) selection events. Indeed, three Eurasian driver genes (i.e. *BCAS3*, *TMEM232*, *PPARD*) and another gene from a multi-gene sweep (*EDAR*) were among the candidate loci reported in ref. (132) when an African population was used as the contrast in XP-EHH testing; however, these loci were typically not outliers when either European or East Asian population contrasts were used instead (1/32 significant population tests across all three loci using either CHB or CEU as the population contrast, cf. 22/32 significant tests when using the YRI population contrast; see table 2 in ref. (132)). These results clearly point to these three loci having an ancient antiquity, replicating the findings in our study. Accordingly, to better discriminate loci under local Arctic selection, we excluded all candidate genes reported in ref. (132) that were among the outliers reported for XP-EHH tests using an African population contrast.

Our preference for local Arctic selection signals was further enabled by the remaining four Arctic human studies (i.e. refs. (130, 131, 133, 134)), using selection criteria that favored the detection of genomic regions under local selection in the Arctic populations. Specifically, two of these studies (refs. (130, 133)) used the population branch statistic (PBS (192)) to test for genomic regions showing excessive differentiation relative to modern Han Chinese (CHB) populations, with Northern Europeans (CEU) as an outgroup. Two further studies used PBS tests and another statistic that scans for regions with depleted haplotype diversity in the focal populations (iHS (190)), with ref. (131) also using a further divergence statistic XP-EHH (191) that contrasts haplotype diversity in the focal population with a Eurasian group (in this case an ethnic Vietnamese population). Notably, while the iHS statistic should in principle be capable of detecting sweeps that arose before the separation of each Arctic populations from other Mainland Eurasian groups, both studies use post-test filtering strategies that greatly reduce the chances of observing such sweeps – ref. (131) ignores the top 5% of iHS windows from the ethnic Vietnamese population, and ref. (134) only reports outliers in the top 1% of PBS and iHS statistics, favoring the detection of locally selected regions over ancient sweep loci reported in the present study.

While these criteria should enrich the AAH gene set for loci selected within Arctic environments, it is possible that there is still some statistical correspondence between the selection scans from these studies and our own sweep regions when looking at more general signals beyond the candidate loci. Further, the extensive Holocene admixture suggested in the present study has likely reduced the sweep haplotype frequencies in many modern European populations, making it possible that some of these sweeps might have moderate PBS signals if they remained at high frequencies in the Arctic populations. To examine these scenarios in more detail, we used the permutation framework outlined in [section 1.8](#) to test if the outlier windows reported for the Arctic populations in ref. (131) were enriched within the sweep regions detected in the present study, with separate tests performed for each of the three statistics employed in this study (i.e. PBS, XP-EHH, and iHS) as well as the combined set of results from all three statistics.

Intriguingly, while the outlier iHS windows were found to be marginally enriched across our 57 sweeps for both unscaled (observed overlap = 7 sweeps; expected overlap = 3.71 sweeps; $p \leq 0.0701$) and recombination-scaled (expected overlap = 3.96 sweeps; $p \leq 0.0905$) genomes, we also observed a significant enrichment for XP-EHH outliers in both scenarios (Unscaled: observed overlap = 11 sweeps; expected overlap = 4.51 sweeps; $p \leq 0.0028$; Scaled: expected overlap = 4.77 sweeps; $p \leq 0.0051$), but not for PBS outliers (Unscaled: observed overlap = 16 sweeps; expected overlap = 20.06 sweeps; $p \leq 0.9197$; Scaled: expected overlap = 19.36 sweeps; $p \leq 0.8779$). The PBS result indicates that there were fewer of these outlier regions overlapping with our sweeps than expected – which is consistent with our hypothesis that inclusion of a European population in this statistic has biased it against the sweeps detected in our study. However, the inclusion of the ethnic Vietnamese population as a contrast in the XP-EHH statistic did not produce a similar bias. Both Vietnamese and Siberian populations are descendants of Eurasian lineages that split from Main Eurasians by 40ka (193, 194), and therefore are expected to have inherited the same subset of the 57 sweeps. Accordingly, the enrichment of outlier XP-EHH signals in Siberian populations suggests that the underlying selection signals have dissipated in modern Vietnamese populations, in comparison to modern European

populations, possibly through one or more admixture events involving a population where these sweeps were less frequent than occurred after their split from Siberian lineages, or perhaps because later occupation of a subtropical climate has resulted in selection against segregating adaptive cold haplotypes in the Vietnamese.

Supplemental Materials 4. Evaluating the hominin source of sweep driver alleles

The growing evidence for adaptively introgressed loci in AMH populations (142–144, 195) suggests that some of the 57 ancient Eurasian sweeps could have been driven by introgressed hominin-derived variants. To explore this possibility in more detail we compared the location of the 57 ancient Eurasian sweeps with putative hominin adaptively introgressed (HAI) loci reported in four recent publications (142–144, 195), and tested if there was a significant excess of HAI loci overlapping our sweeps. Note that these HAI loci include genomic regions that either harbor multiple annotated genes or lack any annotated genes, and therefore represent a much broader class of loci than the HAI gene set outlined in [section 3.2](#) (which comprise selected loci containing only one gene).

Combining all reported outlier loci in these four studies resulted in 2267 distinct HAI loci, which were further refined by combining all loci with identical chromosomal positions from the same study into a single locus, resulting in a final set of 862 distinct HAI loci. We compared our 57 sweep regions with the combined set of 862 HAI loci, identifying 25 distinct loci that overlapped 14 different hard sweeps (~25% of all sweeps) (Fig. S7). Note that because only central positions were reported in candidate loci in ref. (144), we created intervals for each locus by adding 100kb flanking regions either side of this reported position (100kb being the approximate mean size of adaptively introgressed loci in ref. (143)). We tested if the observed number of sweeps that overlap one or more adaptively introgressed locus was greater than expected by chance, applying the permutation test procedure outlined in [section 1.8](#) to the complete set of 862 HAI loci, with additional testing also performed for the HAI loci specific to each study. These tests confirmed that our sweeps were significantly more likely to overlap the combined set of 862 adaptively introgressed regions than expected for both the standard genome ($p \leq 0.0092$) and the recombination rescaled genome ($p \leq 0.0113$) analyses. Moreover, excluding adaptively introgressed loci with Denisovan or ambiguous origins from these analyses showed that our hard sweeps were also more likely to overlap Neandertal-specific adaptively introgressed loci than expected ($p \leq 0.0364$ and 0.0475 for standard and recombining genome tests, respectively). The number of HAI loci overlapping the ancient Eurasian sweeps consistently exceeded expectations across all four studies, though these were only significant ($p < 0.05$) or marginally significant ($p < 0.10$) for the loci from refs. (142, 144). Notably, these two studies also reported much fewer adaptively introgressed loci overall, suggesting that these significant patterns may partly relate to the higher ratio of true positives to false positives in these two studies.

Next, we examined if any of the nine previously published hominin genomes available on AADR v42.4 closely matched alleles at marker SNPs in each overlapping adaptively introgressed region, extending the marker alleles in each sweep to include all SNPs that exceeded the 80th percentile of mean neutral F_{ST} values (see [section 2.1](#)) in order to provide a reasonable amount of SNPs for this calculation. Among the set of 25 adaptively introgressed regions that overlapped a sweep, 18 also overlapped at least one marker SNP across 12 separate sweeps, though many only covered a handful of marker SNPs (Fig. S7). When considering adaptively introgressed regions overlapping at least 4 marker SNPs (after accounting for missingness), the maximum proportion of matching marker alleles at an adaptively introgressed locus for any hominin genome was ~82%, with most cases having less than half the total

number of marker alleles (median proportion of shared marker alleles ~40%, dependent on the hominin allele being present; Fig. S7).

Our results indicate that adaptively introgressed variants are more common among our hard sweeps than expected, but that available hominin genomes do not provide particularly close matches for the putative causal haplotypes when a reasonable number of marker SNPs are available, suggesting that the causal HAI haplotype may have come from a lineage that had diverged from the nine sequenced hominins. However, closer inspection of the HAI loci showed that they were typically located on the periphery of the sweep regions that they overlapped, often at a considerable distance from the peak selection signals from SweepFinder2 CLR scores (Fig. S7). This finding suggests that an introgressed hominin variant is unlikely to be the causal allele for any of the 57 Eurasian sweeps, and that the enrichment of HAI loci proximal to the hard sweep signals may instead be caused by introgressed hominin variants hitchhiking on a beneficial human-derived haplotype.

To further investigate this hypothesis, we applied the recently published admixfrog (196) method to the 27 Anatolian EF samples to investigate if any introgressed hominin haplotypes were segregating at high frequencies near to the CLR peaks in our sweeps. We chose the Anatolian samples for this test as this population had the most significant hard sweep signals among the three ancestral populations that make up modern European ancestry (WHG and Steppe being the other two), and causal allele frequencies in this population are unaffected by subsequent Holocene admixture events. To identify Neandertal introgressed segments in the Anatolian EF genomes we used admixfrog version 0.6.2.dev6 (<https://github.com/BenjaminPeter/admixfrog/>; (196)) applying the parameters used in ref. (38). In short, we used three high-coverage Neandertal genomes (197–199) and 46 African genomes from the Simons Genome Diversity Project (85) as reference genomes, and the panTro4 chimpanzee genome to assign the ancestral hominin allele state for each of the ~1.1 million probe SNPs used in this study.

Among the 28 Anatolian EF samples, we detected thousands of small to moderate length introgressed hominin loci (mean introgressed locus length = 69.6kb, each sample having around 3,890 individual introgressed loci at least 10kb in length on average), all inferred to have a Neandertal origin. We calculated the frequency of the introgressed loci overlapping our sweep regions by counting the number of introgressed hominin alleles at each site in a sweep (noting that when multiple regions overlapped in a single individual, we kept only the highest scoring introgressed region from the overlapping set of loci). Several introgressed loci were found to be segregating at intermediate frequencies – 34 of 56 (~60%) sweeps had a segregating introgressed locus above 20% frequency – with the maximum frequency observed at any introgressed site that overlapped a sweep being ~78% (*MLPH* and *ZMYM6*; Figs. 3, S8). However, all introgressed loci segregating at intermediate frequencies (>20%) tended to be hundreds of thousands of base pairs distant from the maximum CLR score within any sweep (Figs. 3, S8), echoing the patterns we observe among adaptively introgressed loci reported in other studies. Moreover, the frequency of introgressed loci was significantly reduced near to the peak CLR score in each sweep relative to regions >100kb from this peak (i.e. the mean frequency of introgressed fragments minus two times the local standard error exceeds the mean frequency of introgressed fragments at the peak CLR score), which is consistent with positive selection on human-derived variants resulting in the removal of introgressed hominin loci near to the selected site (purifying

selection on introgressed variants not expected to show the same relationship with the peak CLR score). Accordingly, we find no strong support that any of our sweeps are caused by introgressed archaic hominin variants and posit that the majority of these overlapping adaptively introgressed regions may instead be artifacts created by introgressed neutral alleles hitchhiking upon beneficial AMH-derived loci.

Supplemental Figures

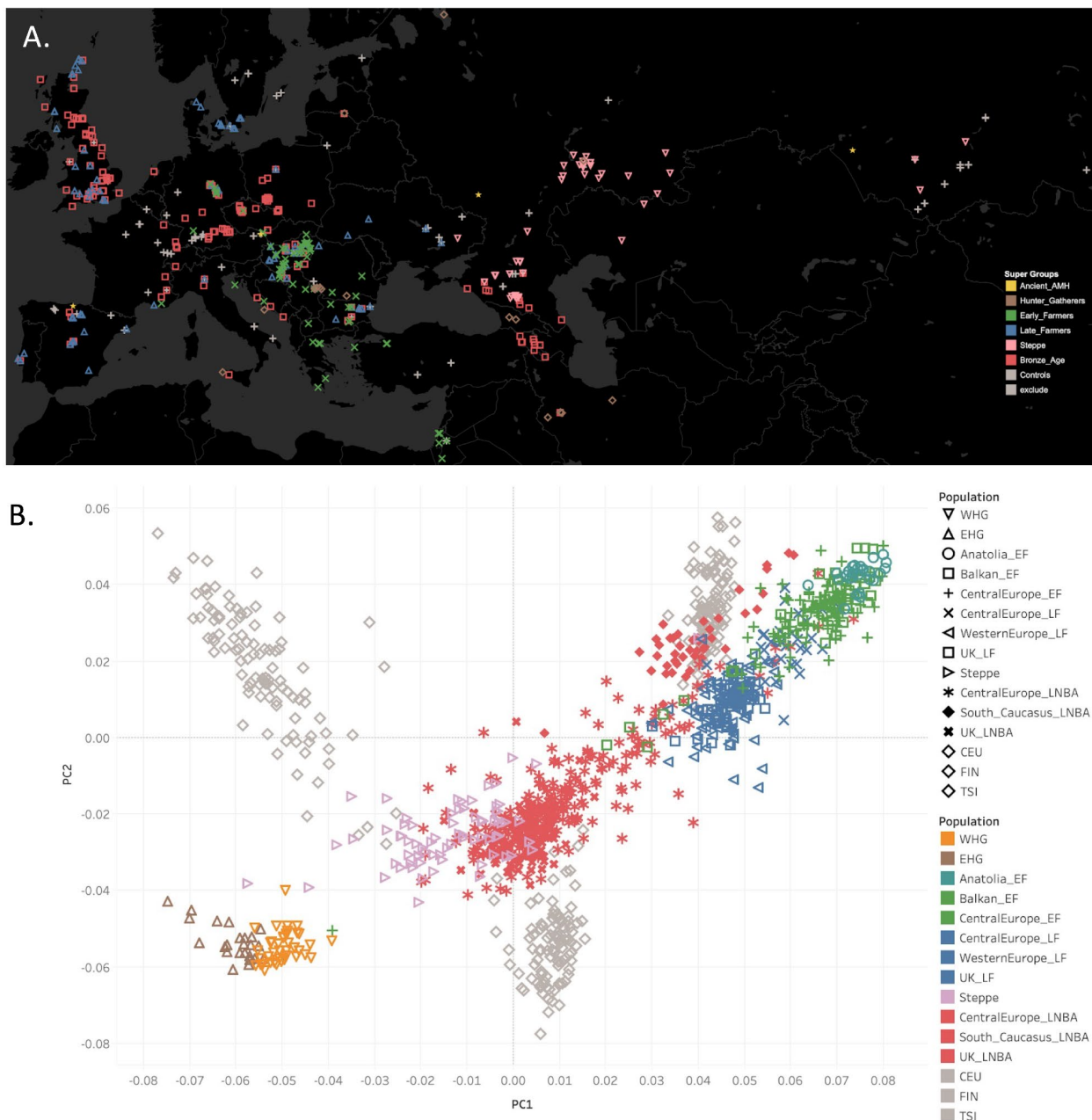


Figure S1. Geographic and genetic properties of ancient Eurasian samples used to detect sweeps.

(A) Full geographic distribution of the 1,162 ancient Eurasian samples, with different populations (indicated by colored symbols) having been classified into broader groupings according to archaeological records of material culture and lifestyle. **(B)** PCA analysis showing the genetic relationships between the different populations used in this study with all ancient populations distinguished (see key).

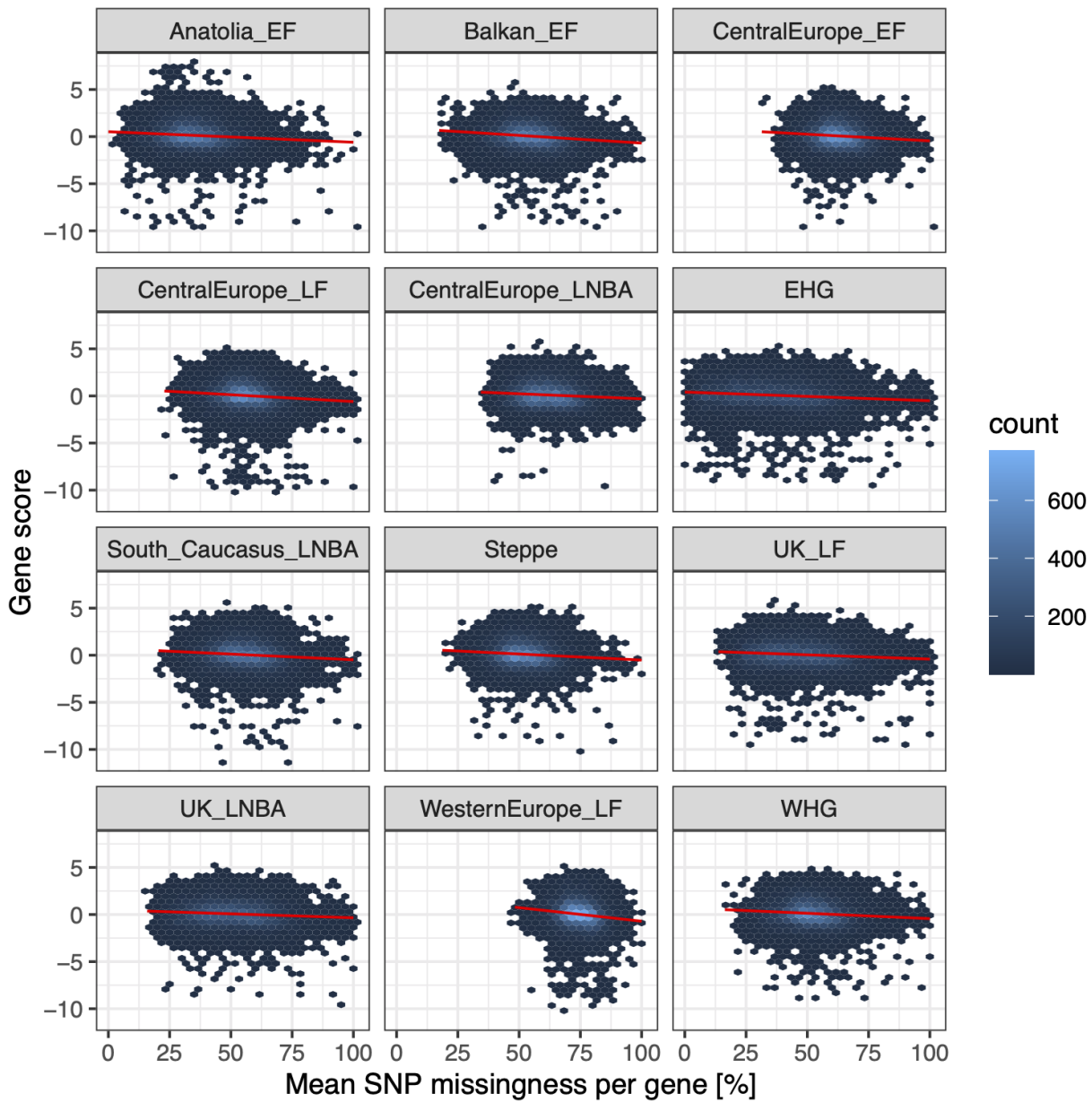


Figure S2. Effect of SNP missingness on gene scores. Linear regression analyses revealed a weak correlation between gene scores and the mean proportion of SNP missingness per gene (i.e. number of samples with missing data per SNP) for each ancient population used to determine sweeps in this study. Accordingly, our sweep signals are unlikely to be artifacts caused by high levels of SNP missingness. Red lines show the estimated linear fit for each population. Data points are aggregated into hexagonal bins (counts indicated by blue shading, see key).

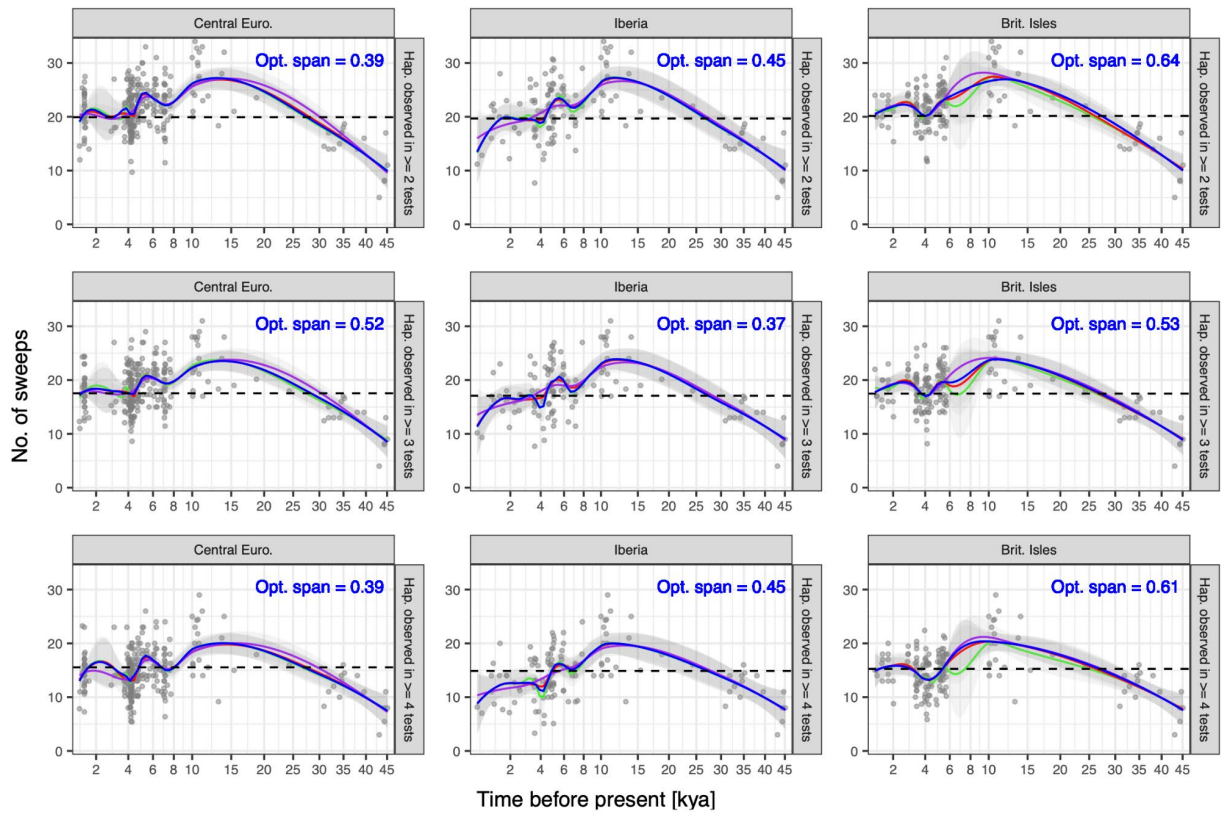


Figure S3. The impact of parameter choice on sweep haplotype accumulation through time. The dynamics of sweep aggregation were assessed by fitting a LOESS regression of sweep haplotype counts against radiocarbon estimates for three sets of regionally bounded Holocene samples (different columns) and a common set of samples from the Eurasian Upper Paleolithic. To examine the robustness of specific trends identified by the fit (e.g. reductions in sweep haplotype presence during periods of the Anatolian and Steppe-related introgression during the Holocene), we ran separate regressions for different haplotype selection criteria (different rows; see Methods) using three plausible span settings (i.e. 0.35, 0.5, 0.65 indicated by green, red, and purple lines respectively) and also the optimal span (blue line; values in upper right corner of each panel) estimated using general cross validation. Separate loess regressions were performed for results from each of the three haplotype detection criteria (different rows; Supplemental Materials 2). Most trends were reasonably robust to these different parameter choices, with inconsistencies being largely consigned to temporal spans with negligible sampling (e.g. between 6 to 10 ka in the British Isles). The mean sweep count in modern samples sourced from compatible regions is indicated by horizontal black dashed lines, which suggest that Iberian populations experienced an additional period of admixture-related sweep haplotype loss in the past 1,000 years prior to rebounding closer to the present. Note that the values on the x-axis have been square rooted to better highlight trends occurring in the Holocene period.

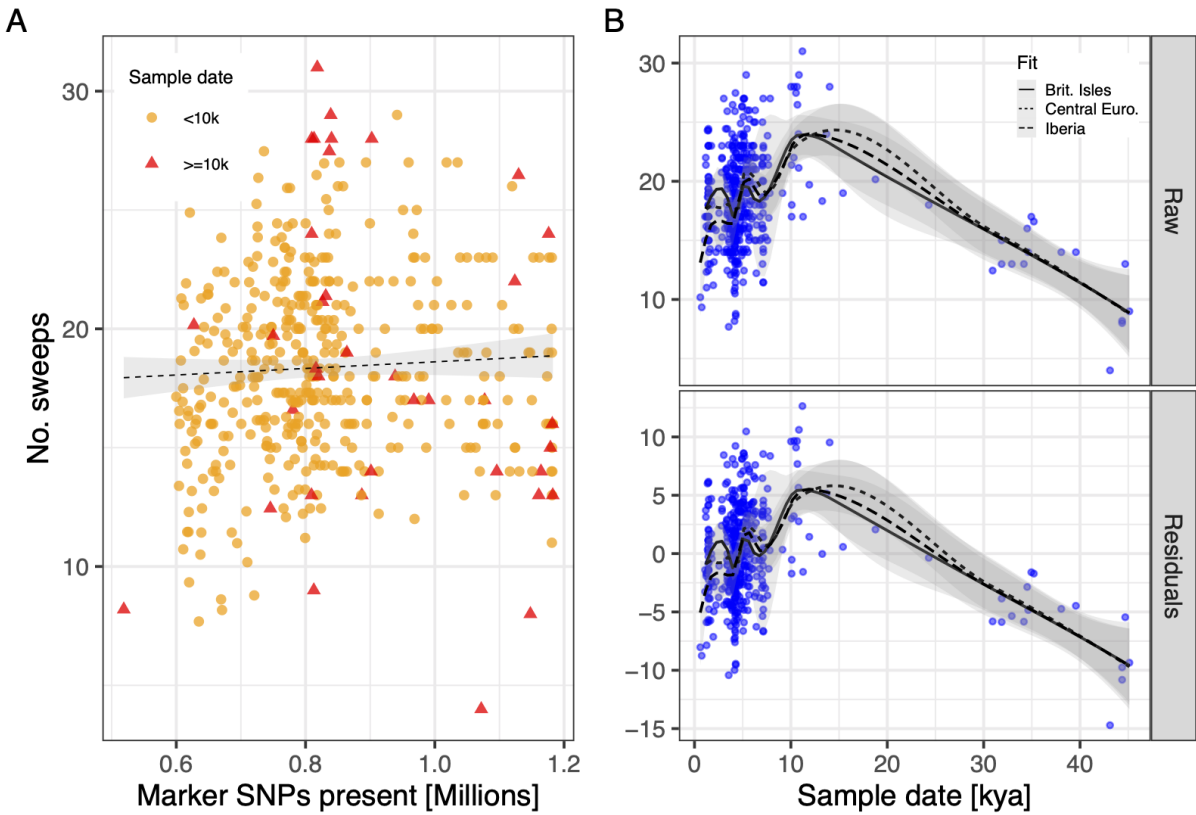


Figure S4. Sweep aggregation correcting for SNP missingness across samples. **(A)** The number of SNPs present in the 456 ancient samples used in the sweep aggregation analysis varied between ~500k and ~1.2M, with the number of sweeps detected in each sample being weakly positively associated with SNP presence (regression slope coefficient $p \sim 0.05$). **(B)** Correcting data for differential SNP missingness across samples (i.e. using residuals from the linear regression) had negligible impact on the fit of the LOESS regression lines (Residuals panel; cf. original data displayed in the Raw panel), indicating that this did not impact the temporal cumulative sweep patterns observed in our analyses (noting that span was set to 0.5 for both regression analyses).

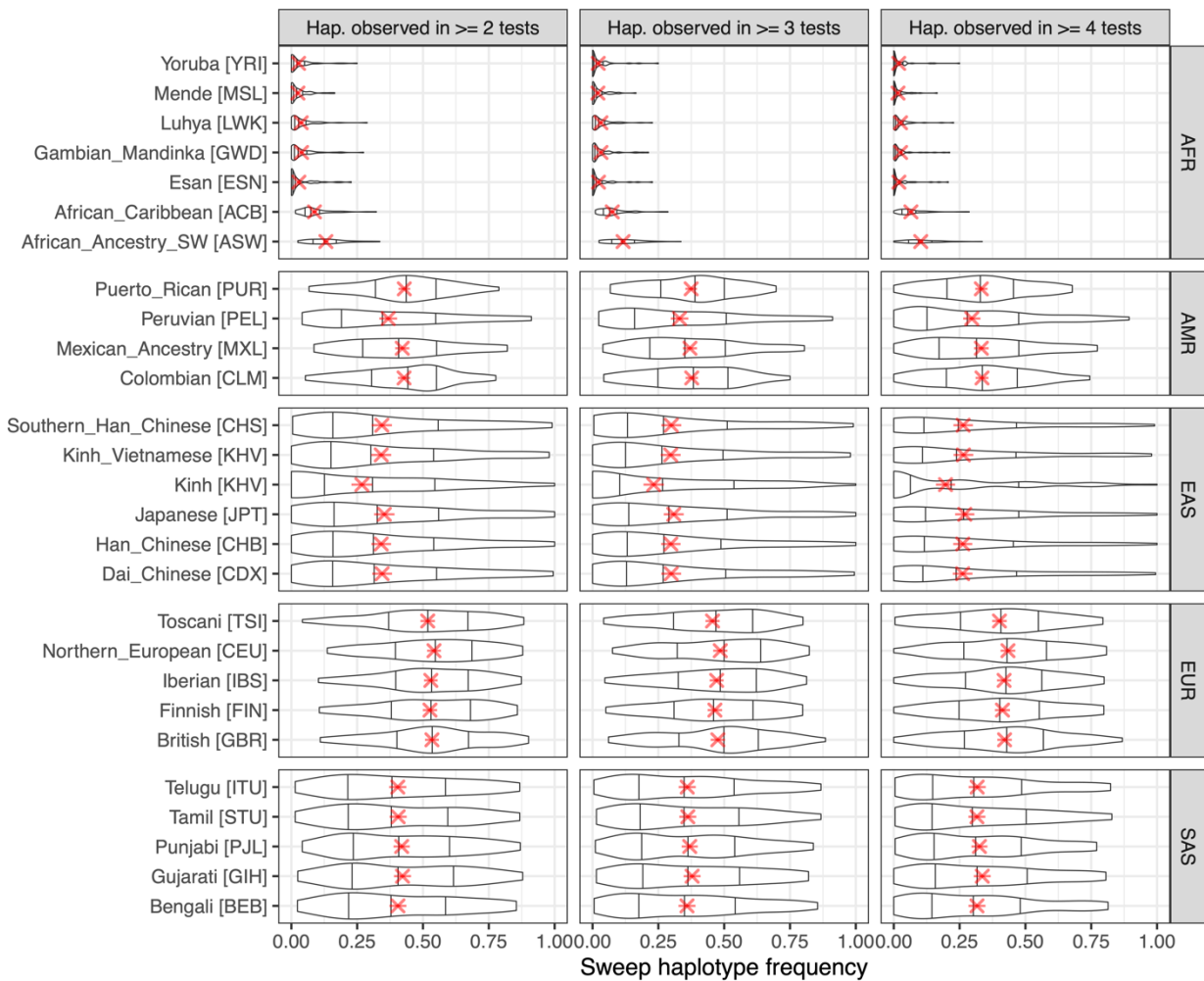


Figure S5. Sweep haplotype frequencies in modern human populations. Sweep haplotypes were enumerated in 2,506 phased samples from the 1,000 Genomes Project. The distribution of frequencies is shown for each population (violins), with mean frequency and associated standard error indicated with red cross and lines. Notably, many sweep haplotypes occur at intermediate frequencies in many contemporary non-African populations. Results are shown for different sweep haplotype detection criteria (separate columns), with the intermediate value (no. significant tests ≥ 3) being used for all results discussed in this study.

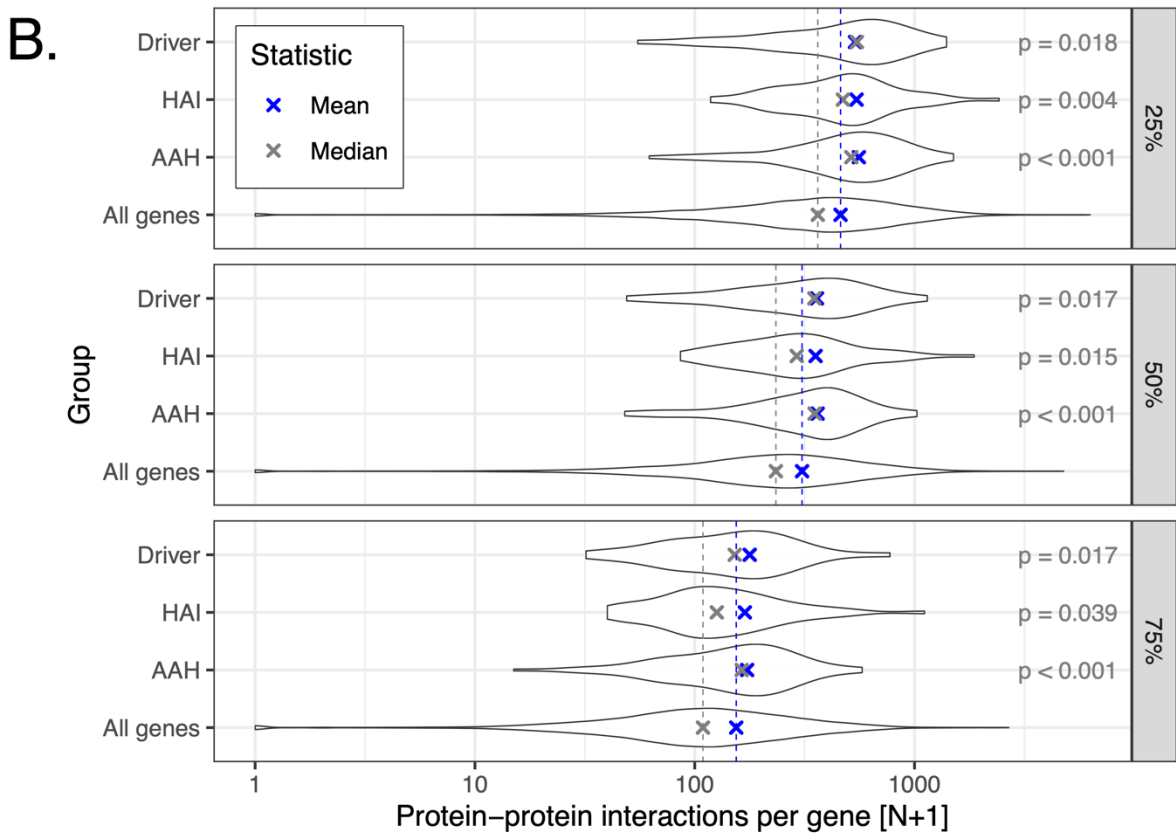
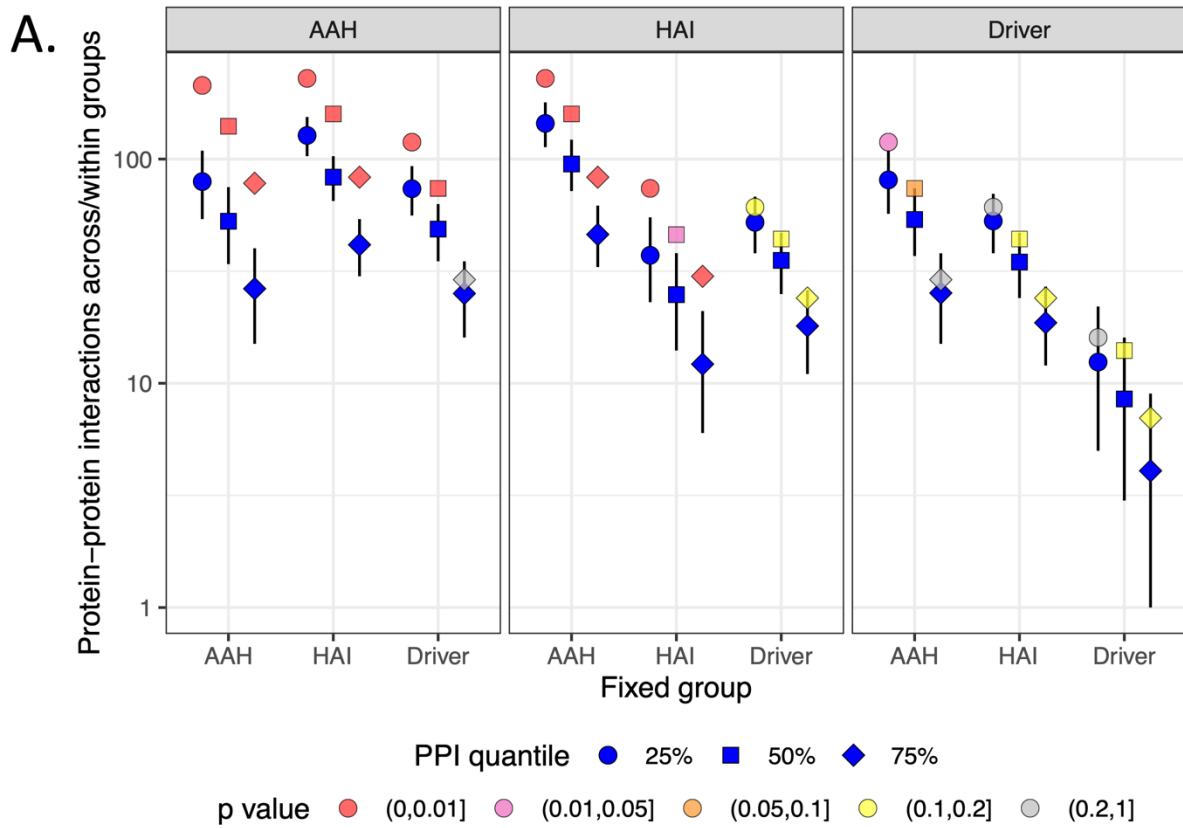


Figure S6. Protein-protein interactions within and between the candidate gene sets. **(A)** Protein-protein interactions (PPIs) were quantified for the three candidate gene sets used in the current study (i.e. 32 ancient Eurasian [Driver] genes in hard sweeps, 82 adaptive Arctic human [AAH] genes, and 61 hominin adaptively introgressed [HAI] genes) and compared to expected values using permutation tests where genes from one set were replaced by randomly chosen genes. For each pair of candidate gene sets, separate tests were performed where genes were randomly replaced for one set (separate panels) while remaining fixed for the other (x-axis). Tests were performed using three different PPI score thresholds (based on score quartiles and indicated by different point shapes; see key). PPIs exceeded expectations in all cases with the majority being significant (point colors, see key; error bars indicating 95% confidence intervals), with tests involving the replacement of larger gene sets (i.e. AAH and HAI candidates) potentially having more statistical power. **(B)** Distribution of the number PPIs among genes in each of the three candidate sets. Regardless of which PPI score threshold was used (separate panels), genes in each candidate set have significantly more PPIs on average relative to all remaining genes (mean and median values shown as blue and gray crosses, respectively; dashed lines are included to facilitate comparison of expected to observed values, with p values from Wilcoxon signed rank tests shown to the right of each distribution).

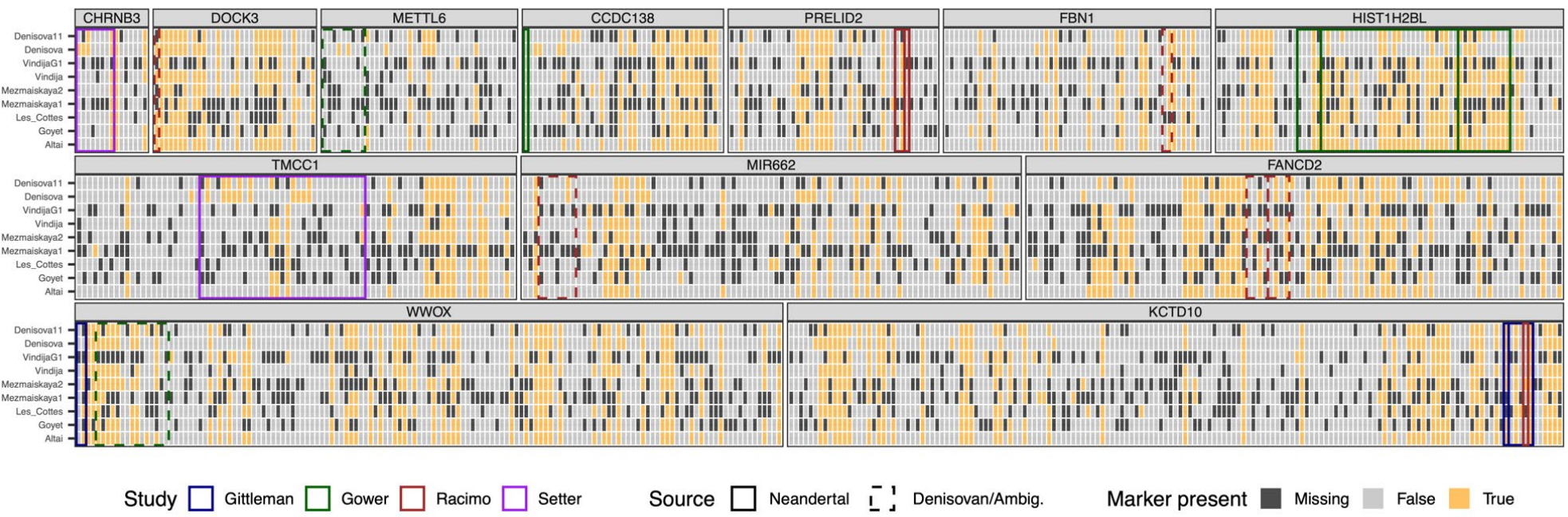
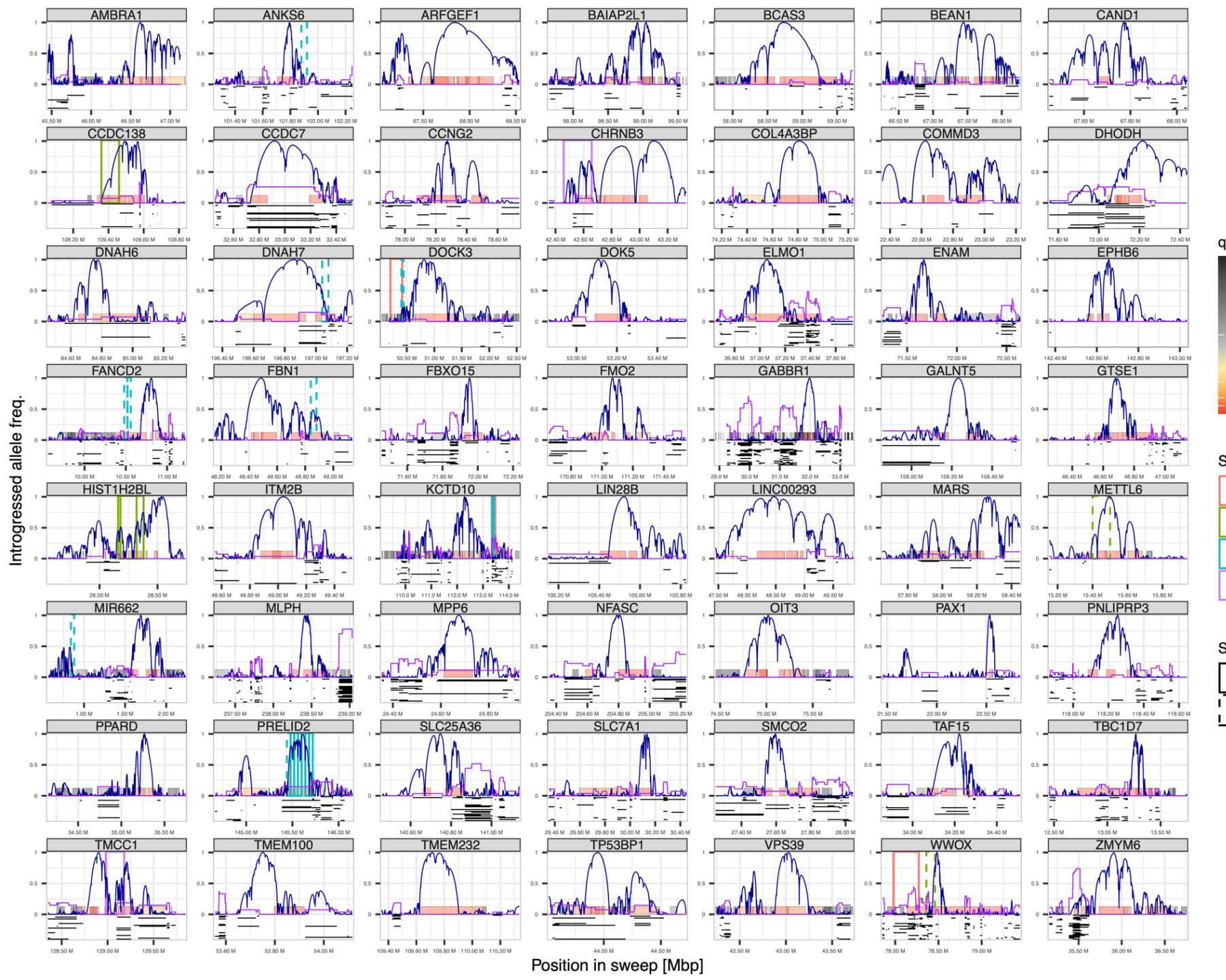
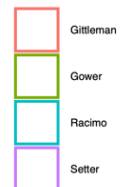


Figure S7. Allelic state of archaic hominin sequences homologous to Eurasian sweeps. To examine if archaic hominin species were a potential source of the beneficial alleles at sweeps, nine previously published pseudohaploid hominin genomes were examined for evidence of the sweep haplotype. The allelic state of diagnostic marker SNPs in each hominin genome were compared to the inferred sweep haplotype allele in 12 sweep regions where a previously reported adaptively introgressed hominin region overlaps at least one marker SNP (orange = same allele as inferred sweep allele, gray = alternate allele from inferred sweep allele, black = no allele called in sample). Hominin introgressed regions are indicated by colored boxes, with different colors used for each study where the hominin region was reported (see key); boxes with solid lines depict introgressed loci observed in Neandertals, dashed lines indicate introgressed loci observed in Denisovans or where the identity of the hominin donor was ambiguous.



q value

Study



Source

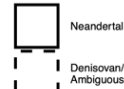


Figure S8. Introgressed archaic hominin sequences in the vicinity of Eurasian hard sweeps.

Similar to Fig. 3 but showing results for all 56 sweeps that were used in dating analyses. See Fig 3. for a full explanation of the plot items. As with Figure S7, the colored boxes indicate the position of introgressed hominin sequences, with different colors for each study (see key).

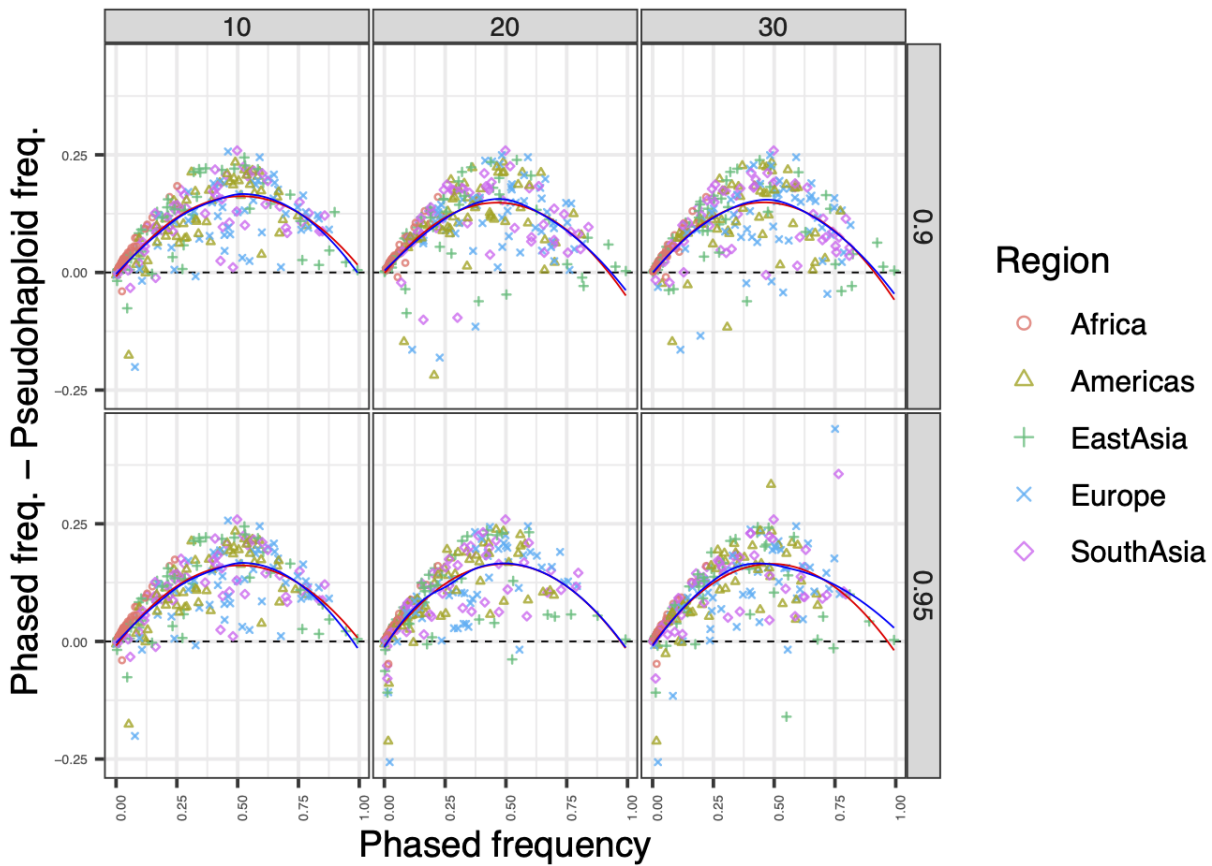


Figure S9. Sweep haplotype frequencies tend to be underestimated in pseudohaploid population genomic data. The presence of sweep haplotypes was inferred at all 56 sweeps for phased genomes from the 1,000 Genomes Project (1kGP) using our marker allele method (Supplemental Materials 2), and the diploid frequency of sweep haplotypes quantified for each continental region (x-axis; see key for populations). Each 1kGP sample was pseudohaploidized by randomly sampling a single allele at each marker SNP, and the difference between the pseudohaploid frequency and phased diploid frequencies calculated (y-axis). The imposition of pseudohaploidy results in the persistent underestimation of the ‘true’ sweep haplotype frequency estimated from the phased samples, and this bias is maximal at intermediate frequencies as a direct result of mixing of sweep and non-sweep alleles in increasingly prevalent heterozygous individuals (see Fig. S10). This bias was consistent across different combinations of SNP marker number (column panels) and minimum marker allele presence (row panels). The blue and red lines show the fit for LOESS and quadratic regressions, respectively.

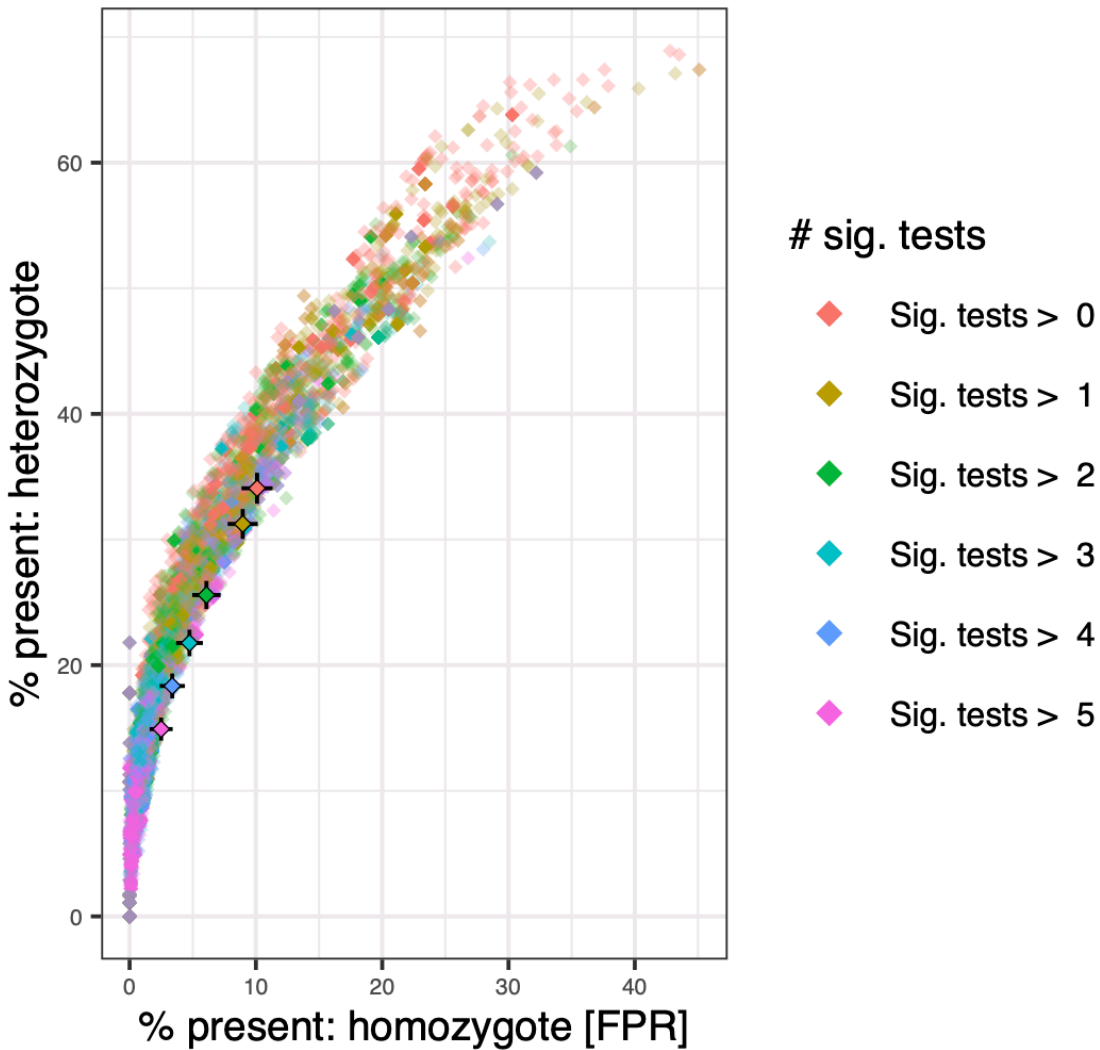


Figure S10. Sweep haplotype detection in samples with one (sweep heterozygotes) or no (non-sweep homozygotes) sweep haplotypes. The performance of our sweep haplotype detection method was evaluated using simulated ancient genomes. Ancient samples were simulated by pseudohaploidizing phased diploid genomes (i.e. randomly selecting a single allele at each previously identified marker SNP) and imposing SNP missingness patterns observed for individual ancient samples (Supplemental Materials 2). Sweep haplotypes were called using six combinations of detection criteria, which are indicated by different colored points. The detection criterion used throughout the current study considered a specific sweep to be present in a sample if it was observed in at least three of six detection criteria (green points). Under this criterion, sweeps are expected to be called in ~26% of sweep heterozygotes and ~6% of non-sweep homozygotes on average, which we considered to be a reasonable tradeoff between statistical power and FPR. Sweep haplotypes are always expected to be called in sweep homozygotes in the absence of sequencing error.

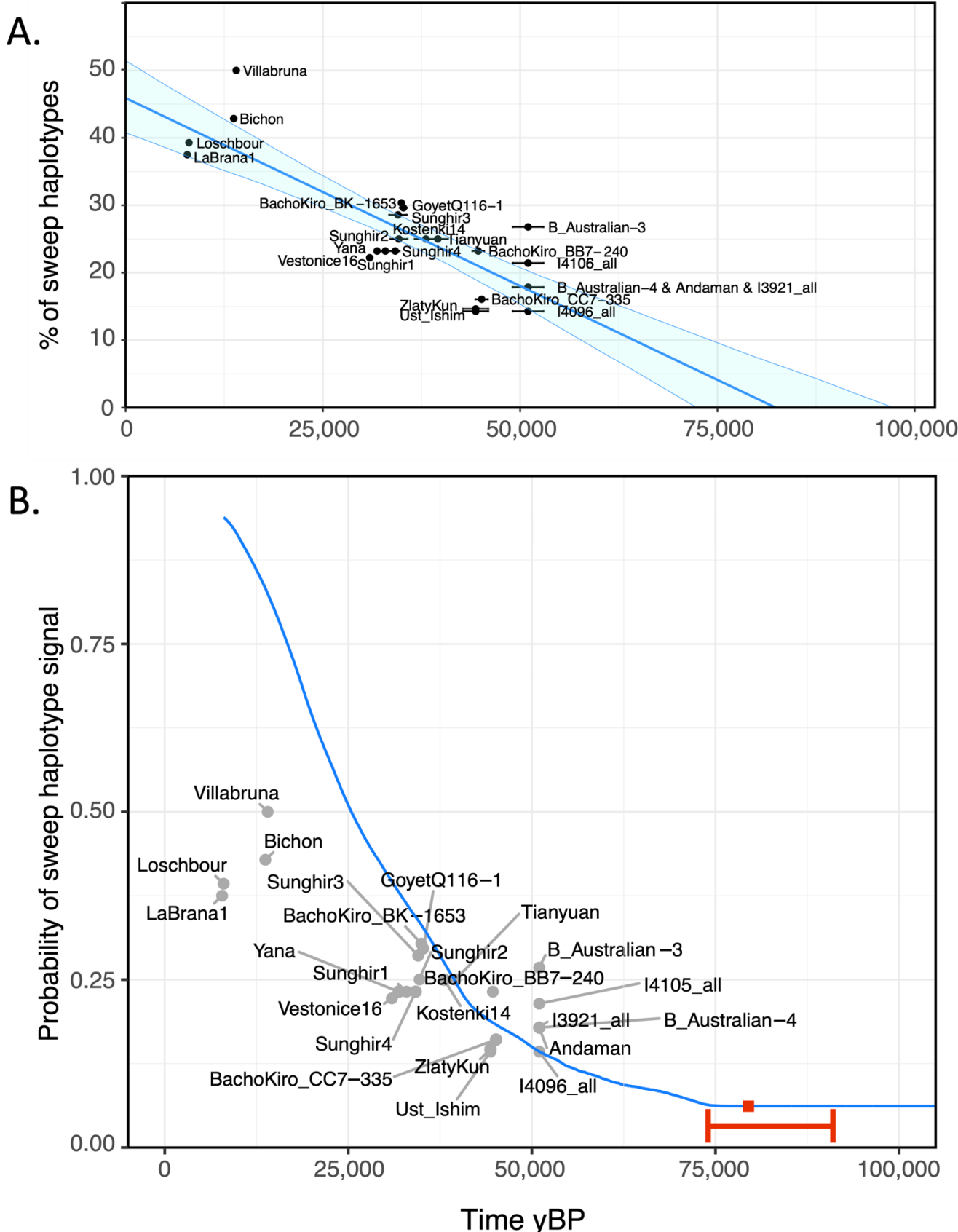


Figure S11. Model-based estimates of the onset of selection. **(A)** Linear regression of the proportion of the 56 sweeps observed in select samples upon sample date. Radiocarbon dates were used for all ancient Eurasian samples, with Andamanese and Oceanian samples assigned a single date that coincides with their point of separation from Main Eurasians (i.e. ~51ka; see Supplementary Materials 2). The diagonal blue line shows the best fitting linear relationship, with the associated 95% confidence interval indicated by the surrounding light blue shading. The predicted x-intercept in the regression model at ~83ka provides an approximate lower bound for the onset of selection, with a 95% confidence interval between ~72-97ka. **(B)** Results from a population genetic model where sweeps were simulated under a demographically informed coalescent model and the resulting trajectories aggregated across time. Simulated patterns were compared to sweep haplotype patterns among the same set of samples used in the linear regression analysis, excluding the Mesolithic samples (these have >30% fewer sweeps than expected assuming sweeps aggregate at the constant rate across time, likely reflecting population structure that is not included in our model; see Supplemental Materials 2). The best fitting trajectory is shown as a blue line, which predicts that selection commenced around 79ka (red point; red bar beneath shows the 95% confidence interval [74ka to 91ka]). Note that the expected probability of sweep presence does not decrease below 6%, as this is the FPR for sweep detection that was directly incorporated into the model.

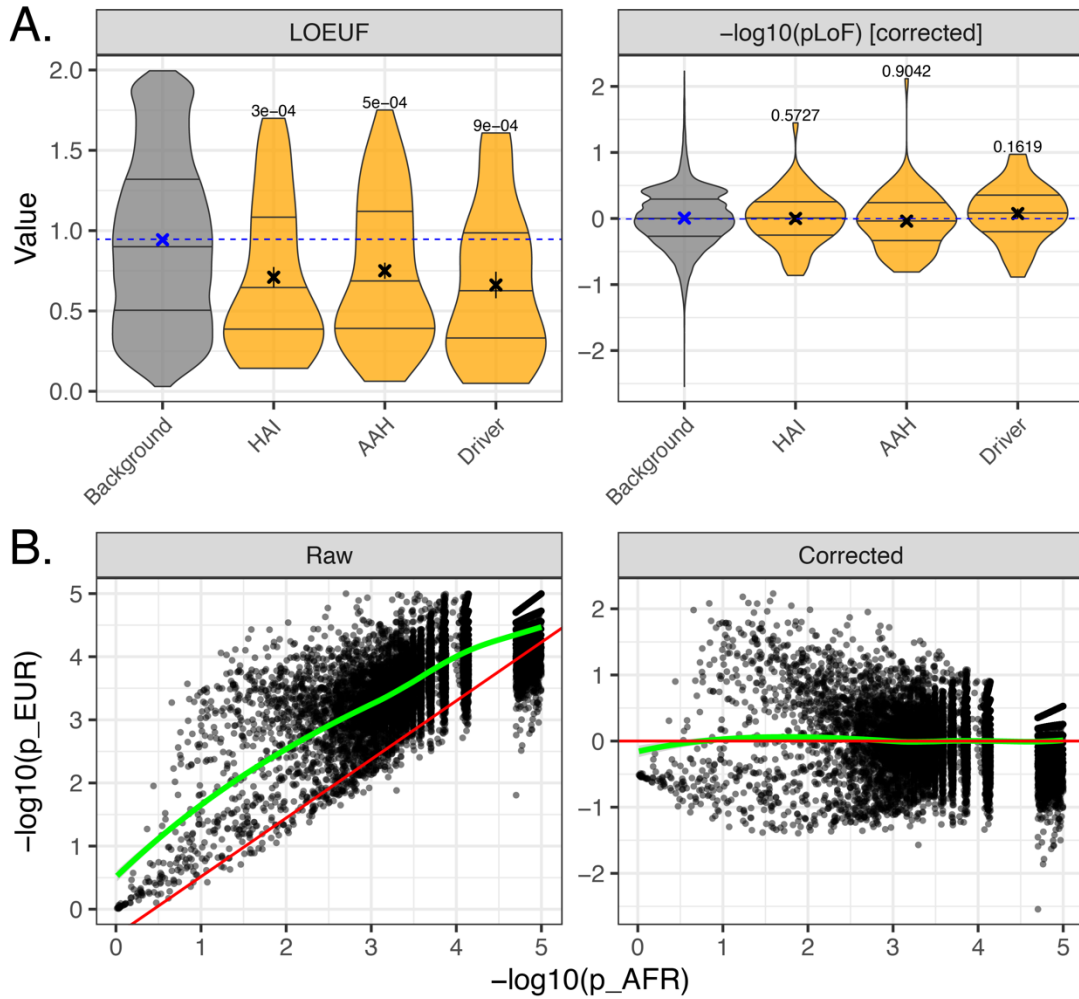


Figure S12. Candidate genes are less tolerant of loss of function mutations than expected. (A) The distribution of two statistics measuring intolerance to loss of function mutations (see Supplemental Materials 3) for each candidate set (i.e. 32 ancient Eurasian [Driver] genes, 82 adaptive Arctic human [AAH] genes, and 61 hominin adaptively introgressed [HAI] genes; orange violins) relative to the scores on all remaining genes (gray violins). Notably, LOEUF scores are significantly lower in each of three categories (p values from permutation tests are shown at the top of each violin), but this is not observed for the corrected p_{lof} statistic, suggesting that the significant LOEUF scores are not due to the erasure of deleterious variation following positive selection at each sweep locus (see Supplemental Materials 3). **(B)** Raw p_{lof} statistics for European populations relative to African populations (right panel). Corrected p_{lof} values were calculated for Europeans (left panel) by taking residuals from a regression against African p_{lof} values. Corrected p_{lof} values should be a proxy for changes in this statistic following the separation of ancestral Eurasian and African AMH lineages. The red and green lines highlight the best fitting linear and LOESS regression trends for the raw and residual datasets.

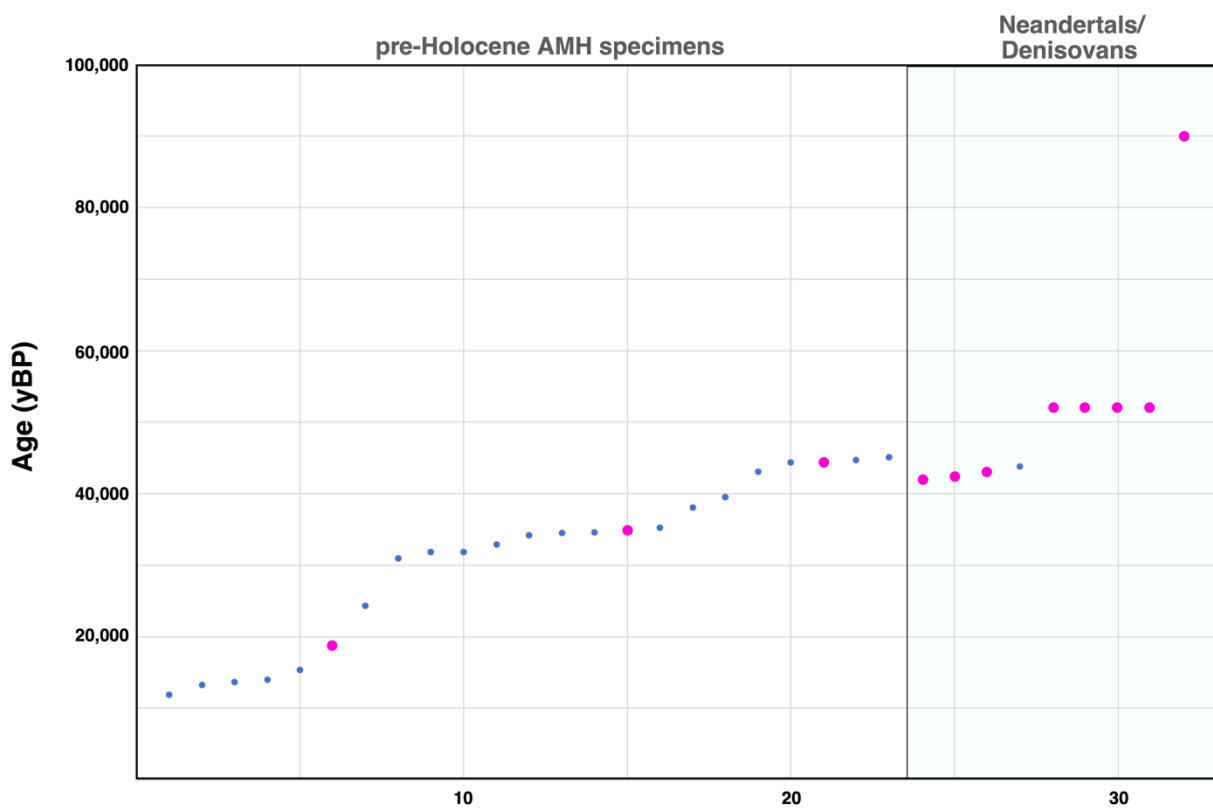


Figure S13. Age and genetically determined sex of pre-Holocene AMH and archaic hominin specimens. All pre-Holocene AMH samples from the Allen Ancient DNA Resource version 42.4 with sufficient genomic coverage to pass the quality filtering criteria. Most are western Eurasian in origin, and include specimens associated with IUP, Aurignacian, Gravettian, and Magdalenian cultures. Samples are arranged along the x-axis by radiocarbon date (sequential number indicated). There is a marked dominance of males (blue dots) relative to females (purple dots) in the pre-Holocene AMH specimens, whereas in comparison available archaic hominins with sufficient genomic coverage appear to show the reverse pattern. Several of the older hominid ages are mid-point estimates from a sizable range.

Supplemental Tables

Table S1. Ancient western Eurasian samples used for hard sweep detection. Summarized metadata includes (across successive columns) sample identifier, population assignment, geographic sampling coordinates, mean sample ages (largely calibrated with IntCal13), source publication, and raw genetic data type. Note that not all samples were able to be assigned to sufficiently large and genetically homogenous groups to be used in the analyses.

Sample ID	Group	Lat.	Long.	Mean date (yBP)	Source Publication	Data type
Bar31	Anatolia_EF	40.27	29.65	8,278	Hofmanova et al. 2016	Shotgun-HS2500
Bar8	Anatolia_EF	40.27	29.65	8,071	Hofmanova et al. 2016	Shotgun-HS2500
I0707	Anatolia_EF	40.30	29.57	8,300	Mathieson et al. 2015	1240K.capture
I0708	Anatolia_EF	40.30	29.57	8,097	Mathieson et al. 2015	1240K.capture
I0709	Anatolia_EF	40.30	29.57	8,300	Mathieson et al. 2015	1240K.capture
I0723	Anatolia_EF	40.26	29.65	7,870	Mathieson et al. 2015	1240K.capture
I0724	Anatolia_EF	40.26	29.65	7,950	Mathieson et al. 2015	1240K.capture
I0726	Anatolia_EF	40.26	29.65	7,950	Mathieson et al. 2015	1240K.capture
I0727	Anatolia_EF	40.26	29.65	7,950	Mathieson et al. 2015	1240K.capture
I0736	Anatolia_EF	40.30	29.57	8,300	Mathieson et al. 2015	1240K.capture
I0744	Anatolia_EF	40.30	29.57	8,273	Mathieson et al. 2015	1240K.capture
I0745	Anatolia_EF	40.30	29.57	8,251	Mathieson et al. 2015	1240K.capture
I0746	Anatolia_EF	40.30	29.57	7,930	Mathieson et al. 2015	1240K.capture
I0854	Anatolia_EF	40.30	29.57	8,300	Mathieson et al. 2015	1240K.capture
I1096	Anatolia_EF	40.30	29.57	8,300	Mathieson et al. 2015	1240K.capture
I1097	Anatolia_EF	40.30	29.57	8,288	Mathieson et al. 2015	1240K.capture
I1098	Anatolia_EF	40.30	29.57	8,300	Mathieson et al. 2015	1240K.capture
I1099	Anatolia_EF	40.30	29.57	8,300	Mathieson et al. 2015	1240K.capture
I1100	Anatolia_EF	40.30	29.57	8,300	Mathieson et al. 2015	1240K.capture
I1101	Anatolia_EF	40.30	29.57	8,300	Mathieson et al. 2015	1240K.capture
I1102	Anatolia_EF	40.30	29.57	8,300	Mathieson et al. 2015	1240K.capture
I1103	Anatolia_EF	40.30	29.57	8,300	Mathieson et al. 2015	1240K.capture
I1579	Anatolia_EF	40.30	29.57	8,300	Mathieson et al. 2015	1240K.capture
I1580	Anatolia_EF	40.30	29.57	8,195	Mathieson et al. 2015	1240K.capture
I1581	Anatolia_EF	40.30	29.57	8,254	Mathieson et al. 2015	1240K.capture
I1583	Anatolia_EF	40.30	29.57	8,281	Mathieson et al. 2015	1240K.capture
I1585	Anatolia_EF	40.30	29.57	8,300	Mathieson et al. 2015	1240K.capture
Kumtepe004	Anatolia_LF	39.98	26.23	6,682	Omrak et al. 2016	Shotgun
Kumtepe006	Anatolia_LF	39.98	26.23	6,682	Omrak et al. 2017	Shotgun
ZBC	Anatolia_preNeo	38.72	36.39	15,308	Feldman et al. 2019	1240K.capture
ZHAG	Anatolia_preNeo	37.75	32.86	10,000	Feldman et al. 2019	1240K.capture
ZHAJ	Anatolia_preNeo	37.75	32.86	10,190	Feldman et al. 2019	1240K.capture
ZHJ	Anatolia_preNeo	37.75	32.86	10,000	Feldman et al. 2019	1240K.capture
ZKO	Anatolia_preNeo	37.75	32.86	10,000	Feldman et al. 2019	1240K.capture
ZMOJ	Anatolia_preNeo	37.75	32.86	10,000	Feldman et al. 2019	1240K.capture
I0633	Balkan_EF	44.90	19.75	7,440	Mathieson et al. 2018	1240K.capture
I0634	Balkan_EF	44.90	19.75	6,557	Mathieson et al. 2018	1240K.capture
I0676	Balkan_EF	41.90	21.35	7,807	Mathieson et al. 2018	1240K.capture
I0679	Balkan_EF	42.02	25.60	7,622	Mathieson et al. 2018	1240K.capture
I0698	Balkan_EF	42.10	25.75	7,601	Mathieson et al. 2018	1240K.capture
I0700	Balkan_EF	43.98	26.4	7,934	Mathieson et al. 2018	1240K.capture
I0704	Balkan_EF	43.16	25.88	7,889	Mathieson et al. 2018	1240K.capture
I0706	Balkan_EF	43.16	25.88	7,905	Mathieson et al. 2018	1240K.capture
I1108	Balkan_EF	43.98	26.40	7,550	Mathieson et al. 2018	1240K.capture
I1109	Balkan_EF	43.98	26.40	7,550	Mathieson et al. 2018	1240K.capture
I1113	Balkan_EF	43.98	26.40	7,550	Mathieson et al. 2018	1240K.capture
I1131	Balkan_EF	44.90	19.75	6,483	Mathieson et al. 2018	1240K.capture
I1295	Balkan_EF	43.98	26.40	7,550	Mathieson et al. 2018	1240K.capture
I1296	Balkan_EF	43.98	26.40	7,550	Mathieson et al. 2018	1240K.capture
I1297	Balkan_EF	43.98	26.40	7,550	Mathieson et al. 2018	1240K.capture
I1298	Balkan_EF	43.37	23.73	7,885	Mathieson et al. 2018	1240K.capture
I2215	Balkan_EF	43.98	26.40	7,980	Mathieson et al. 2018	1240K.capture
I2216	Balkan_EF	43.98	26.40	7,845	Mathieson et al. 2018	1240K.capture
I2318	Balkan_EF	37.42	23.13	5,945	Mathieson et al. 2018	1240K.capture
I2521	Balkan_EF	43.16	25.88	7,505	Mathieson et al. 2018	1240K.capture
I2526	Balkan_EF	43.14	25.60	7,336	Mathieson et al. 2018	1240K.capture
I2529	Balkan_EF	42.10	25.75	7,601	Mathieson et al. 2018	1240K.capture
I2532	Balkan_EF	45.48	27.00	7,621	Mathieson et al. 2018	1240K.capture
I2533	Balkan_EF	44.26	23.90	7,378	Mathieson et al. 2018	1240K.capture

I3433	Balkan_EF	43.59	16.65	7,814	Mathieson et al. 2018	1240K.capture
I3498	Balkan_EF	45.76	18.57	7,698	Mathieson et al. 2018	1240K.capture
I3708	Balkan_EF	36.64	22.38	6,550	Mathieson et al. 2018	1240K.capture
I3709	Balkan_EF	36.64	22.38	5,847	Mathieson et al. 2018	1240K.capture
I3879	Balkan_EF	43.98	26.40	7,828	Mathieson et al. 2018	1240K.capture
I3920	Balkan_EF	36.64	22.38	5,770	Mathieson et al. 2018	1240K.capture
I3947	Balkan_EF	43.59	16.65	7,836	Mathieson et al. 2018	1240K.capture
I3948	Balkan_EF	43.59	16.65	7,860	Mathieson et al. 2018	1240K.capture
I4167	Balkan_EF	45.76	18.57	6,624	Mathieson et al. 2018	1240K.capture
I4168	Balkan_EF	45.76	18.57	6,600	Mathieson et al. 2018	1240K.capture
I4665	Balkan_EF	44.55	22.03	8,006	Mathieson et al. 2018	1240K.capture
I4666	Balkan_EF	44.55	22.03	8,017	Mathieson et al. 2018	1240K.capture
I4918	Balkan_EF	44.49	21.08	7,600	Mathieson et al. 2018	1240K.capture
I5071	Balkan_EF	44.82	13.64	7,571	Mathieson et al. 2018	1240K.capture
I5072	Balkan_EF	44.82	13.64	7,751	Mathieson et al. 2018	1240K.capture
I5077	Balkan_EF	45.32	18.39	7,026	Mathieson et al. 2018	1240K.capture
I5078	Balkan_EF	45.32	18.39	6,569	Mathieson et al. 2018	1240K.capture
I5405	Balkan_EF	44.55	22.03	7,684	Mathieson et al. 2018	1240K.capture
I5427	Balkan_EF	36.64	22.38	7,892	Mathieson et al. 2018	1240K.capture
Kleitos10	Balkan_EF	40.43	21.86	6,063	Hofmanova et al. 2016	1240K.capture
Paliambela7	Balkan_EF	40.27	22.45	6,351	Hofmanova et al. 2016	Shotgun-HS2000
Revenia5	Balkan_EF	40.30	22.62	8,301	Hofmanova et al. 2016	Shotgun-HS2000
ANI153	Balkan_LF	43.21	27.86	6,413	Mathieson et al. 2018	1240K.capture
ANI159_ANI181	Balkan_LF	43.21	27.86	6,571	Mathieson et al. 2018	1240K.capture
ANI160	Balkan_LF	43.21	27.86	6,542	Mathieson et al. 2018	1240K.capture
I0781	Balkan_LF	42.23	24.26	6,400	Mathieson et al. 2018	1240K.capture
I0785	Balkan_LF	42.23	24.26	6,357	Mathieson et al. 2018	1240K.capture
I2181	Balkan_LF	43.06	26.98	6,453	Mathieson et al. 2018	1240K.capture
I2423	Balkan_LF	43.06	26.98	6,388	Mathieson et al. 2018	1240K.capture
I2424	Balkan_LF	43.06	26.98	6,304	Mathieson et al. 2018	1240K.capture
I2425	Balkan_LF	43.06	26.77	6,515	Mathieson et al. 2018	1240K.capture
I2426	Balkan_LF	43.06	26.77	6,307	Mathieson et al. 2018	1240K.capture
I2427	Balkan_LF	43.06	26.77	6,340	Mathieson et al. 2018	1240K.capture
I2430	Balkan_LF	43.06	26.98	6,448	Mathieson et al. 2018	1240K.capture
I2431	Balkan_LF	43.10	26.72	6,615	Mathieson et al. 2018	1240K.capture
I2510	Balkan_LF	43.16	25.88	4,758	Mathieson et al. 2018	1240K.capture
I2519	Balkan_LF	43.16	25.88	6,242	Mathieson et al. 2018	1240K.capture
I2520	Balkan_LF	43.16	25.88	5,132	Mathieson et al. 2018	1240K.capture
I2792	Balkan_LF	45.34	19.06	4,677	Mathieson et al. 2018	1240K.capture
I4088	Balkan_LF	47.73	22.44	6,154	Mathieson et al. 2018	1240K.capture
I4089	Balkan_LF	47.73	22.44	5,653	Mathieson et al. 2018	1240K.capture
I5079	Balkan_LF	45.44	17.56	5,485	Mathieson et al. 2018	1240K.capture
Bul10	Balkan_LNBA	42.43	25.90	4,957	Mathieson et al. 2018	1240K.capture
Bul6	Balkan_LNBA	42.43	25.90	4,450	Mathieson et al. 2018	1240K.capture
Bul8	Balkan_LNBA	42.43	25.90	4,450	Mathieson et al. 2018	1240K.capture
I2163	Balkan_LNBA	42.13	25.49	3,638	Mathieson et al. 2018	1240K.capture
I2165	Balkan_LNBA	42.13	25.49	4,908	Mathieson et al. 2018	1240K.capture
I2175	Balkan_LNBA	43.06	26.98	5,122	Mathieson et al. 2018	1240K.capture
I2176	Balkan_LNBA	43.06	26.98	5,132	Mathieson et al. 2018	1240K.capture
I2509	Balkan_LNBA	43.16	25.88	6,353	Mathieson et al. 2018	1240K.capture
I3313	Balkan_LNBA	43.89	15.98	2,733	Mathieson et al. 2018	1240K.capture
I3499	Balkan_LNBA	45.76	18.57	4,725	Mathieson et al. 2018	1240K.capture
I4175	Balkan_LNBA	45.34	19.06	4,800	Mathieson et al. 2018	1240K.capture
I4331	Balkan_LNBA	43.19	17.34	3,526	Mathieson et al. 2018	1240K.capture
I4332	Balkan_LNBA	43.19	17.34	3,516	Mathieson et al. 2018	1240K.capture
I5769	Balkan_LNBA	43.16	25.88	2,400	Mathieson et al. 2018	1240K.capture
RISE595	Balkan_LNBA	42.38	18.74	3,750	Allentoft et al. 2015	Shotgun
RISE596	Balkan_LNBA	42.38	18.74	3,050	Allentoft et al. 2015	Shotgun
I0022	CentralEurope_EF	48.78	9.18	7,125	Mathieson et al. 2015	840k+390k.capture
I0025	CentralEurope_EF	48.78	9.18	7,125	Mathieson et al. 2015	840k+390k.capture
I0026	CentralEurope_EF	48.78	9.18	7,125	Mathieson et al. 2015	840k+390k.capture

I0046	CentralEurope_EF	51.89	11.04	7,051	Mathieson et al. 2015	840k+390k.capture
I0048	CentralEurope_EF	51.89	11.04	7,056	Mathieson et al. 2015	840k+390k.capture
I0054	CentralEurope_EF	51.66	11.53	7,072	Mathieson et al. 2015	840k+390k.capture
I0057	CentralEurope_EF	51.89	11.04	7,070	Mathieson et al. 2015	840k+390k.capture
I0100	CentralEurope_EF	51.89	11.04	6,977	Mathieson et al. 2015	840k+390k.capture
I0174	CentralEurope_EF	46.20	18.70	7,569	Mathieson et al. 2015	840k+390k.capture
I0176	CentralEurope_EF	46.40	18.74	7,026	Mathieson et al. 2015	840k+390k.capture
I0447	CentralEurope_EF	46.36	20.43	6,700	Lipson et al. 2017	1240K.capture
I0449	CentralEurope_EF	46.36	20.43	6,700	Lipson et al. 2017	1240K.capture
I0659	CentralEurope_EF	51.89	11.04	7,037	Mathieson et al. 2015	840k+390k.capture
I0795	CentralEurope_EF	51.27	11.66	7,079	Mathieson et al. 2015	840k+390k.capture
I0797	CentralEurope_EF	51.28	11.65	7,125	Mathieson et al. 2015	1240K.capture
I0807	CentralEurope_EF	51.42	11.68	5,790	Mathieson et al. 2015	840k+390k.capture
I0821	CentralEurope_EF	51.90	11.05	6,976	Mathieson et al. 2015	840k+390k.capture
I1495	CentralEurope_EF	47.17	19.83	6,374	Mathieson et al. 2015	1240K.capture
I1496	CentralEurope_EF	47.17	19.83	7,052	Mathieson et al. 2015	1240K.capture
I1498	CentralEurope_EF	47.52	21.59	7,124	Mathieson et al. 2015	1240K.capture
I1499	CentralEurope_EF	48.52	21.17	7,060	Mathieson et al. 2015	1240K.capture
I1500	CentralEurope_EF	47.17	20.83	7,050	Mathieson et al. 2015	1240K.capture
I1505	CentralEurope_EF	47.88	21.19	7,061	Mathieson et al. 2015	1240K.capture
I1506	CentralEurope_EF	47.88	21.19	7,139	Mathieson et al. 2015	1240K.capture
I1507	CentralEurope_EF	47.93	21.20	7,660	Mathieson et al. 2015	1240K.capture
I1508	CentralEurope_EF	47.32	21.53	7,590	Mathieson et al. 2015	1240K.capture
I1550	CentralEurope_EF	51.89	11.04	7,125	Mathieson et al. 2015	1240K.capture
I1876	CentralEurope_EF	46.21	18.71	7,544	Lipson et al. 2017	1240K.capture
I1878	CentralEurope_EF	46.21	18.71	7,699	Lipson et al. 2017	1240K.capture
I1880	CentralEurope_EF	45.99	18.58	7,600	Lipson et al. 2017	1240K.capture
I1882	CentralEurope_EF	47.50	18.91	7,050	Lipson et al. 2017	1240K.capture
I1887	CentralEurope_EF	45.59	18.31	7,150	Lipson et al. 2017	1240K.capture
I1890	CentralEurope_EF	46.42	18.92	6,875	Lipson et al. 2017	1240K.capture
I1891	CentralEurope_EF	46.42	18.92	6,968	Lipson et al. 2017	1240K.capture
I1893	CentralEurope_EF	46.20	18.72	6,889	Lipson et al. 2017	1240K.capture
I1894	CentralEurope_EF	45.59	18.31	7,150	Lipson et al. 2017	1240K.capture
I1895	CentralEurope_EF	45.60	18.28	7,151	Lipson et al. 2017	1240K.capture
I1896	CentralEurope_EF	45.60	18.28	7,150	Lipson et al. 2017	1240K.capture
I1899	CentralEurope_EF	47.10	17.91	6,600	Lipson et al. 2017	1240K.capture
I1901	CentralEurope_EF	47.10	17.91	6,789	Lipson et al. 2017	1240K.capture
I1902	CentralEurope_EF	47.02	17.96	6,600	Lipson et al. 2017	1240K.capture
I1903	CentralEurope_EF	46.20	18.70	6,600	Lipson et al. 2017	1240K.capture
I1904	CentralEurope_EF	46.20	18.70	7,028	Lipson et al. 2017	1240K.capture
I1905	CentralEurope_EF	47.51	18.62	6,664	Lipson et al. 2017	1240K.capture
I1906	CentralEurope_EF	47.51	18.62	6,600	Lipson et al. 2017	1240K.capture
I2005	CentralEurope_EF	51.90	11.05	7,126	Lipson et al. 2017	1240K.capture
I2008	CentralEurope_EF	51.90	11.05	7,052	Lipson et al. 2017	1240K.capture
I2012	CentralEurope_EF	51.90	11.05	6,400	Lipson et al. 2017	1240K.capture
I2014	CentralEurope_EF	51.90	11.05	6,978	Lipson et al. 2017	1240K.capture
I2016	CentralEurope_EF	51.90	11.05	7,125	Lipson et al. 2017	1240K.capture
I2017	CentralEurope_EF	51.90	11.05	7,125	Lipson et al. 2017	1240K.capture
I2020	CentralEurope_EF	51.90	11.05	7,125	Lipson et al. 2017	1240K.capture
I2021	CentralEurope_EF	51.90	11.05	7,125	Lipson et al. 2017	1240K.capture
I2022	CentralEurope_EF	51.90	11.05	7,125	Lipson et al. 2017	1240K.capture
I2026	CentralEurope_EF	51.90	11.05	7,125	Lipson et al. 2017	1240K.capture
I2029	CentralEurope_EF	51.90	11.05	7,126	Lipson et al. 2017	1240K.capture
I2030	CentralEurope_EF	51.90	11.05	7,125	Lipson et al. 2017	1240K.capture
I2032	CentralEurope_EF	51.90	11.05	7,125	Lipson et al. 2017	1240K.capture
I2036	CentralEurope_EF	51.90	11.05	7,125	Lipson et al. 2017	1240K.capture
I2037	CentralEurope_EF	51.90	11.05	7,056	Lipson et al. 2017	1240K.capture
I2038	CentralEurope_EF	51.90	11.05	7,125	Lipson et al. 2017	1240K.capture
I2352	CentralEurope_EF	47.10	17.91	6,600	Lipson et al. 2017	1240K.capture
I2355	CentralEurope_EF	47.46	20.51	7,050	Lipson et al. 2017	1240K.capture
I2357	CentralEurope_EF	47.46	20.51	7,050	Lipson et al. 2017	1240K.capture

I2358	CentralEurope_EF	47.46	20.51	6,700	Lipson et al. 2017	1240K.capture
I2375	CentralEurope_EF	48.00	21.18	7,050	Lipson et al. 2017	1240K.capture
I2377	CentralEurope_EF	48.00	21.18	7,025	Lipson et al. 2017	1240K.capture
I2378	CentralEurope_EF	47.86	21.00	7,050	Lipson et al. 2017	1240K.capture
I2379	CentralEurope_EF	47.86	21.00	7,010	Lipson et al. 2017	1240K.capture
I2380	CentralEurope_EF	47.78	20.58	7,350	Lipson et al. 2017	1240K.capture
I2382	CentralEurope_EF	47.78	20.58	7,350	Lipson et al. 2017	1240K.capture
I2384	CentralEurope_EF	47.86	21.43	7,129	Lipson et al. 2017	1240K.capture
I2387	CentralEurope_EF	46.39	20.24	6,700	Lipson et al. 2017	1240K.capture
I2739	CentralEurope_EF	46.21	18.70	7,141	Lipson et al. 2017	1240K.capture
I2744	CentralEurope_EF	47.18	19.86	7,050	Lipson et al. 2017	1240K.capture
I2745	CentralEurope_EF	47.18	19.86	7,050	Lipson et al. 2017	1240K.capture
I2746	CentralEurope_EF	46.94	21.21	6,700	Lipson et al. 2017	1240K.capture
I2794	CentralEurope_EF	47.19	20.40	7,573	Lipson et al. 2017	1240K.capture
I3535	CentralEurope_EF	47.86	21.43	7,060	Lipson et al. 2017	1240K.capture
I3536	CentralEurope_EF	47.64	17.36	7,050	Lipson et al. 2017	1240K.capture
I3537	CentralEurope_EF	47.78	20.58	7,371	Lipson et al. 2017	1240K.capture
I4181	CentralEurope_EF	46.74	18.96	7,050	Lipson et al. 2017	1240K.capture
I4183	CentralEurope_EF	46.03	18.33	6,756	Lipson et al. 2017	1240K.capture
I4184	CentralEurope_EF	46.03	18.33	6,772	Lipson et al. 2017	1240K.capture
I4185	CentralEurope_EF	46.20	18.73	6,877	Lipson et al. 2017	1240K.capture
I4186	CentralEurope_EF	47.48	21.50	7,050	Lipson et al. 2017	1240K.capture
I4187	CentralEurope_EF	47.48	21.50	7,050	Lipson et al. 2017	1240K.capture
I4188	CentralEurope_EF	47.87	21.13	7,050	Lipson et al. 2017	1240K.capture
I4196	CentralEurope_EF	47.50	18.91	7,050	Lipson et al. 2017	1240K.capture
I4199	CentralEurope_EF	48.00	21.18	7,050	Lipson et al. 2017	1240K.capture
I4303	CentralEurope_EF	43.46	5.86	6,632	Olalde et al. 2018	1240K.capture
I4304	CentralEurope_EF	43.46	5.86	6,638	Olalde et al. 2018	1240K.capture
I4305	CentralEurope_EF	43.46	5.86	6,670	Olalde et al. 2018	1240K.capture
I4893	CentralEurope_EF	50.12	14.46	6,348	Olalde et al. 2018	1240K.capture
I4894	CentralEurope_EF	50.12	14.46	6,378	Olalde et al. 2018	1240K.capture
I4971	CentralEurope_EF	47.56	20.72	7,591	Lipson et al. 2017	1240K.capture
I5068	CentralEurope_EF	48.67	16.58	7,088	Mathieson et al. 2018	1240K.capture
I5069	CentralEurope_EF	48.67	16.58	7,088	Mathieson et al. 2018	1240K.capture
I5070	CentralEurope_EF	48.58	16.47	7,088	Mathieson et al. 2018	1240K.capture
I5204	CentralEurope_EF	48.58	16.47	6,950	Mathieson et al. 2018	1240K.capture
I5205	CentralEurope_EF	48.58	16.47	6,950	Mathieson et al. 2018	1240K.capture
I5206	CentralEurope_EF	48.58	16.47	6,950	Mathieson et al. 2018	1240K.capture
I5207	CentralEurope_EF	48.58	16.47	6,950	Mathieson et al. 2018	1240K.capture
I5208	CentralEurope_EF	48.58	16.47	6,950	Mathieson et al. 2018	1240K.capture
Stuttgart	CentralEurope_EF	48.78	9.18	7,140	Lazaridis et al. 2014	Shotgun-HS2500
I0172	CentralEurope_LF	51.42	11.68	5,173	Mathieson et al. 2015	840k+390k.capture
I0551	CentralEurope_LF	51.52	11.85	5,162	Mathieson et al. 2015	1240K.capture
I0559	CentralEurope_LF	51.79	11.14	5,539	Mathieson et al. 2015	840k+390k.capture
I0560	CentralEurope_LF	51.79	11.14	5,458	Mathieson et al. 2015	840k+390k.capture
I0800	CentralEurope_LF	51.53	11.83	5,171	Lipson et al. 2017	1240K.capture
I0802	CentralEurope_LF	51.53	11.83	5,162	Lipson et al. 2017	1240K.capture
I1907	CentralEurope_LF	47.64	17.36	6,152	Lipson et al. 2017	1240K.capture
I1908	CentralEurope_LF	46.71	17.24	6,050	Lipson et al. 2017	1240K.capture
I1909	CentralEurope_LF	46.00	18.58	6,089	Lipson et al. 2017	1240K.capture
I2353	CentralEurope_LF	47.46	20.51	6,200	Lipson et al. 2017	1240K.capture
I2354	CentralEurope_LF	47.46	20.51	6,200	Lipson et al. 2017	1240K.capture
I2366	CentralEurope_LF	47.62	19.04	5,092	Lipson et al. 2017	1240K.capture
I2367	CentralEurope_LF	47.62	19.04	5,080	Lipson et al. 2017	1240K.capture
I2369	CentralEurope_LF	47.62	19.04	5,185	Lipson et al. 2017	1240K.capture
I2370	CentralEurope_LF	47.32	19.17	5,095	Lipson et al. 2017	1240K.capture
I2371	CentralEurope_LF	47.32	19.17	5,178	Lipson et al. 2017	1240K.capture
I2394	CentralEurope_LF	47.10	17.91	6,238	Lipson et al. 2017	1240K.capture
I2395	CentralEurope_LF	47.46	20.51	6,200	Lipson et al. 2017	1240K.capture
I2752	CentralEurope_LF	46.78	17.73	5,175	Lipson et al. 2017	1240K.capture
I2753	CentralEurope_LF	46.78	17.73	5,080	Lipson et al. 2017	1240K.capture

I2763	CentralEurope_LF	46.67	17.27	5,025	Lipson et al. 2017	1240K.capture
I2783	CentralEurope_LF	46.33	19.05	6,045	Lipson et al. 2017	1240K.capture
I2785	CentralEurope_LF	47.68	19.92	5,175	Lipson et al. 2017	1240K.capture
I2788	CentralEurope_LF	47.19	20.00	5,730	Lipson et al. 2017	1240K.capture
I2789	CentralEurope_LF	47.19	20.00	5,650	Lipson et al. 2017	1240K.capture
I2790	CentralEurope_LF	47.19	20.00	5,649	Lipson et al. 2017	1240K.capture
I2791	CentralEurope_LF	47.19	20.00	5,471	Lipson et al. 2017	1240K.capture
I2793	CentralEurope_LF	47.19	20.40	6,300	Lipson et al. 2017	1240K.capture
I4189	CentralEurope_LF	46.20	18.73	6,050	Lipson et al. 2017	1240K.capture
I4308	CentralEurope_LF	43.34	5.06	5,256	Ojalde et al. 2018	1240K.capture
I5116	CentralEurope_LF	47.81	20.89	5,150	Ojalde et al. 2018	1240K.capture
I5117	CentralEurope_LF	47.81	20.89	5,150	Ojalde et al. 2018	1240K.capture
I5118	CentralEurope_LF	47.81	20.89	5,150	Ojalde et al. 2018	1240K.capture
I5119	CentralEurope_LF	47.81	20.89	5,150	Ojalde et al. 2018	1240K.capture
RISE487	CentralEurope_LF	45.26	10.38	5,245	Allentoft et al. 2015	Shotgun-HS2500
E09537	CentralEurope_LNBA	48.32	10.89	4,335	Ojalde et al. 2018	1240K.capture
E09538	CentralEurope_LNBA	48.32	10.89	4,287	Ojalde et al. 2018	1240K.capture
E09568	CentralEurope_LNBA	48.33	10.90	4,285	Ojalde et al. 2018	1240K.capture
E09569	CentralEurope_LNBA	48.32	10.89	4,222	Ojalde et al. 2018	1240K.capture
E09613	CentralEurope_LNBA	48.33	10.90	4,165	Ojalde et al. 2018	1240K.capture
E09614	CentralEurope_LNBA	48.33	10.90	4,107	Ojalde et al. 2018	1240K.capture
I0047	CentralEurope_LNBA	51.89	11.04	3,951	Mathieson et al. 2015	840k+390k.capture
I0049	CentralEurope_LNBA	51.42	11.68	4,287	Mathieson et al. 2015	840k+390k.capture
I0059	CentralEurope_LNBA	51.82	10.91	4,188	Mathieson et al. 2015	840k+390k.capture
I0060	CentralEurope_LNBA	51.45	11.54	4,239	Mathieson et al. 2015	840k+390k.capture
I0099	CentralEurope_LNBA	51.89	11.04	3,036	Mathieson et al. 2015	840k+390k.capture
I0103	CentralEurope_LNBA	51.42	11.68	4,473	Mathieson et al. 2015	840k+390k.capture
I0104	CentralEurope_LNBA	51.42	11.68	4,378	Mathieson et al. 2015	840k+390k.capture
I0106	CentralEurope_LNBA	51.42	11.68	4,287	Mathieson et al. 2015	840k+390k.capture
I0108	CentralEurope_LNBA	51.45	11.54	4,387	Mathieson et al. 2015	840k+390k.capture
I0111	CentralEurope_LNBA	51.45	11.54	4,290	Mathieson et al. 2015	840k+390k.capture
I0112	CentralEurope_LNBA	51.79	11.14	4,250	Mathieson et al. 2015	840k+390k.capture
I0113	CentralEurope_LNBA	51.79	11.14	4,140	Mathieson et al. 2015	840k+390k.capture
I0115	CentralEurope_LNBA	51.42	11.68	3,807	Mathieson et al. 2015	840k+390k.capture
I0116	CentralEurope_LNBA	51.42	11.68	3,987	Mathieson et al. 2015	840k+390k.capture
I0117	CentralEurope_LNBA	51.42	11.68	4,106	Mathieson et al. 2015	840k+390k.capture
I0118	CentralEurope_LNBA	51.45	11.63	4,309	Mathieson et al. 2015	840k+390k.capture
I0164	CentralEurope_LNBA	51.79	11.14	3,909	Mathieson et al. 2015	840k+390k.capture
I0171	CentralEurope_LNBA	51.82	10.91	4,114	Mathieson et al. 2015	840k+390k.capture
I0550	CentralEurope_LNBA	51.27	11.66	4,470	Mathieson et al. 2015	840k+390k.capture
I0803	CentralEurope_LNBA	51.17	11.85	3,987	Mathieson et al. 2015	840k+390k.capture
I0804	CentralEurope_LNBA	51.17	11.85	4,001	Mathieson et al. 2015	840k+390k.capture
I0805	CentralEurope_LNBA	51.79	11.15	4,255	Mathieson et al. 2015	1240K.capture
I0806	CentralEurope_LNBA	51.79	11.14	4,241	Mathieson et al. 2015	840k+390k.capture
I1381	CentralEurope_LNBA	49.15	6.10	4,100	Ojalde et al. 2018	1240K.capture
I1382	CentralEurope_LNBA	49.15	6.10	4,234	Ojalde et al. 2018	1240K.capture
I1388	CentralEurope_LNBA	45.46	6.21	4,244	Ojalde et al. 2018	1240K.capture
I1389	CentralEurope_LNBA	47.65	7.45	4,323	Ojalde et al. 2018	1240K.capture
I1390	CentralEurope_LNBA	47.65	7.45	4,295	Ojalde et al. 2018	1240K.capture
I1391	CentralEurope_LNBA	47.96	7.30	4,178	Ojalde et al. 2018	1240K.capture
I1392	CentralEurope_LNBA	47.56	7.52	4,604	Ojalde et al. 2018	1240K.capture
I1502	CentralEurope_LNBA	47.17	20.83	4,035	Mathieson et al. 2015	1240K.capture
I1504	CentralEurope_LNBA	47.82	19.95	3,140	Mathieson et al. 2015	1240K.capture
I1532	CentralEurope_LNBA	51.42	11.68	4,225	Mathieson et al. 2015	1240K.capture
I1534	CentralEurope_LNBA	51.42	11.68	4,225	Mathieson et al. 2015	1240K.capture
I1536	CentralEurope_LNBA	51.42	11.68	4,225	Mathieson et al. 2015	1240K.capture
I1538	CentralEurope_LNBA	51.42	11.68	4,225	Mathieson et al. 2015	1240K.capture
I1539	CentralEurope_LNBA	51.42	11.68	4,408	Mathieson et al. 2015	1240K.capture
I1540	CentralEurope_LNBA	51.42	11.68	4,225	Mathieson et al. 2015	1240K.capture
I1542	CentralEurope_LNBA	51.42	11.68	4,225	Mathieson et al. 2015	1240K.capture
I1544	CentralEurope_LNBA	51.42	11.68	4,225	Mathieson et al. 2015	1240K.capture

I1546	CentralEurope_LNBA	51.82	10.91	4,225	Mathieson et al. 2015	1240K.capture
I1549	CentralEurope_LNBA	51.82	10.91	4,225	Mathieson et al. 2015	1240K.capture
I1979	CentralEurope_LNBA	44.80	10.33	4,015	Ojalde et al. 2018	1240K.capture
I2364	CentralEurope_LNBA	47.60	19.05	4,215	Ojalde et al. 2018	1240K.capture
I2365	CentralEurope_LNBA	47.60	19.05	4,285	Ojalde et al. 2018	1240K.capture
I2407	CentralEurope_LNBA	52.85	17.88	4,955	Mathieson et al. 2018	1240K.capture
I2477	CentralEurope_LNBA	44.80	10.33	4,015	Ojalde et al. 2018	1240K.capture
I2478	CentralEurope_LNBA	44.80	10.33	4,016	Ojalde et al. 2018	1240K.capture
I2575	CentralEurope_LNBA	43.97	5.81	4,292	Ojalde et al. 2018	1240K.capture
I2741	CentralEurope_LNBA	47.38	19.02	4,255	Ojalde et al. 2018	1240K.capture
I2786	CentralEurope_LNBA	47.38	19.02	4,281	Ojalde et al. 2018	1240K.capture
I2787	CentralEurope_LNBA	47.38	19.02	4,279	Ojalde et al. 2018	1240K.capture
I3528	CentralEurope_LNBA	47.62	19.04	4,380	Ojalde et al. 2018	1240K.capture
I3529	CentralEurope_LNBA	47.62	19.04	4,300	Ojalde et al. 2018	1240K.capture
I3587	CentralEurope_LNBA	48.88	12.53	4,175	Ojalde et al. 2018	1240K.capture
I3588	CentralEurope_LNBA	48.88	12.53	4,175	Ojalde et al. 2018	1240K.capture
I3589	CentralEurope_LNBA	48.88	12.53	4,175	Ojalde et al. 2018	1240K.capture
I3590	CentralEurope_LNBA	48.88	12.53	4,187	Ojalde et al. 2018	1240K.capture
I3592	CentralEurope_LNBA	48.88	12.53	4,280	Ojalde et al. 2018	1240K.capture
I3593	CentralEurope_LNBA	48.88	12.53	4,221	Ojalde et al. 2018	1240K.capture
I3594	CentralEurope_LNBA	48.88	12.53	4,175	Ojalde et al. 2018	1240K.capture
I3596	CentralEurope_LNBA	48.88	12.53	4,175	Ojalde et al. 2018	1240K.capture
I3597	CentralEurope_LNBA	48.88	12.53	4,175	Ojalde et al. 2018	1240K.capture
I3599	CentralEurope_LNBA	48.88	12.53	4,175	Ojalde et al. 2018	1240K.capture
I3600	CentralEurope_LNBA	48.88	12.53	4,175	Ojalde et al. 2018	1240K.capture
I3601	CentralEurope_LNBA	48.88	12.53	4,175	Ojalde et al. 2018	1240K.capture
I3602	CentralEurope_LNBA	48.88	12.53	4,175	Ojalde et al. 2018	1240K.capture
I3604	CentralEurope_LNBA	48.66	13.07	4,250	Ojalde et al. 2018	1240K.capture
I3607	CentralEurope_LNBA	48.66	13.07	4,250	Ojalde et al. 2018	1240K.capture
I3874	CentralEurope_LNBA	44.48	6.37	4,067	Ojalde et al. 2018	1240K.capture
I4067	CentralEurope_LNBA	52.73	5.10	3,768	Ojalde et al. 2018	1240K.capture
I4068	CentralEurope_LNBA	52.73	5.10	3,991	Ojalde et al. 2018	1240K.capture
I4069	CentralEurope_LNBA	52.73	5.10	3,987	Ojalde et al. 2018	1240K.capture
I4070	CentralEurope_LNBA	52.73	5.10	3,718	Ojalde et al. 2018	1240K.capture
I4071	CentralEurope_LNBA	52.73	5.10	3,723	Ojalde et al. 2018	1240K.capture
I4073	CentralEurope_LNBA	52.73	5.10	4,000	Ojalde et al. 2018	1240K.capture
I4074	CentralEurope_LNBA	52.73	5.10	4,046	Ojalde et al. 2018	1240K.capture
I4075	CentralEurope_LNBA	52.73	5.10	3,977	Ojalde et al. 2018	1240K.capture
I4076	CentralEurope_LNBA	52.73	5.10	3,766	Ojalde et al. 2018	1240K.capture
I4132	CentralEurope_LNBA	48.33	10.90	4,200	Ojalde et al. 2018	1240K.capture
I4178	CentralEurope_LNBA	47.38	19.02	4,300	Ojalde et al. 2018	1240K.capture
I4248	CentralEurope_LNBA	48.84	12.75	4,200	Ojalde et al. 2018	1240K.capture
I4249	CentralEurope_LNBA	48.84	12.75	4,200	Ojalde et al. 2018	1240K.capture
I4250	CentralEurope_LNBA	48.84	12.75	4,241	Ojalde et al. 2018	1240K.capture
I4251	CentralEurope_LNBA	50.65	21.66	4,240	Ojalde et al. 2018	1240K.capture
I4252	CentralEurope_LNBA	50.65	21.66	4,161	Ojalde et al. 2018	1240K.capture
I4253	CentralEurope_LNBA	50.65	21.66	4,281	Ojalde et al. 2018	1240K.capture
I4629	CentralEurope_LNBA	56.28	25.13	4,833	Mathieson et al. 2018	1240K.capture
I4884	CentralEurope_LNBA	50.12	14.46	3,763	Ojalde et al. 2018	1240K.capture
I4885	CentralEurope_LNBA	50.12	14.46	4,166	Ojalde et al. 2018	1240K.capture
I4886	CentralEurope_LNBA	50.12	14.46	4,073	Ojalde et al. 2018	1240K.capture
I4887	CentralEurope_LNBA	50.12	14.46	4,070	Ojalde et al. 2018	1240K.capture
I4888	CentralEurope_LNBA	50.12	14.46	4,059	Ojalde et al. 2018	1240K.capture
I4889	CentralEurope_LNBA	50.12	14.46	4,121	Ojalde et al. 2018	1240K.capture
I4890	CentralEurope_LNBA	50.12	14.46	4,200	Ojalde et al. 2018	1240K.capture
I4891	CentralEurope_LNBA	50.12	14.46	4,121	Ojalde et al. 2018	1240K.capture
I4892	CentralEurope_LNBA	50.12	14.46	3,741	Ojalde et al. 2018	1240K.capture
I4895	CentralEurope_LNBA	50.05	14.37	4,110	Ojalde et al. 2018	1240K.capture
I4896	CentralEurope_LNBA	50.05	14.37	4,165	Ojalde et al. 2018	1240K.capture
I4930	CentralEurope_LNBA	37.73	12.96	4,150	Ojalde et al. 2018	1240K.capture
I4933	CentralEurope_LNBA	37.73	12.96	4,150	Ojalde et al. 2018	1240K.capture

I4936	CentralEurope_LNBA	37.73	12.96	4,150	Ojalde et al. 2018	1240K.capture
I4945	CentralEurope_LNBA	50.12	14.46	4,167	Ojalde et al. 2018	1240K.capture
I4946	CentralEurope_LNBA	50.05	14.37	4,171	Ojalde et al. 2018	1240K.capture
I4947	CentralEurope_LNBA	50.05	14.37	4,200	Ojalde et al. 2018	1240K.capture
I5014	CentralEurope_LNBA	48.71	11.45	4,200	Ojalde et al. 2018	1240K.capture
I5015	CentralEurope_LNBA	47.60	19.05	4,288	Ojalde et al. 2018	1240K.capture
I5017	CentralEurope_LNBA	48.33	10.90	4,283	Ojalde et al. 2018	1240K.capture
I5019	CentralEurope_LNBA	48.66	13.07	4,200	Ojalde et al. 2018	1240K.capture
I5020	CentralEurope_LNBA	48.66	12.71	4,281	Ojalde et al. 2018	1240K.capture
I5021	CentralEurope_LNBA	48.69	13.02	4,406	Ojalde et al. 2018	1240K.capture
I5022	CentralEurope_LNBA	48.69	13.02	4,200	Ojalde et al. 2018	1240K.capture
I5023	CentralEurope_LNBA	48.69	13.02	4,200	Ojalde et al. 2018	1240K.capture
I5024	CentralEurope_LNBA	50.12	14.26	4,105	Ojalde et al. 2018	1240K.capture
I5025	CentralEurope_LNBA	50.12	14.26	4,150	Ojalde et al. 2018	1240K.capture
I5035	CentralEurope_LNBA	50.17	14.32	4,050	Ojalde et al. 2018	1240K.capture
I5037	CentralEurope_LNBA	48.80	17.02	4,050	Ojalde et al. 2018	1240K.capture
I5042	CentralEurope_LNBA	48.80	17.02	4,050	Ojalde et al. 2018	1240K.capture
I5043	CentralEurope_LNBA	48.80	17.02	4,050	Ojalde et al. 2018	1240K.capture
I5044	CentralEurope_LNBA	48.80	17.02	4,050	Ojalde et al. 2018	1240K.capture
I5514	CentralEurope_LNBA	50.05	14.37	4,200	Ojalde et al. 2018	1240K.capture
I5519	CentralEurope_LNBA	48.33	10.90	4,200	Ojalde et al. 2018	1240K.capture
I5520	CentralEurope_LNBA	48.33	10.90	4,200	Ojalde et al. 2018	1240K.capture
I5521	CentralEurope_LNBA	48.33	10.90	4,200	Ojalde et al. 2018	1240K.capture
I5522	CentralEurope_LNBA	48.33	10.90	4,200	Ojalde et al. 2018	1240K.capture
I5523	CentralEurope_LNBA	48.66	12.71	4,200	Ojalde et al. 2018	1240K.capture
I5524	CentralEurope_LNBA	48.66	12.71	4,200	Ojalde et al. 2018	1240K.capture
I5525	CentralEurope_LNBA	48.66	12.71	4,200	Ojalde et al. 2018	1240K.capture
I5526	CentralEurope_LNBA	48.66	12.71	4,200	Ojalde et al. 2018	1240K.capture
I5527	CentralEurope_LNBA	48.71	11.45	4,200	Ojalde et al. 2018	1240K.capture
I5529	CentralEurope_LNBA	48.69	13.02	4,200	Ojalde et al. 2018	1240K.capture
I5530	CentralEurope_LNBA	48.71	11.33	4,200	Ojalde et al. 2018	1240K.capture
I5531	CentralEurope_LNBA	48.71	11.33	4,200	Ojalde et al. 2018	1240K.capture
I5655	CentralEurope_LNBA	48.84	12.75	4,200	Ojalde et al. 2018	1240K.capture
I5656	CentralEurope_LNBA	48.84	12.75	4,200	Ojalde et al. 2018	1240K.capture
I5657	CentralEurope_LNBA	48.84	12.75	4,200	Ojalde et al. 2018	1240K.capture
I5658	CentralEurope_LNBA	48.84	12.75	4,200	Ojalde et al. 2018	1240K.capture
I5659	CentralEurope_LNBA	48.84	12.75	4,200	Ojalde et al. 2018	1240K.capture
I5660	CentralEurope_LNBA	48.84	12.75	4,200	Ojalde et al. 2018	1240K.capture
I5661	CentralEurope_LNBA	48.84	12.75	4,200	Ojalde et al. 2018	1240K.capture
I5663	CentralEurope_LNBA	48.84	12.75	4,200	Ojalde et al. 2018	1240K.capture
I5666	CentralEurope_LNBA	50.27	15.81	4,150	Ojalde et al. 2018	1240K.capture
I5748	CentralEurope_LNBA	52.73	5.10	4,356	Ojalde et al. 2018	1240K.capture
I5750	CentralEurope_LNBA	52.73	5.10	4,050	Ojalde et al. 2018	1240K.capture
I5755	CentralEurope_LNBA	46.23	7.35	4,176	Ojalde et al. 2018	1240K.capture
I5757	CentralEurope_LNBA	46.23	7.35	4,176	Ojalde et al. 2018	1240K.capture
I5759	CentralEurope_LNBA	46.23	7.35	4,176	Ojalde et al. 2018	1240K.capture
I5833	CentralEurope_LNBA	48.84	12.75	4,200	Ojalde et al. 2018	1240K.capture
I5834	CentralEurope_LNBA	48.84	12.75	4,200	Ojalde et al. 2018	1240K.capture
I5835	CentralEurope_LNBA	48.84	12.75	4,200	Ojalde et al. 2018	1240K.capture
I5836	CentralEurope_LNBA	49.65	8.33	4,200	Ojalde et al. 2018	1240K.capture
I6468	CentralEurope_LNBA	50.17	14.32	4,150	Ojalde et al. 2018	1240K.capture
I6476	CentralEurope_LNBA	50.51	14.04	4,150	Ojalde et al. 2018	1240K.capture
I6480	CentralEurope_LNBA	50.17	14.32	4,150	Ojalde et al. 2018	1240K.capture
I6481	CentralEurope_LNBA	48.71	11.33	4,200	Ojalde et al. 2018	1240K.capture
I6482	CentralEurope_LNBA	48.71	11.33	4,200	Ojalde et al. 2018	1240K.capture
I6531	CentralEurope_LNBA	50.23	18.22	4,112	Ojalde et al. 2018	1240K.capture
I6534	CentralEurope_LNBA	50.09	18.10	4,252	Ojalde et al. 2018	1240K.capture
I6535	CentralEurope_LNBA	50.09	18.10	4,284	Ojalde et al. 2018	1240K.capture
I6537	CentralEurope_LNBA	50.11	18.21	4,115	Ojalde et al. 2018	1240K.capture
I6538	CentralEurope_LNBA	50.91	16.79	3,836	Ojalde et al. 2018	1240K.capture
I6579	CentralEurope_LNBA	51.04	17.07	4,140	Ojalde et al. 2018	1240K.capture

I6580	CentralEurope_LNBA	50.87	16.86	4,175	Ojalde et al. 2018	1240K.capture
I6581	CentralEurope_LNBA	50.09	18.10	4,250	Ojalde et al. 2018	1240K.capture
I6582	CentralEurope_LNBA	50.09	18.10	4,150	Ojalde et al. 2018	1240K.capture
I6583	CentralEurope_LNBA	50.96	17.02	4,119	Ojalde et al. 2018	1240K.capture
I6590	CentralEurope_LNBA	48.84	12.75	4,200	Ojalde et al. 2018	1240K.capture
I6591	CentralEurope_LNBA	48.84	12.75	4,200	Ojalde et al. 2018	1240K.capture
I6624	CentralEurope_LNBA	48.84	12.75	4,200	Ojalde et al. 2018	1240K.capture
I7040	CentralEurope_LNBA	47.43	19.05	4,300	Ojalde et al. 2018	1240K.capture
I7041	CentralEurope_LNBA	47.43	19.05	4,300	Ojalde et al. 2018	1240K.capture
I7042	CentralEurope_LNBA	47.43	19.05	4,300	Ojalde et al. 2018	1240K.capture
I7043	CentralEurope_LNBA	47.43	19.05	4,300	Ojalde et al. 2018	1240K.capture
I7044	CentralEurope_LNBA	47.43	19.05	4,300	Ojalde et al. 2018	1240K.capture
I7045	CentralEurope_LNBA	47.43	19.05	4,300	Ojalde et al. 2018	1240K.capture
I7195	CentralEurope_LNBA	50.05	14.37	3,900	Ojalde et al. 2018	1240K.capture
I7196	CentralEurope_LNBA	50.05	14.37	3,900	Ojalde et al. 2018	1240K.capture
I7197	CentralEurope_LNBA	50.05	14.37	3,900	Ojalde et al. 2018	1240K.capture
I7198	CentralEurope_LNBA	50.05	14.37	3,900	Ojalde et al. 2018	1240K.capture
I7199	CentralEurope_LNBA	50.05	14.37	3,900	Ojalde et al. 2018	1240K.capture
I7200	CentralEurope_LNBA	50.05	14.37	3,900	Ojalde et al. 2018	1240K.capture
I7201	CentralEurope_LNBA	50.05	14.37	3,900	Ojalde et al. 2018	1240K.capture
I7202	CentralEurope_LNBA	50.05	14.37	3,900	Ojalde et al. 2018	1240K.capture
I7203	CentralEurope_LNBA	50.05	14.37	3,900	Ojalde et al. 2018	1240K.capture
I7205	CentralEurope_LNBA	50.41	14.07	4,300	Ojalde et al. 2018	1240K.capture
I7210	CentralEurope_LNBA	50.41	14.07	4,300	Ojalde et al. 2018	1240K.capture
I7211	CentralEurope_LNBA	50.41	14.07	4,300	Ojalde et al. 2018	1240K.capture
I7212	CentralEurope_LNBA	50.41	14.07	4,300	Ojalde et al. 2018	1240K.capture
I7213	CentralEurope_LNBA	50.41	14.07	4,300	Ojalde et al. 2018	1240K.capture
I7214	CentralEurope_LNBA	50.41	14.07	4,300	Ojalde et al. 2018	1240K.capture
I7249	CentralEurope_LNBA	50.19	14.16	4,300	Ojalde et al. 2018	1240K.capture
I7250	CentralEurope_LNBA	50.19	14.16	4,300	Ojalde et al. 2018	1240K.capture
I7251	CentralEurope_LNBA	50.19	14.16	4,300	Ojalde et al. 2018	1240K.capture
I7269	CentralEurope_LNBA	50.19	14.16	4,300	Ojalde et al. 2018	1240K.capture
I7270	CentralEurope_LNBA	50.19	14.16	4,300	Ojalde et al. 2018	1240K.capture
I7271	CentralEurope_LNBA	50.19	14.16	4,300	Ojalde et al. 2018	1240K.capture
I7272	CentralEurope_LNBA	50.19	14.16	4,500	Ojalde et al. 2018	1240K.capture
I7275	CentralEurope_LNBA	50.19	14.16	4,300	Ojalde et al. 2018	1240K.capture
I7276	CentralEurope_LNBA	50.19	14.16	4,300	Ojalde et al. 2018	1240K.capture
I7278	CentralEurope_LNBA	50.19	14.16	4,300	Ojalde et al. 2018	1240K.capture
I7279	CentralEurope_LNBA	50.19	14.16	4,500	Ojalde et al. 2018	1240K.capture
I7280	CentralEurope_LNBA	50.19	14.16	4,500	Ojalde et al. 2018	1240K.capture
I7281	CentralEurope_LNBA	50.04	14.34	4,300	Ojalde et al. 2018	1240K.capture
I7282	CentralEurope_LNBA	50.41	14.07	4,300	Ojalde et al. 2018	1240K.capture
I7283	CentralEurope_LNBA	50.41	14.07	4,300	Ojalde et al. 2018	1240K.capture
I7286	CentralEurope_LNBA	50.41	14.07	4,300	Ojalde et al. 2018	1240K.capture
I7287	CentralEurope_LNBA	50.41	14.07	4,300	Ojalde et al. 2018	1240K.capture
I7288	CentralEurope_LNBA	50.41	14.07	4,300	Ojalde et al. 2018	1240K.capture
I7289	CentralEurope_LNBA	50.41	14.07	4,300	Ojalde et al. 2018	1240K.capture
I7290	CentralEurope_LNBA	50.41	14.07	4,300	Ojalde et al. 2018	1240K.capture
RISE1	CentralEurope_LNBA	52.29	17.04	4,671	Allentoft et al. 2015	390k.capture
RISE109	CentralEurope_LNBA	50.98	17.07	3,813	Allentoft et al. 2015	3.7M.capture
RISE139	CentralEurope_LNBA	50.80	17.09	3,979	Allentoft et al. 2015	1240K.capture
RISE145	CentralEurope_LNBA	50.91	17.18	4,023	Allentoft et al. 2015	Shotgun-HS2500
RISE150	CentralEurope_LNBA	50.92	16.96	3,739	Allentoft et al. 2015	3.7M.capture
RISE154	CentralEurope_LNBA	50.95	16.94	3,795	Allentoft et al. 2015	1240K.capture
RISE247	CentralEurope_LNBA	47.33	18.96	3,629	Allentoft et al. 2015	Shotgun-HS2500
RISE254	CentralEurope_LNBA	47.33	18.96	3,969	Allentoft et al. 2015	Shotgun-HS2500
RISE349	CentralEurope_LNBA	46.36	20.99	3,859	Allentoft et al. 2015	Shotgun-HS2500
RISE371	CentralEurope_LNBA	46.22	20.20	3,989	Allentoft et al. 2015	Shotgun-HS2500
RISE373	CentralEurope_LNBA	46.22	20.20	3,741	Allentoft et al. 2015	Shotgun-HS2500
RISE374	CentralEurope_LNBA	46.22	20.20	3,693	Allentoft et al. 2015	Shotgun-HS2500
RISE431	CentralEurope_LNBA	52.14	16.54	4,117	Allentoft et al. 2015	Shotgun-HS2500

RISE434	CentralEurope_LNBA	48.93	12.26	4,705	Allentoft et al. 2015	Shotgun-HS2500
RISE435	CentralEurope_LNBA	48.93	12.26	4,631	Allentoft et al. 2015	Shotgun-HS2500
RISE436	CentralEurope_LNBA	48.93	12.26	4,674	Allentoft et al. 2015	Shotgun-HS2500
RISE446	CentralEurope_LNBA	50.01	10.18	4,597	Allentoft et al. 2015	Shotgun-HS2500
RISE471	CentralEurope_LNBA	48.17	10.81	3,555	Allentoft et al. 2015	Shotgun-HS2500
RISE479	CentralEurope_LNBA	47.34	18.90	3,700	Allentoft et al. 2015	Shotgun-HS2500
RISE480	CentralEurope_LNBA	47.34	18.90	3,550	Allentoft et al. 2015	Shotgun-HS2500
RISE483	CentralEurope_LNBA	47.34	18.90	3,700	Allentoft et al. 2015	Shotgun-HS2500
RISE484	CentralEurope_LNBA	47.34	18.90	3,700	Allentoft et al. 2015	Shotgun-HS2500
RISE486	CentralEurope_LNBA	45.26	10.38	3,904	Allentoft et al. 2015	Shotgun-HS2500
RISE559	CentralEurope_LNBA	48.33	10.90	4,284	Allentoft et al. 2015	Shotgun-HS2500
RISE560	CentralEurope_LNBA	48.33	10.90	4,200	Allentoft et al. 2015	Shotgun-HS2500
RISE562	CentralEurope_LNBA	48.66	12.71	4,282	Allentoft et al. 2015	Shotgun-HS2500
RISE563	CentralEurope_LNBA	48.69	13.02	4,492	Allentoft et al. 2015	Shotgun-HS2500
RISE564	CentralEurope_LNBA	48.69	13.02	4,200	Allentoft et al. 2015	Shotgun-HS2500
RISE566	CentralEurope_LNBA	50.12	14.26	4,106	Allentoft et al. 2015	Shotgun-HS2500
RISE567	CentralEurope_LNBA	50.12	14.26	4,250	Allentoft et al. 2015	Shotgun-HS2500
RISE568	CentralEurope_LNBA	50.19	14.16	1,200	Allentoft et al. 2015	Shotgun-HS2500
RISE569	CentralEurope_LNBA	50.19	14.16	1,235	Allentoft et al. 2015	Shotgun-HS2500
RISE577	CentralEurope_LNBA	50.16	14.31	4,000	Allentoft et al. 2015	Shotgun-HS2500
RISE586	CentralEurope_LNBA	48.80	17.02	4,000	Allentoft et al. 2015	Shotgun-HS2500
AH1	CHG_Iran	34.06	46.65	8,832	Broushaki et al. 2016	Shotgun-HS2500
AH2	CHG_Iran	34.06	46.65	8,833	Broushaki et al. 2016	Shotgun-HS2500
AH4	CHG_Iran	34.06	46.65	8,832	Broushaki et al. 2016	Shotgun-HS2500
I1290	CHG_Iran	34.45	48.12	9,846	Lazaridis et al. 2016	1240K.capture
I1293	CHG_Iran	35.59	53.50	8,076	Lazaridis et al. 2016	1240K.capture
I1671	CHG_Iran	34.50	47.96	7,698	Lazaridis et al. 2016	1240K.capture
I1944	CHG_Iran	34.45	48.12	9,800	Lazaridis et al. 2016	1240K.capture
I1945	CHG_Iran	34.45	48.12	9,800	Lazaridis et al. 2016	1240K.capture
I1949	CHG_Iran	34.45	48.12	10,052	Lazaridis et al. 2016	1240K.capture
I1951	CHG_Iran	34.45	48.12	9,891	Lazaridis et al. 2016	1240K.capture
Kotias	CHG_Iran	42.22	43.30	9,720	Jones et al. 2015	1240K.capture
Satsurblia	CHG_Iran	42.38	42.60	13,255	Jones et al. 2015	Shotgun-HS2500
WC1	CHG_Iran	34.06	46.65	8,240	Broushaki et al. 2016	Shotgun-HS2000
I1926	EasternEurope_LF	48.47	25.53	5,736	Mathieson et al. 2018	1240K.capture
I2110	EasternEurope_LF	48.47	25.53	5,735	Mathieson et al. 2018	1240K.capture
I2111	EasternEurope_LF	48.47	25.53	5,647	Mathieson et al. 2018	1240K.capture
I2403	EasternEurope_LF	52.85	17.88	4,673	Mathieson et al. 2018	1240K.capture
I2405	EasternEurope_LF	52.85	17.88	5,128	Mathieson et al. 2018	1240K.capture
I2433	EasternEurope_LF	52.85	17.88	4,950	Mathieson et al. 2018	1240K.capture
I2434	EasternEurope_LF	52.85	17.88	5,050	Mathieson et al. 2018	1240K.capture
I2440	EasternEurope_LF	52.85	17.88	4,950	Mathieson et al. 2018	1240K.capture
I2441	EasternEurope_LF	52.85	17.88	5,050	Mathieson et al. 2018	1240K.capture
I3151	EasternEurope_LF	48.47	25.53	5,750	Mathieson et al. 2018	1240K.capture
I5869	EasternEurope_LF	47.95	35.39	7,200	Mathieson et al. 2018	1240K.capture
I5878	EasternEurope_LF	48.91	33.76	5,966	Mathieson et al. 2018	1240K.capture
I5879	EasternEurope_LF	48.91	33.76	7,100	Mathieson et al. 2018	1240K.capture
I5888	EasternEurope_LF	48.91	33.76	7,100	Mathieson et al. 2018	1240K.capture
ILK001	EasternEurope_LF	49.56	27.69	4,753	Mathieson et al. 2018	1240K.capture
ILK002	EasternEurope_LF	49.56	27.69	4,752	Mathieson et al. 2018	1240K.capture
ILK003	EasternEurope_LF	49.56	27.69	4,752	Mathieson et al. 2018	1240K.capture
I0061	EHG	61.65	35.65	8,280	Mathieson et al. 2015	840k+390k.capture
I0124	EHG	53.40	50.40	7,549	Mathieson et al. 2015	840k+390k.capture
I0211	EHG	61.65	35.65	8,280	Mathieson et al. 2015	1240K.capture
I4432	EHG	56.28	25.13	7,948	Mathieson et al. 2018	1240K.capture
I4434	EHG	56.28	25.13	7,446	Mathieson et al. 2018	1240K.capture
I4435	EHG	56.28	25.13	6,003	Mathieson et al. 2018	1240K.capture
I4436	EHG	56.28	25.13	6,105	Mathieson et al. 2018	1240K.capture
I4437	EHG	56.28	25.13	6,148	Mathieson et al. 2018	1240K.capture
I4438	EHG	56.28	25.13	7,291	Mathieson et al. 2018	1240K.capture
I4439	EHG	56.28	25.13	7,648	Mathieson et al. 2018	1240K.capture

I4440	EHG	56.28	25.13	7,080	Mathieson et al. 2018	1240K.capture
I4441	EHG	56.28	25.13	6,725	Mathieson et al. 2018	1240K.capture
I4550	EHG	56.28	25.13	8,489	Mathieson et al. 2018	1240K.capture
I4551	EHG	56.28	25.13	7,671	Mathieson et al. 2018	1240K.capture
I4552	EHG	56.28	25.13	7,377	Mathieson et al. 2018	1240K.capture
I4553	EHG	56.28	25.13	7,379	Mathieson et al. 2018	1240K.capture
I4554	EHG	56.28	25.13	5,949	Mathieson et al. 2018	1240K.capture
I4595	EHG	56.28	25.13	7,637	Mathieson et al. 2018	1240K.capture
I4596	EHG	56.28	25.13	7,976	Mathieson et al. 2018	1240K.capture
I4626	EHG	56.28	25.13	7,689	Mathieson et al. 2018	1240K.capture
I4627	EHG	56.28	25.13	6,064	Mathieson et al. 2018	1240K.capture
I4628	EHG	56.28	25.13	7,027	Mathieson et al. 2018	1240K.capture
I4630	EHG	56.28	25.13	9,222	Mathieson et al. 2018	1240K.capture
I4632	EHG	56.28	25.13	8,308	Mathieson et al. 2018	1240K.capture
ElMiron	ElMiron	43.26	-3.45	18,720	Fu et al. 2016	3.7M.capture
12880A	exclude	52.08	0.18	2,017	Schieffels et al. 2016	Shotgun
12881A	exclude	52.08	0.18	1,232	Schieffels et al. 2016	Shotgun
12883A	exclude	52.08	0.18	1,246	Schieffels et al. 2016	Shotgun
12884A	exclude	52.08	0.18	2,017	Schieffels et al. 2016	Shotgun
12885A	exclude	52.08	0.18	1,164	Schieffels et al. 2016	Shotgun
AfontovaGora3	exclude	56.05	92.87	17,930	Fu et al. 2016	3.7M.capture
Ajvide52	exclude	57.47	18.49	4,750	Skoglund et al. 2014	Shotgun-HS2000
Ajvide53	exclude	57.47	18.49	4,750	Skoglund et al. 2014	Shotgun-HS2000
Ajvide59	exclude	57.47	18.49	4,750	Skoglund et al. 2014	Shotgun-HS2000
Ajvide70	exclude	57.47	18.49	4,750	Skoglund et al. 2014	Shotgun-HS2000
ANI152	exclude	43.21	27.86	6,495	Mathieson et al. 2018	1240K.capture
ANI159-ANI181	exclude	43.21	27.86	6,571	Mathieson et al. 2018	1240K.capture
ANI163	exclude	43.21	27.86	6,577	Mathieson et al. 2018	1240K.capture
AY2001	exclude	45.69	43.26	5,272	Wang et al. 2019	1240K.capture
AY2003	exclude	45.69	43.26	5,456	Wang et al. 2019	1240K.capture
BerryAuBac	exclude	49.24	3.54	7,245	Fu et al. 2016	1240K.capture
Bichon	exclude	47.15	6.85	13,665	Jones et al. 2015	Shotgun
Bockstein	exclude	48.33	10.09	8,265	Fu et al. 2016	390k.capture
Bul4	exclude	42.43	25.90	4,906	Mathieson et al. 2018	1240K.capture
Burkhardtshohle	exclude	48.32	9.35	14,615	Fu et al. 2016	1240K.capture
CB13	exclude	41.37	1.89	7,348	Olalde et al. 2015	Shotgun-HS2000
Chaudardes1	exclude	49.24	3.46	8,205	Fu et al. 2016	1240K.capture
Falkenstein	exclude	48.06	9.04	9,200	Fu et al. 2016	390k.capture
Gokhem2	exclude	58.18	13.59	4,850	Skoglund et al. 2014	Shotgun-HS2000
Gokhem4	exclude	58.18	13.59	4,850	Skoglund et al. 2014	Shotgun-HS2000
Gokhem5	exclude	58.18	13.59	5,035	Skoglund et al. 2014	Shotgun-HS2000
Gokhem7	exclude	58.18	13.59	4,850	Skoglund et al. 2014	Shotgun-HS2000
GoyetQ-2	exclude	50.26	4.28	15,005	Fu et al. 2016	1240K.capture
GoyetQ53-1	exclude	50.26	4.28	27,975	Fu et al. 2016	1240K.capture
HohleFels49	exclude	48.22	9.45	15,130	Fu et al. 2016	390k.capture
HohleFels79	exclude	48.22	9.45	14,670	Fu et al. 2016	390k.capture
I0011	exclude	58.54	15.05	7,569	Mathieson et al. 2015	840k+390k.capture
I0012	exclude	58.54	15.05	7,595	Mathieson et al. 2015	840k+390k.capture
I0013	exclude	58.54	15.05	7,751	Mathieson et al. 2015	840k+390k.capture
I0014	exclude	58.54	15.05	7,703	Mathieson et al. 2015	840k+390k.capture
I0015	exclude	58.54	15.05	7,747	Mathieson et al. 2015	840k+390k.capture
I0017	exclude	58.54	15.05	7,626	Mathieson et al. 2015	840k+390k.capture
I0360	exclude	53.03	50.39	3,475	Mathieson et al. 2015	1240K.capture
I0374	exclude	49.97	44.67	4,450	Mathieson et al. 2015	1240K.capture
I0409	exclude	42.50	0.50	7,215	Mathieson et al. 2015	840k+390k.capture
I0410	exclude	42.50	0.50	7,130	Mathieson et al. 2015	840k+390k.capture
I0412	exclude	42.50	0.50	7,144	Mathieson et al. 2015	840k+390k.capture
I0413	exclude	42.50	0.50	7,139	Mathieson et al. 2015	840k+390k.capture
I0585	exclude	42.91	-5.38	7,815	Mathieson et al. 2015	1240K.capture
I1378	exclude	48.30	35.14	6,381	Mathieson et al. 2018	1240K.capture
I1497	exclude	47.17	19.83	4,804	Olalde et al. 2018	1240K.capture

I1563	exclude	51.36	7.55	5,360	Lipson et al. 2017	1240K.capture
I1565	exclude	51.36	7.55	5,735	Lipson et al. 2017	1240K.capture
I1593	exclude	51.36	7.55	5,601	Lipson et al. 2017	1240K.capture
I1594	exclude	51.36	7.55	5,130	Lipson et al. 2017	1240K.capture
I1705	exclude	31.99	35.98	4,032	Lazaridis et al. 2016	1240K.capture
I1706	exclude	31.99	35.98	4,345	Lazaridis et al. 2016	1240K.capture
I1730	exclude	31.99	35.98	4,344	Lazaridis et al. 2016	1240K.capture
I1732	exclude	48.30	35.14	7,239	Mathieson et al. 2018	1240K.capture
I1733	exclude	48.30	35.14	10,200	Mathieson et al. 2018	1240K.capture
I1734	exclude	48.30	35.14	9,202	Mathieson et al. 2018	1240K.capture
I1736	exclude	48.30	35.14	8,109	Mathieson et al. 2018	1240K.capture
I1737	exclude	48.30	35.14	10,371	Mathieson et al. 2018	1240K.capture
I1738	exclude	48.30	35.14	7,350	Mathieson et al. 2018	1240K.capture
I1763	exclude	48.30	35.14	10,074	Mathieson et al. 2018	1240K.capture
I1767	exclude	54.52	-1.31	4,035	Olalde et al. 2018	1240K.capture
I1775	exclude	53.33	-3.84	3,597	Olalde et al. 2018	1240K.capture
I1819	exclude	48.30	35.14	10,643	Mathieson et al. 2018	1240K.capture
I1917	exclude	48.99	33.95	4,955	Mathieson et al. 2018	1240K.capture
I1972	exclude	42.63	-3.12	6,709	Lipson et al. 2017	1240K.capture
I2199	exclude	42.63	-3.12	7,073	Lipson et al. 2017	1240K.capture
I2435	exclude	52.85	17.88	4,950	Mathieson et al. 2018	1240K.capture
I3712	exclude	47.95	35.39	7,392	Mathieson et al. 2018	1240K.capture
I3713	exclude	47.95	35.39	7,001	Mathieson et al. 2018	1240K.capture
I3714	exclude	47.95	35.39	7,100	Mathieson et al. 2018	1240K.capture
I3715	exclude	47.95	35.39	7,529	Mathieson et al. 2018	1240K.capture
I3716	exclude	47.95	35.39	7,349	Mathieson et al. 2018	1240K.capture
I3717	exclude	48.91	33.76	7,289	Mathieson et al. 2018	1240K.capture
I3718	exclude	48.91	33.76	7,230	Mathieson et al. 2018	1240K.capture
I3719	exclude	48.91	33.76	6,824	Mathieson et al. 2018	1240K.capture
I3875	exclude	44.48	6.37	3,991	Olalde et al. 2018	1240K.capture
I4110	exclude	48.91	33.76	5,456	Mathieson et al. 2018	1240K.capture
I4111	exclude	48.91	33.76	6,585	Mathieson et al. 2018	1240K.capture
I4112	exclude	48.91	33.76	7,100	Mathieson et al. 2018	1240K.capture
I4114	exclude	48.91	33.76	7,351	Mathieson et al. 2018	1240K.capture
I4882	exclude	44.53	22.05	8,000	Mathieson et al. 2018	1240K.capture
I5232	exclude	44.6	22.01	7,901	Mathieson et al. 2018	1240K.capture
I5241	exclude	44.6	22.01	11,196	Mathieson et al. 2018	1240K.capture
I5868	exclude	47.95	35.39	7,341	Mathieson et al. 2018	1240K.capture
I5870	exclude	47.95	35.39	7,360	Mathieson et al. 2018	1240K.capture
I5872	exclude	47.95	35.39	7,382	Mathieson et al. 2018	1240K.capture
I5873	exclude	47.95	35.39	7,346	Mathieson et al. 2018	1240K.capture
I5875	exclude	48.91	33.76	7,126	Mathieson et al. 2018	1240K.capture
I5876	exclude	48.91	33.76	8,822	Mathieson et al. 2018	1240K.capture
I5881	exclude	48.91	33.76	7,089	Mathieson et al. 2018	1240K.capture
I5882	exclude	48.91	33.76	5,047	Mathieson et al. 2018	1240K.capture
I5883	exclude	48.91	33.76	7,056	Mathieson et al. 2018	1240K.capture
I5884	exclude	48.91	33.76	4,743	Mathieson et al. 2018	1240K.capture
I5885	exclude	48.91	33.76	8,110	Mathieson et al. 2018	1240K.capture
I5886	exclude	48.91	33.76	7,217	Mathieson et al. 2018	1240K.capture
I5889	exclude	48.91	33.76	6,998	Mathieson et al. 2018	1240K.capture
I5890	exclude	48.91	33.76	7,124	Mathieson et al. 2018	1240K.capture
I5891	exclude	48.91	33.76	7,338	Mathieson et al. 2018	1240K.capture
I5892	exclude	48.91	33.76	7,092	Mathieson et al. 2018	1240K.capture
I5893	exclude	48.91	33.76	7,250	Mathieson et al. 2018	1240K.capture
I5957	exclude	47.95	35.39	7,200	Mathieson et al. 2018	1240K.capture
I6133	exclude	47.95	35.39	7,200	Mathieson et al. 2018	1240K.capture
I6561	exclude	49.71	37.58	5,960	Mathieson et al. 2018	1240K.capture
Iboussieres25-1	exclude	44.29	4.46	11,725	Mathieson et al. 2018	1240K.capture
Iboussieres31-2	exclude	44.29	4.46	11,725	Mathieson et al. 2018	1240K.capture
Iboussieres39	exclude	44.29	4.46	11,725	Fu et al. 2016	1240K.capture
IV3002	exclude	45.69	42.92	5,207	Wang et al. 2019	1240K.capture

KremsWA3	exclude	48.41	15.59	30,970	Fu et al. 2016	1240K.capture
LaBranca1	exclude	43.05	-5.49	6,980	Olalde et al. 2014	Shotgun
LesCloseaux13	exclude	48.52	2.11	9,900	Fu et al. 2016	1240K.capture
Loschbour	exclude	49.81	6.40	8,050	Lazaridis et al. 2014	Shotgun-HS2500
MA1	exclude	52.83	103.55	24,157	Raghavan et al. 2013	Shotgun
Motala9	exclude	58.54	15.05	7,888	Lazaridis et al. 2014	Shotgun-HS2500
NV3001	exclude	44.73	41.94	3,971	Wang et al. 2019	1240K.capture
Oase1	exclude	45.12	21.90	39,610	Fu et al. 2015	Shotgun-HS2000
Ofnet	exclude	48.49	10.27	8,245	Fu et al. 2016	1240K.capture
Ostuni1	exclude	40.73	17.57	27,620	Fu et al. 2016	Shotgun-HS2500
Pagliacci133	exclude	41.65	15.61	32,895	Fu et al. 2016	Shotgun-HS2500
Pavlov1	exclude	48.53	16.39	30,260	Fu et al. 2016	1240K.capture
Ranchot88	exclude	47.91	5.43	10,085	Fu et al. 2016	Shotgun-HS2000
Rigney1	exclude	47.23	6.10	15,465	Fu et al. 2016	Shotgun-HS2000
RISE00	exclude	59.41	27.03	4,412	Allentoft et al. 2015	Shotgun-HS2500
RISE174	exclude	55.55	13.10	1,431	Allentoft et al. 2015	Shotgun-HS2500
RISE489	exclude	45.26	10.38	4,693	Allentoft et al. 2015	Shotgun-HS2500
RISE492	exclude	53.15	91.05	2,252	Allentoft et al. 2015	Shotgun-HS2500
RISE493	exclude	53.15	91.05	3,429	Allentoft et al. 2015	Shotgun-HS2500
RISE494	exclude	53.15	91.05	3,242	Allentoft et al. 2015	Shotgun-HS2500
RISE495	exclude	52.95	90.19	3,327	Allentoft et al. 2015	Shotgun-HS2500
RISE496	exclude	52.95	90.19	3,287	Allentoft et al. 2015	Shotgun-HS2500
RISE497	exclude	52.95	90.19	3,327	Allentoft et al. 2015	Shotgun-HS2500
RISE499	exclude	51.91	88.57	3,327	Allentoft et al. 2015	Shotgun-HS2500
RISE502	exclude	51.91	88.57	3,351	Allentoft et al. 2015	Shotgun-HS2500
RISE504	exclude	53.46	85.45	1,149	Allentoft et al. 2015	Shotgun-HS2500
RISE515	exclude	53.15	90.19	4,192	Allentoft et al. 2015	Shotgun-HS2500
RISE516	exclude	53.15	90.19	4,068	Allentoft et al. 2015	Shotgun-HS2500
RISE523	exclude	57.07	53.04	3,448	Allentoft et al. 2015	Shotgun-HS2500
RISE524	exclude	57.07	53.04	3,448	Allentoft et al. 2015	Shotgun-HS2500
RISE525	exclude	57.07	53.04	3,448	Allentoft et al. 2015	Shotgun-HS2500
RISE553	exclude	56.02	92.87	2,820	Allentoft et al. 2015	Shotgun-HS2500
RISE554	exclude	56.02	92.87	2,874	Allentoft et al. 2015	Shotgun-HS2500
RISE598	exclude	54.36	23.30	2,646	Allentoft et al. 2015	Shotgun-HS2500
RISE600	exclude	50.21	85.73	1,700	Allentoft et al. 2015	Shotgun-HS2500
RISE601	exclude	50.21	85.73	1,700	Allentoft et al. 2015	Shotgun-HS2500
RISE602	exclude	50.62	86.46	1,700	Allentoft et al. 2015	Shotgun-HS2500
Rochedane	exclude	47.21	6.45	12,960	Fu et al. 2016	Shotgun-HS2500
SA6001	exclude	45.73	43.99	5,444	Wang et al. 2019	1240K.capture
SA6003	exclude	45.73	43.99	4,293	Wang et al. 2019	1240K.capture
SA6010	exclude	45.73	43.99	4,732	Wang et al. 2019	1240K.capture
SfF11	exclude	57.29	17.97	7,375	Skoglund et al. 2014	Shotgun-HS2500
Vestonice13	exclude	48.53	16.39	30,870	Fu et al. 2016	Shotgun-HS2500
Vestonice15	exclude	48.53	16.39	30,870	Fu et al. 2016	Shotgun-HS2500
Vestonice43	exclude	48.53	16.39	30,010	Fu et al. 2016	Shotgun-HS2500
Villabruna	exclude	46.15	12.21	13,980	Fu et al. 2016	1240K.capture
Kostenki14	Kostenki14	51.23	39.3	37,470	Seguin-Orlando et al. 2014	Shotgun
BAJ001	Levant_EF	30.42	35.46	8,806	Feldman et al. 2019	1240K.capture
I0861	Levant_EF	32.65	35.07	12,750	Lazaridis et al. 2016	1240K.capture
I0867	Levant_EF	31.79	35.17	8,700	Lazaridis et al. 2016	1240K.capture
I1069	Levant_EF	32.65	35.07	12,750	Lazaridis et al. 2016	1240K.capture
I1072	Levant_EF	32.65	35.07	12,750	Lazaridis et al. 2016	1240K.capture
I1414	Levant_EF	31.99	35.98	10,050	Lazaridis et al. 2016	1240K.capture
I1415	Levant_EF	31.99	35.98	9,875	Lazaridis et al. 2016	1240K.capture
I1416	Levant_EF	31.99	35.98	10,050	Lazaridis et al. 2016	1240K.capture
I1679	Levant_EF	31.99	35.98	8,800	Lazaridis et al. 2016	1240K.capture
I1685	Levant_EF	32.65	35.07	12,750	Lazaridis et al. 2016	1240K.capture
I1687	Levant_EF	32.65	35.07	13,265	Lazaridis et al. 2016	1240K.capture
I1690	Levant_EF	32.65	35.07	12,750	Lazaridis et al. 2016	1240K.capture
I1699	Levant_EF	31.99	35.98	8,700	Lazaridis et al. 2016	1240K.capture
I1700	Levant_EF	31.99	35.98	10,050	Lazaridis et al. 2016	1240K.capture

I1701	Levant_EF	31.99	35.98	9,610	Lazaridis et al. 2016	1240K.capture
I1704	Levant_EF	31.99	35.98	9,202	Lazaridis et al. 2016	1240K.capture
I1707	Levant_EF	31.99	35.98	9,582	Lazaridis et al. 2016	1240K.capture
I1709	Levant_EF	31.99	35.98	10,050	Lazaridis et al. 2016	1240K.capture
I1710	Levant_EF	31.99	35.98	9,580	Lazaridis et al. 2016	1240K.capture
I1727	Levant_EF	31.99	35.98	10,050	Lazaridis et al. 2016	1240K.capture
KFH2	Levant_EF	32.70	35.27	9,601	Feldman et al. 2019	1240K.capture
RISE175	Scandinavian_LF	55.40	13.60	3,214	Allentoft et al. 2015	1240K.capture
RISE179	Scandinavian_LF	55.40	13.60	3,843	Allentoft et al. 2015	Shotgun-HS2500
RISE207	Scandinavian_LF	56.00	14.10	3,347	Allentoft et al. 2015	Shotgun-HS2500
RISE21	Scandinavian_LF	55.55	12.21	3,303	Allentoft et al. 2015	Shotgun
RISE210	Scandinavian_LF	56.00	14.10	3,312	Allentoft et al. 2015	Shotgun-HS2500
RISE42	Scandinavian_LF	55.66	12.15	4,031	Allentoft et al. 2015	Shotgun
RISE47	Scandinavian_LF	56.97	9.55	3,361	Allentoft et al. 2015	Shotgun
RISE61	Scandinavian_LF	55.7	11.86	4,621	Allentoft et al. 2015	Shotgun
RISE71	Scandinavian_LF	56.68	10.03	4,059	Allentoft et al. 2015	Shotgun
RISE94	Scandinavian_LF	56.03	14.23	4,497	Allentoft et al. 2015	Shotgun-HS2500
RISE97	Scandinavian_LF	55.56	13.06	3,905	Allentoft et al. 2015	Shotgun-HS2500
RISE98	Scandinavian_LF	55.38	13.45	4,104	Allentoft et al. 2015	Shotgun-HS2500
ARM001	South_Caucasus_LNBA	40.87	43.72	5,330	Wang et al. 2019	1240K.capture
ARM002_ARM003	South_Caucasus_LNBA	40.87	43.72	5,148	Wang et al. 2019	1240K.capture
I1407	South_Caucasus_LNBA	39.73	45.20	5,975	Lazaridis et al. 2016	1240K.capture
I1409	South_Caucasus_LNBA	39.73	45.20	6,057	Lazaridis et al. 2016	1240K.capture
I1631	South_Caucasus_LNBA	39.73	45.20	6,100	Lazaridis et al. 2016	1240K.capture
I1632	South_Caucasus_LNBA	39.73	45.20	6,065	Lazaridis et al. 2016	1240K.capture
I1633	South_Caucasus_LNBA	40.65	45.12	4,464	Lazaridis et al. 2016	1240K.capture
I1634	South_Caucasus_LNBA	39.73	45.20	6,145	Lazaridis et al. 2016	1240K.capture
I1635	South_Caucasus_LNBA	40.65	45.12	4,492	Lazaridis et al. 2016	1240K.capture
I1656	South_Caucasus_LNBA	40.38	43.94	3,401	Lazaridis et al. 2016	1240K.capture
I1658	South_Caucasus_LNBA	40.38	43.87	5,169	Lazaridis et al. 2016	1240K.capture
I1661	South_Caucasus_LNBA	34.50	47.96	6,543	Lazaridis et al. 2016	1240K.capture
I1662	South_Caucasus_LNBA	34.50	47.96	6,671	Lazaridis et al. 2016	1240K.capture
I1665	South_Caucasus_LNBA	34.50	47.96	5,826	Lazaridis et al. 2016	1240K.capture
I1670	South_Caucasus_LNBA	34.50	47.96	6,678	Lazaridis et al. 2016	1240K.capture
I1674	South_Caucasus_LNBA	34.50	47.96	5,836	Lazaridis et al. 2016	1240K.capture
I1720	South_Caucasus_LNBA	43.69	43.65	5,300	Wang et al. 2019	1240K.capture
I1722	South_Caucasus_LNBA	44.45	40.10	6,404	Wang et al. 2019	1240K.capture
I2051	South_Caucasus_LNBA	44.58	38.17	3,260	Wang et al. 2019	1240K.capture
I2055	South_Caucasus_LNBA	44.45	40.10	6,533	Wang et al. 2019	1240K.capture
I2056	South_Caucasus_LNBA	44.45	40.10	6,478	Wang et al. 2019	1240K.capture
I6266	South_Caucasus_LNBA	44.39	40.39	5,200	Wang et al. 2019	1240K.capture
I6267	South_Caucasus_LNBA	44.39	40.39	5,438	Wang et al. 2019	1240K.capture
I6268	South_Caucasus_LNBA	44.39	40.39	5,564	Wang et al. 2019	1240K.capture
I6272	South_Caucasus_LNBA	44.39	40.39	5,200	Wang et al. 2019	1240K.capture
KDC001	South_Caucasus_LNBA	43.35	43.72	3,824	Wang et al. 2019	1240K.capture
KDC002	South_Caucasus_LNBA	43.35	43.72	3,735	Wang et al. 2019	1240K.capture
MK5001	South_Caucasus_LNBA	43.91	43.52	5,142	Wang et al. 2019	1240K.capture
MK5004	South_Caucasus_LNBA	43.91	43.52	5,171	Wang et al. 2019	1240K.capture
MK5008	South_Caucasus_LNBA	43.91	43.52	5,186	Wang et al. 2019	1240K.capture
OSS001	South_Caucasus_LNBA	43.08	44.63	5,570	Wang et al. 2019	1240K.capture
RISE396	South_Caucasus_LNBA	39.20	46.40	3,014	Allentoft et al. 2015	Shotgun-HS2500
RISE397	South_Caucasus_LNBA	39.20	46.40	2,901	Allentoft et al. 2015	Shotgun-HS2500
RISE407	South_Caucasus_LNBA	40.15	45.86	2,955	Allentoft et al. 2015	Shotgun-HS2500
RISE408	South_Caucasus_LNBA	40.15	45.86	3,059	Allentoft et al. 2015	Shotgun-HS2500
RISE412	South_Caucasus_LNBA	40.38	45.18	3,019	Allentoft et al. 2015	Shotgun-HS2500
RISE413	South_Caucasus_LNBA	40.14	45.26	3,752	Allentoft et al. 2015	Shotgun-HS2500
RISE416	South_Caucasus_LNBA	40.14	45.26	3,494	Allentoft et al. 2015	Shotgun-HS2500
RISE423	South_Caucasus_LNBA	40.14	45.26	3,256	Allentoft et al. 2015	Shotgun-HS2500
SA6013	South_Caucasus_LNBA	45.73	43.99	5,180	Wang et al. 2019	1240K.capture
SIJ002	South_Caucasus_LNBA	45.05	39.91	5,174	Wang et al. 2019	1240K.capture
SIJ003	South_Caucasus_LNBA	45.05	39.91	5,174	Wang et al. 2019	1240K.capture

VEK006	South_Caucasus_LNBA	42.18	48.07	4,850	Wang et al. 2019	1240K.capture
VEK007_VEK009	South_Caucasus_LNBA	42.18	48.07	4,850	Wang et al. 2019	1240K.capture
BU2001	Steppe	44.02	42.82	4,674	Wang et al. 2019	1240K.capture
GW1001	Steppe	44.03	43.13	4,726	Wang et al. 2019	1240K.capture
I0122	Steppe	52.22	48.10	6,550	Mathieson et al. 2015	1240K.capture
I0126	Steppe	53.31	51.15	4,627	Mathieson et al. 2015	1240K.capture
I0231	Steppe	52.42	48.24	4,792	Mathieson et al. 2015	840k+390k.capture
I0232	Steppe	48.10	54.44	3,475	Mathieson et al. 2015	1240K.capture
I0234	Steppe	53.14	50.01	3,675	Mathieson et al. 2015	1240K.capture
I0235	Steppe	53.14	50.01	3,675	Mathieson et al. 2015	1240K.capture
I0246	Steppe	52.56	52.30	4,149	Mathieson et al. 2015	1240K.capture
I0354	Steppe	53.03	50.39	3,804	Mathieson et al. 2015	1240K.capture
I0357	Steppe	53.38	50.39	4,950	Mathieson et al. 2015	840k+390k.capture
I0358	Steppe	53.03	50.39	3,721	Mathieson et al. 2015	1240K.capture
I0359	Steppe	53.03	50.39	3,475	Mathieson et al. 2015	1240K.capture
I0361	Steppe	53.03	50.39	3,475	Mathieson et al. 2015	1240K.capture
I0370	Steppe	51.27	58.18	4,950	Mathieson et al. 2015	840k+390k.capture
I0371	Steppe	53.34	50.34	4,678	Mathieson et al. 2015	1240K.capture
I0418	Steppe	52.56	52.30	3,897	Mathieson et al. 2015	1240K.capture
I0419	Steppe	52.56	52.30	4,000	Mathieson et al. 2015	1240K.capture
I0421	Steppe	53.08	50.36	4,000	Mathieson et al. 2015	1240K.capture
I0422	Steppe	52.54	50.50	3,475	Mathieson et al. 2015	1240K.capture
I0423	Steppe	52.54	50.50	3,475	Mathieson et al. 2015	1240K.capture
I0424	Steppe	53.12	48.37	3,675	Mathieson et al. 2015	1240K.capture
I0429	Steppe	53.38	50.39	5,079	Mathieson et al. 2015	840k+390k.capture
I0430	Steppe	53.08	50.36	3,675	Mathieson et al. 2015	1240K.capture
I0431	Steppe	53.08	50.36	3,675	Mathieson et al. 2015	1240K.capture
I0432	Steppe	53.66	50.67	4,658	Mathieson et al. 2015	1240K.capture
I0433	Steppe	52.22	48.10	6,550	Mathieson et al. 2015	1240K.capture
I0434	Steppe	52.22	48.10	6,550	Mathieson et al. 2015	1240K.capture
I0438	Steppe	53.38	50.38	4,778	Mathieson et al. 2015	840k+390k.capture
I0439	Steppe	53.38	50.39	5,071	Mathieson et al. 2015	840k+390k.capture
I0440	Steppe	53.74	49.38	4,727	Mathieson et al. 2015	1240K.capture
I0441	Steppe	52.30	52.05	4,766	Mathieson et al. 2015	840k+390k.capture
I0443	Steppe	53.38	50.38	4,950	Mathieson et al. 2015	840k+390k.capture
I0444	Steppe	53.10	51.13	5,059	Mathieson et al. 2015	840k+390k.capture
I1723	Steppe	44.03	43.13	4,702	Wang et al. 2019	1240K.capture
I2105	Steppe	48.22	37.15	4,950	Mathieson et al. 2018	1240K.capture
I3141	Steppe	48.22	37.15	4,950	Mathieson et al. 2018	1240K.capture
KBD001	Steppe	43.83	42.72	4,037	Wang et al. 2019	1240K.capture
KBD002	Steppe	43.83	42.72	4,057	Wang et al. 2019	1240K.capture
LYG001	Steppe	44.05	43.21	4,672	Wang et al. 2019	1240K.capture
MK3003	Steppe	43.93	43.53	4,477	Wang et al. 2019	1240K.capture
MK5009	Steppe	43.91	43.52	4,710	Wang et al. 2019	1240K.capture
PG2001	Steppe	43.82	43.35	6,207	Wang et al. 2019	1240K.capture
PG2002	Steppe	43.82	43.35	4,363	Wang et al. 2019	1240K.capture
PG2004	Steppe	43.82	43.35	6,090	Wang et al. 2019	1240K.capture
RISE240	Steppe	46.58	43.68	4,706	Allentoft et al. 2015	Shotgun-HS2500
RISE386	Steppe	52.45	55.16	4,122	Allentoft et al. 2015	Shotgun-HS2500
RISE391	Steppe	50.59	56.83	3,954	Allentoft et al. 2015	Shotgun-HS2500
RISE392	Steppe	53.88	59.08	3,961	Allentoft et al. 2015	Shotgun-HS2500
RISE394	Steppe	52.45	55.16	3,802	Allentoft et al. 2015	Shotgun-HS2500
RISE395	Steppe	52.64	59.54	3,808	Allentoft et al. 2015	Shotgun-HS2500
RISE500	Steppe	53.46	85.45	3,550	Allentoft et al. 2015	Shotgun-HS2500
RISE503	Steppe	53.46	85.45	3,569	Allentoft et al. 2015	Shotgun-HS2500
RISE505	Steppe	53.46	85.45	3,636	Allentoft et al. 2015	Shotgun-HS2500
RISE507	Steppe	51.50	85.97	5,077	Allentoft et al. 2015	Shotgun-HS2500
RISE508	Steppe	51.50	85.97	5,077	Allentoft et al. 2015	Shotgun-HS2500
RISE509	Steppe	54.58	90.78	4,732	Allentoft et al. 2015	Shotgun-HS2500
RISE510	Steppe	54.58	90.78	4,610	Allentoft et al. 2015	Shotgun-HS2500
RISE511	Steppe	54.58	90.78	4,744	Allentoft et al. 2015	Shotgun-HS2500

RISE512	Steppe	53.46	85.45	3,322	Allentoft et al. 2015	Shotgun-HS2500
RISE546	Steppe	46.54	43.70	4,650	Allentoft et al. 2015	Shotgun-HS2500
RISE547	Steppe	46.54	43.70	4,711	Allentoft et al. 2015	Shotgun-HS2500
RISE548	Steppe	46.54	43.70	4,650	Allentoft et al. 2015	Shotgun-HS2500
RISE550	Steppe	46.56	43.68	4,935	Allentoft et al. 2015	Shotgun-HS2500
RISE552	Steppe	46.62	43.33	4,446	Allentoft et al. 2015	Shotgun-HS2500
RISE555	Steppe	48.72	44.50	4,627	Allentoft et al. 2015	Shotgun-HS2500
RK1001	Steppe	45.54	41.12	4,726	Wang et al. 2019	1240K.capture
RK1003	Steppe	45.54	41.12	4,751	Wang et al. 2019	1240K.capture
RK1007	Steppe	45.54	41.12	5,123	Wang et al. 2019	1240K.capture
RK4001	Steppe	45.54	41.06	4,277	Wang et al. 2019	1240K.capture
RK4002	Steppe	45.54	41.06	4,610	Wang et al. 2019	1240K.capture
SA6004	Steppe	45.73	43.99	5,171	Wang et al. 2019	1240K.capture
SIJ001	Steppe	45.05	39.91	5,126	Wang et al. 2019	1240K.capture
VJ1001	Steppe	44.02	43.16	6,242	Wang et al. 2019	1240K.capture
ZO2002	Steppe	45.66	42.61	4,850	Wang et al. 2019	1240K.capture
I0518	UK_LF	52.22	-0.94	5,180	Olalde et al. 2018	1240K.capture
I0519	UK_LF	52.22	-0.94	5,180	Olalde et al. 2018	1240K.capture
I0520	UK_LF	52.22	-0.94	5,180	Olalde et al. 2018	1240K.capture
I2605	UK_LF	51.49	-0.67	5,237	Olalde et al. 2018	1240K.capture
I2606	UK_LF	51.49	-0.67	5,065	Olalde et al. 2018	1240K.capture
I2629	UK_LF	58.74	-2.92	4,930	Olalde et al. 2018	1240K.capture
I2630	UK_LF	58.74	-2.92	4,471	Olalde et al. 2018	1240K.capture
I2631	UK_LF	59.23	-2.57	4,951	Olalde et al. 2018	1240K.capture
I2633	UK_LF	58.53	-3.60	5,653	Olalde et al. 2018	1240K.capture
I2634	UK_LF	58.54	-3.60	5,568	Olalde et al. 2018	1240K.capture
I2635	UK_LF	58.53	-3.60	5,470	Olalde et al. 2018	1240K.capture
I2636	UK_LF	59.35	-2.87	5,390	Olalde et al. 2018	1240K.capture
I2637	UK_LF	59.35	-2.87	5,449	Olalde et al. 2018	1240K.capture
I2650	UK_LF	59.35	-2.87	5,459	Olalde et al. 2018	1240K.capture
I2651	UK_LF	59.35	-2.87	5,179	Olalde et al. 2018	1240K.capture
I2657	UK_LF	56.42	-5.47	5,815	Olalde et al. 2018	1240K.capture
I2659	UK_LF	56.41	-5.47	5,652	Olalde et al. 2018	1240K.capture
I2660	UK_LF	56.41	-5.47	5,382	Olalde et al. 2018	1240K.capture
I2691	UK_LF	56.41	-5.47	5,619	Olalde et al. 2018	1240K.capture
I2796	UK_LF	59.31	-2.94	5,570	Olalde et al. 2018	1240K.capture
I2932	UK_LF	58.74	-2.92	4,408	Olalde et al. 2018	1240K.capture
I2933	UK_LF	58.74	-2.92	4,897	Olalde et al. 2018	1240K.capture
I2934	UK_LF	58.74	-2.92	5,130	Olalde et al. 2018	1240K.capture
I2935	UK_LF	58.74	-2.92	5,123	Olalde et al. 2018	1240K.capture
I2977	UK_LF	58.74	-2.92	4,835	Olalde et al. 2018	1240K.capture
I2978	UK_LF	58.74	-2.92	5,129	Olalde et al. 2018	1240K.capture
I2979	UK_LF	58.74	-2.92	5,087	Olalde et al. 2018	1240K.capture
I2980	UK_LF	59.31	-2.94	5,180	Olalde et al. 2018	1240K.capture
I2988	UK_LF	55.40	-5.20	5,388	Olalde et al. 2018	1240K.capture
I3041	UK_LF	56.40	-5.48	5,439	Olalde et al. 2018	1240K.capture
I3068	UK_LF	53.08	-1.64	5,557	Olalde et al. 2018	1240K.capture
I3085	UK_LF	58.74	-2.92	5,132	Olalde et al. 2018	1240K.capture
I3133	UK_LF	56.40	-5.48	5,454	Olalde et al. 2018	1240K.capture
I3134	UK_LF	56.40	-5.48	5,455	Olalde et al. 2018	1240K.capture
I3135	UK_LF	56.40	-5.48	5,461	Olalde et al. 2018	1240K.capture
I3136	UK_LF	56.40	-5.48	5,392	Olalde et al. 2018	1240K.capture
I3137	UK_LF	56.40	-5.48	5,450	Olalde et al. 2018	1240K.capture
I3138	UK_LF	56.40	-5.48	5,043	Olalde et al. 2018	1240K.capture
I4949	UK_LF	51.44	-1.85	5,452	Olalde et al. 2018	1240K.capture
I5358	UK_LF	53.06	-3.25	4,942	Olalde et al. 2018	1240K.capture
I5359	UK_LF	51.45	-3.31	5,600	Olalde et al. 2018	1240K.capture
I5366	UK_LF	50.86	-0.38	5,464	Olalde et al. 2018	1240K.capture
I5370	UK_LF	56.41	-5.47	5,600	Olalde et al. 2018	1240K.capture
I5371	UK_LF	56.41	-5.47	5,600	Olalde et al. 2018	1240K.capture
I5374	UK_LF	51.28	-2.74	4,596	Olalde et al. 2018	1240K.capture

I6750	UK_LF	51.09	-1.73	5,658	Ojalde et al. 2018	1240K.capture
I6751	UK_LF	51.09	-1.73	5,638	Ojalde et al. 2018	1240K.capture
I6759	UK_LF	54.07	-2.29	5,536	Ojalde et al. 2018	1240K.capture
I6761	UK_LF	50.83	-0.11	5,525	Ojalde et al. 2018	1240K.capture
I6762	UK_LF	51.56	-1.45	5,700	Ojalde et al. 2018	1240K.capture
I7554	UK_LF	58.99	-3.25	5,050	Ojalde et al. 2018	1240K.capture
I1770	UK_LNBA	54.20	-0.43	3,950	Ojalde et al. 2018	1240K.capture
I2416	UK_LNBA	51.16	-1.77	4,253	Ojalde et al. 2018	1240K.capture
I2417	UK_LNBA	51.16	-1.77	4,270	Ojalde et al. 2018	1240K.capture
I2418	UK_LNBA	51.16	-1.77	4,277	Ojalde et al. 2018	1240K.capture
I2421	UK_LNBA	54.88	-1.45	3,794	Ojalde et al. 2018	1240K.capture
I2443	UK_LNBA	51.80	-1.32	4,106	Ojalde et al. 2018	1240K.capture
I2445	UK_LNBA	51.80	-1.32	4,112	Ojalde et al. 2018	1240K.capture
I2446	UK_LNBA	51.80	-1.32	4,247	Ojalde et al. 2018	1240K.capture
I2447	UK_LNBA	51.80	-1.32	3,962	Ojalde et al. 2018	1240K.capture
I2450	UK_LNBA	51.68	-1.30	4,253	Ojalde et al. 2018	1240K.capture
I2452	UK_LNBA	52.15	-0.38	4,078	Ojalde et al. 2018	1240K.capture
I2453	UK_LNBA	52.67	-0.35	4,114	Ojalde et al. 2018	1240K.capture
I2454	UK_LNBA	52.34	0.03	4,040	Ojalde et al. 2018	1240K.capture
I2455	UK_LNBA	52.34	0.03	3,968	Ojalde et al. 2018	1240K.capture
I2457	UK_LNBA	51.16	-1.77	4,198	Ojalde et al. 2018	1240K.capture
I2458	UK_LNBA	51.16	-1.77	3,339	Ojalde et al. 2018	1240K.capture
I2459	UK_LNBA	51.16	-1.77	4,252	Ojalde et al. 2018	1240K.capture
I2460	UK_LNBA	51.16	-1.77	3,874	Ojalde et al. 2018	1240K.capture
I2461	UK_LNBA	51.13	-1.69	4,270	Ojalde et al. 2018	1240K.capture
I2462	UK_LNBA	51.33	1.36	3,959	Ojalde et al. 2018	1240K.capture
I2463	UK_LNBA	51.33	1.36	3,762	Ojalde et al. 2018	1240K.capture
I2464	UK_LNBA	51.15	-1.75	3,629	Ojalde et al. 2018	1240K.capture
I2565	UK_LNBA	51.16	-1.77	4,252	Ojalde et al. 2018	1240K.capture
I2566	UK_LNBA	51.16	-1.77	4,069	Ojalde et al. 2018	1240K.capture
I2567	UK_LNBA	55.97	-2.44	4,029	Ojalde et al. 2018	1240K.capture
I2568	UK_LNBA	55.97	-2.44	4,112	Ojalde et al. 2018	1240K.capture
I2569	UK_LNBA	55.99	-2.54	3,977	Ojalde et al. 2018	1240K.capture
I2573	UK_LNBA	55.98	-2.90	3,350	Ojalde et al. 2018	1240K.capture
I2574	UK_LNBA	53.33	-3.78	3,270	Ojalde et al. 2018	1240K.capture
I2596	UK_LNBA	51.16	-1.77	4,103	Ojalde et al. 2018	1240K.capture
I2597	UK_LNBA	51.16	-1.77	4,101	Ojalde et al. 2018	1240K.capture
I2598	UK_LNBA	51.16	-1.77	3,994	Ojalde et al. 2018	1240K.capture
I2600	UK_LNBA	51.13	-1.69	3,985	Ojalde et al. 2018	1240K.capture
I2601	UK_LNBA	51.33	1.36	3,802	Ojalde et al. 2018	1240K.capture
I2602	UK_LNBA	51.33	1.36	3,745	Ojalde et al. 2018	1240K.capture
I2604	UK_LNBA	51.15	-1.36	4,098	Ojalde et al. 2018	1240K.capture
I2609	UK_LNBA	54.98	-2.12	3,846	Ojalde et al. 2018	1240K.capture
I2610	UK_LNBA	54.97	-1.73	3,790	Ojalde et al. 2018	1240K.capture
I2612	UK_LNBA	54.88	-1.45	4,286	Ojalde et al. 2018	1240K.capture
I2618	UK_LNBA	55.06	-2.15	3,992	Ojalde et al. 2018	1240K.capture
I2639	UK_LNBA	51.16	-1.77	3,465	Ojalde et al. 2018	1240K.capture
I2653	UK_LNBA	55.98	-2.90	3,350	Ojalde et al. 2018	1240K.capture
I2654	UK_LNBA	55.98	-2.90	3,350	Ojalde et al. 2018	1240K.capture
I2655	UK_LNBA	58.23	-6.94	3,306	Ojalde et al. 2018	1240K.capture
I2656	UK_LNBA	55.97	-2.90	3,078	Ojalde et al. 2018	1240K.capture
I2859	UK_LNBA	57.72	-3.39	2,809	Ojalde et al. 2018	1240K.capture
I2860	UK_LNBA	57.72	-3.39	2,842	Ojalde et al. 2018	1240K.capture
I2861	UK_LNBA	57.72	-3.39	2,852	Ojalde et al. 2018	1240K.capture
I2981	UK_LNBA	59.28	-2.43	3,673	Ojalde et al. 2018	1240K.capture
I3082	UK_LNBA	50.92	-2.02	3,396	Ojalde et al. 2018	1240K.capture
I3130	UK_LNBA	57.72	-3.39	2,853	Ojalde et al. 2018	1240K.capture
I3132	UK_LNBA	57.72	-3.39	3,952	Ojalde et al. 2018	1240K.capture
I3255	UK_LNBA	52.17	0.10	3,992	Ojalde et al. 2018	1240K.capture
I3256	UK_LNBA	52.17	0.10	4,066	Ojalde et al. 2018	1240K.capture
I4950	UK_LNBA	51.29	-1.81	4,100	Ojalde et al. 2018	1240K.capture

I4951	UK_LNBA	51.24	-1.76	4,100	Ojalde et al. 2018	1240K.capture
I5364	UK_LNBA	51.54	-4.21	3,150	Ojalde et al. 2018	1240K.capture
I5367	UK_LNBA	56.68	-6.46	4,299	Ojalde et al. 2018	1240K.capture
I5373	UK_LNBA	53.08	-1.64	4,037	Ojalde et al. 2018	1240K.capture
I5376	UK_LNBA	51.47	-0.31	4,247	Ojalde et al. 2018	1240K.capture
I5377	UK_LNBA	51.47	-0.27	3,744	Ojalde et al. 2018	1240K.capture
I5379	UK_LNBA	50.92	-2.02	4,332	Ojalde et al. 2018	1240K.capture
I5382	UK_LNBA	54.52	-1.31	4,079	Ojalde et al. 2018	1240K.capture
I5383	UK_LNBA	54.16	-2.47	2,945	Ojalde et al. 2018	1240K.capture
I5385	UK_LNBA	58.36	-3.40	4,251	Ojalde et al. 2018	1240K.capture
I5441	UK_LNBA	50.43	-3.58	3,791	Ojalde et al. 2018	1240K.capture
I5469	UK_LNBA	55.97	-3.18	3,522	Ojalde et al. 2018	1240K.capture
I5470	UK_LNBA	55.97	-3.18	3,484	Ojalde et al. 2018	1240K.capture
I5471	UK_LNBA	55.95	-2.47	4,095	Ojalde et al. 2018	1240K.capture
I5473	UK_LNBA	55.62	-3.62	4,200	Ojalde et al. 2018	1240K.capture
I5512	UK_LNBA	51.24	-1.76	4,100	Ojalde et al. 2018	1240K.capture
I5513	UK_LNBA	51.22	-1.77	4,100	Ojalde et al. 2018	1240K.capture
I5515	UK_LNBA	56.06	-3.42	3,854	Ojalde et al. 2018	1240K.capture
I5516	UK_LNBA	56.19	-4.06	3,690	Ojalde et al. 2018	1240K.capture
I6679	UK_LNBA	55.31	-1.55	3,957	Ojalde et al. 2018	1240K.capture
I6680	UK_LNBA	55.31	-1.55	3,700	Ojalde et al. 2018	1240K.capture
I6774	UK_LNBA	50.86	-0.12	4,115	Ojalde et al. 2018	1240K.capture
I6775	UK_LNBA	51.12	-3.08	4,150	Ojalde et al. 2018	1240K.capture
I6777	UK_LNBA	51.15	-1.81	4,150	Ojalde et al. 2018	1240K.capture
I6778	UK_LNBA	51.15	-1.81	4,150	Ojalde et al. 2018	1240K.capture
I7568	UK_LNBA	52.34	0.03	3,400	Ojalde et al. 2018	1240K.capture
I7569	UK_LNBA	52.70	-0.34	3,488	Ojalde et al. 2018	1240K.capture
I7570	UK_LNBA	52.70	-0.34	3,583	Ojalde et al. 2018	1240K.capture
I7571	UK_LNBA	52.34	0.03	3,303	Ojalde et al. 2018	1240K.capture
I7572	UK_LNBA	52.34	0.03	3,356	Ojalde et al. 2018	1240K.capture
I7573	UK_LNBA	52.31	0.39	3,524	Ojalde et al. 2018	1240K.capture
I7574	UK_LNBA	52.18	0.12	3,268	Ojalde et al. 2018	1240K.capture
I7575	UK_LNBA	52.12	-0.51	3,103	Ojalde et al. 2018	1240K.capture
I7576	UK_LNBA	52.12	-0.51	3,054	Ojalde et al. 2018	1240K.capture
I7577	UK_LNBA	52.12	-0.51	3,204	Ojalde et al. 2018	1240K.capture
I7578	UK_LNBA	52.12	-0.51	3,069	Ojalde et al. 2018	1240K.capture
I7579	UK_LNBA	52.12	-0.51	3,348	Ojalde et al. 2018	1240K.capture
I7580	UK_LNBA	52.12	-0.51	3,087	Ojalde et al. 2018	1240K.capture
I7626	UK_LNBA	52.12	-0.51	3,212	Ojalde et al. 2018	1240K.capture
I7627	UK_LNBA	52.12	-0.51	3,266	Ojalde et al. 2018	1240K.capture
I7628	UK_LNBA	52.12	-0.51	3,043	Ojalde et al. 2018	1240K.capture
I7630	UK_LNBA	53.73	-0.53	3,735	Ojalde et al. 2018	1240K.capture
I7635	UK_LNBA	54.52	-1.31	4,035	Ojalde et al. 2018	1240K.capture
I7638	UK_LNBA	51.41	-1.15	3,982	Ojalde et al. 2018	1240K.capture
I7639	UK_LNBA	52.28	0.46	3,798	Ojalde et al. 2018	1240K.capture
I7640	UK_LNBA	52.18	0.12	3,306	Ojalde et al. 2018	1240K.capture
Ustlshim	Ustlshim	54.06	78.83	45,045	Fu et al. 2014	Shotgun
Vestonice16	Vestonice16	48.53	16.39	30,010	Fu et al. 2016	Shotgun-HS2500
ATP16	WesternEurope_LF	42.40	-3.55	5,038	Gunther et al. 2015	Shotgun-HS2000
ATP17	WesternEurope_LF	42.37	-3.55	4,889	Gunther et al. 2015	Shotgun-HS2000
ATP2	WesternEurope_LF	42.37	-3.55	4,738	Gunther et al. 2015	Shotgun-HS2000
ATP20	WesternEurope_LF	42.37	-3.55	4,119	Gunther et al. 2015	Shotgun-HS2000
ATP3	WesternEurope_LF	42.37	-3.55	5,389	Gunther et al. 2015	Shotgun-HS2000
ATP7	WesternEurope_LF	42.37	-3.55	5,094	Gunther et al. 2015	Shotgun-HS2000
ATP9	WesternEurope_LF	42.37	-3.55	3,634	Gunther et al. 2015	Shotgun-HS2000
I0257	WesternEurope_LF	41.49	2.14	4,952	Ojalde et al. 2018	1240K.capture
I0258	WesternEurope_LF	41.49	2.14	3,719	Ojalde et al. 2018	1240K.capture
I0260	WesternEurope_LF	41.49	2.14	4,500	Ojalde et al. 2018	1240K.capture
I0261	WesternEurope_LF	41.49	2.14	3,475	Ojalde et al. 2018	1240K.capture
I0262	WesternEurope_LF	41.49	2.14	4,500	Ojalde et al. 2018	1240K.capture
I0263	WesternEurope_LF	41.49	2.14	4,500	Ojalde et al. 2018	1240K.capture

I0405	WesternEurope_LF	41.25	-2.33	5,700	Mathieson et al. 2015	840k+390k.capture
I0406	WesternEurope_LF	41.25	-2.33	5,700	Mathieson et al. 2015	840k+390k.capture
I0407	WesternEurope_LF	41.25	-2.33	5,700	Mathieson et al. 2015	840k+390k.capture
I0408	WesternEurope_LF	41.25	-2.33	5,727	Mathieson et al. 2015	840k+390k.capture
I0453	WesternEurope_LF	38.10	-1.85	4,252	Olalde et al. 2018	1240K.capture
I0455	WesternEurope_LF	38.10	-1.85	4,735	Olalde et al. 2018	1240K.capture
I0456	WesternEurope_LF	38.10	-1.85	4,580	Olalde et al. 2018	1240K.capture
I0457	WesternEurope_LF	38.10	-1.85	4,580	Olalde et al. 2018	1240K.capture
I0581	WesternEurope_LF	42.33	-3.50	4,942	Mathieson et al. 2015	1240K.capture
I0823	WesternEurope_LF	41.49	2.14	4,500	Olalde et al. 2018	1240K.capture
I0825	WesternEurope_LF	41.49	2.14	4,336	Olalde et al. 2018	1240K.capture
I0826	WesternEurope_LF	41.49	2.14	4,608	Olalde et al. 2018	1240K.capture
I0839	WesternEurope_LF	39.50	-8.62	4,280	Olalde et al. 2018	1240K.capture
I0840	WesternEurope_LF	39.50	-8.62	4,277	Olalde et al. 2018	1240K.capture
I1271	WesternEurope_LF	42.33	-3.50	4,583	Mathieson et al. 2015	1240K.capture
I1272	WesternEurope_LF	42.33	-3.50	4,627	Mathieson et al. 2015	1240K.capture
I1276	WesternEurope_LF	42.33	-3.50	4,583	Mathieson et al. 2015	1240K.capture
I1277	WesternEurope_LF	42.33	-3.50	4,407	Mathieson et al. 2015	1240K.capture
I1280	WesternEurope_LF	42.33	-3.50	4,583	Mathieson et al. 2015	1240K.capture
I1281	WesternEurope_LF	42.33	-3.50	4,670	Mathieson et al. 2015	1240K.capture
I1282	WesternEurope_LF	42.33	-3.50	4,583	Mathieson et al. 2015	1240K.capture
I1284	WesternEurope_LF	42.33	-3.50	4,583	Mathieson et al. 2015	1240K.capture
I1300	WesternEurope_LF	42.33	-3.50	4,583	Mathieson et al. 2015	1240K.capture
I1302	WesternEurope_LF	42.33	-3.50	4,705	Mathieson et al. 2015	1240K.capture
I1303	WesternEurope_LF	42.33	-3.50	4,583	Mathieson et al. 2015	1240K.capture
I1314	WesternEurope_LF	42.33	-3.50	4,583	Mathieson et al. 2015	1240K.capture
I1553	WesternEurope_LF	41.49	2.14	4,500	Olalde et al. 2018	1240K.capture
I1838	WesternEurope_LF	42.63	-2.70	5,098	Lipson et al. 2017	1240K.capture
I1843	WesternEurope_LF	42.57	-2.57	4,934	Lipson et al. 2017	1240K.capture
I1970	WesternEurope_LF	38.88	-9.08	4,450	Olalde et al. 2018	1240K.capture
I1975	WesternEurope_LF	42.57	-2.55	4,942	Lipson et al. 2017	1240K.capture
I1976	WesternEurope_LF	42.57	-2.62	4,409	Lipson et al. 2017	1240K.capture
I1981	WesternEurope_LF	42.57	-2.57	4,902	Lipson et al. 2017	1240K.capture
I2467	WesternEurope_LF	42.57	-2.62	4,296	Lipson et al. 2017	1240K.capture
I2473	WesternEurope_LF	42.57	-2.62	4,765	Lipson et al. 2017	1240K.capture
I3269	WesternEurope_LF	42.63	-2.70	5,000	Lipson et al. 2017	1240K.capture
I3270	WesternEurope_LF	42.63	-2.70	5,000	Lipson et al. 2017	1240K.capture
I3271	WesternEurope_LF	42.63	-2.70	5,000	Lipson et al. 2017	1240K.capture
I3272	WesternEurope_LF	42.57	-2.55	5,033	Lipson et al. 2017	1240K.capture
I3273	WesternEurope_LF	42.57	-2.55	5,445	Lipson et al. 2017	1240K.capture
I3276	WesternEurope_LF	42.57	-2.57	4,955	Lipson et al. 2017	1240K.capture
I3277	WesternEurope_LF	42.57	-2.57	4,925	Lipson et al. 2017	1240K.capture
I4229	WesternEurope_LF	39.09	-9.25	4,149	Olalde et al. 2018	1240K.capture
I4245	WesternEurope_LF	40.43	-3.54	4,325	Olalde et al. 2018	1240K.capture
I4247	WesternEurope_LF	40.43	-3.54	4,287	Olalde et al. 2018	1240K.capture
I5838	WesternEurope_LF	42.33	-3.50	4,573	Lipson et al. 2017	1240K.capture
I6467	WesternEurope_LF	38.88	-9.08	4,450	Olalde et al. 2018	1240K.capture
I6475	WesternEurope_LF	40.49	-3.37	4,200	Olalde et al. 2018	1240K.capture
I6542	WesternEurope_LF	40.44	-3.50	4,075	Olalde et al. 2018	1240K.capture
I6543	WesternEurope_LF	40.44	-3.50	4,162	Olalde et al. 2018	1240K.capture
I6584	WesternEurope_LF	40.22	-3.76	4,200	Olalde et al. 2018	1240K.capture
I6587	WesternEurope_LF	40.22	-3.76	4,200	Olalde et al. 2018	1240K.capture
I6596	WesternEurope_LF	40.22	-3.76	4,550	Olalde et al. 2018	1240K.capture
I6601	WesternEurope_LF	39.09	-9.29	4,650	Olalde et al. 2018	1240K.capture
I6604	WesternEurope_LF	40.44	-3.50	3,966	Olalde et al. 2018	1240K.capture
I6605	WesternEurope_LF	40.44	-3.50	4,333	Olalde et al. 2018	1240K.capture
I6608	WesternEurope_LF	40.44	-3.50	3,844	Olalde et al. 2018	1240K.capture
I6609	WesternEurope_LF	40.44	-3.50	4,239	Olalde et al. 2018	1240K.capture
I6610	WesternEurope_LF	40.44	-3.50	3,808	Olalde et al. 2018	1240K.capture
I6612	WesternEurope_LF	40.44	-3.50	4,162	Olalde et al. 2018	1240K.capture
I6613	WesternEurope_LF	40.44	-3.50	4,162	Olalde et al. 2018	1240K.capture

I6617	WesternEurope_LF	40.22	-3.76	4,550	Ojalde et al. 2018	1240K.capture
I6622	WesternEurope_LF	40.44	-3.50	4,225	Ojalde et al. 2018	1240K.capture
I6628	WesternEurope_LF	40.22	-3.76	4,550	Ojalde et al. 2018	1240K.capture
I6629	WesternEurope_LF	40.22	-3.76	4,550	Ojalde et al. 2018	1240K.capture
I6630	WesternEurope_LF	40.22	-3.76	4,550	Ojalde et al. 2018	1240K.capture
MATOJO	WesternEurope_LF	42.35	-3.52	5,394	Gunther et al. 2015	Shotgun-HS2000
I0458	WesternEurope_LNBA	42.40	-3.75	4,281	Ojalde et al. 2018	1240K.capture
I0459	WesternEurope_LNBA	42.40	-3.75	4,350	Ojalde et al. 2018	1240K.capture
I0460	WesternEurope_LNBA	42.40	-3.75	4,285	Ojalde et al. 2018	1240K.capture
I0461	WesternEurope_LNBA	42.40	-3.75	4,278	Ojalde et al. 2018	1240K.capture
I0462	WesternEurope_LNBA	42.40	-3.75	4,405	Ojalde et al. 2018	1240K.capture
I5665	WesternEurope_LNBA	42.73	-3.84	4,082	Ojalde et al. 2018	1240K.capture
I6466	WesternEurope_LNBA	38.88	-9.08	4,450	Ojalde et al. 2018	1240K.capture
I6471	WesternEurope_LNBA	40.49	-3.37	4,200	Ojalde et al. 2018	1240K.capture
I6472	WesternEurope_LNBA	40.49	-3.37	4,200	Ojalde et al. 2018	1240K.capture
I6539	WesternEurope_LNBA	40.22	-3.76	4,200	Ojalde et al. 2018	1240K.capture
I6585	WesternEurope_LNBA	40.22	-3.76	4,189	Ojalde et al. 2018	1240K.capture
I6588	WesternEurope_LNBA	40.22	-3.76	4,200	Ojalde et al. 2018	1240K.capture
I6589	WesternEurope_LNBA	40.22	-3.76	4,200	Ojalde et al. 2018	1240K.capture
I6623	WesternEurope_LNBA	40.44	-3.50	3,799	Ojalde et al. 2018	1240K.capture
I6626	WesternEurope_LNBA	40.44	-3.50	4,075	Ojalde et al. 2018	1240K.capture
I1875	WHG	42.97	16.71	9,118	Mathieson et al. 2018	1240K.capture
I2158	WHG	37.93	12.33	14,275	Mathieson et al. 2018	1240K.capture
I2534	WHG	44.02	25.40	7,973	Mathieson et al. 2018	1240K.capture
I4081	WHG	44.52	22.72	9,335	Mathieson et al. 2018	1240K.capture
I4582	WHG	44.52	22.72	8,697	Mathieson et al. 2018	1240K.capture
I4607	WHG	44.63	22.61	8,940	Mathieson et al. 2018	1240K.capture
I4655	WHG	44.63	22.61	8,765	Mathieson et al. 2018	1240K.capture
I4657	WHG	44.53	22.05	11,465	Mathieson et al. 2018	1240K.capture
I4660	WHG	44.53	22.05	9,713	Mathieson et al. 2018	1240K.capture
I4870	WHG	44.53	22.05	8,740	Mathieson et al. 2018	1240K.capture
I4871	WHG	44.53	22.05	8,450	Mathieson et al. 2018	1240K.capture
I4872	WHG	44.53	22.05	8,450	Mathieson et al. 2018	1240K.capture
I4873	WHG	44.53	22.05	7,872	Mathieson et al. 2018	1240K.capture
I4874	WHG	44.53	22.05	8,506	Mathieson et al. 2018	1240K.capture
I4875	WHG	44.53	22.05	8,458	Mathieson et al. 2018	1240K.capture
I4876	WHG	44.53	22.05	8,455	Mathieson et al. 2018	1240K.capture
I4877	WHG	44.53	22.05	8,505	Mathieson et al. 2018	1240K.capture
I4878	WHG	44.53	22.05	7,803	Mathieson et al. 2018	1240K.capture
I4880	WHG	44.53	22.05	7,813	Mathieson et al. 2018	1240K.capture
I4881	WHG	44.53	22.05	8,363	Mathieson et al. 2018	1240K.capture
I4914	WHG	44.64	22.30	8,123	Mathieson et al. 2018	1240K.capture
I4915	WHG	44.64	22.30	8,115	Mathieson et al. 2018	1240K.capture
I4916	WHG	44.64	22.30	8,763	Mathieson et al. 2018	1240K.capture
I4917	WHG	44.64	22.30	8,058	Mathieson et al. 2018	1240K.capture
I5233	WHG	44.60	22.01	8,001	Mathieson et al. 2018	1240K.capture
I5234	WHG	44.60	22.01	9,800	Mathieson et al. 2018	1240K.capture
I5235	WHG	44.60	22.01	10,835	Mathieson et al. 2018	1240K.capture
I5236	WHG	44.60	22.01	10,008	Mathieson et al. 2018	1240K.capture
I5237	WHG	44.60	22.01	9,800	Mathieson et al. 2018	1240K.capture
I5238	WHG	44.60	22.01	9,993	Mathieson et al. 2018	1240K.capture
I5239	WHG	44.60	22.01	10,333	Mathieson et al. 2018	1240K.capture
I5240	WHG	44.60	22.01	10,805	Mathieson et al. 2018	1240K.capture
I5242	WHG	44.60	22.01	10,530	Mathieson et al. 2018	1240K.capture
I5244	WHG	44.60	22.01	10,785	Mathieson et al. 2018	1240K.capture
I5401	WHG	44.64	22.30	8,838	Mathieson et al. 2018	1240K.capture
I5402	WHG	44.64	22.30	8,156	Mathieson et al. 2018	1240K.capture
I5407	WHG	44.55	22.03	9,800	Mathieson et al. 2018	1240K.capture
I5408	WHG	44.52	22.72	7,450	Mathieson et al. 2018	1240K.capture
I5409	WHG	44.60	22.01	9,800	Mathieson et al. 2018	1240K.capture
I5411	WHG	44.63	22.61	8,600	Mathieson et al. 2018	1240K.capture

I5436	WHG	44.63	22.61	9,025	Mathieson et al. 2018	1240K.capture
I5771	WHG	44.53	22.05	8,325	Mathieson et al. 2018	1240K.capture
I5772	WHG	44.53	22.05	8,450	Mathieson et al. 2018	1240K.capture
I5773	WHG	44.53	22.05	10,040	Mathieson et al. 2018	1240K.capture

Table S2. Sweep haplotype presence in ancient and modern genomic datasets. Sweep haplotypes were quantified for pseudohaploid ancient samples and modern populations for each of the 56 sweeps, after adjusting for missing data (see Supplemental Materials 2). For individual ancient samples, sweep haplotype presence is indicated using a binary indicator (i.e. present = 1 and absent = 0), whereas sweep frequencies were calculated for modern populations. Ancient samples with missing data are indicated with a blank cell. Results are shown for the three different sweep haplotype detection criteria (Criteria column; see Supplemental Materials 2). For each sample, broad geographical origin (Region column) and abbreviated labels are provided (Sample / Pop. column). For ancient samples, archaeological metadata (Group column), and sample ages (Date; largely calibrated with IntCal13) from the Allen Ancient DNA Resource version 42.4 are listed. For modern data, population labels (Sample / Pop.) and dataset source (Group) are provided instead.

Table S3. Sweep haplotype data used to estimate selection onset and Eurasian migrations.

Summary of samples and metadata, which include (over successive columns) abbreviated and full sample IDs, sampling region and country, sample age (largely calibrated with IntCal13), SNP count (among 1.2M probe set), and number of sweeps (adjusted for missing data; see Supplemental Materials 2). All metadata was obtained from the Allen Ancient DNA Resource version 42.4.

Sample ID	ID	Region	Country	Date	# SNPs	# Sweeps
I17268	NO3423.SG	British Isles	Great Britain	1,170	768,658	24.00
I0157	I0157.SG	British Isles	Great Britain	1,232	1,075,331	20.00
I0159	I0159.SG	British Isles	Great Britain	1,247	1,053,950	20.00
I0769	I0769.SG	British Isles	Great Britain	1,455	934,424	18.33
I0777	I0777.SG	British Isles	Great Britain	1,478	1,123,743	20.00
I0774	I0774.SG	British Isles	Great Britain	1,483	1,129,556	24.00
I0773	I0773.SG	British Isles	Great Britain	1,490	830,230	21.00
3DT26	3DT26.SG	British Isles	Great Britain	1,750	789,900	23.00
6DT18	6DT18.SG	British Isles	Great Britain	1,750	774,489	24.00
6DT21	6DT21.SG	British Isles	Great Britain	1,750	809,862	21.38
6DT22	6DT22.SG	British Isles	Great Britain	1,750	795,475	22.00
6DT3	6DT3.SG	British Isles	Great Britain	1,750	959,069	18.00
I0160	I0160.SG	British Isles	Great Britain	1,995	1,172,478	21.00
I0156	I0156.SG	British Isles	Great Britain	2,017	658,217	15.37
I2859	I2859	British Isles	Great Britain	2,811	810,185	23.85
I2860	I2860	British Isles	Great Britain	2,843	830,544	26.00
I2861	I2861	British Isles	Great Britain	2,853	615,178	24.35
I3130	I3130	British Isles	Great Britain	2,854	811,519	24.00
I2655	I2655	British Isles	Great Britain	3,308	835,188	21.38
I7640	I7640	British Isles	Great Britain	3,316	801,057	17.00
I2458	I2458	British Isles	Great Britain	3,340	812,721	20.36
I2573	I2573	British Isles	Great Britain	3,352	611,500	21.00
I7568	I7568	British Isles	Great Britain	3,400	769,990	18.33
I7570	I7570	British Isles	Great Britain	3,400	776,537	19.35
I7571	I7571	British Isles	Great Britain	3,400	771,850	20.74
I7572	I7572	British Isles	Great Britain	3,400	653,485	21.71
I7573	I7573	British Isles	Great Britain	3,400	709,969	21.54
I7574	I7574	British Isles	Great Britain	3,400	789,405	24.30
I7575	I7575	British Isles	Great Britain	3,400	804,207	22.40
I7576	I7576	British Isles	Great Britain	3,400	785,241	22.40
I7577	I7577	British Isles	Great Britain	3,400	778,782	22.00
I7578	I7578	British Isles	Great Britain	3,400	775,926	26.96
I7579	I7579	British Isles	Great Britain	3,400	766,013	18.67
I7580	I7580	British Isles	Great Britain	3,400	770,757	23.42
I7626	I7626	British Isles	Great Britain	3,400	768,487	25.36
I7627	I7627	British Isles	Great Britain	3,400	780,131	25.45
I3082	I3082	British Isles	Great Britain	3,455	692,741	20.86
rath3	rath3.SG	British Isles	Ireland	3,585	673,050	17.14
I6680	I6680	British Isles	Great Britain	3,702	891,333	16.00
I2981	I2981	British Isles	Great Britain	3,703	788,384	20.00
I2602	I2602	British Isles	Great Britain	3,745	641,305	16.18
I5377	I5377	British Isles	Great Britain	3,745	836,940	19.35
rath2	rath2.SG	British Isles	Ireland	3,833	946,668	22.00
rath1	rath1.SG	British Isles	Ireland	3,906	1,181,857	20.00
I3132	I3132	British Isles	Great Britain	3,954	773,258	22.19
I2462	I2462	British Isles	Great Britain	3,960	816,976	27.49
I2447	I2447	British Isles	Great Britain	3,964	913,061	19.00
I7638	I7638	British Isles	Great Britain	3,980	600,005	17.14
I2618	I2618	British Isles	Great Britain	3,993	643,010	21.13
I3255	I3255	British Isles	Great Britain	3,994	861,509	24.00
I1767	I1767	British Isles	Great Britain	4,035	729,987	20.46
I2454	I2454	British Isles	Great Britain	4,040	818,929	23.42
I2452	I2452	British Isles	Great Britain	4,049	913,255	23.00
I2457	I2457	British Isles	Great Britain	4,066	718,630	25.85
I3256	I3256	British Isles	Great Britain	4,067	843,389	20.00
I2604	I2604	British Isles	Great Britain	4,070	760,401	23.25

I2443	I2443	British Isles	Great Britain	4,085	894,847	19.00
I5471	I5471_published	British Isles	Great Britain	4,096	619,372	12.29
I2597	I2597	British Isles	Great Britain	4,105	824,991	23.85
I2445	I2445	British Isles	Great Britain	4,114	854,563	19.00
I2453	I2453	British Isles	Great Britain	4,115	610,725	11.91
I6775	I6775	British Isles	Great Britain	4,150	670,798	11.67
I6777	I6777	British Isles	Great Britain	4,150	783,327	19.70
I4950	I4950	British Isles	Great Britain	4,250	777,787	21.38
I5512	I5512	British Isles	Great Britain	4,250	863,895	19.00
I5513	I5513	British Isles	Great Britain	4,250	816,408	23.42
I5367	I5367	British Isles	Great Britain	4,255	750,069	22.81
I2417	I2417	British Isles	Great Britain	4,270	829,575	21.00
I2418	I2418	British Isles	Great Britain	4,270	656,573	21.54
I2461	I2461	British Isles	Great Britain	4,270	771,469	17.63
I2450	I2450	British Isles	Great Britain	4,283	904,314	23.00
I5379	I5379	British Isles	Great Britain	4,330	700,532	17.14
I2932	I2932	British Isles	Great Britain	4,409	786,582	22.81
I2630	I2630	British Isles	Great Britain	4,472	932,048	20.00
I2977	I2977	British Isles	Great Britain	4,836	784,516	16.91
I2933	I2933	British Isles	Great Britain	4,898	736,264	20.46
I2631	I2631	British Isles	Great Britain	4,952	869,547	23.85
I3138	I3138	British Isles	Great Britain	5,044	813,553	25.93
I2606	I2606	British Isles	Great Britain	5,065	676,373	24.16
I2979	I2979	British Isles	Great Britain	5,087	799,002	25.00
I6766	I6766.SG	British Isles	Great Britain	5,100	744,205	22.40
I2935	I2935	British Isles	Great Britain	5,123	805,005	24.44
I2978	I2978	British Isles	Great Britain	5,129	801,316	20.36
I2934	I2934	British Isles	Great Britain	5,130	745,801	25.93
I3085	I3085	British Isles	Great Britain	5,132	726,028	23.85
bally	bally.SG	British Isles	Ireland	5,132	1,150,887	21.00
I2651	I2651	British Isles	Great Britain	5,160	768,079	27.49
I2980	I2980	British Isles	Great Britain	5,181	802,432	20.36
I7554	I7554	British Isles	Great Britain	5,185	789,511	19.35
I2605	I2605	British Isles	Great Britain	5,238	609,777	18.23
I6753	I6753_all.SG	British Isles	Great Britain	5,305	936,079	26.00
I2637	I2637	British Isles	Great Britain	5,375	843,761	24.44
I2650	I2650	British Isles	Great Britain	5,380	770,497	26.47
prs008/009	prs009-ALL_DATA.SG	British Isles	Great Britain	5,380	1,122,257	20.00
I2660	I2660	British Isles	Great Britain	5,383	822,865	19.35
I2988	I2988	British Isles	Great Britain	5,389	795,840	25.00
I2636	I2636	British Isles	Great Britain	5,390	848,224	22.40
I3136	I3136	British Isles	Great Britain	5,394	791,804	24.44
I3041	I3041_all.SG	British Isles	Great Britain	5,440	675,911	21.96
prs013/014	prs013-ALL_DATA.SG	British Isles	Ireland	5,450	1,145,014	24.00
I3133	I3133	British Isles	Great Britain	5,455	800,141	26.47
I3134	I3134	British Isles	Great Britain	5,456	807,346	19.35
I3135	I3135	British Isles	Great Britain	5,463	791,590	23.00
I6757	I6757.SG	British Isles	Great Britain	5,463	858,108	29.00
I2635	I2635	British Isles	Great Britain	5,471	761,604	24.89
I6746	I6746_all.SG	British Isles	Great Britain	5,490	908,673	25.00
I6759	I6759.SG	British Isles	Great Britain	5,536	817,441	18.67
I6747	I6747_all.SG	British Isles	Great Britain	5,539	1,180,398	16.00
prs016	prs016-ALL_DATA.SG	British Isles	Ireland	5,560	1,161,741	26.00
I2691	I2691	British Isles	Great Britain	5,620	785,482	25.00
I6751	I6751_all.SG	British Isles	Great Britain	5,638	953,729	23.00
I2659	I2659	British Isles	Great Britain	5,652	792,497	22.00
I2633	I2633	British Isles	Great Britain	5,653	724,631	23.69

I3005	I3005	British Isles	Great Britain	5,665	652,889	18.29
prs002	prs002-ALL_DATA.SG	British Isles	Ireland	5,675	1,119,566	31.00
I6762	I6762_all.SG	British Isles	Great Britain	5,700	632,621	19.09
I6760	I6760_all.SG	British Isles	Great Britain	5,770	752,745	24.00
I4137	RISE569.SG	Central Europe	Czech Republic	1,235	708,529	14.56
SZ1	SZ1.SG	Central Europe	Hungary	1,250	1,181,117	12.00
AV2	AV2	Central Europe	Hungary	1,356	772,227	25.36
AV1	AV1	Central Europe	Hungary	1,361	802,843	19.70
SZ43	SZ43.SG	Central Europe	Hungary	1,431	1,181,334	15.00
SZ11	SZ11.SG	Central Europe	Hungary	1,442	1,180,814	21.00
SZ15	SZ15.SG	Central Europe	Hungary	1,442	1,181,035	24.00
SZ16	SZ16	Central Europe	Hungary	1,442	639,815	15.56
SZ18	SZ18	Central Europe	Hungary	1,442	716,518	20.08
SZ2	SZ2.SG	Central Europe	Hungary	1,442	1,176,754	25.00
SZ22	SZ22	Central Europe	Hungary	1,442	695,137	22.40
SZ23	SZ23	Central Europe	Hungary	1,442	718,162	24.30
SZ28	SZ28	Central Europe	Hungary	1,442	756,041	26.47
SZ3	SZ3.SG	Central Europe	Hungary	1,442	1,181,309	16.00
SZ32	SZ32	Central Europe	Hungary	1,442	775,053	24.44
SZ36	SZ36.SG	Central Europe	Hungary	1,442	1,173,847	22.00
SZ38	SZ38	Central Europe	Hungary	1,442	725,637	24.30
SZ4	SZ4.SG	Central Europe	Hungary	1,442	1,181,245	21.00
SZ40	SZ40	Central Europe	Hungary	1,442	722,333	23.06
SZ42	SZ42	Central Europe	Hungary	1,442	840,821	19.00
SZ45	SZ45.SG	Central Europe	Hungary	1,442	1,181,237	20.00
SZ5	SZ5.SG	Central Europe	Hungary	1,442	1,176,362	20.00
SZ7	SZ7	Central Europe	Hungary	1,442	748,887	23.69
SZ9	SZ9	Central Europe	Hungary	1,442	809,957	22.00
SZ19	SZ19	Central Europe	Hungary	1,463	754,662	18.00
SZ13	SZ13	Central Europe	Hungary	1,469	825,443	27.49
SZ27	SZ27	Central Europe	Hungary	1,475	894,808	20.00
Alh10	Alh10.SG	Central Europe	Germany	1,489	1,100,414	18.00
Alh1	Alh1.SG	Central Europe	Germany	1,500	1,116,070	19.00
FN2	FN2.SG	Central Europe	Germany	1,650	1,094,129	14.00
I1503	IR1.SG	Central Europe	Hungary	2,855	793,281	17.31
I0099	I0099_published	Central Europe	Germany	3,036	959,437	27.00
I7949	I7949	Central Europe	Czech Republic	3,046	857,331	18.00
I1504	BR2.SG	Central Europe	Hungary	3,140	1,182,644	18.00
RISE479	RISE479.SG	Central Europe	Hungary	3,700	861,756	18.00
RISE150	RISE150.SG	Central Europe	Poland	3,739	635,649	20.26
I4892	I4892	Central Europe	Czech Republic	3,741	808,531	22.40
AITI_2	AITI_2	Central Europe	Germany	3,741	769,657	15.37
AITI_78	AITI_78	Central Europe	Germany	3,741	679,165	21.71
AITI_43	AITI_43	Central Europe	Germany	3,745	883,256	16.29
I4884	I4884	Central Europe	Czech Republic	3,764	854,624	19.00
AITI_72	AITI_72	Central Europe	Germany	3,766	721,397	22.62
N17	N17.SG	Central Europe	Poland	3,846	1,074,631	20.00
POST_6	POST_6	Central Europe	Germany	3,896	966,701	27.00
I0164	I0164	Central Europe	Germany	3,909	834,837	27.00
I0047	I0047_published	Central Europe	Germany	3,951	806,227	28.00
I0116	I0116	Central Europe	Germany	3,987	629,665	19.43
I0114	I0114	Central Europe	Germany	3,995	721,918	19.02
OBKR_80	OBKR_80	Central Europe	Germany	3,997	742,188	19.02
I4139	RISE577.SG	Central Europe	Czech Republic	4,000	711,716	24.89
I7249	I7249	Central Europe	Czech Republic	4,007	779,011	19.70
I7043	I7043	Central Europe	Hungary	4,007	801,297	18.67
POST_44	POST_44	Central Europe	Germany	4,009	882,117	23.00

I7198	I7198	Central Europe	Czech Republic	4,034	767,682	28.51
I1502	I1502	Central Europe	Hungary	4,035	795,741	22.40
I7199	I7199	Central Europe	Czech Republic	4,041	789,281	22.40
I4888	I4888	Central Europe	Czech Republic	4,060	833,166	24.44
POST_50	POST_50	Central Europe	Germany	4,063	793,520	23.42
I4887	I4887	Central Europe	Czech Republic	4,070	817,605	20.00
I7210	I7210	Central Europe	Czech Republic	4,070	747,429	23.25
I4886	I4886	Central Europe	Czech Republic	4,074	846,480	21.38
I0117	I0117	Central Europe	Germany	4,106	843,093	18.00
I4895	I4895	Central Europe	Czech Republic	4,110	814,836	17.31
I6531	I6531	Central Europe	Poland	4,113	793,534	20.00
I6583	I6583	Central Europe	Poland	4,121	828,828	19.00
I4889	I4889	Central Europe	Czech Republic	4,122	848,054	25.00
I4891	I4891	Central Europe	Czech Republic	4,122	841,976	15.27
I6579	I6579	Central Europe	Poland	4,142	788,610	19.02
I6582	I6582	Central Europe	Poland	4,151	791,514	23.42
I5514	I5514	Central Europe	Czech Republic	4,163	861,406	17.31
I4896	I4896	Central Europe	Czech Republic	4,165	806,027	21.00
I4885	I4885	Central Europe	Czech Republic	4,166	816,324	24.00
I7211	I7211	Central Europe	Czech Republic	4,170	753,333	25.85
I3594	I3594	Central Europe	Germany	4,175	613,980	18.29
I3601	I3601	Central Europe	Germany	4,175	656,910	17.14
I6580	I6580	Central Europe	Poland	4,175	658,471	21.16
I0059	I0059	Central Europe	Germany	4,188	725,307	17.00
WEHR_1192SkA	WEHR_1192SkA	Central Europe	Germany	4,191	968,607	16.00
I7281	I7281	Central Europe	Czech Republic	4,192	744,708	18.67
I7205	I7205	Central Europe	Czech Republic	4,200	771,399	26.96
I7214	I7214	Central Europe	Czech Republic	4,200	752,197	17.23
I7251	I7251	Central Europe	Czech Republic	4,200	756,643	26.42
I7269	I7269	Central Europe	Czech Republic	4,200	703,041	23.25
I7275	I7275	Central Europe	Czech Republic	4,200	708,042	23.25
I7276	I7276	Central Europe	Czech Republic	4,200	765,003	23.42
I7279	I7279	Central Europe	Czech Republic	4,200	636,343	19.53
I7280	I7280	Central Europe	Czech Republic	4,200	780,479	19.02
I7282	I7282	Central Europe	Czech Republic	4,200	785,327	20.08
I7283	I7283	Central Europe	Czech Republic	4,200	740,433	21.96
I7287	I7287	Central Europe	Czech Republic	4,200	637,279	11.67
I7290	I7290	Central Europe	Czech Republic	4,200	796,476	20.00
I5519	I5519	Central Europe	Germany	4,200	726,140	20.08
I5833	I5833	Central Europe	Germany	4,200	680,513	16.68
I5834	I5834	Central Europe	Germany	4,200	605,212	18.29
I5835	I5835	Central Europe	Germany	4,200	635,245	19.91
I6590	I6590	Central Europe	Germany	4,200	823,913	15.56
I6591	I6591	Central Europe	Germany	4,200	815,600	19.70
I6624	I6624	Central Europe	Germany	4,200	624,057	16.47
I2364	I2364	Central Europe	Hungary	4,215	767,419	20.36
UNTA85_1343	UNTA85_1343	Central Europe	Germany	4,223	820,798	20.36
I1549	I1549	Central Europe	Germany	4,225	780,302	16.00
I7195	I7195	Central Europe	Czech Republic	4,250	685,817	17.14
I7196	I7196	Central Europe	Czech Republic	4,250	720,414	21.96
I7200	I7200	Central Europe	Czech Republic	4,250	735,642	27.47
I7201	I7201	Central Europe	Czech Republic	4,250	689,010	17.57
I7286	I7286	Central Europe	Czech Republic	4,250	799,421	15.27
I0112	I0112	Central Europe	Germany	4,250	949,947	24.00
I5521	I5521	Central Europe	Germany	4,250	673,566	20.08
I5525	I5525	Central Europe	Germany	4,250	777,278	26.42
I5531	I5531	Central Europe	Germany	4,250	610,570	18.67

I6581	I6581	Central Europe	Poland	4,251	628,199	22.64
I2741	I2741	Central Europe	Hungary	4,256	871,912	20.00
I7213	I7213	Central Europe	Czech Republic	4,267	739,544	16.15
I7045	I7045	Central Europe	Hungary	4,267	755,038	23.42
I7212	I7212	Central Europe	Czech Republic	4,280	747,056	22.19
I2787	I2787	Central Europe	Hungary	4,280	669,314	9.69
I7209	I7209	Central Europe	Czech Republic	4,283	869,434	17.00
I2786	I2786	Central Europe	Hungary	4,283	795,354	17.00
I2365	I2365	Central Europe	Hungary	4,285	922,704	22.00
I7289	I7289	Central Europe	Czech Republic	4,287	767,739	25.45
I7044	I7044	Central Europe	Hungary	4,300	783,765	22.00
I0118	I0118	Central Europe	Germany	4,309	1,048,626	17.00
I7208	I7208	Central Europe	Czech Republic	4,330	811,518	20.00
I7278	I7278	Central Europe	Czech Republic	4,332	795,922	16.29
I0104	I0104	Central Europe	Germany	4,378	962,767	27.00
I0108	I0108	Central Europe	Germany	4,387	735,474	18.31
I7207	I7207	Central Europe	Czech Republic	4,400	789,641	18.33
N44	N44.SG	Central Europe	Poland	4,405	1,017,645	20.00
N45	N45.SG	Central Europe	Poland	4,405	1,050,046	24.00
N47	N47.SG	Central Europe	Poland	4,405	1,074,445	19.00
N49	N49.SG	Central Europe	Poland	4,405	1,045,306	18.00
RISE1164	RISE1164.SG	Central Europe	Poland	4,470	751,938	18.33
I0103	I0103	Central Europe	Germany	4,473	1,049,840	26.00
I6695	I6695	Central Europe	Czech Republic	4,575	818,786	24.00
I6696	I6696	Central Europe	Czech Republic	4,575	850,315	24.00
RISE1173	RISE1173.SG	Central Europe	Poland	4,634	1,097,337	17.00
RISE1172	RISE1172.SG	Central Europe	Poland	4,675	1,076,411	20.00
RISE1168	RISE1168.SG	Central Europe	Poland	4,676	1,063,074	23.00
poz81	poz81	Central Europe	Poland	4,705	773,809	16.29
RISE1160	RISE1160.SG	Central Europe	Poland	4,714	996,013	25.00
RISE1248	RISE1248.SG	Central Europe	Poland	4,725	604,561	20.36
RISE1167	RISE1167.SG	Central Europe	Poland	4,728	1,039,137	29.00
RISE1159	RISE1159.SG	Central Europe	Poland	4,730	1,068,129	27.00
RISE1163	RISE1163.SG	Central Europe	Poland	4,735	1,147,530	22.00
RISE1249	RISE1249.SG	Central Europe	Poland	4,737	710,701	25.93
RISE1169	RISE1169.SG	Central Europe	Poland	4,741	730,820	23.06
RISE1165	RISE1165.SG	Central Europe	Poland	4,743	1,025,600	24.00
RISE1162	RISE1162.SG	Central Europe	Poland	4,747	1,104,048	24.00
RISE1170	RISE1170.SG	Central Europe	Poland	4,749	1,112,811	20.00
I1497	I1497	Central Europe	Hungary	4,750	813,947	26.00
RISE1241	RISE1241.SG	Central Europe	Poland	4,753	654,308	19.43
RISE1161	RISE1161.SG	Central Europe	Poland	4,757	813,323	21.00
RISE1171	RISE1171.SG	Central Europe	Poland	4,768	1,075,219	19.00
RISE1166	RISE1166.SG	Central Europe	Poland	4,908	1,079,562	26.00
N38	N38.SG	Central Europe	Poland	5,033	1,022,642	21.00
I2367	I2367_published	Central Europe	Hungary	5,081	836,355	30.00
I2753	I2753	Central Europe	Hungary	5,081	867,336	21.00
I2366	I2366_published	Central Europe	Hungary	5,093	798,237	23.00
I2370	I2370	Central Europe	Hungary	5,096	852,351	30.00
I5118	I5118	Central Europe	Hungary	5,100	690,337	25.25
I5119	I5119	Central Europe	Hungary	5,123	687,360	22.40
I0172	I0172	Central Europe	Germany	5,173	1,035,229	28.00
I2369	I2369	Central Europe	Hungary	5,185	758,484	19.35
I1563	I1563	Central Europe	Germany	5,361	941,629	33.00
I7272	I7272	Central Europe	Czech Republic	5,454	773,560	21.78
N19	N19.SG	Central Europe	Poland	5,462	1,004,527	24.00
N20	N20.SG	Central Europe	Poland	5,462	735,974	22.00

N18	N18.SG	Central Europe	Poland	5,463	974,168	26.00
I2791	I2791_published	Central Europe	Hungary	5,471	832,892	23.42
I6677	I6677	Central Europe	Czech Republic	5,550	873,182	24.89
I2790	I2790_published	Central Europe	Hungary	5,649	943,394	19.00
I2788	I2788	Central Europe	Hungary	5,730	822,177	22.40
I1565	I1565	Central Europe	Germany	5,735	864,619	18.33
I2783	I2783	Central Europe	Hungary	6,046	648,306	20.46
I4189	I4189	Central Europe	Hungary	6,050	764,910	25.00
N42	N42.SG	Central Europe	Poland	6,055	607,894	21.28
N28	N28.SG	Central Europe	Poland	6,074	984,960	24.00
I7042	I7042	Central Europe	Hungary	6,089	783,888	22.00
N31	N31.SG	Central Europe	Poland	6,138	969,046	24.00
N26	N26.SG	Central Europe	Poland	6,151	1,049,737	26.00
I1907	I1907_published	Central Europe	Hungary	6,153	835,823	27.00
N25	N25.SG	Central Europe	Poland	6,250	1,055,361	21.00
N27	N27.SG	Central Europe	Poland	6,250	1,003,248	27.00
N36	N36.SG	Central Europe	Poland	6,250	976,414	23.00
N22	N22.SG	Central Europe	Poland	6,291	972,044	26.00
I2793	I2793_published	Central Europe	Hungary	6,301	850,019	31.00
I4893	I4893	Central Europe	Czech Republic	6,349	836,569	24.00
I1495	I1495	Central Europe	Hungary	6,374	829,966	18.00
I4894	I4894	Central Europe	Czech Republic	6,378	816,890	24.00
I7197	I7197	Central Europe	Czech Republic	6,449	738,450	17.31
I0449	I0449	Central Europe	Hungary	6,700	955,623	21.00
kol006	kol6-ALL_DATA.SG	Central Europe	Czech Republic	6,775	777,676	22.00
I0821	I0821_published	Central Europe	Germany	6,976	629,014	17.50
I0100	I0100	Central Europe	Germany	6,977	982,315	18.00
I2379	I2379	Central Europe	Hungary	7,011	618,281	18.67
I2377	I2377	Central Europe	Hungary	7,025	649,593	23.83
I1904	I1904	Central Europe	Hungary	7,028	804,922	21.00
I0659	I0659_published	Central Europe	Germany	7,037	648,193	26.21
I1500	I1500	Central Europe	Hungary	7,050	830,691	24.00
I4196	I4196	Central Europe	Hungary	7,050	638,509	23.52
I0046	I0046_published	Central Europe	Germany	7,051	950,914	26.00
I1496	I1496	Central Europe	Hungary	7,052	812,201	20.74
I1499	I1499	Central Europe	Hungary	7,060	817,728	16.00
I1505	I1505	Central Europe	Hungary	7,061	769,987	21.13
I0054	I0054	Central Europe	Germany	7,072	978,534	23.00
I1498	I1498	Central Europe	Hungary	7,124	810,430	21.00
I0025	I0025	Central Europe	Germany	7,125	836,923	24.00
I0026	I0026	Central Europe	Germany	7,125	893,563	29.00
I1550	I1550_published	Central Europe	Germany	7,125	616,873	11.45
I2384	I2384_published	Central Europe	Hungary	7,130	683,331	15.37
I1506	NE1.SG	Central Europe	Hungary	7,139	1,152,433	28.00
I0018	Stuttgart_published.DG	Central Europe	Germany	7,140	1,130,723	16.00
I2739	I2739_published	Central Europe	Hungary	7,142	749,828	25.93
I1895	I1895_published	Central Europe	Hungary	7,151	673,444	23.85
I2380	I2380	Central Europe	Hungary	7,350	740,659	19.35
I2794	I2794	Central Europe	Hungary	7,574	986,747	24.00
I1877	I1877_all	Central Europe	Hungary	7,580	763,053	24.89
I1880	I1880	Central Europe	Hungary	7,600	810,907	22.00
I1507	I1507	Central Europe	Hungary	7,660	800,965	27.49
I1878	I1878_published	Central Europe	Hungary	7,700	709,555	20.08
I5236	I5236	Eurasia	Serbia	10,008	840,166	25.00
I1763	I1763	Eurasia	Ukraine	10,074	831,221	16.29
Bon002	Bon002.SG	Eurasia	Turkey	10,078	1,077,088	14.00
I1954	I1954	Eurasia	Iran	10,093	938,523	16.00

I6767_all	I6767_all.SG	Eurasia	Great Britain	10,300	1,123,721	20.00
I5239	I5239	Eurasia	Serbia	10,333	809,534	23.00
I5242	I5242	Eurasia	Serbia	10,530	836,819	24.30
I1819	I1819	Eurasia	Ukraine	10,643	813,114	21.78
R7	R7.SG	Eurasia	Italy	10,682	1,129,613	24.44
I5244	I5244	Eurasia	Serbia	10,785	809,448	20.00
I5240	I5240	Eurasia	Serbia	10,805	826,331	16.91
I5235	I5235	Eurasia	Serbia	10,835	838,984	29.00
I5241	I5241	Eurasia	Serbia	11,196	818,133	26.00
Sidelkino	Sidelkino.SG	Eurasia	Russia	11,259	967,604	14.00
R11	R11.SG	Eurasia	Italy	11,908	750,119	15.56
SATP	SATP.SG	Eurasia	Georgia	13,255	816,136	9.16
Bichon	Bichon.SG	Eurasia	Switzerland	13,698	1,176,132	21.00
Villabruna	Villabruna	Eurasia	Italy	14,021	902,419	25.00
ZBC	ZBC_IPB001.B-C0101_Luk2-Pinarbasi	Eurasia	Turkey	15,405	863,964	15.00
ElMiron	ElMiron_d	Eurasia	Spain	18,775	627,275	17.92
MA1	MA1.SG	Eurasia	Russia	24,305	820,035	16.00
Vestonice16	Vestonice16	Eurasia	Czech Republic	30,929	745,560	8.30
Yana	Yana_old.SG	Eurasia	Russia	31,866	1,182,458	11.00
Yana2	Yana_old2.SG	Eurasia	Russia	31,866	1,178,800	14.00
Sunghir1	Sunghir1.SG	Eurasia	Russia	32,920	809,229	12.00
Sunghir4	Sunghir4.SG	Eurasia	Russia	34,173	1,160,873	10.00
Sunghir3	Sunghir3.SG	Eurasia	Russia	34,517	1,181,712	14.00
Sunghir2	Sunghir2.SG	Eurasia	Russia	34,629	1,164,216	13.00
BachoKiro_BK-1653	NA	Eurasia	Hungary	34,948		16.00
GoyetQ116-1	GoyetQ116-1_published	Eurasia	Belgium	35,208	780,462	14.52
Kostenki14	Kostenki14	Eurasia	Russia	38,052	1,095,867	14.00
Tianyuan	Tianyuan	Eurasia	China	39,565	901,237	11.00
BachoKiro_F6-620	NA	Eurasia	Hungary	43,106		3.00
Ust_Ishim	Ust_Ishim_published.DG	Eurasia	Russia	44,364	1,147,829	8.00
ZlatyKun	NA	Eurasia	Czech Republic	44,364		5.46
BachoKiro_BB7-240	NA	Eurasia	Hungary	44,687		11.00
BachoKiro_CC7-335	NA	Eurasia	Hungary	45,117		8.00
I7425	I7425	Iberia	Spain	600	709,907	11.20
I12647	I12647	Iberia	Spain	750	619,870	12.83
I7498	I7498	Iberia	Spain	1,100	746,152	16.00
I7499	I7499	Iberia	Spain	1,100	847,037	22.00
I3585	I3585	Iberia	Spain	1,179	736,749	22.40
I10895	I10895	Iberia	Spain	1,215	631,258	21.16
I3982	I3982	Iberia	Spain	1,450	811,030	20.00
I3576	I3576	Iberia	Spain	1,477	825,464	28.00
I3983	I3983	Iberia	Spain	1,604	661,285	15.37
I8209	I8209	Iberia	Spain	1,800	868,050	20.00
I8215	I8215	Iberia	Spain	1,800	829,948	23.00
I10866	I10866	Iberia	Spain	1,948	799,391	12.22
I3759	I3759	Iberia	Spain	2,228	738,525	17.96
I3758	I3758	Iberia	Spain	2,235	859,767	18.00
I3322	I3322	Iberia	Spain	2,500	616,808	16.93
I12410	I12410	Iberia	Spain	2,550	818,626	22.40
I12208	I12208	Iberia	Spain	3,240	860,198	27.00
I12209	I12209	Iberia	Spain	3,240	899,574	25.45
esp005	esp005.SG	Iberia	Spain	3,370	943,381	23.00
I1840	I1840	Iberia	Spain	3,507	661,465	17.50
MonteGato104	MonteGato104.SG	Iberia	Portugal	3,535	739,513	16.15
TV32032extra	TV32032extra.SG	Iberia	Portugal	3,550	664,207	22.62
TV3831	TV3831.SG	Iberia	Portugal	3,550	725,249	23.06
I4558	I4558	Iberia	Spain	3,550	634,917	7.69

I4560	I4560	Iberia	Spain	3,550	871,169	20.00
I4561	I4561	Iberia	Spain	3,550	894,637	18.00
I6470	I6470	Iberia	Spain	3,601	687,251	16.47
I4562	I4562	Iberia	Spain	3,631	714,863	17.63
I3997	I3997	Iberia	Spain	3,635	979,277	26.00
I3494	I3494	Iberia	Spain	3,787	698,862	21.13
I3756	I3756	Iberia	Spain	3,848	604,170	14.61
I4229	I4229	Iberia	Portugal	4,150	875,453	21.00
I4246	I4246_published	Iberia	Spain	4,202	694,170	12.08
I6623	I6623	Iberia	Spain	4,250	618,697	19.09
I0461	I0461	Iberia	Spain	4,278	720,612	13.18
EHU002	EHU002	Iberia	Spain	4,363	674,286	28.00
I1300	I1300	Iberia	Spain	4,573	779,093	24.00
I5838	I5838	Iberia	Spain	4,573	712,753	24.16
I8364	I8364	Iberia	Spain	4,588	807,822	22.00
I8365	I8365	Iberia	Spain	4,588	886,223	15.00
I8197	I8197	Iberia	Spain	4,650	843,473	26.00
I8198	I8198	Iberia	Spain	4,650	673,223	17.87
I8199	I8199	Iberia	Spain	4,650	844,129	21.00
I1281	I1281	Iberia	Spain	4,670	623,901	17.92
I8569	I8569	Iberia	Spain	4,699	607,128	22.40
atp002	atp002.SG	Iberia	Spain	4,740	1,175,853	22.00
I7642	I7642	Iberia	Spain	4,784	620,981	24.89
I1846	I1846	Iberia	Spain	4,800	650,008	25.14
I1978	I1978	Iberia	Spain	4,800	846,972	25.00
atp12-1420	atp12-1420.SG	Iberia	Spain	4,896	1,044,624	20.00
I5429	I5429	Iberia	Portugal	4,899	899,025	25.00
CovaMoura364	CovaMoura364.SG	Iberia	Portugal	4,900	666,359	16.00
CovaMoura9B	CovaMoura9B.SG	Iberia	Portugal	4,900	1,069,564	15.00
I4565	I4565	Iberia	Spain	4,915	680,128	28.57
I1843	I1843	Iberia	Spain	4,935	642,557	17.87
I3276	I3276_published	Iberia	Spain	4,955	726,934	30.75
I3269	I3269	Iberia	Spain	5,000	669,669	26.21
atp016	atp016.SG	Iberia	Spain	5,040	1,150,106	20.00
I11600	CabecoArruda122A.SG	Iberia	Portugal	5,050	966,588	26.00
I11248	I11248	Iberia	Spain	5,050	829,527	19.35
I11249	I11249	Iberia	Spain	5,050	727,030	19.02
I7602	I7602	Iberia	Spain	5,050	618,920	15.27
I7604	I7604	Iberia	Spain	5,050	698,628	21.78
I7606	I7606	Iberia	Spain	5,050	831,931	30.55
I1838	I1838	Iberia	Spain	5,099	828,755	29.04
I5076	I5076	Iberia	Portugal	5,131	806,951	16.59
DolmenAnsiao96B	DolmenAnsiao96B.SG	Iberia	Portugal	5,450	995,212	24.00
I0406	I0406	Iberia	Spain	5,700	724,111	27.45
I0408	I0408	Iberia	Spain	5,727	907,690	22.00
ELT002	ELT002_merged	Iberia	Spain	5,771	831,758	23.00
ELT006	ELT006_merged	Iberia	Spain	5,807	716,426	25.25
LugarCanto41	LugarCanto41.SG	Iberia	Portugal	5,950	759,210	22.40
LugarCanto42	LugarCanto42.SG	Iberia	Portugal	5,950	1,089,508	25.00
LugarCanto44	LugarCanto44.SG	Iberia	Portugal	5,950	998,856	24.00
I7550	I7550	Iberia	Spain	5,950	638,374	20.16
I8134	I8134	Iberia	Spain	5,950	663,508	25.76
LD270	LD270.SG	Iberia	Portugal	6,336	855,937	22.81
LD1174	LD1174.SG	Iberia	Spain	6,415	913,135	16.29
LU339	LU339.SG	Iberia	Portugal	6,798	1,124,350	20.00
Canes	Canes.SG	Iberia	Spain	7,115	804,993	18.33
mur	mur.SG	Iberia	Spain	7,136	1,078,491	19.00

I0413	I0413	Iberia	Spain	7,139	638,681	13.71
I0412	I0412	Iberia	Spain	7,144	983,710	24.00
CB13	CB13.SG	Iberia	Spain	7,348	717,337	21.78
I0585	LaBrana1_published.SG	Iberia	Spain	7,815	1,079,840	22.00
I0843	I0843	Iberia	Spain	7,853	1,018,252	29.00
Chan	Chan.SG	Iberia	Spain	9,131	1,036,284	23.00

Table S4. Summary of 57 sweeps. Information includes (across successive columns) chromosomal location, sweep labels used throughout the manuscript, functional classification (possible for sweeps that contained only a single gene or where candidate genes were inferred using iSAFE), estimated sweep onset (based on age of oldest sample sweep was observed in and binned into broad spatiotemporal / archaeological categories), and list of all genes situated within the sweep boundaries.

Chr.	Start pos.	End pos.	Label	Functional category	Sweep time consensus	All Genes	
1	204,586,298	204,991,950	NFASC	iSAFE	Arabian_Standstill	LRRN2;NFASC	
2	84,650,647	85,134,132	DNAH6	iSAFE	Arabian_Standstill	SUCLG1;DNAH6;TRABD2A;TM5B10	
2	158,114,110	158,345,473	GALNT5	iSAFE	Arabian_Standstill	GALNT5;ERMN;CYTIP	
2	196,602,427	197,041,227	DNAH7	iSAFE	Aurignacian	DNAH7;STK17B	
2	237,476,430	238,751,451	MLPH	iSAFE	Arabian_Standstill	ACKR3;COPSS8;COL6A3;MLPH;PRHL;RAB17;LRRKIP1;RBM44	
3	50,400,233	52,188,706	DOCK3	iSAFE	Initial_Upper_Paleolithic	CACNA2D2;C3orf18;HEMK1;CISH;MAPKAPK3;MIR4787;DOCK3;MANF;RBM15B;RAD54L2;TEX264;GRM2;IQCF6;IQCF3;IQCF2;IQCF5;IQCF1;R9P9;PARP3;GP62;PCBP4;ABHD14B;ABHD14A;ACY1;RP129;DUSP7;POCA1	
3	128,628,709	129,612,419	TMCC1	iSAFE	Arabian_Standstill	KIAA1257;EFCC1;GP9;RAB43;ISY1-RAB43;ISY1;CNBP;COPG1;HMCE3;H1FX;SNORA7B;EFCAB12;MBD4;IFT122;RHO;H1FOO;PLXND1;TMCC1	
4	78,078,304	78,532,988	CCNG2	iSAFE	Arabian_Standstill	CCNG2;CXCL13	
5	109,624,934	110,100,857	TMEM232	iSAFE	Arabian_Standstill	TMEM232;MIRS48F3;SLC25A46	
5	144,851,362	145,891,524	PRELID2	iSAFE	Arabian_Standstill	PRELUD2;GRXCR2;SH3RF2;PLAC8L1;LARS;RBM27;POU4F3;TCERG1	
6	12,717,893	13,487,894	TBC1D7	iSAFE	Aurignacian	PHACTR1;TBC1D7;GFOD1	
6	34,433,916	35,464,853	PPARD	iSAFE	Eastern_or_Basal_Eurasian	PACSIN1;SPDEF;C6orf106;SNRPC;UHRF1BP1;TAF11;ANKS1A;TCP11;SCUBE3;ZNF76;DEF6;PPARD;FANCE;RPL10A;TEAD3	
7	36,893,961	37,488,852	ELMO1	iSAFE	Aurignacian	ELMO1;MIR1200	
8	67,341,263	68,255,912	ARFGEF1	iSAFE	Arabian_Standstill	RBS1;ADHFE1;MYBL1;VCPIP1;C8orf44;SGK3;C8orf44;SGK3;MCMDC2;SNHG6;TCF24;PPP1R42;COPSS5;CSPP1;ARFGEF1	
11	45,670,427	46,940,193	AMBRA1	iSAFE	Arabian_Standstill	CHST1;SLC35C1;CRY1;MAPK8IP1;C11orf94;PEX16;PHF21A;CREB3L1;DGKZ;MIR4688;MDK;CHR4;AMBRA1;MIR3160-1;MIR3160-2;HARBI1;ATG13;ARHGAP1;ZNF408;F2;CKAP5;MIR5582;SNORD67;LRP4	
12	27,485,787	27,848,497	SMCO2	iSAFE	Gravettian	ARNTL2;SMCO2;PPFBP1	
13	29,598,748	30,169,825	SLC7A1	iSAFE	Eastern_or_Basal_Eurasian	MTUS2;SLC7A1	
15	48,413,169	48,938,046	FBN1	iSAFE	Eastern_or_Basal_Eurasian	SLC24A5;MYEF2;CTXN2;SLC12A1;DUT;FBN1	
17	34,071,530	34,329,100	TAF15	iSAFE	Arabian_Standstill	GAS2L2;MMP28;C17orf50;TAF15;CCL5;RDM1;LYZL6;CCL16;CCL14;CCL15	
17	58,039,724	59,470,199	BCAS3	iSAFE	Arabian_Standstill	TBC1D3P1-DHX40P1;MIR4737;HEATR6;CA4;USP32;SCARNA20;C17orf64;APPBP2;PPM1D;BCAS3	
18	71,740,588	72,026,422	FBXO15	iSAFE	Magdalenian	FBXO15;TIMM21;CYB5A;C18orf63	
22	46,546,424	46,933,067	GTSE1	iSAFE	Arabian_Standstill	PPARA;CDPFI;PKDREJ;TTC38;GTSE1;TRMU;CELSR1	
1	170,904,612	171,255,117	FMO2	iSAFE.edge	Arabian_Standstill	MROH9;FM03;MIR1295A;FM02;FM01	
2	109,335,937	109,605,828	CCDC138	iSAFE.edge	Eastern_or_Basal_Eurasian	RANBP2;CCDC138;EDAR	
3	9,834,766	10,982,419	FANCD2	iSAFE.edge	Aurignacian	ARP4C- TTLL3;TTLL3;RPUSD3;CIDE;JAGN1;I17RE;I17RC;CRELD1;PRRT3;EMC3;FANCD2OS;BRK1;VHL;IRAK2;TATDN2;GHRL;SEC13;ATP2B2 ;MIR378B;MR885;LINC00606;SLC6A11	
5	74,364,100	75,013,313	COL4A3BP	iSAFE.edge	Arabian_Standstill	ANKRD31;HMGR;COL4A3BP;POLK;ANKDD18;POCS	
10	118,083,940	118,368,687	PNL1PRP3	iSAFE.edge	Arabian_Standstill	CCCD172;PNL1PRP3;PNUP;PNL1PRP1	
15	43,699,407	44,487,450	TP53BP1	iSAFE.edge	Arabian_Standstill	TP53BP1;MAP1A;PP1PSK1;CKMT1B;STRC;CATSPER2;CKMT1A;PDIA3;ELL3;SERF2;MIR1282;SERINC4;HYPK;MFAP1;WDR76;FRMD5	
7	24,612,887	24,733,812	MPP6	Single	Arabian_Standstill	MPP6	
10	122,938,214	122,945,480	LINC01153	Single	NA	LINC01153	
12	67,663,061	67,713,731	CAND1	Single	Arabian_Standstill	CAND1	
16	78,133,310	79,246,564	WWOX	Single	Initial_Upper_Paleolithic	WWOX	
20	53,092,136	53,267,710	DOK5	Single	Arabian_Standstill	DOK5	
1	35,449,523	36,538,101	ZMYM6	Initial_Upper_Paleolithic	ZMYM6;ZMYM1;SFQ;ZMYM4;KIAA0319L;NCDN;TFAP2E;PSMB2;C1orf216;CLSPN;AGO4;AGO1;AGO3		
3	15,422,782	15,687,329	METTL6	Initial_Upper_Paleolithic	METTL6;EAF1;COLQ;MIR4270;HACLI;BTD		
3	140,660,672	140,867,453	SLC25A36	Arabian_Standstill	SLC25A36;SPSB4		
4	71,494,461	72,437,804	ENAM	Aurignacian	ENAM;UTP3;RUFY3;GRSF1;MOB1B;DCK;SLC4A4		
6	27,775,257	28,502,729	HIST1H2BL	Arabian_Standstill	HIST1H2BL;HIST1H2A1;HIST1H3;HIST1H2A1;HIST1H2BM;HIST1H4J;HIST1H4K;HIST1H2AK;HIST1H2BN;HIST1H2AL;HIST1H1B;HIST1H3J;HIST1H4L;HIST1H3J;HIST1H2AM;HIST1H2BO;OR2B2;OR2B6;ZNF165;ZSCAN16;ZSCAN8;ZSCAN9;ZKSCAN4;NKAPL;PGBD1;ZSCAN31;ZKSCAN3;ZSCAN12;ZSCAN23;GPX6;GPX5		
6	29,523,406	32,806,557	GABBR1	Eastern_or_Basal_Eurasian	GABBR1;SNORD3B2;OR2H2;MOGZP57;HLA-F;HLA-G;HLA-A;HCGB9;ZNRD1;PP1R1R1;RNF39;TRIM31;TRIM40;TRIM10;TRIM15;TRIM26;HCG17;TRIM39;TRIM39-RPP21;RPP21;HLA-E;GNL1;PRR3;ABC1;MIR877;PP1R10;MIR518B;ATT1;60r1f136;DHX16;PP1R18;NRM;MDC1;TUBB;FLOT1;ER3;DDR1;MIR4640;GTF2H4;B;SFTA2;MUC22;MUC22;HG22;C6orf1;PSORS1C1;CDSN;PSORS1C2;CCHCR1;TCF19;POU5F1;HCG27;HLA-C;HLA-B;MICA;LINC01149;MICB;MCDC1;DDX39B;SNORD17;SNORD84;ATP6V1G2;NFKBIL1;LTA;TNF;LTB;LST1;NCR3;AIF1;PRC2A;SNORA38;BA6;APOM;C6orf47;GPNK1;SNK2A1;LYG5B;LYG5C;ABHD16A;MIR4646;LY6G6;LY6G6C;DAAH2;CLUC1;MSHS;SAPCD1;VWA7;VARS;LSM2;HSPA11A;HSPA1A;HSPA1B;C6orf48;SNORD5F;NEU1;S1C44A4;EHMT2;C2;ZBTB12;CBP;NEUFE;MIR1236;SKIV2L;DXO;STK19;C4A;C4B;CYP21A2;TNXB;ATF6B;FKBP1;PRR1;PT2;GFB1;CBP;NEUFE;MIR1236;GPR53;NOTCH4;C6orf10;BTNL2;HLA-DRA;HLA-DRB5;HLA-DRB1;HLA-DQA1;HLA-DQB1;HLA-DQA2;MIR315B;HLA-DQB2;HLA-DOB;TAP2		
6	105,404,923	105,627,870	LIN28B	Arabian_Standstill	LIN28B;BVE5;POPD3		
7	97,920,963	99,332,819	BAIAP2L1	Aurignacian	BAIAP2L1;NPTX2;TMEM130;TRRAP;MIR3609;SMURF1;KPNAA7;ARPC1A;ARPC1B;PDAP1;BUD31;PTCD1;CPsf4;ZNF789;ZNF394;ZKSCAN5;FA M200A;ZNF655;ZSCAN25;CYP3A5;CYP3A7		
7	142,552,792	142,836,839	EPHB6	Arabian_Standstill	EPHB6;TRPV6;TRPV5;KE1;OR942;OR6V1;PIP		
8	42,552,519	43,057,998	CHRN3	Arabian_Standstill	CHRN3;CHRNA6;THAP1;RNF170;MIR4469;HOOK3;FNTA;POMK;HGSNAT		
8	47,733,859	49,647,870	LINC00293	Initial_Upper_Paleolithic	LINC00293;PI1D;CEBDP;PRKDC;MCMD4;UBE2V2;EFCAB1		
9	101,493,611	101,992,897	ANKS6	Aurignacian	ANKS6;GALT12;COL15A1;TGFBR1;ALG2;SEC61B		
10	22,604,903	23,003,484	COMM3D	Arabian_Standstill	COMM3D;COMM3D-BM1;BM1;SPAG6;PIP4K2A		
10	32,735,068	33,294,720	CCDC7	Initial_Upper_Paleolithic	CCDC7;ITGB1		
10	74,653,339	75,682,535	OIT3	Aurignacian	OIT3;PLA2G12B;P4HA1;NUDT13;ECDFAM149B1;DNAJ9;MRPS16;ANXA7;MSS51;PPP3CB;USP54;MYOZ1;SYNPO2L;AGAP5;SEC24C;FUT11;CHCHD1;ZSWIM8;NDST2;CAMK2G;PLAU;C10orf55		
12	57,869,228	58,240,522	MARS	Aurignacian	MARS;DDIT3;MIR616;MDB6;DCTN2;KIF5A;PIP4K2C;DTX3;ARHGEF25;SLC26A10;B4GA1NT1;OS9;AGAP2;TSPAN31;CDK4;MARCH9;CY27B1;METTL1;TSF1;AVIL;CTDS2;MIR26A2		
12	109,886,461	113,910,085	KCTD10	Arabian_Standstill	KCTD10;UBE3B;MMAB;MVK;FAM222A;TRPV4;MIR4497;GLTP;TCHP;GIT2;ANKRD13A;C12orf76;ITF81;PTP2A;ANAPC7;ARPC3;GPN3;FAM16A;VP529;RA9DB7;PTC7;TCNT1;HVCN1;PPP1CC;CCDG3;MYL1;CUX2;SH2B3;ATXN2;BRAP;ACAD10;ALDH2;MAPKAPK5-AS1;MAPKAPK5-T;TMEM116;ERP29;NAA25;MIR3657;TRAFF1;HECTD4;RPL6;PTPN11;RPH3A;MIR1302-1;OAS1;OAS3;OAS2;DTX1;RASAL1;DDX54;RITA1;QCD7;TPCN1;SLCB81;PLBD2;SDS;DSL;LH5		
13	48,807,294	49,283,498	ITM2B	Arabian_Standstill	ITM2B;RB1;LPA6;RCBTB2;LINC00462;CYSLTR2		
15	42,450,899	43,513,481	VPS39	Arabian_Standstill	VPS39;MIR627;TMEM87A;GANC;CAPN3;ZNF106;SNAP23;LRRK2;HAUS2;STARD9;CDAN1;TTBK2;UBR1;EPB42;TMEM62;CCNDBP1		
16	820,183	1,968,441	MIR662	Eastern_or_Basal_Eurasian	A51;S5TRS;C1QTNF8;CACNA1H;PSG1;TPS2;TPSAB1;TPS1D1;UBE1;BAIAP3;TSR3;GNPTG;UNKL;C16orf91;CCDC154;CLCN7;PTX4;TEL02;IFT140;TMEM204;MAPK8IP3;MIR3177;NME3;MRPS34;EME2;SPSB3;NUBP2;IGFALS;HAGH;FAHD1;MEIOB;HS3T6		
16	66,461,200	67,963,581	BEAN1	Arabian_Standstill	BEAN1;TK2;CKLF;CKLF-CMTM1;CMTM1;CMTM2;CMTM3;CMTM4;DYN1LU;NAE1;CA7;PDP2;CDH16;RRA6;CES2;CES3;CE54A;CBFB;C16orf70;B3GNT9;TRADD;FBX18;HSF4;NOL3;KIAAO895LEXC0311;E2F4;ELMO3;MR328;LRRK2;TMEM208;FHOD1;SLC9A5;PLEKH4;KCTD19;LRRK3;C6;TPP3;ZDHHC1;HSD11B2;ATP6V0D1;AGR;CTCF;ACD;PARD6A;ENKD1;C16orf86;GFOD2;RANBP10;TSNAX1P1;CENP;THAP11;NUTF2;EDC4;NRN1;PSKH1		
16	72,042,487	72,210,777	DHODH	Initial_Upper_Paleolithic	DHODH;TXN4B;HP;PR;DHX38;PMFBP1		
17	53,796,988	53,920,191	TMEM100	Arabian_Standstill	TMEM100;PCTP		
20	21,686,297	22,566,093	PAX1	Initial_Upper_Paleolithic	PAX1;LINC00261;FOXA2		

Table S5. Summary of iSAFE analyses. For each sweep, genes with at least one of the top 20 ranked iSAFE SNPs (i.e. those with the highest 20 iSAFE scores) are indicated (maximum of five genes shown for each sweep). Genes are ranked according to the number of the top 20 iSAFE SNPs they carry. The proportion of top ranked iSAFE SNPs carried by each gene are shown on the left-hand columns. Gene names are listed in the right-hand columns, with the fraction of the top 20 iSAFE SNPs (numerator) relative to the total number of SNPs found in each gene (denominator) also shown in square parentheses.

Sweep Label	Proportion of top iSAFE SNPs					Gene ID and # SNPs				
	1st	2nd	3rd	4th	5th	1st	2nd	3rd	4th	5th
FBN1	1	0	0	0	0	FBN1 [20/83]	MYEF2 [0/3]	DUT [0/4]	SLC12A1 [0/40]	SLC24A5 [0/0]
BCAS3	1	0	0	0	0	BCAS3 [20/236]	PPM1D [0/1]	APPBP2 [0/2]	C17orf64 [0/4]	CA4 [0/7]
DNAH6	1	0	0	0		DNAH6 [20/123]	SUCLG1 [0/8]	TRABD2A [0/56]	TMSB10 [0/0]	
DOCK3	1	0	0	0	0	DOCK3 [20/289]	IQCF2 [0/1]	PCBP4 [0/1]	DUSP7 [0/1]	HEMK1 [0/2]
TMEM232	1	0	0			TMEM232 [20/180]	SLC25A46 [0/10]	MIR548F3 [0/0]		
PRELID2	1	0	0	0	0	PRELID2 [20/192]	GRXCR2 [0/2]	PLAC8L1 [0/9]	TCERG1 [0/38]	LARS [0/46]
CCNG2	1	0				CCNG2 [20/255]	CXCL13 [0/25]			
ELMO1	1	0				ELMO1 [20/343]	MIR1200 [0/0]			
FANCD2	0.95	0.55	0	0	0	FANCD2 [19/49]	FANCD2OS [11/16]	RPUSD3 [0/2]	PRRT3 [0/3]	JAGN1 [0/4]
TBC1D7	0.95	0.15	0			TBC1D7 [19/44]	PHACTR1 [3/278]	GFOD1 [0/72]		
MLPH	0.9	0	0	0	0	MLPH [18/56]	ACKR3 [0/3]	COPS8 [0/3]	RBM44 [0/17]	RAB17 [0/25]
DNAH7	0.9	0				DNAH7 [18/136]	STK17B [0/20]			
AMBRA1	0.7	0.15	0.1	0.05	0	AMBRA1 [14/61]	ATG13 [3/22]	HARBI1 [2/6]	DGKZ [1/13]	ZNF408 [0/2]
TAF15	0.65	0.1	0	0	0	TAF15 [13/24]	CCL5 [2/5]	GAS2L2 [0/3]	C17orf50 [0/3]	LYZL6 [0/3]
GALNT5	0.65	0	0			GALNT5 [13/32]	CYTIP [0/26]	ERMN [0/0]		
PPARD	0.65	0	0	0	0	PPARD [13/38]	RPL10A [0/1]	SPDEF [0/5]	TAF11 [0/5]	FANCE [0/5]
GTSE1	0.6	0.2	0.15	0	0	GTSE1 [12/22]	TRMU [4/10]	TTC38 [3/16]	CDPF1 [0/8]	PKDREJ [0/8]
SMCO2	0.6	0	0			SMCO2 [12/15]	ARNTL2 [0/47]	PPFIBP1 [0/109]		
FBXO15	0.6	0	0	0		FBXO15 [12/32]	TIMM21 [0/3]	CYB5A [0/22]	C18orf63 [0/33]	
CCDC138	0.55	0.3	0			CCDC138 [11/49]	RANBP2 [6/32]	EDAR [0/50]		
ARFGEF1	0.55	0.1	0.1	0.1	0.05	ARFGEF1 [11/41]	SGK3 [2/5]	CSPP1 [2/6]	C8orf44-SGK3 [2/7]	COPSS5 [1/2]
SLC7A1	0.55	0				SLC7A1 [11/43]	MTUS2 [0/326]			
COL4A3BP	0.5	0.4	0.05	0	0	COL4A3BP [10/51]	POLK [8/30]	ANKDD1B [1/24]	HMGCR [0/9]	POC5 [0/26]
TMCC1	0.5	0.1	0.05	0	0	TMCC1 [10/72]	IFT122 [2/38]	RHO [1/3]	RAB43 [0/1]	ISY1 [0/2]
NFASC	0.5	0				NFASC [10/98]	LRRN2 [0/35]			
VPS39	0.45	0.35	0.15	0.05	0	GANC [9/47]	TMEM87A [7/26]	CAPN3 [3/29]	ZNF106 [1/31]	CCNDBP1 [0/8]
KCTD10	0.45	0.3	0.15	0.1	0	HECTD4 [9/61]	NAA25 [6/21]	MAPKAPK5 [3/30]	TMEM116 [2/33]	VPS29 [0/2]
OIT3	0.4	0.25	0.15	0.1	0.05	ANXA7 [8/17]	USP54 [5/32]	DNAJC9 [3/27]	PPP3CB [2/8]	MRPS16 [1/3]
ZMYM6	0.4	0.2	0.1	0.05	0	KIAA0319L [8/15]	ZMYM4 [4/9]	PSMB2 [2/4]	NCDN [1/1]	ZMYM6 [0/1]
ITM2B	0.35	0.3	0.15	0	0	RB1 [7/16]	RCBTB2 [6/8]	LPAR6 [3/3]	CYSLTR2 [0/1]	ITM2B [0/8]
BAIAP2L1	0.35	0.3	0.15	0.15	0.1	PTCD1 [7/18]	ARPCA1A [6/29]	CPSF4 [3/7]	ARPC1B [3/11]	BUD31 [2/4]
PNLIPRP3	0.35	0	0	0		PNLIPRP3 [7/22]	PNLIP [0/3]	CCDC172 [0/6]	PNLIPRP1 [0/11]	
TP53BP1	0.35	0	0	0	0	TP53BP1 [7/58]	CKMT1B [0/5]	MAP1A [0/6]	SERF2 [0/9]	CATSPER2 [0/11]
FMO2	0.3	0	0	0	0	FMO2 [6/17]	FMO3 [0/19]	FMO1 [0/22]	MROH9 [0/79]	MIR1295A [0/0]
MARS	0.25	0.2	0.15	0.15	0.05	OS9 [5/14]	TSFM [4/11]	AGAP2 [3/5]	AVIL [3/7]	CDK4 [1/2]
HIST1H2BL	0.2	0.15	0.1	0.1	0.05	ZKSCAN8 [4/8]	ZSCAN31 [3/18]	ZSCAN9 [2/7]	PGBD1 [2/11]	ZNF165 [1/4]
MIR662	0.2	0.05	0.05	0	0	HAGH [4/40]	FAHD1 [1/18]	IFT140 [1/68]	GNG13 [0/1]	TPSAB1 [0/1]
GABBR1	0.2	0	0	0	0	RNF39 [4/10]	ZNRD1 [0/1]	TRIM15 [0/1]	HLA-E [0/1]	PRR3 [0/1]
BEAN1	0.1	0.1	0.05	0.05	0.05	ZDHHC1 [2/3]	CTCF [2/26]	PLEKHG4 [1/5]	HSD11B2 [1/5]	ATP6V0D1 [1/6]
EPHB6	0.05	0	0	0	0	OR6V1 [1/1]	EPHB6 [0/2]	KEL [0/5]	PIP [0/8]	TRPV6 [0/12]
COMM3D	0	0	0	0	0	COMM3D-BMI1 [0/1]	SPAG6 [0/10]	PIP4K2A [0/109]	COMM3D [0/0]	BMI1 [0/0]
DHODH	0	0	0	0	0	HP [0/6]	DHODH [0/10]	HPR [0/12]	DHX38 [0/13]	TXNL4B [0/37]
METTL6	0	0	0	0	0	EAF1 [0/6]	HAACL1 [0/15]	METTL6 [0/22]	BTD [0/22]	COLQ [0/42]
ENAM	0	0	0	0	0	GRSF1 [0/4]	RUFY3 [0/6]	DCK [0/7]	MOB1B [0/10]	ENAM [0/14]
LIN28B	0	0	0			POPDC3 [0/15]	BVES [0/23]	LIN28B [0/54]		
CHRNB3	0	0	0	0	0	THAP1 [0/1]	POMK [0/4]	RNF170 [0/7]	CHRNB3 [0/11]	FNTA [0/13]
LINC00293	0	0	0	0	0	CEBDP [0/2]	MCM4 [0/5]	EFCAB1 [0/13]	LINC00293 [0/14]	UBE2V2 [0/14]
ANKS6	0	0	0	0	0	ALG2 [0/1]	SEC61B [0/3]	GALNT12 [0/20]	TGFBR1 [0/20]	ANKS6 [0/27]
CCDC7	0	0				ITGB1 [0/51]	CCDC7 [0/91]			
TMEM100	0	0				TMEM100 [0/1]	PCTP [0/40]			
PAX1	0	0				FOXA2 [0/1]	LINC00261 [0/19]			
SLC25A36	0	0				SLC25A36 [0/23]	SPSB4 [0/43]			

Table S6A. Functional classifications of candidate genes identified within Eurasian hard sweeps.
Genes were assigned into a broad functional category and subclass (first two columns) via a systematic review of human disease literature, as well as animal and cell knockout phenotypic data sets, available on GnomAD, OMIM, PubMed and GeneCards databases. Additional information is provided in the footnotes located at base of table (see Supplemental Materials 3).

Functional class	Functional subclass	Selected gene [1]	Constraint [LOUEF] [2]	Description [3]	Molecular Function [4]	Human deletion phenotype [5]	Animal haploinsufficiency and/or homozygous deletion phenotype [6]	GWAS Association [7]	Key literature [8]
Neurological		AMBRA1	0.14	protein; intracellular; WD40 repeat protein	Autophagy	premature lethality; neuro-pathology; autism	Embryonic lethality; neuro-pathology; autism exencephaly; spina bifida	GWAS for autism	[PMID: 17589504]; [PMID: 24904333]; [PMID: 21743397]
Neurological		ARFGEF1	0.143	protein; intracellular; GEF for GTPase	Vesicle trafficking	Lennox-Gastaut Syndrome [developmental retardation]			[PMID: 31678406]; [PMID: 31678406]
Neurological		COL4A3BP	0.364	protein; intracellular; Good Pastures antigen binding protein	ceramide transport; basement membrane assembly	Embryonic lethality; developmental retardation			[PMID: 25533962]; [PMID: 25356899]; [PMID: 19139267]
Neurological		DOCK3	0.158	protein; intracellular; DOCK B family of GEF's	axonal outgrowth;	developmental retardation; Spontaneous limb weakness; ataxia	abnormal neuro architecture		[PMID: 28195381]; [PMID: 19129390]
Neurological		DOK5	0.834	protein; intracellular; Neurotrophin family protein	signal transduction; neuronal survival, development, function	ND **	ND		[PMID: 23954828]; [PMID: 11470823]
Neurological		MPP6	0.381	protein; intracellular; membrane associated; MAGUK family;	myelin formation	Spontaneous hyper-myelination peripheral nerves			[PMID: 30357511]
Neurological		NFASC	0.215	protein; cell surface; neurofascin; Ig-family adhesion molecule	organises axon initial segment; site of action potential initiation	premature lethality; motor function impairment and intellectual disability	Spontaneous severe ataxia, motor paresis, early lethality.		[PMID: 28940097]; [PMID: 30124836]; [PMID: 19185024]
Neurological		TAF15	0.398	protein; intracellular; TATA box protein associated factor; FET family RNA binding protein	Component of the transcription initiation factor TFIID complex; role in synaptic plasticity	motor neuron disease; amyotrophic lateral sclerosis; frontotemporal dementia	Spontaneous neuro-degeneration phenotype in drosophila		[PMID: 21438137]; [PMID: PMID: 30357887]; [PMID: 28889094]; [PMID: 22065782]
Neurological		TMEM232	1.078	protein; intracellular; TMEM trans-membrane family	Unknown function	GWAS association to synaptic transport and Alzheimers	ND	GWAS association to synaptic transport and Alzheimers	[PMID: 31640099]
Neurological		WWOX	1.532	protein; intracellular; enzyme; oxidoreductase	Transcription regulator; CNS development & function	premature lethality; neurodegeneration; spinocerebellar ataxia; epileptic encephalopathy	Early lethality; spontaneous neuro-degeneration and seizures		[PMID: 17470496]; [PMID: 24369382]; [PMID: 25411445]

Development		BCAS3	0.467	protein; intracellular	Cytoskeletal angiogenesis; involved in actin organisation	ND	Embryonic lethality; severe vascular pathology [avascular]		[PMID: 22300583]; [PMID: 29618843]
Development	Skp1-cullin-F-box (SCF) complex	CAND1	0.101	protein; intracellular; F-box exchange factor	Cell cycle; regulates SCF complex	ND	SCF molecular complex conserved across yeast, plants, insects and vertebrates		[PMID: 23528706]; [PMID: 10508527]
Development	Cilia formation	CCDC138	0.913	protein; intracellular; coiled coiled domain containing;	cilia basal body component	ND	ND		[PMID: 28596423]
Development	DNA damage response	CCNG2	0.756	protein; intracellular; cyclin G2 [atypical cyclin]	negative regulator cell cycle	ND	Exhibit sensitivity to disease triggers.		[PMID: 30420966]
Development	Cilia formation	DNAH6	0.573	protein; intracellular; axonemal; dynein motor component	Cilia function; force generator for cilia motility	primary ciliary dyskinesia	Deletion in zebrafish leads to body pattern malformations [dysregulated orientation of heart and gut looping].		[PMID: 8812413]; [PMID: 26918822]
Development	Cilia formation	DNAH7	0.837	protein; intracellular; axonemal protein; dynein motor component	Cilia function; force generator for cilia motility	primary ciliary dyskinesia	ND		[PMID: 11877439]; [PMID: 15937072]
Development	DNA damage response	FANCD2	0.886	protein; intracellular; cytoplasmic; Fanconi anemia complementation group	DNA damage [ATM response pathway]	premature lethality; developmental abnormalities	Early lethality; developmental abnormalities; and dysregulated control of cell death pathways		[PMID: 24237972]; [PMID: 20506303]; [PMID: 31078270]
Development		FBN1	0.049	protein; Pro-protein produces mature glycoprotein of the fibrillin family [fibrillin 1]; & asprosin [hormone]	Fibrillin glycoprotein: structural component of connective tissue; Asporin hormone: regulates glucose homeostasis	premature lethality; premature ageing; developmental abnormalities	Spontaneous lethality; with Marfan-like symptoms		[PMID: 1852208]; [PMID: 1569206]; [PMID: 9326947]; [PMID: 21152435]
Development	Skp1-cullin-F-box (SCF) complex	FBXO15	0.424	protein; intracellular; F Box domain containing; interacts with SCF complex [*relates to CAND1]	regulate SCF ubiquitin editing complex [cell cycle]	ND	No gross developmental defect		[PMID: 12665572]; [PMID: 16904174]
Development	DNA damage response	GTSE1	0.738	protein; intracellular;	Cell cycle; DNA replication; chromosome alignment	ND	ND		[PMID: 10974554]
Development	DNA damage response	TP53BP1	0.253	protein; intracellular; P53 binding protein	DNA damage response [main cellular check point for cell cycle and apoptosis]	developmental defects; cancer and immune sensitivities	Growth retardation; Extreme sensitivity [lethality] to irradiation; increased cancers; immune deficiencies [impaired B cell antibody responses]		[PMID: 12578828]; [PMID: 12640136]
Metabolism		FMO2	1.06	protein; intracellular; enzyme; flavin-containing monooxygenase	Enzyme involved in metabolism [detoxification] of drugs and xenobiotics.	ND	ND		[PMID: 1417778]; [PMID: 31873300]

Metabolism		GALNT5	0.981	protein; intracellular; membrane bound; enzyme; N-acetylgalactosaminyl transferase	Protein glycosylation of proteins [mucin-type O]; typically cell wall products or secreted proteins; may be significant in gut biology	ND	ND		[PMID: 20977886]
Metabolism	Skin physiology	MLPH	0.9	protein; intracellular; RAB binding effector protein [RAS superfamily]	interacts with RAS GTPase; tethers pigment organelles to actin cyto skel in melanocytes for transport; pigmentation	Griscelli syndrome [hypopigmentation]	Gene for 'dilute' phenotype in cats; "leaden" phenotype in mice. Alters coat colour.		[PMID: 12148598]; [PMID: 16860533]; [PMID: 11504925]
Metabolism		PNLIPRP3	1.185	protein; intracellular; homology with pancreatic lipase family	Lipases hydrolyze fats [mediate fat digestion]	ND	ND		ND
Metabolism	Adipocyte & FFA	PPARD	0.19	protein; intracellular; PPAR family; PPAR delta	Nuclear hormone receptor; mediates nutrient response and fat metabolism.	ND	Embryonic lethality; surviving mice ~10-15% smaller; reduced gonadal fat; metabolically less active and glucose intolerant [pre diabetes phenotype]		[PMID: 16492734]; [PMID: 12705865]; [PMID: 10866668]
Metabolism		SLC7A1	0.267	protein; cellular membrane receptor; SLC7 family; also called REC1;	Nutrient transporter for cationic amino acids [Arg, Lys, Orn] involved in urea pathway	ND	ND		[PMID: 1348489]
Metabolism	Adipocyte & FFA	SMCO2	1.516	protein; intracellular;	ND	ND	GWAS association with fat deposition and metabolism		[PMID: 30925743]
Metabolism		TBC1D7	1.608	protein; intracellular; regulatory component of the TSC-TBC complex	Energy sensing pathway responsive molecular complex; involved in cell signalling; regulates TSC1-TSC2 complex activation	macrocephaly/megalencephaly syndrome; enlarged cranium; dysmorphic face; intellectual disability; can have other body malformations; may be linked to cancer;intellectual disability	ND		[PMID: 23687350]
Metabolism	Adipocyte & FFA	TMCC1	0.386	protein; intracellular; ER associated	Tethers proteins to the ER; regulates fission events between endosomes and ER.	ND	ND	GWAS association for body fat disposition and adiposity.	[PMID: 30220460]; [PMID: 2434551]
Reproduction		ELMO1	0.333	protein; intracellular; cytoplasmic; kinase	Involved in cytoskeletal function for phagocytosis; specifically required for removal of apoptotic germ [sperm] cells	ND	Testicular pathology; decreased sperm output; fertilization defects, sperm entry to oocytes		[PMID: 20844538]; [PMID: 31575859]

Reproduction		PRELID2	1.497	protein; intracellular; PRELI domain containing family; may locate to mitochondria	ND	ND	ND	GWAS association for reproduction traits in animals; involved in embryo development	[PMID: 29411893]; [PMID: 32939704]; [PMID: 19847657]
Unknown		LINCO1153	ND	long non coding RNA	ND	ND	ND		

FOOTNOTES:

- 1 Single gene sweep; gene name from OMIM
- 2 Constraint definition based on LOUFE score whereby < 0.3 highly constrained (intolerant of deletion); 0.3-0.5 intermediate constraint; 0.5-1.0 moderate constraint; >1.0 no constraint [PMID: 32461654]
- 3 Sourced from OMIM & PubMed search
- 4 Sourced from PubMed search
- 5 Human haploinsufficiency data sourced from OMIM & PubMed search
- 6 Animal and or cell data sourced from OMIM & PubMed search
- 7 Sourced from GWAS Central and PubMed
- 8 Sourced from PubMed
- ND No data

Table S6B. Functional classifications of candidate genes identified within adaptively introgressed hominin loci. Genes were assigned into a broad functional category and subclass (first two columns) via a systematic review of human disease literature, as well as animal and cell knockout phenotypic data sets, available on GnomAD, OMIM, PubMed and GeneCards databases. The final three columns successively show the study source for each gene, population(s) where the AI variant was observed, and the reported hominin source. Additional information is provided in the footnotes located at base of table (see Supplemental Materials 3).

Functional class	Functional subclass	Selected gene [1]	Constraint [LOUUF] [2]	Description [3]	Molecular Function [4]	Human deletion phenotype [5]	Animal haploinsufficiency and/or homozygous deletion phenotype [6]	GWAS Association [7]	Key literature [8]	Publication	Population AI Observed	AI source
Neurological		CAPN11	1.151	protein; intracellular; cysteine protease; Calpain family [atypical]	Control protein function by limited proteolysis	ND**	ND	GWAS for neuropathic pain	[PMID:10559499]; [PMID:32432769]	Gittleman	EUR;SAS	Neandertal
Neurological		CDH10	0.419	protein; plasma membrane; Cadherin family;	neuronal circuit control [retinal]; cell adhesion; brain expressed	ND	ND		[PMID:30197236]; [PMID:16181616]	Gittleman	EUR;SAS	Neandertal
Neurological		CDH13	0.594	protein; plasma membrane; Cadherin family [atypical]	cell adhesion; brain expressed	ND	mKO hippocampal neuron signal defect; defects in learning and memory; rKO response to psychomotor (addiction) stimulants		[PMID:22765916]; [PMID:26460479]; [PMID:28387990]	Setter	EUR	Unknown
Neurological		CNTNS	0.485	protein; plasma membrane; Contactin family; immunoglobulin superfamily	neural adhesion molecule; iPS cells from ASD (autism spectrum) patients show dysregulated neuronal circuits and lack CNTNS	ND	ND		[PMID:30747104]	Gittleman	EAS	Neandertal
Neurological		GLB1	0.86	protein; intracellular; lysosome; enzyme; hydrolyse	cleaves b-galactosidase from substrates	GM1-gangliosidosis; nerve degeneration; neurodegeneration	Neuodegeneration in dogs		[PMID:1907800]; [PMID:1907800]; [PMID:3925555]; [PMID:3925555]	Gittleman	EAS	Neandertal
Neurological		GRM4	0.285	protein; plasma membrane; metabotropic G-coupled membrane R family;	binds L-glutamate (neurotransmitter)	ND	mKO viable; impaired learning of complex motor tasks; impaired synaptic plasticity	GWAS depression; epilepsy	[PMID:8738157]; [PMID:8815915]; [PMID:27792966]; [PMID:24840839]	Setter	EUR	Unknown
Neurological		GTF2IRD1	0.329	protein; intracellular; homology to helix-loop-helix transcription factor TFII-I	transcription factor	William-Beuren Syndrome; craniofacial and cognitive development	mKO craniofacial deformities		[PMID:16293761]; [PMID:16293761]; [PMID:9676970]; [PMID:11073954]	Setter	EUR	Unknown
Neurological		ITSN2	0.491	protein; intersectin family; intracellular; adapter protein	plays a role in protein-protein interactions to mediate endocytosis/synaptic vesicle re-cycling	ND	mKO viable; no major neuro phenotype but sensitises to defects in bimanual coordination (learning and memory); drosKO abnormal neuronal architecture; c elegans KO abnormal synaptic activity		[PMID:10922467]; [PMID:23447614]; [PMID:23447614]; [PMID:15260956]; [PMID:18298590]	Setter	EUR	Unknown
Neurological		KCNH5	0.442	protein; plasma membrane; K+ voltage gated channel	Maintain K+ gradient across membrane; decrease membrane potential; nervous system expressed	causal mutation in child with epilepsy	ND		[PMID:24133262]; [PMID:23647072]	Gower	MEL	Denisovan
Neurological		LYPD6B	1.126	protein; plasma membrane; Ly-6 protein family;	neuronal; mediates nicotinic ACh R signalling	severe intellectual disability with microduplication	ND		[PMID:26586467]; [PMID:22085900]	Gittleman	EAS;EUR;SAS	Neandertal
Neurological		RAB3C	1.174	protein; intracellular; RAS family; GTP binding protein;	regulates exocytosis in neurons; neuororansmitter release	ND	ND		[PMID:10488439]	Gower	EUR	Neandertal

Neurological		RPS6KA2	0.445	protein; intracellular; kinase; S6 ribosomal family	mediate MAPK signaling pathway	ND	ND	Mouse embryo expression data locates to developing neural tube, dorsal root ganglia and mature brain	[PMID:12393804]	Gittleman	EAS	Neandertal
Neurological		SESTD1	0.265	protein; intracellular; GTPase regulatory protein	role in neuronal synapse; component of planar cell polarity (PCP) pathway; PCP interacts with WNT	ND	neurodevelopmental and neuro functional defects; major embryo developmental defects		[PMID:29474518]; [PMID:23696638]	Gower	EUR	Neandertal
Neurological		SIPA1L2	0.287	protein; intracellular; Rap GTPase activating protein (apGAPs)	abundant in brain; regulates neurotransmitter release	ND	mKO impaired stimulus triggered presynaptic plasticity		[PMID:26364583]; [PMID:31784514]	Gittleman	EAS	Neandertal
Neurological		SLC6A1	0.15	protein; plasma membrane; solute carrier	GABA (neurotransmitter) transporter	Spontaneous seizures (epilepsy)	mKO spontaneous seizures with unconsciousness		[PMID:8412566]; [PMID:25865495]; [PMID:19966779]	Gittleman	EUR	Neandertal
Neurological		SMOX	0.467	protein; intracellular; enzyme	catalyzes polyamine catabolism (cell nutrient)	ND	mKO viable; develop spontaneous cerebellar damage and ataxia; Transgenic mice spontaneous epileptic seizures		[PMID:12141946]; [PMID:33054763]; [PMID:31197571]	Gittleman	EUR	Neandertal
Neurological		TMEM132D	0.232	protein; plasma membrane; Ig and cohesion domain containing protein	putative cellular adhesion[?]; oligodendrocyte expressed	ND	ND	GWAS panic disorder and anxiety	[PMID:12966072]; [PMID:22948381]; [PMID:20368705]; [PMID:29317594]	Gittleman	EAS	Neandertal
Neurological		WWOX	1.532	protein; intracellular; enzyme	oxidoreductase; regulates apoptosis & cell proliferation	autosomal recessive spinocerebellar ataxia-12; developmental and epileptic encephalopathy-28	mKO & rats; premature lethality; neurodegeneration; spontaneous seizures [sound induced]; hets spontaneous cancers		[PMID:17470496]; [PMID:24369382]; [PMID:25411445]; [PMID:32000863]	Gower	MEL	Denisovan
Neurological		ZNF385D	0.47	non coding RNA; intracellular	unknown	ND	ND	GWAS for reading disability an language impairment	[PMID:24024963]	Gittleman	SAS	Neandertal
Metabolism		ACO1	0.932	protein; intracellular; enzyme	iron response element; binds 3UTR and 5'-ferritin mRNA	ND	ND			Gittleman	SAS	Neandertal
Metabolism	Adipocyte & FFA	AGL	0.795	protein; intracellular; enzyme	glycogen degradation; cleaves glycogen branches	Glycogen storage disease; infantile hepatomegaly, myopathy x	ND		[PMID:28708136]; [PMID:8755644]	Gittleman	MEL	Ambiguous
Metabolism		ALLC	1.483	protein; intracellular; enzyme; allantoicase	allantoicase; uric acid metabolism; conserved to yeast; in mammals[vertebrates] enzyme inactive	ND	ND		[PMID:12036579]	Gittleman	MEL	Neanderthal
Metabolism		BNC2	0.34	protein; intracellular; evolutionary conserevd zinc finger protein	putative transcription factor	human pigmentation	pigment/skin colour role: mice; early lethality [cranio facial abnorm]		[PMID:19706529]	Gittleman/Gower	EUR	Neandertal
Metabolism		GALNT13	0.285	protein; plasma membrane; enzyme; galactosaminyltransferase family	catalyses glycosylation of protein substrates	ND	ND		[PMID:20977886]	Gittleman	EUR	Neandertal

Metabolism		JAKMIP3	0.399	protein; intracellular; golgin family	expressed in adipocytes; regulates signaling through lipid rafts [caveola]; regulates insulin AKT activation	ND	ND		[PMID:30160359]	Gittleman	EUR	Neandertal
Metabolism	Skin physiology	OCA2	0.856	protein; intracellular	melanocyte expressed; human "P" gene, organic molecule transporter	human eye colour variation	'pink eye' phenotype in mice		[PMID:7874125]; [PMID:17236130]; [PMID:1495987]	Gittleman	EAS;SAS	Neandertal
Metabolism	Adipocyte & FFA	PPARG*	0.635	protein; intracellular; PPAR nuclear receptor family protein	transcription factor; energy metabolism; activate gene transcriptional response to metabolic triggers	severe insulin resistance; diabetes; lipodystrophy	embryonic lethal		[PMID:10622252]; [PMID:12453919]; [PMID:10549290]	Jacobs	MEL	Denisovan
Metabolism	Adipocyte & FFA	SFRP4*	0.948	protein; secreted; frizzled related protein; sfrp family	soluble mediators of WNT signalling	impaired glucose sensing and homeostasis; role in adipose tissue mass	mKO weight gain on high fat diet; reduced energy expenditure; mTg decreased adipocyte size and metabolic programming		[PMID:23140642]; [PMID:25322919]; [PMID:26406932]; [PMID:32657640]	Gower	MEL	Denisovan
Metabolism		TSHR	1.259	protein; plasma membrane	thyroid receptor for TSH	hyperthyroidism	runted; hypothyroid; premature lethality		[PMID:9385128]; [PMID:14567913]	Setter	EUR	Unknown
Metabolism	Adipocyte & FFA	WDFY2*	0.994	protein; intracellular	energy sensing pathway; protein; intracellular; signal transduction; hormone responsive; interacts with INS R; binds AKT	ND	insulin resistance; increased gluconogenesis; promotes adipogenesis		[PMID:16792529]; [PMID:32641353]; [PMID:18388859]	Jacobs	MEL	Denisovan
Metabolism		ZBTB20	0.317	protein; intracellular; zinc finger protein; POK family	transcriptional repressor; DNA binding [zinc finger domain]	primrose syndrome [ossification of ears]	growth retardation and hypoglycemia, metabolic dysfunction		[PMID:21567911]; [PMID:19273596]	Gower	EUR	Neandertal
Development	Transcription	7SK	ND	non coding RNA; intracellular; small nuclear RNA	binds CDK9 and regulates transcription elongation [interacts with pol II]	ND	ND		[PMID:11713533]; [PMID:33046273]	Gittleman	EAS	Neandertal
Development		ABI3BP	0.558	protein; intracellular; adapter protein	binds NESH (ABI family); possible role in cytoskeletal arrangement and cell migration	ND	ND			Gittleman	SAS	Neandertal
Development		ATP1B1	0.153	protein; plasma membrane; Na/K ATPase pump	maintain ionic homeostasis; play a role in diverse biologies [hence broad disease impact]	Severe neurological disease; link to Wolfram Syndrome [diabetes]	ND	GWAS for hypertension	[PMID:32301109]; [PubMed: 17947299]; [PMID:17236131]	Gittleman	EUR	Neandertal

Development	Transcription	CBX6	0.262	protein; intracellular; Chromobox protein family	component of polycomb repressive complex (PRC1); binds methylated DNA, transcriptional regulator	ND	Highly expressed in ES cells; required for stem-cell'ness' (pluripotency)		[PMID:11242053]; [PMID:29089522]	Gittleman	SAS	Neandertal
Development		CDC73	0.188	protein; intracellular	cell cycle; component of PAF complex; regulates pol II subunit POLR2A; transcription control (elongation, initiation); cell cycle	Hyperthyroidism-jaw tumor syndrome (HPT-JT)	Spontaneous hyperthyroid jaw tumors		[PMID:15632063]; [PMID:12434154]; [PMID:28288139]	Gittleman	EUR	Neandertal
Development	DNA damage response	FAM46A	0.374	protein; intracellular; enzyme; nucleotidyltransferase family	catalyse transfer of nucleoside triphosphates; role in cell cycle	ND	mouse: fetal cardiomyocyte formation of heart; xenoKO embryonic abnormalities [eye formation; body colour]		[PMID:28667270]; [PMID:30291163]	Gower	MEL	Denisovan
Development	Transcription	FOXB2	1.516	protein; intracellular; forkhead box transcription factor family;	transcriptional regulator conserved to unicellular organisms; foxb2 unknown; general developmental role; possibly controls neuroendocrine cell differentiation	ND	ND		[PMID:2733165]; [PMID:31611391]	Setter	EUR	Unknown
Development		GJA3	1.488	protein; plasma membrane; connexin family;	gap junction protein; specific to ocular lens; maintains lens transparency	congenital cataracts	mKO viable, fertile, spontaneous cataracts		[PMID:15286166]; [PMID:10205266]; [PMID:9413992]	Gittleman	EUR	Neandertal
Development		KCNE4	1.362	protein; plasma membrane; type 1 membrane protein; voltage gated K+ channel; KCNE family	negative regulator of K channel function; wide tissue distribution	ND	mKO regulates ischemic injury response		[PMID:19029186]; [PMID:30758982]	Setter	EUR	Unknown
Development	DNA damage response	MACROD2	0.434	protein; intracellular; enzyme; deacetylase	regulates APC/C dependent chromosome stability, DNA repair/damage response	Kabuki Syn [congenital mental retardation; skeletal abnormalities; facial dysmorphisms]	mKO; controls PARP1 activity and DNA repair response		[PMID:29880585]; [PMID:17586838]; [PMID:29880585]	Gittleman	EUR	Neandertal
Development	Transcription	MBD2	0.522	protein; intracellular; nuclear protein family [methyl-CpG binding domain]	binds methylated DNA, demethylase transcriptional activator	ND	mKO viable, fertile, regulates intestinal tumorigenesis; mice lack maternal behaviour!!!		[PMID:12730693]; [PMID:11274056]	Gittleman	EAS;EUR	Neandertal
Development		NEBL	1.139	protein; intracellular; related to avian nebulette protein	skeletal muscle expressed; binds actin; component of 'z disc' [striated muscle]	DSG2 syndrome with cardiac and craniofacial abnormalities	mKO muscle defect [z line widening, increased cardiac stress markers]		[PMID:9733644]; [PMID:12504851]; [PMID:25987543]	Gittleman	EAS	Neandertal

Development		PRKCH	0.388	protein; cytoplasm; enzyme; PKC family [PKCeta]	phospho lipid metabolic/signalling; role in signalling cascades mediated by 1,2, DAG	ND	ND	GWAS cerebral infarction in asians	[PMID:17206144]	Gower	MEL	Denisovan
Metabolism	Skin physiology	RAB27A*	1.653	protein; intracellular; RAS family;	GTP binding protein; regulate exocytosis; vesicle transport	Griscelli Syndrome; impaired melanophilin interactions and transport	'dilute' 'leaden' 'ashen' colour phenotype in mice		[PMID:10488439]; [PMID:12531900]; [PMID:10859366]	Gower	MEL	Denisovan
Development		RBM19	0.73	protein; intracellular	predicted RNA binding protein; ribosome biogenesis	ND	zfko; absence gut; liver; exo panc		[PMID:12874115]	Gower	MEL	Denisovan
Development	Transcription	TFCP2L1	0.143	protein; intracellular	transcription factor; plays a role in embryo development	ND	Controls ES differentiation state(pluripotency)		[PMID:11073954]; [PMID:30241344]; [PMID:28843285]	Setter	EUR	Unknown
Development	DNA damage response	TLK1	0.165	protein; intracellular; enzyme; Tousled-like kinase family	DNA damage control (ATM path)	ND	mKO viable; deletion of TLK1 & 2 spontaneous genome instability (high freq DNA damage resulting in serious mutations)		[PMID:12660173]; [PMID:28708136]	Setter	EUR	Unknown
Development	Cilia formation	WDR88*	1.106	protein; intracellular	candidate cilia component; parologue interacts with dynein motor components	ND	ND			Gower/Gittleman	EUR	Neandertal
Reproduction		CSMD1	0.211	protein; extracellular	enriched expression in gonads; regulates C' [complement]	ND	mKO male show gonadal and fertility defects; females show reduced ovarian quality and breeding success	GWAS gonadal dysfunction [azoospermia]	[PMID:31604923]; [PMID:23555275]; [PMID:31604923]	Gower	MEL	Denisovan
Immunity		ALX1	0.607	protein; intracellular;	role in T cell activation [downstream of TCR and CD28]	ND	ND		[PMID:11700021]	Gower	EUR	Neandertal
Immunity	C1orf168 [FYB2]		1.699	protein; intracellular; adapter protein	component of signalling network associated to TCR; triggered by TCR	ND	ND		[PMID:27335501]	Gittleman	SAS	Neandertal
Immunity		SLC46A2	1.63	protein; plasma membrane; glycoprotein; solute carrier family	membrane transporter; thymus expressed [possible T cell function]; recognises bacterial toxins in drosophila	ND	drosKO impaired immune response to microbial pathogens		[PMID:10978518]; [PMID:28539433]	Setter	EUR	Unknown
Immunity		TNFAIP3	0.196	protein; intracellular; enzyme; Zinc finger protein; TNFAIP3 family	Ubiquitin editing enzyme; regulation of inflammatory signalling [NF- κ B]	highly penetrant inflammatory disease	mKO premature lethality; uncontrolled inflammation		[PMID:15258597]; [PMID:26642243]; [PMID:31534238]	Gower	MEL	Denisovan
Unknown		AK055368	ND	ND	ND	ND	ND			Gittleman	EUR	Neandertal
Unknown		CWF19L2	0.839	protein; cytoplasmic; unknown	ND	ND	ND			Gittleman	SAS	Neandertal
Unknown		KBTBD12	1.233	ND	ND	ND	ND			Setter	EUR	Unknown
Unknown		LIN00615	ND	ND	ND	ND	ND			Gittleman	EUR;SAS	Neandertal
Unknown		LINC00470	ND	ND	ND	ND	ND			Gittleman	EUR;SAS	Neandertal
Unknown		LOC286370	ND	ND	ND	ND	ND			Gittleman	SAS	Neandertal

Unknown		SNORD81	ND	non coding RNA; small nucleolar RNA C/D box family; snoRNA class	unknown; may mediate RNA processing, modifications	ND	ND			[PMID:22094949]	Gittleman	EUR	Neandertal
---------	--	---------	----	--	--	----	----	--	--	-----------------	-----------	-----	------------

FOOTNOTES:

- 1 Single gene sweep; gene name from OMIM
- 2 Constraint definition based on LOUEF score whereby < 0.3 highly constrained (intolerant of deletion); 0.3-0.5 intermediate constraint; 0.5-1.0 moderate constraint; >1.0 no constraint [PMID: 32461654]
- 3 Sourced from OMIM & PubMed search
- 4 Sourced from PubMed search
- 5 Human haploinsufficiency data sourced from OMIM & PubMed search
- 6 Animal and/or cell data sourced from OMIM & PubMed search
- 7 Sourced from GWAS Central and PubMed
- 8 Sourced from PubMed
- ND No data

Table S6C. Functional classifications of candidate genes identified within contemporary Arctic human populations. Genes were assigned into a broad functional category and subclass (first two columns) via a systematic review of human disease literature, as well as animal and cell knockout phenotypic data sets, available on GnomAD, OMIM, PubMed and GeneCards databases. The study source for each gene is shown in the final column. Additional information is provided in the footnotes located at base of table (see Supplemental Materials 3).

Functional class	Functional subclass	Selected gene [1]	Constraint [LOUEF] [2]	Publication
Neurological		CAMK2A	0.251	Cardona
Neurological		CNTN4	0.519	Cardona
Neurological		CNTNAP2	0.547	Cardona
Neurological		DISC1	0.789	Cardona
Neurological		DSCAM	0.189	Cardona
Neurological		GRM4	0.285	Cardona
Neurological		KCNH1	0.387	Reynolds
Neurological		KCNN3	0.319	Khrunin
Neurological		LIPT2	0.944	Cardona
Neurological		NBEA	0.074	Khrunin
Neurological		NKAIN2	0.768	Cardona
Neurological		NRG1	0.258	Cardona
Neurological		NRG3	0.462	Khrunin
Neurological		NRXN1	0.254	Cardona
Neurological		PLXNA4	0.229	Cardona
Neurological		PPFIA2	0.139	Cardona
Neurological		SDK1	0.398	Cardona
Neurological		TMPRSS3	1.119	Cardona
Neurological		TRPM2	1.112	Cardona
Neurological		WARS2	0.666	Fumagalli
Metabolism	Adipocyte & FFA	ANGPTL6	1.193	Fumagalli
Metabolism		CYP11B1	0.955	Fumagalli/Zhou
Metabolism	Adipocyte & FFA	FADS1	0.445	Fumagalli
Metabolism	Adipocyte & FFA	FADS2	0.232	Fumagalli
Metabolism	Adipocyte & FFA	FADS3	0.622	Fumagalli
Metabolism	Adipocyte & FFA	FN3K	1.363	Fumagalli
Metabolism		HS3ST4	0.494	Reynolds
Metabolism		LAMA2	0.732	Cardona
Metabolism		MYL2	1.751	Fumagalli
Metabolism	Skin physiology	OCA2	0.856	Reynolds
Metabolism		PCSK9	1.341	Khrunin
Metabolism	Skin physiology	SLC24A5	1.163	Zhou
Metabolism		SLC38A4	0.413	Cardona
Development	Skin physiology	SREBF2	0.382	Zhou
Development		ALK	0.448	Cardona
Development		CCDC63	1.294	Fumagalli
Development		CORIN	1.232	Cardona
Development		DNMT3L	1.297	Cardona
Development	Skin physiology	DSP	0.26	Fumagalli
Development	Skin physiology	EDAR	0.906	Zhou
Development		GML	1.47	Zhou
Development		GPC6	0.511	Cardona
Development		MEIS2	0.184	Cardona
Development		NSMCE1	1.178	Zhou
Development		PTPRM	0.233	Khrunin
Development	Cilia formation	SDCCAG8	0.784	Cardona
Development		TBX15	0.437	Fumagalli
Development		TCOF1	0.311	Cardona
Development		WNT5B	0.49	Khrunin
Immunity		AIM2	1.006	Zhou
Immunity		AIRE	1.115	Cardona
Immunity		CD74	0.564	Cardona
Immunity		ICOSLG [B7RP1]	0.919	Cardona
Immunity		ITGB8	0.264	Cardona
Immunity		MKL1	0.259	Cardona
Immunity		NCR1	1.454	Zhou
Immunity		STAT2	0.319	Zhou
Immunity		ZXDC	1.005	Zhou
Unknown		ARSI	1.414	Cardona
Unknown		ATP10D	0.787	Zhou
Unknown		C1orf227 [SPATA45]	1.543	Zhou
Unknown		C21orf2	1.396	Cardona

Unknown		CHERP	0.062	Fumagalli
Unknown		FOXN3	0.363	Cardona
Unknown		GALNTL1 [GALNT16]	0.588	Cardona
Unknown		LONP2	1.349	Cardona
Unknown		MX2	0.798	Cardona
Unknown		PCNP	0.502	Cardona
Unknown		PFKL	1.035	Cardona
Unknown		PGK2	1.608	Zhou
Unknown		PLD5	0.523	Cardona
Unknown		POLD3	0.236	Cardona
Unknown		PSCA	1.663	Zhou
Unknown		PSD3	0.445	Cardona
Unknown		SGSM3	0.902	Cardona/Fumagalli
Unknown		SLC35F3	0.535	Fumagalli
Unknown		SLC6A7	0.884	Cardona
Unknown		SNX21	1.447	Fumagalli
Unknown		SORCS2	0.428	Cardona
Unknown		TSPAN13	1.106	Cardona
Unknown		ZNF283	1.122	Zhou
Unknown		ZNF518B	0.577	Fumagalli

FOOTNOTES:

- 1 Single gene sweep; gene name from OMIM
 2 Constraint definition based on LOUEF score whereby < 0.3 highly constrained (intolerant of deletion);
 0.3-0.5 intermediate constraint; 0.5-1.0 moderate constraint; >1.0 no constraint [PMID: 32461654]

Table S6D. Summary of functional classifications of candidate genes across all datasets.

Counts (N) and proportion of genes per function (after removing genes with no known function) for each of the three candidate sources (first column).

Category	Function	N	Proportion [Unknown removed]
Artic	Development	16	27.6%
Artic	Metabolism	13	22.4%
Artic	Neurological	20	34.5%
Artic	Immunity	9	15.5%
Artic	Reproduction	0	0.0%
Artic	Not classified	27	NA
AI	Development	17	31.5%
AI	Metabolism	13	24.1%
AI	Neurological	19	35.2%
AI	Immunity	4	7.4%
AI	Reproduction	1	1.9%
AI	Not classified	7	NA
Ancient Eur.	Development	11	34.4%
Ancient Eur.	Metabolism	9	28.1%
Ancient Eur.	Neurological	10	31.3%
Ancient Eur.	Immunity	0	0.0%
Ancient Eur.	Reproduction	2	6.3%
Ancient Eur.	Not classified	1	NA

Table S7A. Protein-protein interaction (PPI) test results. Results from permutation tests evaluating if there were more interactions between putatively adaptive genes from three different sources: i.e. driver genes from the current study (Driver) and candidate genes from Arctic human groups (AAH) and hominin adaptively introgressed (HAI) loci. Genes were randomly replaced from one of the three groups (Test group column) and the number of PPIs compared to another group where the genes were not changed (Fixed group column). Observed and expected numbers of PPIs are shown, along with the percentage excess and associated empirical *p* values (based on 10,000 permutations). Results are shown for different quantiles based on minimum PPI scores (first two columns).

PPI quantile	Min. PPI score	Test group	Fixed group	# obs	# exp	% excess	<i>p</i>
25%	0.175	AI	AAH	229	144.22	58.8%	0.0002
25%	0.175	AI	AI	74	37.22	98.8%	0.0025
25%	0.175	AI	Driver	61	52.23	16.8%	0.1757
25%	0.175	AAH	AAH	213	79.37	168.4%	0.0001
25%	0.175	AAH	AI	229	127.43	79.7%	0.0001
25%	0.175	AAH	Driver	119	73.73	61.4%	0.0003
25%	0.175	Driver	AAH	119	80.72	47.4%	0.0178
25%	0.175	Driver	AI	61	52.96	15.2%	0.2116
25%	0.175	Driver	Driver	16	12.44	28.7%	0.2426
50%	0.216	AI	AAH	159	95.04	67.3%	0.0002
50%	0.216	AI	AI	46	24.85	85.1%	0.0104
50%	0.216	AI	Driver	44	35.32	24.6%	0.1209
50%	0.216	AAH	AAH	140	52.80	165.1%	0.0001
50%	0.216	AAH	AI	159	83.04	91.5%	0.0001
50%	0.216	AAH	Driver	74	48.71	51.9%	0.0037
50%	0.216	Driver	AAH	74	53.73	37.7%	0.0518
50%	0.216	Driver	AI	44	34.71	26.7%	0.1150
50%	0.216	Driver	Driver	14	8.51	64.5%	0.1027
75%	0.309	AI	AAH	83	46.10	80.0%	0.0011
75%	0.309	AI	AI	30	12.18	146.3%	0.0025
75%	0.309	AI	Driver	24	18.01	33.2%	0.1219
75%	0.309	AAH	AAH	78	26.42	195.2%	0.0001
75%	0.309	AAH	AI	83	41.49	100.1%	0.0001
75%	0.309	AAH	Driver	29	25.14	15.3%	0.2695
75%	0.309	Driver	AAH	29	25.27	14.8%	0.2900
75%	0.309	Driver	AI	24	18.63	28.9%	0.1373
75%	0.309	Driver	Driver	7	4.07	71.9%	0.1551

Table S7B. Protein-protein interaction (PPI) test results. PPI enrichment test results for the combined set of candidate genes and for candidate genes assigned to a predefined functional class. Results for three different PPI thresholds shown in separate columns. The original STRING categories are reproduced, whereby nodes denote genes and edges indicate an interaction between two proteins (PPI) encoded by genes in a functional class.

Candidate set	PPI category	Quantile		
		25%	50%	75%
All candidates	number of nodes	166	166	166
All candidates	number of edges	669	447	231
All candidates	average node degree	8.06	5.39	2.78
All candidates	avg. local clustering coefficient	0.309	0.332	0.4
All candidates	expected number of edges	339	248	124
All candidates	PPI enrichment p-value	< 1.0e-16	< 1.0e-16	< 1.0e-16
Neurological	number of nodes	47	47	47
Neurological	number of edges	168	124	70
Neurological	average node degree	7.15	5.28	2.98
Neurological	avg. local clustering coefficient	0.442	0.434	0.399
Neurological	expected number of edges	33	23	11
Neurological	PPI enrichment p-value	< 1.0e-16	< 1.0e-16	< 1.0e-16
Metabolism	number of nodes	34	34	34
Metabolism	number of edges	40	28	21
Metabolism	average node degree	2.35	1.65	1.24
Metabolism	avg. local clustering coefficient	0.516	0.413	0.472
Metabolism	expected number of edges	13	9	5
Metabolism	PPI enrichment p-value	6.47E-10	4.99E-07	5.65E-08
Development	number of nodes	43	43	43
Development	number of edges	48	33	12
Development	average node degree	2.23	1.53	0.558
Development	avg. local clustering coefficient	0.303	0.388	0.326
Development	expected number of edges	25	18	9
Development	PPI enrichment p-value	2.42E-05	1.41E-03	2.43E-01
Immune	number of nodes	13	13	13
Immune	number of edges	10	6	3
Immune	average node degree	1.54	0.923	0.462
Immune	avg. local clustering coefficient	0.395	0.321	0.308
Immune	expected number of edges	2	1	1
Immune	PPI enrichment p-value	2.61E-05	4.49E-03	5.13E-02
Cilia formation	number of nodes	9	9	9
Cilia formation	number of edges	7	5	4
Cilia formation	average node degree	1.56	1.11	0.889
Cilia formation	avg. local clustering coefficient	0.222	0.37	0.556
Cilia formation	expected number of edges	1	1	1
Cilia formation	PPI enrichment p-value	2.96E-04	3.66E-03	2.63E-03
Adipocyte + FFA	number of nodes	12	12	12
Adipocyte + FFA	number of edges	9	7	4
Adipocyte + FFA	average node degree	1.5	1.17	0.667
Adipocyte + FFA	avg. local clustering coefficient	0.319	0.306	0.417
Adipocyte + FFA	expected number of edges	2	1	1
Adipocyte + FFA	PPI enrichment p-value	7.99E-05	5.19E-04	7.22E-03
Skin physiology	number of nodes	7	7	7
Skin physiology	number of edges	9	7	7
Skin physiology	average node degree	2.57	2	2
Skin physiology	avg. local clustering coefficient	0.69	0.548	0.548

Skin physiology	expected number of edges	1	0	0
Skin physiology	PPI enrichment p-value	7.13E-09	2.25E-07	1.55E-09
DNA damage repair	number of nodes	7	7	7
DNA damage repair	number of edges	7	6	3
DNA damage repair	average node degree	2	1.71	0.857
DNA damage repair	avg. local clustering coefficient	0.357	0.238	0.571
DNA damage repair	expected number of edges	1	1	0
DNA damage repair	PPI enrichment p-value	2.78E-05	9.48E-05	1.23E-02
OutFlank canidates	number of nodes	516	516	516
OutFlank canidates	number of edges	6095	3906	1845
OutFlank canidates	average node degree	23.6	15.1	7.15
OutFlank canidates	avg. local clustering coefficient	0.201	0.186	0.232
OutFlank canidates	expected number of edges	3433	2475	1243
OutFlank canidates	PPI enrichment p-value	< 1.0e-16	< 1.0e-16	< 1.0e-16

Table S8. STRING Enrichment test results. Results are collated for combined candidate genes and for subsets of candidate genes in each predefined functional class. Results are provided in original STRING categories (see <https://string-db.org> for more details).

Candidate set	Category	Term ID	Term description	Observed gene count	Background gene count	Strength	FDR	matching proteins in your network (IDs)
All candidates	STRING clusters	CL:22534	Mixed, incl. protein-protein interactions at synapses, and neurotransmitter transport	12	167	0.93	0.00018	ENSP00000222644,ENSP00000282878,ENSP00000287766,ENSP00000344786,ENSP00000354778,ENSP00000381412,ENSP00000383295,ENSP00000385142,ENSP00000435637,ENSP00000440556,ENSP00000450337,ENSP00000463325
All candidates	STRING clusters	CL:22536	Mixed, incl. protein-protein interactions at synapses, and synaptic transmission, glutamatergic	8	118	0.9	0.0261	ENSP00000222644,ENSP00000282878,ENSP00000287766,ENSP00000381412,ENSP00000383295,ENSP00000385142,ENSP00000440556,ENSP00000450337
All candidates	UniProt Keywords	KW-0621	Polymorphism	125	11,669	0.1	0.012	ENSP00000207157,ENSP0000020929,ENSP00000217246,ENSP00000220940,ENSP00000222573,ENSP00000223551,ENSP00000241125,ENSP00000248929,ENSP00000252505,ENSP00000258443,ENSP0000259056,ENSP00000262215,ENSP00000263681,ENSP00000264463,ENSP00000264605,ENSP00000268613,ENSP00000269848,ENSP00000270172,ENSP00000273857,ENSP00000273859,ENSP00000278829,ENSP00000281523,ENSP0000028305,ENSP000002882251,ENSP00000287647,ENSP00000287766,ENSP00000287820,ENSP00000291532,ENSP00000291890,ENSP00000292427,ENSP00000294724,ENSP00000295124,ENSP00000298622,ENSP00000301258,ENSP00000303208,ENSP00000306920,ENSP00000309477,ENSP00000311273,ENSP00000312185,ENSP00000312399,ENSP00000315743,ENSP00000315768,ENSP00000317614,ENSP00000318298,ENSP00000321427,ENSP00000322229,ENSP00000324127,ENSP00000325527,ENSP00000329127,ENSP00000330605,ENSP00000335675,ENSP00000336729,ENSP00000339477,ENSP00000341550,ENSP00000343288,ENSP00000344786,ENSP00000345972,ENSP00000346659,ENSP00000347244,ENSP00000347847,ENSP00000348129,ENSP00000354476,ENSP00000354778,ENSP00000355077,ENSP00000355499,ENSP00000355589,ENSP00000355593,ENSP00000357112,ENSP00000358232,ENSP00000361214,ENSP0000036345,ENSP00000366246,ENSP00000366326,ENSP00000367028,ENSP00000369129,ENSP00000369862,ENSP00000370047,ENSP00000371475,ENSP00000372405,ENSP00000374359,ENSP00000375067,ENSP00000375907,ENSP00000376930,ENSP00000379601,ENSP00000380602,ENSP00000381023,ENSP00000381273,ENSP00000381412,ENSP000003818298,ENSP00000383293,ENSP00000384620,ENSP00000385142,ENSP00000385899,ENSP00000385957,ENSP00000389843,E,ENSP00000391514,ENSP00000397566,ENSP0000040365,ENSP00000408581,ENSP00000410715,ENSP00000411099,ENSP00000415332,ENSP00000415430,ENSP00000418593,ENSP00000419160,ENSP00000422185,ENSP00000427015,ENSP00000430733,ENSP00000435637,ENSP00000439856,ENSP00000441235,ENSP00000442053,ENSP00000442318,ENSP00000457230,ENSP00000463325,ENSP00000475727,ENSP00000478305,ENSP00000481570,ENSP00000481848
All candidates	UniProt Keywords	KW-0025	Alternative splicing	111	10,179	0.11	0.0272	ENSP00000009530,ENSP00000207157,ENSP00000217246,ENSP00000222573,ENSP00000223551,ENSP00000248929,ENSP00000252505,ENSP00000256429,ENSP00000258443,ENSP00000262593,ENSP00000263681,ENSP00000264605,ENSP00000265260,ENSP00000268613,ENSP00000269848,ENSP00000270172,ENSP00000271751,ENSP00000273857,ENSP00000273859,ENSP00000278840,ENSP00000282251,ENSP00000284322,ENSP00000285737,ENSP00000287647,ENSP00000288225,ENSP00000291532,ENSP00000291890,ENSP00000292427,ENSP00000294724,ENSP00000295124,ENSP00000298622,ENSP00000301258,ENSP00000303208,ENSP00000306920,ENSP00000321427,ENSP00000322229,ENSP00000329127,ENSP00000333395,ENSP00000333657,ENSP00000336729,ENSP00000339477,ENSP00000341550,ENSP00000343288,ENSP00000344786,ENSP00000345972,ENSP00000346659,ENSP00000347244,ENSP00000348129,ENSP00000352882,ENSP00000354476,ENSP00000354778,ENSP00000355499,ENSP00000355577,ENSP00000355588,ENSP00000357067,ENSP00000376930,ENSP00000379601,ENSP00000380602,ENSP00000381023,ENSP00000381273,ENSP00000381412,ENSP000003818298,ENSP00000383293,ENSP00000384620,ENSP00000385142,ENSP00000385899,ENSP00000385957,ENSP00000389843,E,ENSP00000391514,ENSP00000397566,ENSP0000040365,ENSP00000408581,ENSP00000410715,ENSP00000411099,ENSP00000415332,ENSP00000415430,ENSP00000418593,ENSP00000419160,ENSP00000422185,ENSP00000427015,ENSP00000430733,ENSP00000435637,ENSP00000439856,ENSP00000441235,ENSP00000442053,ENSP00000442318,ENSP00000457230,ENSP00000463325,ENSP00000475727,ENSP00000478305,ENSP00000481570,ENSP00000481848
All candidates	UniProt Keywords	KW-0160	Chromosomal rearrangement	11	307	0.63	0.0272	ENSP00000266037,ENSP00000347847,ENSP00000354778,ENSP00000355593,ENSP00000357402,ENSP00000371475,ENSP00000373700,ENSP00000375067,ENSP00000380602,ENSP00000384620,ENSP00000435637,ENSP00000474096
All candidates	UniProt Keywords	KW-0130	Cell adhesion	13	474	0.51	0.0388	ENSP00000222573,ENSP00000264463,ENSP00000268613,ENSP00000344786,ENSP00000354778,ENSP00000356790,ENSP00000380602,ENSP00000383303,ENSP00000385142,ENSP00000385899,ENSP0000040365,ENSP00000435637,ENSP00000463322
All candidates	UniProt Keywords	KW-0325	Glycoprotein	57	4,349	0.19	0.0388	ENSP00000009530,ENSP0000020940,ENSP00000222573,ENSP00000230671,ENSP00000253109,ENSP00000258443,ENSP00000259056,ENSP00000262067,ENSP00000264463,ENSP00000268613,ENSP00000269848,ENSP00000271751,ENSP00000273857,ENSP00000281830,ENSP00000284322,ENSP00000287766,ENSP00000291532,ENSP00000291890,ENSP00000301258,ENSP00000303208,ENSP00000306920,ENSP00000321427,ENSP00000322229,ENSP00000329127,ENSP00000333395,ENSP00000333657,ENSP00000336729,ENSP00000339477,ENSP00000341550,ENSP00000343288,ENSP00000344786,ENSP00000345972,ENSP00000346659,ENSP00000347244,ENSP00000348129,ENSP00000352882,ENSP00000354476,ENSP00000354778,ENSP00000355499,ENSP00000355577,ENSP00000355588,ENSP00000357067,ENSP00000376930,ENSP00000379601,ENSP00000380602,ENSP00000381023,ENSP00000381273,ENSP00000381412,ENSP000003818298,ENSP00000383293,ENSP00000384620,ENSP00000385142,ENSP00000385899,ENSP00000385957,ENSP00000389843,E,ENSP00000391514,ENSP00000397566,ENSP0000040365,ENSP00000408581,ENSP00000410715,ENSP00000411099,ENSP00000415332,ENSP00000415430,ENSP00000418593,ENSP00000419153,ENSP00000420453,ENSP00000430733,ENSP00000435637,ENSP00000439856,ENSP00000441235,ENSP00000442053,ENSP00000442318,ENSP00000457230,ENSP00000463325,ENSP00000475727,ENSP00000478305,ENSP00000481570,ENSP00000481848
All candidates	UniProt Keywords	KW-0336	GPL-anchor	7	138	0.78	0.0388	ENSP0000020940,ENSP00000268613,ENSP00000301258,ENSP0000030620,ENSP00000380707,ENSP00000435637
Neurological	GO Process	GO:0000902	Cell morphogenesis	11	726	0.8	0.0032	ENSP00000262593,ENSP00000264463,ENSP00000268613,ENSP00000344786,ENSP00000354778,ENSP00000369862,ENSP00000380602,ENSP00000383303,ENSP00000385142,ENSP00000385899,ENSP00000435637,ENSP00000474096
Neurological	GO Process	GO:0034329	Cell junction assembly	8	280	1.08	0.0032	ENSP00000264463,ENSP00000268613,ENSP00000344786,ENSP00000383303,ENSP00000384620,ENSP00000385142,ENSP00000385899,ENSP00000435637
Neurological	GO Process	GO:0034330	Cell junction organization	10	493	0.93	0.0032	ENSP00000264463,ENSP00000268613,ENSP00000287766,ENSP00000344786,ENSP00000383303,ENSP00000384620,ENSP00000385142,ENSP00000385899,ENSP00000435637,ENSP00000450337
Neurological	GO Process	GO:0050808	Synapse organization	8	283	1.07	0.0032	ENSP00000287766,ENSP00000344786,ENSP00000383303,ENSP00000384620,ENSP00000385142,ENSP00000385899,ENSP00000435637,ENSP00000450337
Neurological	GO Process	GO:0048699	Generation of neurons	15	1,551	0.6	0.0053	ENSP00000262215,ENSP00000262593,ENSP00000344786,ENSP00000354778,ENSP0000035593,ENSP00000361214,ENSP00000380602,ENSP00000383303,ENSP00000384620,ENSP00000385142,ENSP00000385899,ENSP00000403537
Neurological	GO Process	GO:0098742	Cell-cell adhesion via plasma-membrane adhesion molecules	7	257	1.05	0.0063	ENSP00000264463,ENSP00000268613,ENSP00000380602,ENSP00000383303,ENSP00000384620,ENSP00000385142,ENSP00000385899
Neurological	GO Process	GO:007416	Synapse assembly	5	96	1.34	0.0078	ENSP00000383303,ENSP00000384620,ENSP00000385142,ENSP00000385899,ENSP00000435637
Neurological	GO Process	GO:0006935	Chemotaxis	9	545	0.84	0.008	ENSP00000262593,ENSP00000344786,ENSP00000352882,ENSP00000361214,ENSP00000380602,ENSP00000383303,ENSP00000384620,ENSP00000385142,ENSP00000385899,ENSP00000435637,ENSP00000450337
Neurological	GO Process	GO:0007155	Cell adhesion	11	925	0.69	0.0115	ENSP00000264463,ENSP00000268613,ENSP00000344786,ENSP00000354778,ENSP00000380602,ENSP00000383303,ENSP00000384620,ENSP00000385142,ENSP00000385899,ENSP00000435637,ENSP00000450337
Neurological	GO Process	GO:0050804	Modulation of chemical synaptic transmission	8	446	0.87	0.0115	ENSP00000287766,ENSP00000355593,ENSP00000361214,ENSP00000380602,ENSP00000381412,ENSP00000385142,ENSP00000440556,ENSP00000450337
Neurological	GO Process	GO:0051960	Regulation of nervous system development	11	942	0.69	0.0115	ENSP00000347244,ENSP00000352882,ENSP00000355593,ENSP00000361214,ENSP00000380602,ENSP00000381412,ENSP00000383303,ENSP00000384620,ENSP00000385142,ENSP00000385899,ENSP00000403537

Neurological	GO Process	GO:0007399	Nervous system development	17	2,371	0.47	0.016	ENSP00000262215,ENSP00000262593,ENSP00000344786,ENSP00000347244,ENSP00000352882,ENSP00000354778,ENSP00000355593,ENSP00000361214,ENSP00000380602,ENSP00000381412,ENSP00000383303,ENSP00000384620,ENSP00000385142,ENSP00000385899,ENSP00000431926,ENSP00000435637,ENSP00000450337
Neurological	GO Process	GO:0009653	Anatomical structure morphogenesis	16	2,165	0.49	0.0177	ENSP00000235521,ENSP00000262593,ENSP00000264463,ENSP00000268613,ENSP00000271751,ENSP00000344786,ENSP00000352882,ENSP00000354778,ENSP00000355593,ENSP00000380602,ENSP00000381412,ENSP00000383303,ENSP00000384620,ENSP00000385142,ENSP00000385899,ENSP00000457230
Neurological	GO Process	GO:0030182	Neuron differentiation	11	1,019	0.65	0.0177	ENSP00000262215,ENSP00000262593,ENSP00000344786,ENSP00000352882,ENSP00000354778,ENSP00000355593,ENSP00000380602,ENSP00000381412,ENSP00000383303,ENSP00000384620,ENSP00000385142
Neurological	GO Process	GO:0048666	Neuron development	10	827	0.7	0.0177	ENSP00000262215,ENSP00000262593,ENSP00000344786,ENSP00000352882,ENSP00000354778,ENSP00000355593,ENSP00000380602,ENSP00000381412,ENSP00000383303,ENSP00000385142
Neurological	GO Process	GO:0050767	Regulation of neurogenesis	10	828	0.7	0.0177	ENSP00000347244,ENSP00000352882,ENSP00000355593,ENSP00000361214,ENSP00000380602,ENSP00000381412,ENSP00000383303,ENSP00000384620,ENSP00000385899,ENSP00000450337
Neurological	GO Process	GO:0098609	Cell-cell adhesion	8	505	0.82	0.0177	ENSP00000264463,ENSP00000268613,ENSP00000344786,ENSP00000380602,ENSP00000383303,ENSP00000384620,ENSP00000385142,ENSP00000385899
Neurological	GO Process	GO:0031175	Neuron projection development	9	680	0.74	0.0186	ENSP00000262215,ENSP00000262593,ENSP00000344786,ENSP00000352882,ENSP00000354778,ENSP00000380602,ENSP00000381412,ENSP00000383303,ENSP00000385142
Neurological	GO Process	GO:0021842	Chemorepulsion involved in interneuron migration from the subpallium to the cortex	2	2	2.62	0.0188	ENSP00000361214,ENSP00000384620
Neurological	GO Process	GO:0032990	Cell part morphogenesis	8	525	0.8	0.0188	ENSP00000262593,ENSP00000344786,ENSP00000352882,ENSP00000354778,ENSP00000369862,ENSP00000380602,ENSP00000383303,ENSP00000385142
Neurological	GO Process	GO:0099172	Presynapse organization	3	24	1.72	0.0188	ENSP00000385142,ENSP00000435637,ENSP00000450337
Neurological	GO Process	GO:0007156	Homophilic cell adhesion via plasma membrane adhesion molecules	5	164	1.1	0.0244	ENSP00000264463,ENSP00000268613,ENSP00000380602,ENSP00000383303,ENSP00000385899
Neurological	GO Process	GO:0007411	Axon guidance	6	275	0.96	0.0247	ENSP00000262593,ENSP00000344786,ENSP00000352882,ENSP00000380602,ENSP00000383303,ENSP00000385142
Neurological	GO Process	GO:0120036	Plasma membrane bounded cell projection organization	11	1,122	0.61	0.0248	ENSP00000262215,ENSP00000262593,ENSP00000268613,ENSP00000344786,ENSP00000352882,ENSP00000354778,ENSP00000355593,ENSP00000380602,ENSP00000381412,ENSP00000383303,ENSP00000385142
Neurological	GO Process	GO:0048869	Cellular developmental process	21	3,757	0.37	0.0256	ENSP00000235521,ENSP00000262215,ENSP00000262593,ENSP00000271751,ENSP00000344786,ENSP00000347244,ENSP00000352882,ENSP00000354778,ENSP00000355593,ENSP00000361214,ENSP00000369862,ENSP00000380602,ENSP00000385142,ENSP00000385899,ENSP00000431926,ENSP00000450337,ENSP00000457230
Neurological	GO Process	GO:0010665	Regulation of cardiac muscle cell apoptotic process	3	35	1.55	0.0388	ENSP00000381412,ENSP00000384620,ENSP00000431926
Neurological	GO Process	GO:0071205	Protein localization to juxtaparanode region of axon	2	5	2.22	0.0418	ENSP00000344786,ENSP00000354778
Neurological	GO Component	GO:0045202	Synapse	16	1,351	0.69	6.08E-05	ENSP00000264463,ENSP00000268613,ENSP00000271751,ENSP00000282878,ENSP00000287766,ENSP00000347244,ENSP00000355593,ENSP00000361214,ENSP00000381412,ENSP00000383303,ENSP00000384620,ENSP00000385142,ENSP00000385899,ENSP00000435637,ENSP00000440556,ENSP00000450337
Neurological	GO Component	GO:0098793	Presynapse	11	526	0.94	6.08E-05	ENSP00000264463,ENSP00000271751,ENSP00000282878,ENSP00000287766,ENSP00000347244,ENSP00000355593,ENSP00000384620,ENSP00000385142,ENSP00000435637,ENSP00000440556,ENSP00000450337
Neurological	GO Component	GO:0098889	Intrinsic component of presynaptic membrane	6	86	1.46	6.08E-05	ENSP00000264463,ENSP00000271751,ENSP00000287766,ENSP00000348620,ENSP00000385142,ENSP00000435637
Neurological	GO Component	GO:0098982	GABA-ergic synapse	6	74	1.53	6.08E-05	ENSP00000264463,ENSP00000268613,ENSP00000287766,ENSP00000348620,ENSP00000385142,ENSP00000435637
Neurological	GO Component	GO:0030054	Cell junction	18	2,075	0.56	0.00022	ENSP00000264463,ENSP00000268613,ENSP00000271751,ENSP00000282878,ENSP00000287766,ENSP00000344786,ENSP00000347244,ENSP00000354778,ENSP00000355593,ENSP00000361214,ENSP00000381412,ENSP00000383303,ENSP00000385142,ENSP00000440556,ENSP00000450337
Neurological	GO Component	GO:0099056	Integral component of presynaptic membrane	5	77	1.43	0.00043	ENSP00000264463,ENSP00000271751,ENSP00000287766,ENSP00000348620,ENSP00000385142
Neurological	GO Component	GO:0030424	Axon	10	646	0.81	0.00061	ENSP00000271751,ENSP00000287766,ENSP00000344786,ENSP00000354778,ENSP00000355593,ENSP00000380602,ENSP00000383303,ENSP00000384620,ENSP00000385142,ENSP00000450337
Neurological	GO Component	GO:0036477	Somatodendritic compartment	11	852	0.73	0.00078	ENSP00000271751,ENSP00000287766,ENSP00000291532,ENSP00000344786,ENSP00000354778,ENSP00000381023,ENSP00000383303,ENSP00000385142,ENSP00000450337,ENSP00000481848
Neurological	GO Component	GO:0044297	Cell body	9	588	0.8	0.0016	ENSP00000271751,ENSP00000287766,ENSP00000291532,ENSP00000345778,ENSP00000381023,ENSP00000383303,ENSP00000385142,ENSP00000481848
Neurological	GO Component	GO:0099059	Integral component of presynaptic active zone membrane	3	16	1.89	0.0017	ENSP00000264463,ENSP00000384620,ENSP00000385142

Neurological	GO Component	GO:0043005	Neuron projection	13	1,366	0.6	0.0019	ENSP00000268613,ENSP00000271751,ENSP00000287766,ENSP00000344786,ENSP00000354778,ENSP00000355593,ENSP00000380602,ENSP00000381412,ENSP00000383303,ENSP00000384620,ENSP00000385142,ENSP00000450337,ENSP00000481848
Neurological	GO Component	GO:0031226	Intrinsic component of plasma membrane	14	1,703	0.53	0.0036	ENSP00000264463,ENSP00000271751,ENSP00000287766,ENSP00000321427,ENSP00000344786,ENSP00000352882,ENSP00000354778,ENSP00000361214,ENSP00000381023,ENSP00000383303,ENSP00000385142,ENSP00000481848
Neurological	GO Component	GO:0043025	Neuronal cell body	8	518	0.81	0.0036	ENSP00000271751,ENSP00000287766,ENSP00000291532,ENSP00000354778,ENSP00000381023,ENSP00000383303,ENSP00000385142,ENSP00000481848
Neurological	GO Component	GO:0048786	Presynaptic active zone	4	78	1.33	0.0042	ENSP00000264463,ENSP00000384620,ENSP00000385142,ENSP00000450337
Neurological	GO Component	GO:0031225	Anchored component of membrane	5	169	1.09	0.0053	ENSP00000268613,ENSP00000282878,ENSP00000380602,ENSP00000387077,ENSP00000435637
Neurological	GO Component	GO:0005887	Integral component of plasma membrane	13	1,623	0.52	0.0069	ENSP00000264463,ENSP00000271751,ENSP00000287766,ENSP00000321427,ENSP00000344786,ENSP00000352882,ENSP00000354778,ENSP00000361214,ENSP00000381023,ENSP00000383303,ENSP00000384620,ENSP00000385142,ENSP00000440556
Neurological	GO Component	GO:0005886	Plasma membrane	25	5,314	0.29	0.0111	ENSP00000222644,ENSP00000235521,ENSP00000264463,ENSP00000268613,ENSP00000271751,ENSP00000282878,ENSP00000287766,ENSP00000321427,ENSP00000344786,ENSP00000347244,ENSP00000352882,ENSP00000354778,ENSP00000357402,ENSP00000435637,ENSP00000440556,ENSP00000481848
Neurological	GO Component	GO:0042995	Cell projection	15	2,287	0.44	0.0149	ENSP00000268613,ENSP00000271751,ENSP00000287766,ENSP00000344786,ENSP00000354778,ENSP00000355593,ENSP00000380602,ENSP00000381023,ENSP00000383303,ENSP00000384620,ENSP00000385142,ENSP00000385899,ENSP00000387077,ENSP00000435637,ENSP00000440556,ENSP00000481848
Neurological	GO Component	GO:0033010	Paranodal junction	2	8	2.02	0.017	ENSP00000344786,ENSP00000354778
Neurological	GO Component	GO:0031224	Intrinsic component of membrane	24	5,345	0.27	0.0294	ENSP00000264463,ENSP00000268613,ENSP00000271751,ENSP00000282878,ENSP00000287766,ENSP00000291532,ENSP00000321427,ENSP00000344786,ENSP00000352882,ENSP00000354778,ENSP00000357402,ENSP00000361214,ENSP00000380602,ENSP00000381023,ENSP00000383303,ENSP00000384620,ENSP00000385142,ENSP00000401477,ENSP000004040581,ENSP00000435637,ENSP00000440556,ENSP00000481848
Neurological	GO Component	GO:0120025	Plasma membrane bounded cell projection	14	2,193	0.42	0.0294	ENSP00000268613,ENSP00000271751,ENSP00000287766,ENSP00000344786,ENSP00000354778,ENSP00000355593,ENSP00000380602,ENSP00000381023,ENSP00000383303,ENSP00000384620,ENSP00000385142,ENSP00000431926,ENSP000004405337,ENSP00000481848
Neurological	GO Component	GO:0044304	Main axon	3	70	1.25	0.0418	ENSP00000271751,ENSP00000344786,ENSP00000354778
Neurological	GO Component	GO:0016020	Membrane	33	9,072	0.18	0.0467	ENSP00000222644,ENSP00000235521,ENSP00000262215,ENSP00000264463,ENSP00000268613,ENSP00000271751,ENSP00000287766,ENSP00000291532,ENSP00000321427,ENSP00000344786,ENSP00000347244,ENSP00000352882,ENSP00000354778,ENSP00000357402,ENSP00000361214,ENSP00000369862,ENSP00000380602,ENSP00000381023,ENSP00000383295,ENSP00000384620,ENSP00000385142,ENSP0000038899,ENSP00000387077,ENSP00000401477,ENSP000004040581,ENSP00000431926,ENSP00000440556,ENSP00000478305,ENSP00000481848
Neurological	GO Component	GO:0030673	Axolemma	2	16	1.72	0.0467	ENSP00000271751,ENSP00000354778
Neurological	GO Component	GO:0098794	Postsynapse	7	643	0.66	0.0467	ENSP00000264463,ENSP00000271751,ENSP00000287766,ENSP00000355593,ENSP00000381023,ENSP00000384620,ENSP00000450337
Neurological	STRING clusters	CL:22534	Mixed, incl. protein-protein interactions at synapses, and neurotransmitter transport	11	167	1.44	1.50E-09	ENSP00000222644,ENSP00000282878,ENSP00000287766,ENSP00000344786,ENSP00000354778,ENSP00000381023,ENSP00000383295,ENSP00000385142,ENSP00000435637,ENSP00000440556,ENSP00000450337
Neurological	STRING clusters	CL:22536	Mixed, incl. protein-protein interactions at synapses, and synaptic transmission, glutamatergic	8	118	1.45	1.34E-06	ENSP00000222644,ENSP00000282878,ENSP00000287766,ENSP00000381023,ENSP00000383295,ENSP00000385142,ENSP00000440556,ENSP00000450337
Neurological	STRING clusters	CL:22537	Mixed, incl. protein-protein interactions at synapses, and synaptic transmission, glutamatergic	7	111	1.42	1.40E-05	ENSP00000282878,ENSP00000287766,ENSP00000381023,ENSP00000383295,ENSP00000385142,ENSP00000440556,ENSP00000450337
Neurological	STRING clusters	CL:22801	Mixed, incl. protein localization to juxtaparanode region of axon, and familial temporal lobe epilepsy 1	3	15	1.92	0.0093	ENSP00000344786,ENSP00000354778,ENSP00000435637
Neurological	STRING clusters	CL:22538	Ionotropic glutamate receptor complex, and disruption of postsynaptic signaling by cnv	4	64	1.42	0.016	ENSP00000381023,ENSP00000383295,ENSP00000385142,ENSP00000440556
Neurological	Reactome	HSA-112316	Neuronal System	10	406	1.01	9.23E-05	ENSP00000271751,ENSP00000287766,ENSP00000321427,ENSP00000381023,ENSP00000383295,ENSP00000384620,ENSP00000385142,ENSP00000427015,ENSP00000450337,ENSP00000481848
Neurological	Reactome	HSA-112315	Transmission across Chemical Synapses	6	267	0.97	0.0497	ENSP00000287766,ENSP00000381023,ENSP00000383295,ENSP00000384620,ENSP00000427015,ENSP00000450337

Neurological	DISEASES	DOID:0060041	Autism spectrum disorder	4	34	1.69	0.0088	ENSP00000354778,ENSP00000380602,ENSP00000383303,ENSP00000385142	
Neurological	UniProt Keywords	KW-0130	Cell adhesion	9	474	0.9	0.0012	ENSP00000264463,ENSP00000268613,ENSP00000344786,ENSP00000354778,ENSP00000380602,ENSP00000383303,ENSP00000385142,ENSP00000385899,ENSP00000435637	
Neurological	UniProt Keywords	KW-0160	Chromosomal rearrangement	7	307	0.98	0.0031	ENSP00000266037,ENSP00000354778,ENSP00000355593,ENSP00000357402,ENSP00000380602,ENSP00000384620,ENSP00000474096	
Neurological	UniProt Keywords	KW-0770	Synapse	8	456	0.86	0.0031	ENSP00000271751,ENSP00000287766,ENSP00000355593,ENSP00000381412,ENSP00000383303,ENSP00000385142,ENSP00000385899,ENSP00000450337	
Neurological	UniProt Keywords	KW-0965	Cell junction	10	801	0.72	0.0031	ENSP00000271751,ENSP00000287766,ENSP00000344786,ENSP00000354778,ENSP00000355593,ENSP00000381412,ENSP00000383303,ENSP00000385142,ENSP00000385899,ENSP00000450337	
Neurological	UniProt Keywords	KW-0025	Alternative splicing	37	10,179	0.18	0.02	ENSP00000235521,ENSP00000262593,ENSP00000268613,ENSP00000271751,ENSP00000291532,ENSP00000306920,ENSP00000321427,ENSP00000344786,ENSP00000347244,ENSP00000352882,ENSP00000354778,ENSP00000355598,ENSP00000355593,ENSP00000357402,ENSP00000361214,ENSP00000369862,ENSP00000380602,ENSP00000381023,ENSP00000381412,ENSP00000383295,ENSP00000384620,ENSP00000385142,ENSP00000385899,ENSP00000418248	
Neurological	UniProt Keywords	KW-1003	Cell membrane	18	3,246	0.36	0.035	ENSP00000264463,ENSP00000268613,ENSP00000271751,ENSP00000287766,ENSP00000344786,ENSP00000352882,ENSP00000357402,ENSP00000361214,ENSP00000381023,ENSP00000383303,ENSP00000385142,ENSP00000385899,ENSP00000387077,ENSP00000435637,ENSP00000440556	
Neurological	UniProt Keywords	KW-0336	GPI-anchor	4	138	1.08	0.0356	ENSP00000268613,ENSP000003080602,ENSP00000387077,ENSP00000435637	
Neurological	UniProt Keywords	KW-0112	Calmodulin-binding	4	152	1.04	0.0445	ENSP00000271751,ENSP00000321427,ENSP00000381412,ENSP00000481848	
Neurological	UniProt Keywords	KW-0677	Repeat	22	4,729	0.29	0.0456	ENSP00000226264,ENSP00000264463,ENSP00000268613,ENSP00000281523,ENSP00000344786,ENSP00000347244,ENSP00000352882,ENSP00000354778,ENSP00000380602,ENSP00000381758,ENSP00000383295,ENSP00000383303,ENSP00000385142,ENSP00000385899,ENSP00000397566,ENSP00000415332,ENSP00000427015,ENSP00000431926,ENSP00000435637,ENSP00000450337,ENSP00000457230,ENSP00000474096	
Neurological	UniProt Keywords	KW-0393	Immunoglobulin domain	6	448	0.75	0.0484	ENSP00000344786,ENSP00000380602,ENSP00000383303,ENSP00000384620,ENSP00000385899,ENSP00000435637	
Neurological	Pfam	PF07679	Immunoglobulin I-set domain	6	202	1.09	0.0341	ENSP00000344786,ENSP00000380602,ENSP00000383303,ENSP00000384620,ENSP00000385899,ENSP00000435637	
Neurological	Pfam	PF00041	Fibronectin type III domain	5	136	1.18	0.0349	ENSP00000344786,ENSP00000380602,ENSP00000383303,ENSP00000385899,ENSP00000435637	
Neurological	Pfam	PF00047	Immunoglobulin domain	6	244	1.01	0.0349	ENSP00000344786,ENSP00000380602,ENSP00000383303,ENSP00000384620,ENSP00000385899,ENSP00000435637	
Neurological	Pfam	PF13895	Immunoglobulin domain	6	230	1.04	0.0349	ENSP00000344786,ENSP00000380602,ENSP00000383303,ENSP00000384620,ENSP00000385899,ENSP00000435637	
Neurological	Pfam	PF02158	Neuregulin family	2	3	2.44	0.0386	ENSP00000361214,ENSP00000384620	
Neurological	Pfam	PF13927	Immunoglobulin domain	6	279	0.95	0.0386	ENSP00000344786,ENSP00000380602,ENSP00000383303,ENSP00000384620,ENSP00000385899,ENSP00000435637	
Neurological	InterPro	IPR013098	Immunoglobulin I-set	6	133	1.27	0.0065	ENSP00000344786,ENSP00000380602,ENSP00000383303,ENSP00000384620,ENSP00000385899,ENSP00000435637	
Neurological	InterPro	IPR043204	Basigin-like	3	11	2.06	0.0156	ENSP00000344786,ENSP00000380602,ENSP00000383303	
Metabolism	STRING clusters	CL:9863	Mixed, incl. pigmentation, and borc complex	4	73	1.5	0.0424	ENSP00000264605,ENSP00000341550,ENSP00000346659,ENSP00000379601	
Metabolism	WikiPathways	WP4586	Metabolism of alpha-linolenic acid	2	6	2.28	0.0414	ENSP00000278840,ENSP00000322229	
Metabolism	WikiPathways	WP4853	Linoleic acid metabolism affected by coronavirus infection	2	5	2.36	0.0414	ENSP00000278840,ENSP00000322229	
Metabolism	DISEASES	DOID:0111375	Fetal akinesia deformation sequence syndrome	3	7	2.39	0.0025	ENSP00000278829,ENSP00000278840,ENSP00000322229	
Metabolism	DISEASES	DOID:4	Disease	23	5,921	0.35	0.0172	ENSP00000209929,ENSP00000228841,ENSP00000252505,ENSP00000253109,ENSP00000264605,ENSP00000278829,ENSP00000278840,ENSP00000287820,ENSP00000292427,ENSP00000294724,ENSP00000298125,ENSP00000303208,ENSP00000309477,ENSP00000322229,ENSP00000341550,ENSP00000346659,ENSP00000370047,ENSP00000370128,ENSP00000379601,ENSP00000400365,ENSP0000041015,ENSP00000419153,ENSP00000441235	
Metabolism	DISEASES	DOID:0050737	Autosomal recessive disease	11	1,422	0.65	0.0265	ENSP00000209929,ENSP00000253109,ENSP00000264605,ENSP00000278840,ENSP00000292427,ENSP0000030208,ENSP00000341550,ENSP00000346659,ENSP00000379601,ENSP00000400365,ENSP00000441235	
Metabolism	DISEASES	DOID:0050177	Monogenic disease	15	2,778	0.49	0.0269	ENSP00000209929,ENSP00000253109,ENSP00000264605,ENSP00000278829,ENSP00000278840,ENSP00000278840,ENSP00000287820,ENSP00000292427,ENSP0000030208,ENSP00000309477,ENSP00000322229,ENSP00000341550,ENSP00000346659,ENSP00000379601,ENSP00000400365,ENSP00000441235	
Metabolism	DISEASES	DOID:0060832	Griscelli syndrome type 1	2	3	2.58	0.0269	ENSP00000264605,ENSP00000379601	
Metabolism	DISEASES	DOID:0070100	Oculocutaneous albinism type vii	2	4	2.46	0.0317	ENSP00000341550,ENSP00000346659	
Metabolism	DISEASES	DOID:0050633	Ocular albinism	2	5	2.36	0.0333	ENSP00000341550,ENSP00000346659	
Metabolism	DISEASES	DOID:0050739	Autosomal genetic disease	13	2,323	0.51	0.0376	ENSP00000209929,ENSP00000253109,ENSP00000264605,ENSP00000278840,ENSP00000287820,ENSP0000030208,ENSP00000309477,ENSP00000341550,ENSP00000346659,ENSP00000379601,ENSP00000400365,ENSP00000441235	

Metabolism	DISEASES	DOID:0070097	Oculocutaneous albinism type iii	2	6	2.28	0.0376	ENSP00000341550,ENSP00000346659
Metabolism	DISEASES	DOID:0070098	Oculocutaneous albinism type iv	2	6	2.28	0.0376	ENSP00000341550,ENSP00000346659
Metabolism	DISEASES	DOID:7	Disease of anatomical entity	18	4,452	0.37	0.0426	ENSP00000228841,ENSP00000252505,ENSP00000253109,ENSP00000264605,ENSP00000278840,ENSP00000287820,ENSP00000292427,ENSP00000298125,ENSP00000303208,ENSP00000322229,ENSP00000341550,ENSP00000346659,ENSP00000370047,ENSP00000370128,ENSP00000379601,ENSP00000400365,ENSP00000410715,ENSP00000441235
Metabolism	Pfam	PF00487	Fatty acid desaturase	3	7	2.39	0.002	ENSP00000278829,ENSP00000278840,ENSP00000322229
Metabolism	Pfam	PF00173	Cytochrome b5-like Heme/Steroid binding domain	3	14	2.09	0.0055	ENSP00000278829,ENSP00000278840,ENSP00000322229
Metabolism	InterPro	IPR012171	Fatty acid desaturase	3	3	2.76	0.00064	ENSP00000278829,ENSP00000278840,ENSP00000322229
Metabolism	InterPro	IPR005804	Fatty acid desaturase domain	3	7	2.39	0.0019	ENSP00000278829,ENSP00000278840,ENSP00000322229
Metabolism	InterPro	IPR001199	Cytochrome b5-like heme/steroi d binding domain	3	14	2.09	0.0072	ENSP00000278829,ENSP00000278840,ENSP00000322229
Metabolism	InterPro	IPR036400	Cytochrome b5-like heme/steroi d binding domain superfamily	3	14	2.09	0.0072	ENSP00000278829,ENSP00000278840,ENSP00000322229
Metabolism	InterPro	IPR003074	Peroxisome proliferator-activated receptor	2	3	2.58	0.0394	ENSP00000287820,ENSP00000310928
Immune	GO Process	GO:0002682	Regulation of immune system process	8	1,514	0.9	0.0152	ENSP00000009530,ENSP00000291582,ENSP00000291890,ENSP00000339477,ENSP00000345972,ENSP00000357112,ENSP00000363345,ENSP00000481570
Immune	GO Process	GO:0002376	Immune system process	9	2,481	0.74	0.0243	ENSP00000009530,ENSP00000291582,ENSP00000291890,ENSP00000315768,ENSP00000339477,ENSP00000345972,ENSP00000357112,ENSP00000363345,ENSP00000481570
Immune	GO Process	GO:0070428	Regulation of nucleotide-binding oligomerization domain containing 1 signaling pathway	2	3	3	0.0243	ENSP00000363345,ENSP00000481570
Immune	GO Process	GO:0048518	Positive regulation of biological process	12	6,112	0.47	0.0259	ENSP00000009530,ENSP00000222573,ENSP00000291582,ENSP00000315417,ENSP00000315768,ENSP00000339477,ENSP00000345972,ENSP00000347847,ENSP00000357112,ENSP00000363345,ENSP00000374359,ENSP00000481570
Immune	GO Process	GO:0050776	Regulation of immune response	6	896	1	0.0314	ENSP00000009530,ENSP00000291890,ENSP00000339477,ENSP00000345972,ENSP00000357112,ENSP00000481570
Adipocyte + FFA	GO Process	GO:0006631	Fatty acid metabolic process	5	311	1.42	0.0098	ENSP00000278829,ENSP00000278840,ENSP00000287820,ENSP00000310928,ENSP00000322229
Adipocyte + FFA	GO Process	GO:0006636	Unsaturated fatty acid biosynthetic process	3	46	2.03	0.0205	ENSP00000278829,ENSP00000278840,ENSP00000322229
Adipocyte + FFA	GO Process	GO:0019752	Carboxylic acid metabolic process	6	853	1.06	0.0221	ENSP00000278829,ENSP00000278840,ENSP00000287820,ENSP00000300784,ENSP00000310928,ENSP00000322229
Adipocyte + FFA	GO Process	GO:0010887	Negative regulation of cholesterol storage	2	9	2.56	0.0283	ENSP00000287820,ENSP00000310928
Adipocyte + FFA	GO Process	GO:0045600	Positive regulation of fat cell differentiation	3	69	1.85	0.0283	ENSP00000287820,ENSP00000298125,ENSP00000310928
Adipocyte + FFA	GO Process	GO:0055114	Oxidation-reduction process	6	939	1.02	0.0283	ENSP00000278829,ENSP00000278840,ENSP00000287820,ENSP00000294724,ENSP00000310928,ENSP00000322229
Adipocyte + FFA	GO Process	GO:0032966	Negative regulation of collagen biosynthetic process	2	11	2.47	0.0344	ENSP00000287820,ENSP00000310928
Adipocyte + FFA	GO Process	GO:0036109	Alpha-linolenic acid metabolic process	2	13	2.4	0.0365	ENSP00000278840,ENSP00000322229
Adipocyte + FFA	GO Function	GO:0016213	linoleoyl-CoA desaturase activity	2	2	3.21	0.0067	ENSP00000278840,ENSP00000322229
Adipocyte + FFA	GO Function	GO:0036041	Long-chain fatty acid binding	2	15	2.34	0.0377	ENSP00000287820,ENSP00000310928

Adipocyte + FFA	STRING clusters	CL:14138	Mixed, incl. fatty acyl-coa biosynthesis, and srebp signaling pathway	3	46	2.03	0.0145	ENSP00000278840,ENSP00000310928,ENSP00000322229
Adipocyte + FFA	KEGG	hsa03320	PPAR signaling pathway	3	75	1.81	0.0044	ENSP00000278840,ENSP00000287820,ENSP00000310928
Adipocyte + FFA	KEGG	hsa01040	Biosynthesis of unsaturated fatty acids	2	26	2.1	0.0217	ENSP00000278840,ENSP00000322229
Adipocyte + FFA	Reactome	HSA-2046105	Linoleic acid (LA) metabolism	2	8	2.61	0.0336	ENSP00000278840,ENSP00000322229
Adipocyte + FFA	Reactome	HSA-2046106	Alpha-linolenic acid (ala) metabolism	2	13	2.4	0.0391	ENSP00000278840,ENSP00000322229
Adipocyte + FFA	WikiPathways	WP3942	PPAR signaling pathway	3	67	1.86	0.0049	ENSP00000278840,ENSP00000287820,ENSP00000310928
Adipocyte + FFA	WikiPathways	WP4586	Metabolism of alpha-linolenic acid	2	6	2.74	0.0049	ENSP00000278840,ENSP00000322229
Adipocyte + FFA	WikiPathways	WP4853	Linoleic acid metabolism affected by coronavirus infection	2	5	2.81	0.0049	ENSP00000278840,ENSP00000322229
Adipocyte + FFA	WikiPathways	WP4723	Omega-3 / omega-6 fatty acid synthesis	2	14	2.37	0.007	ENSP00000278840,ENSP00000322229
Adipocyte + FFA	WikiPathways	WP4724	Omega-9 fatty acid synthesis	2	14	2.37	0.007	ENSP00000278840,ENSP00000322229
Adipocyte + FFA	WikiPathways	WP236	Adipogenesis	3	130	1.58	0.0073	ENSP00000287820,ENSP00000310928,ENSP00000410715
Adipocyte + FFA	WikiPathways	WP299	Nuclear receptors in lipid metabolism and toxicity	2	33	1.99	0.0196	ENSP00000287820,ENSP00000310928
Adipocyte + FFA	WikiPathways	WP170	Nuclear receptors	2	38	1.93	0.0225	ENSP00000287820,ENSP00000310928
Adipocyte + FFA	WikiPathways	WP1541	Energy metabolism	2	47	1.84	0.0288	ENSP00000287820,ENSP00000310928
Adipocyte + FFA	WikiPathways	WP4718	Cholesterol metabolism with Bloch and Kandutsch-Russell pathways	2	46	1.85	0.0288	ENSP00000278840,ENSP00000322229
Adipocyte + FFA	DISEASES	DOID:0111375	Fetal akinesia deformation sequence syndrome	3	7	2.84	9.20E-05	ENSP00000278829,ENSP00000278840,ENSP00000322229
Adipocyte + FFA	UniProt Keywords	KW-0275	Fatty acid biosynthesis	3	50	1.99	0.0027	ENSP00000278829,ENSP00000278840,ENSP00000322229
Adipocyte + FFA	UniProt Keywords	KW-0249	Electron transport	3	106	1.66	0.012	ENSP00000278829,ENSP00000278840,ENSP00000322229
Adipocyte + FFA	Pfam	PF00487	Fatty acid desaturase	3	7	2.84	7.26E-05	ENSP00000278829,ENSP00000278840,ENSP00000322229
Adipocyte + FFA	Pfam	PF00173	Cytochrome b5-like Heme/Steroid binding domain	3	14	2.54	0.00021	ENSP00000278829,ENSP00000278840,ENSP00000322229
Adipocyte + FFA	InterPro	IPR012171	Fatty acid desaturase	3	3	3.21	2.38E-05	ENSP00000278829,ENSP00000278840,ENSP00000322229
Adipocyte + FFA	InterPro	IPR005804	Fatty acid desaturase domain	3	7	2.84	7.13E-05	ENSP00000278829,ENSP00000278840,ENSP00000322229
Adipocyte + FFA	InterPro	IPR001199	Cytochrome b5-like heme/steroid binding domain	3	14	2.54	0.00027	ENSP00000278829,ENSP00000278840,ENSP00000322229
Adipocyte + FFA	InterPro	IPR036400	Cytochrome b5-like heme/steroid binding domain superfamily	3	14	2.54	0.00027	ENSP00000278829,ENSP00000278840,ENSP00000322229

Adipocyte + FFA	InterPro	IPR003074	Peroxisome proliferator-activated receptor	2	3	3.04	0.0047	ENSP0000287820,ENSP0000310928
Adipocyte + FFA	SMART	SM01117	Cytochrome b5-like Heme/Steroid binding domain	2	9	2.56	0.0137	ENSP0000278840,ENSP0000322229
Cilia formation	GO Process	GO:0007017	Microtubule-based process	6	727	1.25	0.0012	ENSP0000261383,ENSP0000311273,ENSP0000355499,ENSP0000374045,ENSP0000374490,ENSP0000458355
Cilia formation	GO Process	GO:0007018	Microtubule-based movement	5	334	1.51	0.0012	ENSP0000261383,ENSP0000311273,ENSP0000374045,ENSP0000374490,ENSP0000458355
Cilia formation	GO Process	GO:0060285	Cilium-dependent cell motility	4	100	1.94	0.0012	ENSP0000261383,ENSP0000311273,ENSP0000374490,ENSP0000458355
Cilia formation	GO Process	GO:0006928	Movement of cell or subcellular component	6	1,501	0.94	0.0363	ENSP0000261383,ENSP0000311273,ENSP0000355499,ENSP0000374045,ENSP0000374490,ENSP0000458355
Cilia formation	GO Function	GO:0008569	ATP-dependent microtubule motor activity, minus-end-directed	5	15	2.86	2.63E-10	ENSP0000261383,ENSP0000311273,ENSP0000374045,ENSP0000374490,ENSP0000458355
Cilia formation	GO Function	GO:0045505	Dynein intermediate chain binding	5	30	2.56	2.36E-09	ENSP0000261383,ENSP0000311273,ENSP0000374045,ENSP0000374490,ENSP0000458355
Cilia formation	GO Function	GO:0051959	Dynein light intermediate chain binding	5	29	2.57	2.36E-09	ENSP0000261383,ENSP0000311273,ENSP0000374045,ENSP0000374490,ENSP0000458355
Cilia formation	GO Component	GO:0030286	Dynein complex	5	52	2.32	3.71E-08	ENSP0000261383,ENSP0000311273,ENSP0000374045,ENSP0000374490,ENSP0000458355
Cilia formation	GO Component	GO:0005858	Axonemal dynein complex	4	20	2.64	1.85E-07	ENSP0000261383,ENSP0000311273,ENSP0000374490,ENSP0000458355
Cilia formation	GO Component	GO:0005929	Cilium	6	637	1.31	4.03E-05	ENSP0000261383,ENSP0000311273,ENSP0000355499,ENSP0000374045,ENSP0000374490,ENSP0000458355
Cilia formation	GO Component	GO:0005874	Microtubule	5	407	1.43	0.00012	ENSP0000261383,ENSP0000311273,ENSP0000374045,ENSP0000374490,ENSP0000458355
Cilia formation	GO Component	GO:0036156	Inner dynein arm	2	4	3.04	0.00053	ENSP0000261383,ENSP0000311273
Cilia formation	GO Component	GO:0015630	Microtubule cytoskeleton	6	1,219	1.03	0.00065	ENSP0000261383,ENSP0000311273,ENSP0000355499,ENSP0000374045,ENSP0000374490,ENSP0000458355
Cilia formation	STRING clusters	CL:10812	Axonemal dynein complex	5	15	2.86	3.70E-10	ENSP0000261383,ENSP0000311273,ENSP0000374045,ENSP0000374490,ENSP0000458355
Cilia formation	STRING clusters	CL:10831	Dynein heavy chain 3, AAA+ lid domain, and LIS1, N-terminal	2	5	2.94	0.0026	ENSP0000261383,ENSP0000374045
Cilia formation	KEGG	hsa05016	Huntington disease	5	298	1.56	3.46E-05	ENSP0000261383,ENSP0000311273,ENSP0000374045,ENSP0000374490,ENSP0000458355
Cilia formation	KEGG	hsa05014	Amyotrophic lateral sclerosis	5	352	1.49	3.91E-05	ENSP0000261383,ENSP0000311273,ENSP0000374045,ENSP0000374490,ENSP0000458355
Cilia formation	TISSUES	BTO:0000913	Nasal polyp	3	11	2.77	4.65E-05	ENSP0000261383,ENSP0000311273,ENSP0000374045
Cilia formation	COMPARTMENTS	GOCC:0030286	Dynein complex	5	51	2.33	4.60E-08	ENSP0000261383,ENSP0000311273,ENSP0000374045,ENSP0000374490,ENSP0000458355
Cilia formation	COMPARTMENTS	GOCC:0005858	Axonemal dynein complex	4	24	2.56	4.85E-07	ENSP0000261383,ENSP0000311273,ENSP0000374490,ENSP0000458355
Cilia formation	COMPARTMENTS	GOCC:0005875	Microtubule associated complex	5	142	1.88	2.11E-06	ENSP0000261383,ENSP0000311273,ENSP0000374045,ENSP0000374490,ENSP0000458355
Cilia formation	COMPARTMENTS	GOCC:0005930	Axoneme	4	100	1.94	5.36E-05	ENSP0000261383,ENSP0000311273,ENSP0000374490,ENSP0000458355
Cilia formation	COMPARTMENTS	GOCC:0097014	Ciliary plasm	4	100	1.94	5.36E-05	ENSP0000261383,ENSP0000311273,ENSP0000374490,ENSP0000458355
Cilia formation	COMPARTMENTS	GOCC:0032838	Plasma membrane bounded cell projection cytoplasm	4	114	1.88	5.95E-05	ENSP0000261383,ENSP0000311273,ENSP0000374490,ENSP0000458355
Cilia formation	COMPARTMENTS	GOCC:0099568	Cytoplasmic region	4	154	1.75	0.00016	ENSP0000261383,ENSP0000311273,ENSP0000374490,ENSP0000458355
Cilia formation	COMPARTMENTS	GOCC:0015630	Microtubule cytoskeleton	6	924	1.15	0.00024	ENSP0000261383,ENSP0000311273,ENSP0000355499,ENSP0000374045,ENSP0000374490,ENSP0000458355
Cilia formation	COMPARTMENTS	GOCC:0005856	Cytoskeleton	6	1,526	0.93	0.004	ENSP0000261383,ENSP0000311273,ENSP0000355499,ENSP0000374045,ENSP0000374490,ENSP0000458355
Cilia formation	COMPARTMENTS	GOCC:0005929	Cilium	4	493	1.25	0.0108	ENSP0000261383,ENSP0000311273,ENSP0000374490,ENSP0000458355
Cilia formation	UniProt Keywords	KW-0243	Dynein	5	33	2.52	1.78E-09	ENSP0000261383,ENSP0000311273,ENSP0000374045,ENSP0000374490,ENSP0000458355

Cilia formation	UniProt Keywords	KW-0505	Motor protein	5	132	1.92	6.50E-07	ENSP00000261383,ENSP00000311273,ENSP00000374045,ENSP00000374490,ENSP00000458355
Cilia formation	UniProt Keywords	KW-0493	Microtubule	5	276	1.6	1.23E-05	ENSP00000261383,ENSP00000311273,ENSP00000374045,ENSP00000374490,ENSP00000458355
Cilia formation	UniProt Keywords	KW-0969	Cilium	5	262	1.62	1.23E-05	ENSP00000261383,ENSP00000311273,ENSP00000374045,ENSP00000374490,ENSP00000458355
Cilia formation	UniProt Keywords	KW-0966	Cell projection	6	1,009	1.11	0.00019	ENSP00000261383,ENSP00000311273,ENSP00000355499,ENSP00000374045,ENSP00000374490,ENSP00000458355
Cilia formation	UniProt Keywords	KW-0206	Cytoskeleton	6	1,215	1.03	0.00047	ENSP00000261383,ENSP00000311273,ENSP00000355499,ENSP00000374045,ENSP00000374490,ENSP00000458355
Cilia formation	UniProt Keywords	KW-0175	Coiled coil	7	2,139	0.85	0.00054	ENSP00000261383,ENSP00000295124,ENSP00000311273,ENSP00000355499,ENSP00000374045,ENSP00000374490,ENSP00000458355
Cilia formation	UniProt Keywords	KW-0067	ATP-binding	5	1,368	0.9	0.0141	ENSP00000261383,ENSP00000311273,ENSP00000374045,ENSP00000374490,ENSP00000458355
Cilia formation	Pfam	PF03028	Dynein heavy chain and region D6 of dynein motor	5	14	2.89	1.55E-10	ENSP00000261383,ENSP00000311273,ENSP00000374045,ENSP00000374490,ENSP00000458355
Cilia formation	Pfam	PF08393	Dynein heavy chain, N-terminal region 2	5	14	2.89	1.55E-10	ENSP00000261383,ENSP00000311273,ENSP00000374045,ENSP00000374490,ENSP00000458355
Cilia formation	Pfam	PF12774	Hydrolytic ATP binding site of dynein motor region D1	5	14	2.89	1.55E-10	ENSP00000261383,ENSP00000311273,ENSP00000374045,ENSP00000374490,ENSP00000458355
Cilia formation	Pfam	PF12775	P-loop containing dynein motor region D3	5	14	2.89	1.55E-10	ENSP00000261383,ENSP00000311273,ENSP00000374045,ENSP00000374490,ENSP00000458355
Cilia formation	Pfam	PF12777	Microtubule-binding stalk of dynein motor	5	14	2.89	1.55E-10	ENSP00000261383,ENSP00000311273,ENSP00000374045,ENSP00000374490,ENSP00000458355
Cilia formation	Pfam	PF12780	P-loop containing dynein motor region D4	5	13	2.92	1.55E-10	ENSP00000261383,ENSP00000311273,ENSP00000374045,ENSP00000374490,ENSP00000458355
Cilia formation	Pfam	PF12781	ATP-binding dynein motor region D5	5	13	2.92	1.55E-10	ENSP00000261383,ENSP00000311273,ENSP00000374045,ENSP00000374490,ENSP00000458355
Cilia formation	Pfam	PF07728	AAA domain (dynein-related subfamily)	4	34	2.41	6.51E-07	ENSP00000261383,ENSP00000374045,ENSP00000374490,ENSP00000458355
Cilia formation	Pfam	PF08385	Dynein heavy chain, N-terminal region 1	2	9	2.68	0.0039	ENSP00000374490,ENSP00000458355
Cilia formation	InterPro	IPR004273	Dynein heavy chain region D6 P-loop domain	5	15	2.86	2.20E-10	ENSP00000261383,ENSP00000311273,ENSP00000374045,ENSP00000374490,ENSP00000458355
Cilia formation	InterPro	IPR013602	Dynein heavy chain, domain-2	5	15	2.86	2.20E-10	ENSP00000261383,ENSP00000311273,ENSP00000374045,ENSP00000374490,ENSP00000458355
Cilia formation	InterPro	IPR024317	Dynein heavy chain, AAA module D4	5	15	2.86	2.20E-10	ENSP00000261383,ENSP00000311273,ENSP00000374045,ENSP00000374490,ENSP00000458355
Cilia formation	InterPro	IPR024743	Dynein heavy chain, coiled coil stalk	5	14	2.89	2.20E-10	ENSP00000261383,ENSP00000311273,ENSP00000374045,ENSP00000374490,ENSP00000458355
Cilia formation	InterPro	IPR035699	Dynein heavy chain, hydrolytic ATP-binding dynein motor region	5	15	2.86	2.20E-10	ENSP00000261383,ENSP00000311273,ENSP00000374045,ENSP00000374490,ENSP00000458355
Cilia formation	InterPro	IPR035706	Dynein heavy chain, ATP-binding dynein motor region	5	13	2.92	2.20E-10	ENSP00000261383,ENSP00000311273,ENSP00000374045,ENSP00000374490,ENSP00000458355
Cilia formation	InterPro	IPR041228	Dynein heavy chain, C-terminal domain	5	15	2.86	2.20E-10	ENSP00000261383,ENSP00000311273,ENSP00000374045,ENSP00000374490,ENSP00000458355
Cilia formation	InterPro	IPR041466	Dynein heavy chain, AAA 5 extension domain	5	14	2.89	2.20E-10	ENSP00000261383,ENSP00000311273,ENSP00000374045,ENSP00000374490,ENSP00000458355
Cilia formation	InterPro	IPR041589	Dynein heavy chain 3, AAA+ lid domain	5	12	2.96	2.20E-10	ENSP00000261383,ENSP00000311273,ENSP00000374045,ENSP00000374490,ENSP00000458355
Cilia formation	InterPro	IPR041658	Dynein heavy chain AAA lid domain	5	14	2.89	2.20E-10	ENSP00000261383,ENSP00000311273,ENSP00000374045,ENSP00000374490,ENSP00000458355
Cilia formation	InterPro	IPR042219	Dynein heavy chain AAA lid domain superfamily	5	14	2.89	2.20E-10	ENSP00000261383,ENSP00000311273,ENSP00000374045,ENSP00000374490,ENSP00000458355

Cilia formation	InterPro	IPR042222	Dynein heavy chain, domain 2, N-terminal	5	15	2.86	2.20E-10	ENSP00000261383,ENSP00000311273,ENSP00000374045,ENSP00000374490,ENSP00000458355
Cilia formation	InterPro	IPR042228	Dynein heavy chain, domain 2, C-terminal	5	15	2.86	2.20E-10	ENSP00000261383,ENSP00000311273,ENSP00000374045,ENSP00000374490,ENSP00000458355
Cilia formation	InterPro	IPR043157	Dynein heavy chain, AAA1 domain, small subdomain	5	14	2.89	2.20E-10	ENSP00000261383,ENSP00000311273,ENSP00000374045,ENSP00000374490,ENSP00000458355
Cilia formation	InterPro	IPR043160	Dynein heavy chain, C-terminal domain, barrel region	5	14	2.89	2.20E-10	ENSP00000261383,ENSP00000311273,ENSP00000374045,ENSP00000374490,ENSP00000458355
Cilia formation	InterPro	IPR003593	AAA+ ATPase domain	4	134	1.81	0.00012	ENSP00000261383,ENSP00000311273,ENSP00000374045,ENSP00000458355
Cilia formation	InterPro	IPR026983	Dynein heavy chain	2	7	2.79	0.0027	ENSP00000261383,ENSP00000374490
Cilia formation	InterPro	IPR013594	Dynein heavy chain, domain-1	2	9	2.68	0.0039	ENSP00000374490,ENSP00000458355
Cilia formation	InterPro	IPR027417	P-loop containing nucleoside triphosphate hydrolase	5	861	1.1	0.0065	ENSP00000261383,ENSP00000311273,ENSP00000374045,ENSP00000374490,ENSP00000458355
Cilia formation	SMART	SM00382	ATPases associated with a variety of cellular activities	4	120	1.86	0.00014	ENSP00000261383,ENSP00000311273,ENSP00000374045,ENSP00000458355
Skin physiology	GO Process	GO:0043473	Pigmentation	5	92	2.18	7.21E-07	ENSP00000258443,ENSP00000264605,ENSP00000341550,ENSP00000346659,ENSP00000379601
Skin physiology	GO Process	GO:0030318	Melanocyte differentiation	3	21	2.6	0.00036	ENSP00000341550,ENSP00000346659,ENSP00000379601
Skin physiology	GO Component	GO:0033162	Melanosome membrane	2	14	2.6	0.0093	ENSP00000346659,ENSP00000379601
Skin physiology	GO Component	GO:0042470	Melanosome	3	104	1.91	0.0093	ENSP00000341550,ENSP00000346659,ENSP00000379601
Skin physiology	GO Component	GO:0030659	Cytoplasmic vesicle membrane	4	770	1.16	0.0219	ENSP00000346659,ENSP00000354476,ENSP00000369129,ENSP00000379601
Skin physiology	STRING clusters	CL:9863	Mixed, incl. pigmentation, and borc complex	4	73	2.19	3.49E-05	ENSP00000264605,ENSP00000341550,ENSP00000346659,ENSP00000379601
Skin physiology	STRING clusters	CL:9978	Griscelli syndrome type 1, and Melanoregulin	2	5	3.05	0.0052	ENSP00000264605,ENSP00000379601
Skin physiology	STRING clusters	CL:9869	Melanin biosynthetic process, and protein melan-a	2	12	2.67	0.0113	ENSP00000341550,ENSP00000346659
Skin physiology	WikiPathways	WP2291	Deregulation of Rab and Rab effector genes in bladder cancer	2	16	2.54	0.0113	ENSP00000264605,ENSP00000379601
Skin physiology	DISEASES	DOID:16	Integumentary system disease	5	534	1.42	0.0014	ENSP00000258443,ENSP00000264605,ENSP00000341550,ENSP00000369129,ENSP00000379601
Skin physiology	DISEASES	DOID:0060832	Griscelli syndrome type 1	2	3	3.27	0.0024	ENSP00000264605,ENSP00000379601
Skin physiology	DISEASES	DOID:0070100	Oculocutaneous albinism type vii	2	4	3.15	0.0024	ENSP00000341550,ENSP00000346659
Skin physiology	DISEASES	DOID:0050633	Ocular albinism	2	5	3.05	0.0025	ENSP00000341550,ENSP00000346659
Skin physiology	DISEASES	DOID:0070097	Oculocutaneous albinism type iii	2	6	2.97	0.0027	ENSP00000341550,ENSP00000346659
Skin physiology	DISEASES	DOID:0070098	Oculocutaneous albinism type iv	2	6	2.97	0.0027	ENSP00000341550,ENSP00000346659
Skin physiology	DISEASES	DOID:0050739	Autosomal genetic disease	6	2,323	0.86	0.0086	ENSP00000258443,ENSP00000264605,ENSP00000341550,ENSP00000346659,ENSP00000369129,ENSP00000379601

Skin physiology	DISEASES	DOID:0050737	Autosomal recessive disease	5	1,422	0.99	0.0166	ENSP00000258443,ENSP00000264605,ENSP00000341550,ENSP00000346659,ENSP00000379601
Skin physiology	TISSUES	BTO:0000634	Integument	7	1,970	1	0.0002	ENSP00000258443,ENSP00000264605,ENSP00000341550,ENSP00000346659,ENSP00000354476,ENSP00000369129,ENSP00000379601
Skin physiology	TISSUES	BTO:0001253	Skin	6	1,069	1.2	0.0002	ENSP00000258443,ENSP00000264605,ENSP00000346659,ENSP00000379601
Skin physiology	COMPARTMENTS	GOCC:0042470	Melanosome	3	43	2.29	0.0098	ENSP00000341550,ENSP00000346659,ENSP00000379601
Skin physiology	COMPARTMENTS	GOCC:0048770	Pigment granule	3	47	2.25	0.0098	ENSP00000341550,ENSP00000346659,ENSP00000379601
Skin physiology	COMPARTMENTS	GOCC:0033162	Melanosome membrane	2	14	2.6	0.0101	ENSP00000346659,ENSP00000379601
Skin physiology	COMPARTMENTS	GOCC:0045009	Chitosome	2	14	2.6	0.0101	ENSP00000346659,ENSP00000379601
Skin physiology	COMPARTMENTS	GOCC:0090741	Pigment granule membrane	2	14	2.6	0.0101	ENSP00000346659,ENSP00000379601
Skin physiology	COMPARTMENTS	GOCC:0098588	Bounding membrane of organelle	5	1,416	0.99	0.0143	ENSP00000341550,ENSP00000346659,ENSP00000354476,ENSP00000369129,ENSP00000379601
Skin physiology	UniProt Keywords	KW-0015	Albinism	2	19	2.47	0.0155	ENSP00000341550,ENSP00000346659
Skin physiology	GO Process	GO:0006631	Fatty acid metabolic process	5	311	1.46	0.0058	ENSP00000278829,ENSP00000278840,ENSP00000287820,ENSP00000310928,ENSP00000322229
Skin physiology	GO Process	GO:0006636	Unsaturated fatty acid biosynthetic process	3	46	2.06	0.0154	ENSP00000278829,ENSP00000278840,ENSP00000322229
Skin physiology	GO Process	GO:0019752	Carboxylic acid metabolic process	6	853	1.1	0.0154	ENSP00000278829,ENSP00000278840,ENSP00000287820,ENSP00000300784,ENSP00000310928,ENSP00000322229
Skin physiology	GO Process	GO:0045600	Positive regulation of fat cell differentiation	3	69	1.89	0.0154	ENSP00000287820,ENSP00000298125,ENSP00000310928
Skin physiology	GO Process	GO:0055114	Oxidation-reduction process	6	939	1.06	0.0154	ENSP00000278829,ENSP00000278840,ENSP00000287820,ENSP00000294724,ENSP00000310928,ENSP00000322229
Skin physiology	GO Process	GO:0010887	Negative regulation of cholesterol storage	2	9	2.6	0.0225	ENSP00000287820,ENSP00000310928
Skin physiology	GO Process	GO:0032966	Negative regulation of collagen biosynthetic process	2	11	2.51	0.0287	ENSP00000287820,ENSP00000310928
Skin physiology	GO Process	GO:0036109	Alpha-linolenic acid metabolic process	2	13	2.44	0.0297	ENSP00000278840,ENSP00000322229
Skin physiology	GO Process	GO:0033189	Response to vitamin a	2	19	2.27	0.0453	ENSP00000287820,ENSP00000310928
Skin physiology	GO Process	GO:0043651	Linoleic acid metabolic process	2	20	2.25	0.047	ENSP00000278840,ENSP00000322229
Skin physiology	GO Function	GO:0016213	linoleoyl-CoA desaturase activity	2	2	3.25	0.0056	ENSP00000278840,ENSP00000322229
Skin physiology	GO Function	GO:0036041	Long-chain fatty acid binding	2	15	2.38	0.0314	ENSP00000287820,ENSP00000310928
Skin physiology	STRING clusters	CL:14138	Mixed, incl. fatty acyl-coa biosynthesis, and srebp signaling pathway	3	46	2.06	0.0109	ENSP00000278840,ENSP00000310928,ENSP00000322229
Skin physiology	KEGG	hsa03320	PPAR signaling pathway	3	75	1.85	0.0033	ENSP00000278840,ENSP00000287820,ENSP00000310928
Skin physiology	KEGG	hsa01040	Biosynthesis of unsaturated fatty acids	2	26	2.14	0.0181	ENSP00000278840,ENSP00000322229
Skin physiology	KEGG	hsa01212	Fatty acid metabolism	2	54	1.82	0.0487	ENSP00000278840,ENSP00000322229
Skin physiology	Reactome	HSA-2046105	Linoleic acid (LA) metabolism	2	8	2.65	0.028	ENSP00000278840,ENSP00000322229
Skin physiology	Reactome	HSA-2046106	Alpha-linolenic acid (ala) metabolism	2	13	2.44	0.0326	ENSP00000278840,ENSP00000322229
Skin physiology	WikiPathways	WP3942	PPAR signaling pathway	3	67	1.9	0.0041	ENSP00000278840,ENSP00000287820,ENSP00000310928
Skin physiology	WikiPathways	WP4586	Metabolism of alpha-linolenic acid	2	6	2.77	0.0041	ENSP00000278840,ENSP00000322229

Skin physiology	WikiPathways	WP4853	Linoleic acid metabolism affected by coronavirus infection	2	5	2.85	0.0041	ENSP00000278840,ENSP00000322229
Skin physiology	WikiPathways	WP236	Adipogenesis	3	130	1.61	0.0058	ENSP00000287820,ENSP00000310928,ENSP00000410715
Skin physiology	WikiPathways	WP4723	Omega-3 / omega-6 fatty acid synthesis	2	14	2.41	0.0058	ENSP00000278840,ENSP00000322229
Skin physiology	WikiPathways	WP4724	Omega-9 fatty acid synthesis	2	14	2.41	0.0058	ENSP00000278840,ENSP00000322229
Skin physiology	WikiPathways	WP299	Nuclear receptors in lipid metabolism and toxicity	2	33	2.03	0.0164	ENSP00000287820,ENSP00000310928
Skin physiology	WikiPathways	WP170	Nuclear receptors	2	38	1.97	0.0188	ENSP00000287820,ENSP00000310928
Skin physiology	WikiPathways	WP1541	Energy metabolism	2	47	1.88	0.024	ENSP00000287820,ENSP00000310928
Skin physiology	WikiPathways	WP4718	Cholesterol metabolism with Bloch and Kandutsch-Russell pathways	2	46	1.89	0.024	ENSP00000278840,ENSP00000322229
Skin physiology	DISEASES	DOID:0111375	Fetal akinesia deformation sequence syndrome	3	7	2.88	6.90E-05	ENSP00000278829,ENSP00000278840,ENSP00000322229
Skin physiology	UniProt Keywords	KW-0275	Fatty acid biosynthesis	3	50	2.03	0.0021	ENSP00000278829,ENSP00000278840,ENSP00000322229
Skin physiology	UniProt Keywords	KW-0249	Electron transport	3	106	1.7	0.0091	ENSP00000278829,ENSP00000278840,ENSP00000322229
Skin physiology	Pfam	PF00487	Fatty acid desaturase	3	7	2.88	5.45E-05	ENSP00000278829,ENSP00000278840,ENSP00000322229
Skin physiology	Pfam	PF00173	Cytochrome b5-like Heme/Steroid binding domain	3	14	2.58	0.00015	ENSP00000278829,ENSP00000278840,ENSP00000322229
Skin physiology	InterPro	IPR012171	Fatty acid desaturase	3	3	3.25	1.79E-05	ENSP00000278829,ENSP00000278840,ENSP00000322229
Skin physiology	InterPro	IPR005804	Fatty acid desaturase domain	3	7	2.88	5.35E-05	ENSP00000278829,ENSP00000278840,ENSP00000322229
Skin physiology	InterPro	IPR001199	Cytochrome b5-like heme/steroid binding domain	3	14	2.58	0.0002	ENSP00000278829,ENSP00000278840,ENSP00000322229
Skin physiology	InterPro	IPR036400	Cytochrome b5-like heme/steroid binding domain superfamily	3	14	2.58	0.0002	ENSP00000278829,ENSP00000278840,ENSP00000322229
Skin physiology	InterPro	IPR003074	Peroxisome proliferator-activated receptor	2	3	3.07	0.0039	ENSP00000287820,ENSP00000310928
Skin physiology	SMART	SM01117	Cytochrome b5-like Heme/Steroid binding domain	2	9	2.6	0.0114	ENSP00000278840,ENSP00000322229
DNA damage repair	GO Process	GO:0006974	Cellular response to dna damage stimulus	5	793	1.25	0.028	ENSP00000217246,ENSP00000287647,ENSP00000371475,ENSP00000411099,ENSP00000415430
DNA damage repair	WikiPathways	WP2516	ATM signaling pathway	3	39	2.33	0.00022	ENSP00000287647,ENSP00000371475,ENSP00000411099
DNA damage repair	UniProt Keywords	KW-0227	DNA damage	4	383	1.47	0.0034	ENSP00000217246,ENSP00000287647,ENSP00000371475,ENSP00000411099
OutFLANK candidates	GO Process	GO:0000902	Cell morphogenesis	49	726	0.41	8.45E-05	ENSP00000229922,ENSP00000256646,ENSP00000263791,ENSP00000267163,ENSP00000272771,ENSP00000301945,ENSP00000304292,ENSP00000307134,ENSP00000324857,ENSP00000324960,ENSP00000330633,ENSP00000332737,ENSP00000339299,ENSP00000340874,ENSP00000344786,ENSP00000347591,ENSP00000352882,ENSP00000353508,ENSP00000354778,ENSP00000356000,ENSP00000367316,ENSP00000369981,ENSP00000370340,ENSP00000373433,ENSP00000374323,ENSP00000376345,ENSP00000376921,ENSP00000378306,ENSP00000379258,ENSP00000379644,ENSP00000379901,ENSP00000381793,ENSP00000384620,ENSP00000384638,ENSP00000385143,ENSP00000385451,ENSP00000389588,ENSP00000392423,ENSP00000401633,ENSP00000407822,ENSP00000420213,ENSP00000425093,ENSP00000428564,ENSP00000451648,ENSP00000463325,ENSP00000481581,ENSP00000484928
OutFLANK candidates	GO Process	GO:0000904	Cell morphogenesis involved in differentiation	38	566	0.41	0.0013	ENSP00000256646,ENSP00000267163,ENSP00000272771,ENSP00000301945,ENSP00000307134,ENSP00000324857,ENSP00000324960,ENSP00000330633,ENSP00000332737,ENSP00000339299,ENSP00000340874,ENSP00000344786,ENSP00000347591,ENSP00000352882,ENSP00000353508,ENSP00000356000,ENSP00000367316,ENSP00000373433,ENSP00000374323,ENSP00000376345,ENSP00000376921,ENSP00000378306,ENSP00000379258,ENSP00000381793,ENSP00000384638,ENSP00000385143,ENSP00000389588,ENSP00000392423,ENSP00000407822,ENSP00000420213,ENSP00000428564,ENSP00000451648,ENSP00000463325,ENSP00000481581,ENSP00000484928

OutFLANK candidates	GO Process	GO:0009653	Anatomical structure morphogenesis	97	2,165	0.23	0.0013	ENSP00000070846,ENSP00000229922,ENSP00000236273,ENSP00000240335,ENSP00000242261,ENSP00000256078,ENSP00000256646,ENSP00000257863,ENSP00000259241,ENSP00000261523,ENSP00000263640,ENSP00000263791,ENSP00000265421,ENSP00000267163,ENSP00000268613,ENSP00000269216,ENSP00000272771,ENSP00000273261,ENSP00000278550,ENSP00000281081,ENSP00000286758,ENSP00000301945,ENSP00000304292,ENSP00000306335,ENSP0000030737,ENSP00000334563,ENSP00000339299,ENSP00000340874,ENSP00000344786,ENSP00000346151,ENSP00000347591,ENSP00000352882,ENSP00000353452,ENSP00000353508,ENSP00000354487,ENSP00000354778,ENSP00000356000,ENSP00000356774,ENSP00000360120,ENSP00000369891,ENSP00000376345,ENSP00000376899,ENSP00000376921,ENSP00000378306,ENSP00000379210,ENSP00000379258,ENSP00000379644,ENSP00000379901,ENSP00000381793,ENSP00000384620,ENSP00000384638,ENSP00000385143,ENSP00000385451,ENSP00000385545,ENSP00000385545,ENSP00000407822,ENSP00000412461,ENSP00000412940,ENSP00000418735,ENSP00000420213,ENSP00000425093,ENSP00000428564,ENSP00000432770,ENSP00000437621,ENSP00000451648,ENSP00000457230,ENSP00000463325,ENSP00000480043,ENSP00000480791,ENSP00000481581,ENSP00000484855,ENSP00000484928
OutFLANK candidates	GO Process	GO:0022008	Neurogenesis	80	1,657	0.26	0.0013	ENSP00000242261,ENSP00000256078,ENSP00000256646,ENSP00000259241,ENSP00000261205,ENSP00000261523,ENSP00000263791,ENSP00000265022,ENSP00000265342,ENSP00000267163,ENSP00000272771,ENSP00000278550,ENSP00000303053,ENSP000003031831,ENSP00000303769,ENSP00000304292,ENSP000003042857,ENSP00000310841,ENSP00000316950,ENSP00000324857,ENSP00000324960,ENSP000003329
OutFLANK candidates	GO Process	GO:0032990	Cell part morphogenesis	36	525	0.41	0.0013	ENSP00000256646,ENSP00000263791,ENSP00000281081,ENSP00000304292,ENSP00000307134,ENSP00000324857,ENSP00000330633,ENSP00000332737,ENSP000003376921,ENSP00000378306,ENSP00000379258,ENSP00000379901,ENSP00000381793,ENSP00000384638,ENSP00000385143,ENSP00000385451,ENSP00000389588,ENSP00000392423,ENSP00000401633,ENSP00000407822,ENSP00000451648,ENSP00000463325,ENSP00000480043,ENSP00000483424,ENSP00000484928
OutFLANK candidates	GO Process	GO:0048667	Cell morphogenesis involved in neuron differentiation	33	445	0.45	0.0013	ENSP00000256646,ENSP00000267163,ENSP00000272771,ENSP00000307134,ENSP00000324857,ENSP00000330633,ENSP00000332737,ENSP00000339299,ENSP00000340874,ENSP00000344786,ENSP00000347591,ENSP00000356774,ENSP00000360120,ENSP00000369891,ENSP00000376345,ENSP00000376806,ENSP00000379258,ENSP00000379901,ENSP00000381793,ENSP00000384638,ENSP00000385183,ENSP00000385451,ENSP00000389588,ENSP00000392423,ENSP00000407822,ENSP00000428564,ENSP00000451648,ENSP00000463325,ENSP000004801581,ENSP00000484928
OutFLANK candidates	GO Process	GO:0048699	Generation of neurons	76	1,551	0.27	0.0013	ENSP00000242261,ENSP00000256646,ENSP00000259241,ENSP00000261205,ENSP00000261523,ENSP00000263791,ENSP00000264896,ENSP00000265022,ENSP00000265342,ENSP00000267163,ENSP00000272771,ENSP00000278550,ENSP00000303053,ENSP000003031831,ENSP000003037134,ENSP00000310841,ENSP00000316950,ENSP00000324857,ENSP00000324960,ENSP000003329
OutFLANK candidates	GO Process	GO:0048858	Cell projection morphogenesis	35	503	0.42	0.0013	ENSP00000256646,ENSP00000263791,ENSP00000272771,ENSP00000307134,ENSP00000324857,ENSP00000330633,ENSP00000332737,ENSP00000339299,ENSP00000344786,ENSP00000345772,ENSP00000346151,ENSP00000347591,ENSP00000352882,ENSP00000353414,ENSP00000353508,ENSP00000353518,ENSP00000354487,ENSP00000354621,ENSP00000354778,ENSP00000357494,ENSP00000356000,ENSP00000356774,ENSP00000360120,ENSP00000369891,ENSP00000370340,ENSP0000037314,ENSP000003737806,ENSP00000379258,ENSP00000379901,ENSP00000381793,ENSP00000384638,ENSP00000385183,ENSP00000385451,ENSP00000389588,ENSP00000392423,ENSP00000401633,ENSP00000407822,ENSP00000428564,ENSP00000451648,ENSP00000463325,ENSP00000480043,ENSP00000481581,ENSP00000484928
OutFLANK candidates	GO Process	GO:0032989	Cellular component morphogenesis	39	614	0.38	0.0015	ENSP00000256646,ENSP00000263791,ENSP00000272771,ENSP00000278550,ENSP00000281081,ENSP00000304292,ENSP00000306335,ENSP00000307134,ENSP000003147591,ENSP0000032882,ENSP00000353508,ENSP0000036000,ENSP00000369891,ENSP00000370340,ENSP00000371958,ENSP00000376345,ENSP00000401633,ENSP00000407822,ENSP00000428564,ENSP00000463325,ENSP000004801581,ENSP00000484928
OutFLANK candidates	GO Process	GO:0048812	Neuron projection morphogenesis	34	495	0.42	0.0015	ENSP00000256646,ENSP00000263791,ENSP00000272771,ENSP00000304292,ENSP00000307134,ENSP00000324857,ENSP00000330633,ENSP00000332737,ENSP00000339299,ENSP00000344786,ENSP00000347591,ENSP00000352882,ENSP00000353508,ENSP00000356000,ENSP00000369891,ENSP00000370340,ENSP00000373423,ENSP00000376345,ENSP00000401633,ENSP00000407822,ENSP00000428564,ENSP00000463325,ENSP000004801581,ENSP00000484928
OutFLANK candidates	GO Process	GO:0007411	Axon guidance	23	275	0.5	0.003	ENSP00000256646,ENSP00000263771,ENSP00000272771,ENSP000003030633,ENSP00000307134,ENSP00000324857,ENSP00000330633,ENSP00000332737,ENSP00000339299,ENSP00000344786,ENSP00000347591,ENSP00000352882,ENSP00000353508,ENSP00000356000,ENSP00000369891,ENSP00000370340,ENSP00000371958,ENSP00000376345,ENSP00000401633,ENSP00000407822,ENSP00000428564,ENSP00000463325,ENSP000004801581,ENSP00000484928
OutFLANK candidates	GO Process	GO:0048468	Cell development	75	1,629	0.24	0.003	ENSP00000256645,ENSP00000262165,ENSP00000263791,ENSP00000264997,ENSP00000265022,ENSP00000265773,ENSP00000267163,ENSP00000272771,ENSP00000278550,ENSP000003030633,ENSP000003031845,ENSP000003037134,ENSP00000310841,ENSP00000316950,ENSP00000324857,ENSP00000324960,ENSP00000332296,ENSP00000346151,ENSP00000347591,ENSP00000352882,ENSP00000356774,ENSP00000359713,ENSP00000365811,ENSP00000366506,ENSP00000367316,ENSP00000369891,ENSP00000370340,ENSP00000371958,ENSP00000373433,ENSP00000376316,ENSP00000376921,ENSP00000381793,ENSP00000384638,ENSP00000385183,ENSP00000385451,ENSP00000389588,ENSP00000392423,ENSP00000401633,ENSP00000407822,ENSP00000428564,ENSP00000463325,ENSP000004801581,ENSP00000484928
OutFLANK candidates	GO Process	GO:0048666	Neuron development	46	827	0.32	0.003	ENSP00000256646,ENSP00000263791,ENSP00000265022,ENSP00000265773,ENSP00000267163,ENSP0000026771,ENSP00000278550,ENSP00000303053,ENSP000003031845,ENSP000003037134,ENSP00000310841,ENSP00000316950,ENSP00000324857,ENSP00000324960,ENSP00000332296,ENSP00000346151,ENSP00000347591,ENSP00000352882,ENSP00000356774,ENSP00000359713,ENSP00000365811,ENSP00000366506,ENSP00000367316,ENSP00000369891,ENSP00000370340,ENSP00000371958,ENSP00000373433,ENSP00000376316,ENSP00000376921,ENSP00000381793,ENSP00000384638,ENSP00000385183,ENSP00000385451,ENSP00000389588,ENSP00000392423,ENSP00000401633,ENSP00000407822,ENSP00000428564,ENSP00000463325,ENSP000004801581,ENSP00000484928
OutFLANK candidates	GO Process	GO:0007399	Nervous system development	99	2,371	0.2	0.0031	ENSP00000256646,ENSP00000263791,ENSP00000265022,ENSP00000265773,ENSP00000267163,ENSP0000026771,ENSP00000278550,ENSP00000303053,ENSP000003031845,ENSP000003037134,ENSP00000310841,ENSP00000316950,ENSP00000324857,ENSP00000324960,ENSP00000332296,ENSP00000346151,ENSP00000347591,ENSP00000352882,ENSP00000356774,ENSP00000359713,ENSP00000365811,ENSP00000366506,ENSP00000367316,ENSP00000369891,ENSP00000370340,ENSP00000371958,ENSP00000373433,ENSP00000376316,ENSP00000376921,ENSP00000381793,ENSP00000384638,ENSP00000385183,ENSP00000385451,ENSP00000389588,ENSP00000392423,ENSP00000401633,ENSP00000407822,ENSP00000428564,ENSP00000463325,ENSP000004801581,ENSP00000484928
OutFLANK candidates	GO Process	GO:0030182	Neuron differentiation	53	1,019	0.29	0.0031	ENSP00000256646,ENSP00000259241,ENSP00000261523,ENSP00000263791,ENSP00000265022,ENSP00000267163,ENSP0000026771,ENSP00000278550,ENSP00000303053,ENSP000003031845,ENSP000003032737,ENSP000003037134,ENSP00000310841,ENSP00000316950,ENSP00000324857,ENSP00000324960,ENSP00000332296,ENSP00000346151,ENSP00000347591,ENSP00000352882,ENSP00000356774,ENSP00000359713,ENSP00000365811,ENSP00000366506,ENSP00000367316,ENSP00000369891,ENSP00000370340,ENSP00000371958,ENSP00000373433,ENSP00000376316,ENSP00000376921,ENSP00000381793,ENSP00000384638,ENSP00000385183,ENSP00000385451,ENSP00000389588,ENSP00000392423,ENSP00000401633,ENSP00000407822,ENSP00000428564,ENSP00000463325,ENSP000004801581,ENSP00000484928

OutFLANK candidates	GO Component	GO:0120025	Plasma membrane bounded cell projection	87	2,193	0.18	0.0089	ENSP00000225823,ENSP00000254579,ENSP00000255380,ENSP00000255674,ENSP00000256646,ENSP00000261047,ENSP00000261205,ENSP00000262442,ENSP00000262942,ENSP00000265382,ENSP00000268613,ENSP00000278550,ENSP0000029172,ENSP00000288919,ENSP0000028919,ENSP00000296496,ENSP00000297044,ENSP00000301945,ENSP00000304292,ENSP00000307134,ENSP00000307272,ENSP00000307449,ENSP00000315006,ENSP00000324127,ENSP00000324960,ENSP00000325296,ENSP00000330633,ENSP00000332737,ENSP00000342144,ENSP00000344786,ENSP00000346151,ENSP00000349748,ENSP00000352544,ENSP00000353452,ENSP00000353508,ENSP00000353518,ENSP00000354621,ENSP00000354778,ENSP00000354896,ENSP00000354916,ENSP00000356515,ENSP00000356774,ENSP00000360120,ENSP00000360423,ENSP00000361471,ENSP00000363458,ENSP00000365272,ENSP00000365811,ENSP00000366505,ENSP00000367316,ENSP00000367762,ENSP00000367991,ENSP00000369891,ENSP00000370420,ENSP00000374323,ENSP00000375647,ENSP00000376132,ENSP00000376921,ENSP00000379258,ENSP00000384620,ENSP0000038463,ENSP00000386227,ENSP00000387739,ENSP00000389714,ENSP00000391249,ENSP00000392423,ENSP00000394888,ENSP00000398930,ENSP00000402460,ENSP00000407213,ENSP00000407822,ENSP00000416040,ENSP00000417901,ENSP00000420182,ENSP00000422185,ENSP00000429842,ENSP00000431926,ENSP00000440207,ENSP00000445306,ENSP00000453293,ENSP00000459962,ENSP00000463325,ENSP00000479113,ENSP00000482968,ENSP00000483424
OutFLANK candidates	GO Component	GO:0070161	Anchoring junction	41	820	0.28	0.0099	ENSP00000011898,ENSP00000070846,ENSP00000227507,ENSP00000256078,ENSP00000264896,ENSP00000268613,ENSP00000274498,ENSP00000280979,ENSP00000289968,ENSP00000297044,ENSP00000307134,ENSP00000309830,ENSP00000319096,ENSP00000344786,ENSP00000346151,ENSP00000348381,ENSP00000351618,ENSP00000354774,ENSP00000357106,ENSP00000358490,ENSP00000365198,ENSP00000367263,ENSP00000367316,ENSP00000371,ENSP00000445306,ENSP00000463325,ENSP00000472929,ENSP00000484928
OutFLANK candidates	GO Component	GO:0098688	Parallel fiber to purkinje cell synapse	5	16	1.07	0.0129	ENSP0000035791,ENSP00000357106,ENSP00000367762,ENSP00000384638,ENSP00000407822
OutFLANK candidates	GO Component	GO:0005887	Integral component of plasma membrane	67	1,623	0.19	0.0188	ENSP00000011898,ENSP00000225823,ENSP00000255380,ENSP00000256646,ENSP00000257863,ENSP00000259241,ENSP00000262308,ENSP00000263640,ENSP00000264360,ENSP00000275230,ENSP00000278198,ENSP00000287850,ENSP000002880200,ENSP000002881172,ENSP00000288243,ENSP00000303960,ENSP00000307822,ENSP00000315006,ENSP00000315654,ENSP00000324857,ENSP00000325296,ENSP00000327417,ENSP00000331727,ENSP00000333519,ENSP0000033333919,ENSP00000340465,ENSP00000344786,ENSP00000348401,ENSP00000345055,ENSP00000345751,ENSP00000347583,ENSP00000348888,ENSP00000352779,ENSP00000352882,ENSP00000353791,ENSP00000354238,ENSP00000354751,ENSP00000356500,ENSP00000357507,ENSP00000358106,ENSP00000358301,ENSP00000358715,ENSP00000360120,ENSP00000366506,ENSP00000367316,ENSP00000370593,ENSP00000371587,ENSP00000441802,ENSP0000044545036,ENSP000004451648,ENSP00000459962,ENSP00000463325,ENSP00000479113,ENSP00000484928
OutFLANK candidates	GO Component	GO:0045211	Postsynaptic membrane	19	281	0.41	0.0222	ENSP000000255380,ENSP000000262138,ENSP00000278198,ENSP00000288490,ENSP0000030633,ENSP00000353414,ENSP00000353791,ENSP00000354896,ENSP00000356515,ENSP00000358715,ENSP00000365272,ENSP00000375647,ENSP00000384620,ENSP00000402460,ENSP00000417901,ENSP00000422185,ENSP00000459962,ENSP00000479113
OutFLANK candidates	GO Component	GO:0060076	Excitatory synapse	7	51	0.72	0.0486	ENSP00000261205,ENSP00000288490,ENSP0000035791,ENSP00000357106,ENSP00000367762,ENSP00000384638,ENSP00000407822
OutFLANK candidates	STRING clusters	CL:16691	Defective B3GALT1 causes Peters-plus syndrome (PpS)	8	27	1.05	0.0104	ENSP00000268070,ENSP00000272643,ENSP00000347484,ENSP00000355751,ENSP00000369921,ENSP00000370443,ENSP00000389588,ENSP00000418735
OutFLANK candidates	Reactome	HSA-5083635	Defective B3GALT1 causes Peters-plus syndrome (PpS)	9	37	0.96	0.0047	ENSP00000251582,ENSP00000268070,ENSP00000272643,ENSP00000347484,ENSP00000355751,ENSP00000369921,ENSP00000370443,ENSP00000389588,ENSP00000418735
OutFLANK candidates	Reactome	HSA-5173105	O-linked glycosylation	14	108	0.69	0.0047	ENSP00000227756,ENSP00000251582,ENSP00000259056,ENSP00000265000,ENSP00000268070,ENSP00000272643,ENSP00000347484,ENSP00000355632,ENSP00000355751,ENSP00000369921,ENSP00000370443,ENSP00000389588,ENSP00000418735
OutFLANK candidates	Reactome	HSA-5173214	O-glycosylation of TSR domain-containing proteins	9	38	0.95	0.0047	ENSP00000251582,ENSP00000268070,ENSP00000272643,ENSP00000347484,ENSP00000355751,ENSP00000369921,ENSP00000370443,ENSP00000389588,ENSP00000418735
OutFLANK candidates	Reactome	HSA-3906995	Diseases associated with O-glycosylation of proteins	10	67	0.75	0.0146	ENSP00000251582,ENSP00000256646,ENSP00000268070,ENSP00000272643,ENSP00000347484,ENSP00000355751,ENSP00000369921,ENSP00000370443,ENSP00000389588,ENSP00000418735
OutFLANK candidates	DISEASES	DOID:4	Disease	207	5,921	0.12	0.0075	ENSP00000070846,ENSP00000166345,ENSP00000181839,ENSP00000219431,ENSP00000220597,ENSP00000227507,ENSP00000238667,ENSP00000240335,ENSP00000242261,ENSP00000245564,ENSP00000249806,ENSP00000251582,ENSP00000253354,ENSP00000255674,ENSP00000256078,ENSP00000256646,ENSP00000257776,ENSP00000257863,ENSP00000259241,ENSP00000259808,ENSP00000261170,ENSP00000261381,ENSP00000261609,ENSP0000026442,ENSP00000268070,ENSP00000268097,ENSP00000269216,ENSP00000269503,ENSP00000272371,ENSP00000274498,ENSP00000278550,ENSP00000279146,ENSP00000281081,ENSP00000281172,ENSP00000282538,ENSP00000282908,ENSP00000283243,ENSP00000283928,ENSP00000286758,ENSP00000287239,ENSP00000288912,ENSP00000294309,ENSP00000295902,ENSP00000296498,ENSP00000297770,ENSP00000300305,ENSP00000309009,ENSP00000301732,ENSP00000301764,ENSP00000301945,ENSP00000302111,ENSP00000303960,ENSP00000306522,ENSP00000306682,ENSP00000306822,ENSP00000307134,ENSP00000309338,ENSP00000312284,ENSP00000313601,ENSP00000315371,ENSP00000315775,ENSP00000316950,ENSP00000320246,ENSP00000323926,ENSP00000324960,ENSP00000325376,ENSP00000328118,ENSP00000329468,ENSP00000330633,ENSP00000332256,ENSP000003333519,ENSP00000342323,ENSP00000334563,ENSP00000336724,ENSP00000337353,ENSP00000337443,ENSP00000337452,ENSP00000339086,ENSP00000340465,ENSP00000340874,ENSP00000341550,ENSP00000342144,ENSP00000343847,ENSP00000344546,ENSP000003453508,ENSP00000353518,ENSP00000353791,ENSP00000354238,ENSP00000354487,ENSP00000354778,ENSP00000354916,ENSP00000355577,ENSP00000355632,ENSP0000035571,ENSP00000355893,ENSP00000355929,ENSP00000356515,ENSP00000356774,ENSP00000357052,ENSP00000358490,ENSP00000358532,ENSP00000359114,ENSP00000360423,ENSP00000360569,ENSP00000368970,ENSP00000369328,ENSP00000369695,ENSP00000370047,ENSP00000370404,ENSP00000370740,ENSP00000370931,ENSP00000371169,ENSP00000373301,ENSP00000374443,ENSP00000375067,ENSP00000376587,ENSP00000376851,ENSP00000376921,ENSP00000379065,ENSP00000379210,ENSP00000379258,ENSP00000379822,ENSP00000381382,ENSP00000381793,ENSP00000382770,ENSP00000384620,ENSP00000384638,ENSP00000385899,ENSP00000386104,ENSP00000386227,ENSP00000389714,ENSP000003931249,ENSP00000392423,ENSP00000393566,ENSP00000394888,ENSP00000402460,ENSP00000407822,ENSP00000410852,ENSP00000411770,ENSP00000412940,ENSP00000415151,ENSP00000416040,ENSP00000417901,ENSP00000417963,ENSP00000417980,ENSP00000420213,ENSP00000422185,ENSP00000428564,ENSP00000430684,ENSP00000432770,ENSP00000437621,ENSP00000438346,ENSP00000445306,ENSP00000457230,ENSP00000459962,ENSP00000472929,ENSP00000473686,ENSP00000479113,ENSP00000480043,ENSP00000482968,ENSP000004848803

Table S9. Sweep haplotype patterns used to reconstruct Eurasian migrations. For each named sample(s) or population, sweep haplotype presence is indicated with an ‘X’, absence with a blank, and inability to call due to lack of data with a ‘?’.

The upper table contains sweeps inferred for the Arabian Standstill phase, based on their broad presence across ISEA/Oceania as well as early Paleolithic Europe. The lower table contains sweeps that are only identified in western Eurasian samples and are grouped according to sample archaeological designations. Where multiple samples exist (e.g. for the IUP, Sunghir 1-4, Yana 1-2) the individual specimens are listed, rather than a simple X. Disjunct groupings of sweeps can be seen between the IUP (light blue) and Aurignacian (red). For the BK-1653 specimen which falls at the Aurignacian/Gravettian boundary, the suite of sweeps is more consistent with the Gravettian specimens (mauve and pink) than the Aurignacian, although the signal is not completely clear. The Gravettian and Magdalenian contain many sweeps identified in earlier archaeological periods, and only a few novel sweeps (e.g. *SMCO2* and *FBX015*).

Sweep ID	Arabian Standstill sweeps									
	Oceanic group				Initial Upper Paleolithic		Ust'-Ishim	Aurignacian	Gravettian	Magdalian
	Andaman	Australia	Vanuatu	PNG	Bacho Kiro/Zlaty Kun	Tianyuan		Kostenki/Goyet	Vestonice, Sunghir	El Miron
AMBRA1			X						X	X
ARFGEF1	X	X							X	
BCAS3		X			X BK	X		X	X	
BEAN1	X	X	X	X	X BK Zk			X	X	X
CAND1		X	X	X	X BK				X	
CCNG2				X		X		X	X	X
CHRN83	X		X	X	X BK	X	X	X	X	X
COL4A3BP		X	X							
COMM3D		X	X	X	X BK				X	
DNAH6			X	X	X BK		X		X	X
DOK5	X	X	X	X	X BK	X	X	X	X	
EPHB6		X	X	X	X BK			X	X	X
FMO2			X			X			X	X
GALNT5	X	X	X	X	X BK	X			X	X
GTSE1	X	X	X	X	X Zk	X				X
HIST1H2BL	X	X	X	X	X BK					X
ITM2B		X		X				X		?
KCTD10				X	X BK					X
LIN28B	X	X	X	X	X BK	X	X	X	X	X
MLPH		X	X		X Zk				X	
MPP6		X			X Zk			X		?
NFASC		X	X	X		X	X		X	X
PNLIPRP3	X		X	X	X BK	X		X	X	?
PRELID2		X	X	X	X BK		X	X	X	
SLC25A36		X	X	X	X BK	X		X	X	
TAF15				X			X		X	X
TMCC1		X	X		X BK Zk				X	
TMEM100	X	X							X	X
TMEM232	X				X BK	X			X	X
TP53BP1	X		X	X	X Zk			X	X	
VPC39		X	X						X	

West Eurasian sweeps									
Sweep period	Sweep ID	Initial Upper Paleolithic	Aurignacian		B.Kiro-1653	Gravettian		Ancient North Siberians	Magdalenian
		Bacho Kiro/Zlaty Kun/Tianyuan	Kostenki14	GoyetQ116-1		Sunghir 1-4	Vestonice16	Yana 1-2	El Miron
Initial Upper Paleolithic	CCDC7	Tianyuan			X			X Y2	?
	DHODH	BK 240			X	X S3 S1		X Y1	
	DOCK3	BK 335						X Y2	
	LINC00293	BK 335	X	X	X	X S3 S4			
	METTL6	BK 240							
	PAX1	Bk 240				X S2			
	TP53BP1	ZK	X				X		
	WWOX	Tianyuan		X					X
	ZMYM6	Tianyuan BK 335				X S3 S4		X Y1 Y2	
Aurignacian	ANKS6		X		X		?		X
	BAIAP2L1		X	X	X	X S1 S2 S4		X Y1	X
	DNAH7		X	X	X	X S1-4	X	X Y2	X
	ELMO1			X					X
	ENAM			X	X	X S2 S3 S4		X Y1 Y2	
	FANCD2		X	X					
	MARS			X					
	OIT3			X		X S1			
	TBC1D7		X				X		
Gravettian	SMC02					X S2	X		?
Magdalenian	FBX015								X

Table S10. Radiocarbon ages of key ancient Eurasian samples recalibrated with IntCal20.

Key samples used for the quantification of sweep dynamics were recalibrated with IntCal20 (41), with mean age estimates and associated uncertainty (calculated at one and two standard deviations) provided.

Sample	IntCal20 calibrated ages				Mean
	1 sd range	2 sd range	3 sd range	4 sd range	
Ust'Ishim	44,946	43,348	45,924	42,905	44,364
Tianyuan	40,313	39,132	40,845	38,079	39,565
Bacho Kiro 1653	35,146	34,746	35,282	34,616	34,948
Bacho Kiro F6-597	36,226	35,874	36,320	35,600	36,002
Kostenki 1	36,588	36,186	36,879	36,074	36,430
Kosteniki 14	38,841	37,265	39,375	36,675	38,052
Pestera cu Oase 1	40,550	38,100	41,350	36,960	39,227
Bacho Kiro Cave AA7-738	43,239	42,709	43,925	42,585	43,106
Bacho Kiro Cave BB7-240	45,009	44,329	45,545	43,945	44,687
Bacho Kiro Cave CC7-2289	44,078	43,241	44,395	42,995	43,689
Bacho Kiro Cave CC7-335	45,423	44,647	45,924	44,427	45,117
Grotte du rennes at Arcy-sur-Cure	40,238	39,675	40,509	39,493	39,984
les Cottes	40,619	39,967	40,918	39,696	40,300
Labeko Koba	42,150	41,192	42,514	40,531	41,587
Abric Romani	41,347	40,963	41,611	40,711	41,159
Keilberg	43,743	41,900	44,579	41,295	42,852
Riparo Mochi	42,691	41,075	44,100	40,060	41,978
Goyet	35,463	34,920	35,627	34,720	35,208
Sunghir 2	35,200	34,155	35,782	33,435	34,629
Sunghir 3	35,140	34,046	35,634	33,277	34,517
Sunghir 4	34,470	33,956	34,699	33,537	34,173
Sunghir 1	33,485	32,200	34,036	31,843	32,920
Yana Bone Layer	31,538	31,137	31,793	31,033	31,382
Yana Bone Layer	32,142	31,116	33,172	30,943	31,855
Vestonice	31,052	30,869	31,134	30,474	30,929
Villabruna	14,127	13,863	14,217	13,800	14,021
Bichon	13,782	13,610	13,799	13,528	13,698
La Brana 1	7,920	7,746	7,931	7,690	7,811
Loschbour	8,156	7,944	8,170	7,935	8,025
Malta	24,461	24,175	24,570	24,120	24,320
AfontovaGora2	16,868	16,663	16,950	16,589	16,767
El Miron	18,820	18,741	18,847	18,696	18,775
Satsurblia	13,334	13,188	13,410	13,174	13,282
Grotte du Renne AR-14	42,080	41,276	42,370	40,778	41,617
Saint-Césaire SP 28	41,861	40,697	42,206	39,960	41,163

References

1. Y. Souilmi, et al., Admixture has obscured signals of historical hard sweeps in humans. *Nat Ecol Evol* (2022) <https://doi.org/10.1038/s41559-022-01914-9>.
2. W. Haak, et al., Massive migration from the steppe was a source for Indo-European languages in Europe. *Nature* 522, 207–211 (2015).
3. I. Mathieson, et al., Genome-wide patterns of selection in 230 ancient Eurasians. *Nature* 528, 499–503 (2015).
4. I. Mathieson, et al., The genomic history of southeastern Europe. *Nature* 555, 197–203 (2018).
5. S. Eisenmann, et al., Reconciling material cultures in archaeology with genetic data: The nomenclature of clusters emerging from archaeogenomic analysis. *Sci. Rep.* 8, 13003 (2018).
6. J. M. Smith, J. Haigh, The hitch-hiking effect of a favourable gene. *Genetical Research* 23, 23–35 (1974).
7. J. Hermisson, P. S. Pennings, Soft sweeps and beyond: Understanding the patterns and probabilities of selection footprints under rapid adaptation. *Methods in Ecology and Evolution* 8, 700–716 (2017).
8. I. Höllinger, P. S. Pennings, J. Hermisson, Polygenic adaptation: From sweeps to subtle frequency shifts. *PLoS Genet.* 15, e1008035 (2019).
9. W. Stephan, Signatures of positive selection: from selective sweeps at individual loci to subtle allele frequency changes in polygenic adaptation. *Mol. Ecol.* 25, 79–88 (2016).
10. S. Chen, Y. Zhou, Y. Chen, J. Gu, fastp: an ultra-fast all-in-one FASTQ preprocessor. *Bioinformatics* 34, i884–i890 (2018).
11. H. Li, Aligning sequence reads, clone sequences and assembly contigs with BWA-MEM. *arXiv [q-bio.GN]* (2013).
12. H. Li, et al., The Sequence Alignment/Map format and SAMtools. *Bioinformatics* 25, 2078–2079 (2009).
13. A. McKenna, et al., The Genome Analysis Toolkit: a MapReduce framework for analyzing next-generation DNA sequencing data. *Genome Res.* 20, 1297–1303 (2010).
14. H. Jónsson, A. Ginolhac, M. Schubert, P. L. F. Johnson, L. Orlando, mapDamage2.0: fast approximate Bayesian estimates of ancient DNA damage parameters. *Bioinformatics* 29, 1682–1684 (2013).
15. M. Kircher, “Analysis of High-Throughput Ancient DNA Sequencing Data” in *Ancient DNA: Methods and Protocols*, B. Shapiro, M. Hofreiter, Eds. (Humana Press, 2012), pp. 197–228.
16. G. Jun, M. K. Wing, G. R. Abecasis, H. M. Kang, An efficient and scalable analysis framework for variant extraction and refinement from population-scale DNA sequence data. *Genome Res.* 25, 918–925 (2015).
17. H. Li, A statistical framework for SNP calling, mutation discovery, association mapping and population genetical parameter estimation from sequencing data. *Bioinformatics* 27, 2987–2993 (2011).
18. A. L. Price, et al., Principal components analysis corrects for stratification in genome-wide association studies. *Nat. Genet.* 38, 904–909 (2006).
19. N. Patterson, A. L. Price, D. Reich, Population structure and eigenanalysis. *PLoS Genet.* 2, e190 (2006).
20. C. C. Chang, et al., Second-generation PLINK: rising to the challenge of larger and richer datasets. *Gigascience* 4, 7 (2015).
21. S. Purcell, et al., PLINK: a tool set for whole-genome association and population-based linkage analyses. *Am. J. Hum. Genet.* 81, 559–575 (2007).
22. C. D. Huber, M. DeGiorgio, I. Hellmann, R. Nielsen, Detecting recent selective sweeps while controlling for mutation rate and background selection. *Mol. Ecol.* 25, 142–156 (2016).

23. M. DeGiorgio, C. D. Huber, M. J. Hubisz, I. Hellmann, R. Nielsen, S weep F inder 2: increased sensitivity, robustness and flexibility. *Bioinformatics* 32, 1895–1897 (2016).
24. 1000 Genomes Project Consortium, et al., A global reference for human genetic variation. *Nature* 526, 68–74 (2015).
25. R. Nielsen, et al., Genomic scans for selective sweeps using SNP data. *Genome Res.* 15, 1566–1575 (2005).
26. R. J. Kinsella, et al., Ensembl BioMarts: a hub for data retrieval across taxonomic space. *Database* 2011, bar030–bar030 (2011).
27. J. D. Storey, The positive false discovery rate: a Bayesian interpretation and the q -value. *The Annals of Statistics* 31, 2013–2035 (2003).
28. S. Durinck, P. T. Spellman, E. Birney, W. Huber, Mapping identifiers for the integration of genomic datasets with the R/Bioconductor package biomaRt. *Nature Protocols* 4, 1184–1191 (2009).
29. B. Iglewicz, D. C. Hoaglin, *How to Detect and Handle Outliers* (Asq Press, 1993).
30. J. T. Daub, et al., Evidence for Polygenic Adaptation to Pathogens in the Human Genome. *Molecular Biology and Evolution* 30, 1544–1558 (2013).
31. A. Ferrer-Admetlla, M. Liang, T. Korneliussen, R. Nielsen, On detecting incomplete soft or hard selective sweeps using haplotype structure. *Mol. Biol. Evol.* 31, 1275–1291 (2014).
32. A. Choudhury, et al., High-depth African genomes inform human migration and health. *Nature* 586, 741–748 (2020).
33. B. Gel, et al., regioneR: an R/Bioconductor package for the association analysis of genomic regions based on permutation tests. *Bioinformatics* 32, 289–291 (2016).
34. C. Bhérer, C. L. Campbell, A. Auton, Refined genetic maps reveal sexual dimorphism in human meiotic recombination at multiple scales. *Nat. Commun.* 8, 14994 (2017).
35. A. Bergström, C. Stringer, M. Hajdinjak, E. M. L. Scerri, P. Skoglund, Origins of modern human ancestry. *Nature* 590, 229–237 (2021).
36. G. Bhatia, N. Patterson, S. Sankararaman, A. L. Price, Estimating and interpreting FST: The impact of rare variants. *Genome Res.* 23, 1514 (2013).
37. K. Prüfer, et al., A genome sequence from a modern human skull over 45,000 years old from Zlatý kůň in Czechia. *Nat Ecol Evol* 5, 820–825 (2021).
38. M. Hajdinjak, et al., Initial Upper Palaeolithic humans in Europe had recent Neanderthal ancestry. *Nature* 592, 253–257 (2021).
39. I. Olalde, et al., The genomic history of the Iberian Peninsula over the past 8000 years. *Science* 363, 1230–1234 (2019).
40. A. Bergström, et al., Insights into human genetic variation and population history from 929 diverse genomes. *Science* 367, 674986 (2020).
41. P. J. Reimer, et al., The IntCal20 Northern Hemisphere Radiocarbon Age Calibration Curve (0–55 cal kBP). *Radiocarbon* 62, 725–757 (2020).
42. G. Gower, et al., Widespread male sex bias in mammal fossil and museum collections. *Proc. Natl. Acad. Sci. U. S. A.* 116, 19019–19024 (2019).
43. M. Petr, et al., The evolutionary history of Neanderthal and Denisovan Y chromosomes. *Science* 369, 1653–1656 (2020).
44. Canty, Ripley, Others, boot: Bootstrap R (S-Plus) functions. R package version 1, 3–20 (2017).
45. X. Wang, fANCOVA: Nonparametric Analysis of Covariance (2020).

46. A. Mitnik, et al., The genetic prehistory of the Baltic Sea region. *Nat. Commun.* 9, 442 (2018).
47. T. Günther, et al., Ancient genomes link early farmers from Atapuerca in Spain to modern-day Basques. *Proc. Natl. Acad. Sci. U. S. A.* 112, 11917–11922 (2015).
48. D. M. Fernandes, et al., A genomic Neolithic time transect of hunter-farmer admixture in central Poland. *Sci. Rep.* 8, 14879 (2018).
49. R Core Team, R: A Language and Environment for Statistical Computing (R Foundation for Statistical Computing, 2021).
50. J. Kamm, J. Terhorst, R. Durbin, Y. S. Song, Efficiently inferring the demographic history of many populations with allele count data. *J. Am. Stat. Assoc.* 115, 1472–1487 (2020).
51. G. Ewing, J. Hermisson, MSMS: a coalescent simulation program including recombination, demographic structure and selection at a single locus. *Bioinformatics* 26, 2064–2065 (2010).
52. Q. Fu, et al., The genetic history of Ice Age Europe. *Nature* 534, 200–205 (2016).
53. R. M. Beyer, M. Krapp, A. Eriksson, A. Manica, Climatic windows for human migration out of Africa in the past 300,000 years. *Nat. Commun.* 12, 4889 (2021).
54. J. I. Rose, An Introduction to Human Prehistory in Arabia: The Lost World of the Southern Crescent (Springer International Publishing, 2022) (December 1, 2022).
55. I. Hershkovitz, et al., A Middle Pleistocene Homo from Nesher Ramla, Israel. *Science* 372, 1424–1428 (2021).
56. P. Moorjani, et al., A genetic method for dating ancient genomes provides a direct estimate of human generation interval in the last 45,000 years. *Proc. Natl. Acad. Sci. U. S. A.* 113, 5652–5657 (2016).
57. L. N. M. Iasi, H. Ringbauer, B. M. Peter, An extended admixture pulse model reveals the limitations to Human-Neandertal introgression dating. *bioRxiv*, 2021.04.04.438357 (2021).
58. R. Tobler, et al., Aboriginal mitogenomes reveal 50,000 years of regionalism in Australia. *Nature* 544, 180–184 (2017).
59. B. David, et al., 45,610–52,160 years of site and landscape occupation at Nawarla Gabarnmang, Arnhem Land plateau (northern Australia). *Quat. Sci. Rev.* 215, 64–85 (2019).
60. T. Maloney, S. O'Connor, R. Wood, K. Aplin, J. Balme, Carpenters Gap 1: A 47,000 year old record of indigenous adaption and innovation. *Quat. Sci. Rev.* 191, 204–228 (2018).
61. Y. Kaifu, et al., Modern human teeth unearthed from below the ~128,000-year-old level at Punung, Java: A case highlighting the problem of recent intrusion in cave sediments. *J. Hum. Evol.* 163, 103122 (2022).
62. J. F. O'Connell, et al., When did *Homo sapiens* first reach Southeast Asia and Sahul? *Proc. Natl. Acad. Sci. U. S. A.* 115, 8482–8490 (2018).
63. J. C. Teixeira, A. Cooper, Using hominin introgression to trace modern human dispersals. *Proc. Natl. Acad. Sci. U. S. A.* 116, 15327–15332 (2019).
64. T. A. Surovell, Early Paleoindian women, children, mobility, and fertility. *Am. Antiq.* 65, 493–508 (2000).
65. J. Allen, J. F. O'Connell, A different paradigm for the initial colonisation of Sahul. *Archaeol. Ocean.* 55, 1–14 (2020).
66. S. O'Connor, S. Kealy, C. Reepmeyer, S. C. Samper Carro, C. Shipton, Terminal Pleistocene emergence of maritime interaction networks across Wallacea. *World Archaeol.*, 1–20 (2023).
67. J. I. Rose, New Light on Human Prehistory in the Arabo-Persian Gulf Oasis. *Curr. Anthropol.* 51, 849–883 (2010).
68. E. K. F. Chan, et al., Human origins in a southern African palaeo-wetland and first migrations. *Nature* 575, 185–189 (2019).

69. L. Slimak, et al., Modern human incursion into Neanderthal territories 54,000 years ago at Mandrin, France. *Sci Adv* 8, eabj9496 (2022).
70. H. Fewlass, et al., A 14C chronology for the Middle to Upper Palaeolithic transition at Bacho Kiro Cave, Bulgaria. *Nat Ecol Evol* 4, 794–801 (2020).
71. J.-J. Hublin, et al., Initial Upper Palaeolithic Homo sapiens from Bacho Kiro Cave, Bulgaria. *Nature* 581, 299–302 (2020).
72. K. Harris, R. Nielsen, The Genetic Cost of Neanderthal Introgression. *Genetics* 203, 881–891 (2016).
73. M. Petr, S. Pääbo, J. Kelso, B. Vernot, Limits of long-term selection against Neandertal introgression. *Proc. Natl. Acad. Sci. U. S. A.* 116, 1639–1644 (2019).
74. M. J. Shoaei, H. Vahdati Nasab, M. D. Petraglia, The Paleolithic of the Iranian Plateau: Hominin occupation history and implications for human dispersals across southern Asia. *Journal of Anthropological Archaeology* 62, 101292 (2021).
75. H. S. Groucutt, et al., Multiple hominin dispersals into Southwest Asia over the past 400,000 years. *Nature* 597, 376–380 (2021).
76. M. Stewart, et al., Human footprints provide snapshot of last interglacial ecology in the Arabian interior. *Sci Adv* 6 (2020).
77. S. J. Armitage, et al., The Southern Route “Out of Africa”: Evidence for an Early Expansion of Modern Humans into Arabia. *Science* 331, 453–456 (2011).
78. J. E. Tierney, P. B. deMenocal, P. D. Zander, A climatic context for the out-of-Africa migration. *Geology* 45, 1023–1026 (2017).
79. M. D. Petraglia, P. S. Breeze, H. S. Groucutt, “Blue Arabia, Green Arabia: Examining Human Colonisation and Dispersal Models” in *Geological Setting, Palaeoenvironment and Archaeology of the Red Sea*, N. M. A. Rasul, I. C. F. Stewart, Eds. (Springer International Publishing, 2019), pp. 675–683.
80. M. D. Petraglia, Archaeology: Trailblazers across Arabia. *Nature* 470, 50–51 (2011).
81. S. H. Ambrose, Chronological calibration of Late Pleistocene modern human dispersals, climate change and archaeology with geochemical isochrons. Sahle Yonatan, Reyes-Centeno Hugo, Bentz Christian, Sahle Y, Reyes-Centeno H, Bentz C, editors. *Modern Human Origins and Dispersal*. Tübingen: Kerns Verlag, 171–213 (2017).
82. J. C. Ferreira, et al., Projecting Ancient Ancestry in Modern-Day Arabians and Iranians: A Key Role of the Past Exposed Arabo-Persian Gulf on Human Migrations. *Genome Biol. Evol.* 13 (2021).
83. P. S. Breeze, et al., Palaeohydrological corridors for hominin dispersals in the Middle East 250–70,000 years ago. *Quat. Sci. Rev.* 144, 155–185 (2016).
84. J. V. Moreno-Mayar, et al., Early human dispersals within the Americas. *Science* 362 (2018).
85. S. Mallick, et al., The Simons Genome Diversity Project: 300 genomes from 142 diverse populations. *Nature* 538, 201–206 (2016).
86. M. Lipson, et al., Population Turnover in Remote Oceania Shortly after Initial Settlement. *Curr. Biol.* 28, 1157–1165.e7 (2018).
87. X.-F. Sun, et al., Ancient DNA and multimethod dating confirm the late arrival of anatomically modern humans in southern China. *Proc. Natl. Acad. Sci. U. S. A.* 118, e2019158118 (2021).
88. J. F. Hoffecker, Out of Africa: modern human origins special feature: the spread of modern humans in Europe. *Proc. Natl. Acad. Sci. U. S. A.* 106, 16040–16045 (2009).

89. T. Higham, et al., Precision dating of the Palaeolithic: a new radiocarbon chronology for the Abri Pataud (France), a key Aurignacian sequence. *J. Hum. Evol.* 61, 549–563 (2011).
90. A. Cooper, et al., A global environmental crisis 42,000 years ago. *Science* 371, 811–818 (2021).
91. W. E. Banks, et al., An application of hierarchical Bayesian modeling to better constrain the chronologies of Upper Paleolithic archaeological cultures in France between ca. 32,000–21,000 calibrated years before present. *Quat. Sci. Rev.* 220, 188–214 (2019).
92. E. Andrew Bennett, et al., The origin of the Gravettians: genomic evidence from a 36,000-year-old Eastern European. Cold Spring Harbor Laboratory, 685404 (2019).
93. I. Lazaridis, The evolutionary history of human populations in Europe. *Curr. Opin. Genet. Dev.* 53, 21–27 (2018).
94. J. E. T. Channell, B. S. Singer, B. R. Jicha, Timing of Quaternary geomagnetic reversals and excursions in volcanic and sedimentary archives. *Quat. Sci. Rev.* 228, 106114 (2020).
95. M. Baca, et al., Ancient DNA of narrow-headed vole reveal common features of the Late Pleistocene population dynamics in cold-adapted small mammals. *Proc. Biol. Sci.* 290, 20222238 (2023).
96. M. Feldman, et al., Late Pleistocene human genome suggests a local origin for the first farmers of central Anatolia. *Nat. Commun.* 10, 1218 (2019).
97. D. L. Hoffmann, et al., U-Th dating of carbonate crusts reveals Neandertal origin of Iberian cave art. *Science* 359, 912–915 (2018).
98. M. C. Langley, et al., Bows and arrows and complex symbolic displays 48,000 years ago in the South Asian tropics. *Sci Adv* 6, eaba3831 (2020).
99. S. O. Rasmussen, et al., A stratigraphic framework for abrupt climatic changes during the Last Glacial period based on three synchronized Greenland ice-core records: refining and extending the INTIMATE event stratigraphy. *Quaternary Science Reviews* 106, 14–28 (2014).
100. H. Paeth, et al., Comparison of climate change from Cenozoic surface uplift and glacial-interglacial episodes in the Himalaya-Tibet region: Insights from a regional climate model and proxy data. *Global and Planetary Change* 177, 10–26 (2019).
101. J. E. Kutzbach, et al., African climate response to orbital and glacial forcing in 140,000-y simulation with implications for early modern human environments. *Proc. Natl. Acad. Sci. U. S. A.* 117, 2255–2264 (2020).
102. F. Rostek, E. Bard, L. Beaufort, C. Sonzogni, G. Ganssen, Sea surface temperature and productivity records for the past 240 kyr in the Arabian Sea. *Deep Sea Research Part II: Topical Studies in Oceanography* 44, 1461–1480 (1997).
103. H. S. Groucutt, et al., Homo sapiens in Arabia by 85,000 years ago. *Nat Ecol Evol* 2, 800–809 (2018).
104. P. Scussolini, et al., Agreement between reconstructed and modeled boreal precipitation of the Last Interglacial. *Sci Adv* 5, eaax7047 (2019).
105. R. P. Jennings, et al., The greening of Arabia: Multiple opportunities for human occupation of the Arabian Peninsula during the Late Pleistocene inferred from an ensemble of climate model simulations. *Quat. Int.* 382, 181–199 (2015).
106. C. S. M. Turney, et al., A global mean sea surface temperature dataset for the Last Interglacial (129–116 ka) and contribution of thermal expansion to sea level change. *Earth System Science Data* 12, 3341–3356 (2020).
107. L. Al Harthy, R. Grenyer, Classification and ordination of the main plant communities of the Eastern Hajar Mountains, Oman. *J. Arid Environ.* 169, 1–18 (2019).
108. A. Amonkar, S. D. Iyer, E. V. S. S. K. Babu, S. Manju, Extending the limit of widespread dispersed Toba volcanic glass shards and identification of new in-situ volcanic events in the Central Indian Ocean Basin. *J. Earth Syst. Sci.* 129, 175 (2020).

109. J. A. Westgate, et al., Tephrochronology of the Toba tuffs: four primary glass populations define the 75-ka Youngest Toba Tuff, northern Sumatra, Indonesia. *J. Quat. Sci.* 28, 772–776 (2013).
110. M. R. Rampino, S. Self, Volcanic winter and accelerated glaciation following the Toba super-eruption. *Nature* 359, 50–52 (1992).
111. G. S. Jones, J. M. Gregory, P. A. Stott, S. F. B. Tett, R. B. Thorpe, An AOGCM simulation of the climate response to a volcanic super-eruption. *Clim. Dyn.* 25, 725–738 (2005).
112. M. A. J. Williams, et al., Environmental impact of the 73ka Toba super-eruption in South Asia. *Palaeogeogr. Palaeoclimatol. Palaeoecol.* 284, 295–314 (2009).
113. E. Camillo, J. P. Quadros, A. C. A. Santarosa, K. B. Costa, F. A. L. Toledo, An abrupt cooling event recorded around 73 kyr in western South Atlantic. *Quat. Int.* 542, 80–87 (2020).
114. W. Du, et al., Timing and structure of the weak Asian Monsoon event about 73,000 years ago. *Quat. Geochronol.* 53, 101003 (2019).
115. M. A. J. Williams, et al., Reply to the comment on “Environmental impact of the 73ka Toba super-eruption in South Asia” by M. A. J. Williams, S. H. Ambrose, S. van der Kaars, C. Ruehlemann, U. Chattopadhyaya, J. Pal, P. R. Chauhan [Palaeogeography, Palaeoclimatology, Palaeoecology 284 (2009) 295–314]. *Palaeogeogr. Palaeoclimatol. Palaeoecol.* 296, 204–211 (2010).
116. G. A. Zielinski, et al., Potential atmospheric impact of the Toba Mega-Eruption ~71,000 years ago. *Geophys. Res. Lett.* 23, 837–840 (1996).
117. B. A. Black, J.-F. Lamarque, D. R. Marsh, A. Schmidt, C. G. Bardeen, Global climate disruption and regional climate shelters after the Toba supereruption. *Proc. Natl. Acad. Sci. U. S. A.* 118 (2021).
118. A. Akbari, et al., Identifying the favored mutation in a positive selective sweep. *Nat. Methods* 15, 279–282 (2018).
119. L. G. Moore, Human genetic adaptation to high altitude. *High Alt. Med. Biol.* 2, 257–279 (2001).
120. L. G. Moore, et al., Maternal adaptation to high-altitude pregnancy: an experiment of nature--a review. *Placenta* 25 Suppl A, S60–71 (2004).
121. X. Zhang, et al., The history and evolution of the Denisovan- haplotype in Tibetans. *Proc. Natl. Acad. Sci. U. S. A.* 118 (2021).
122. J. S. Rees, S. Castellano, A. M. Andrés, The Genomics of Human Local Adaptation. *Trends Genet.* 36, 415–428 (2020).
123. L. T. Buck, et al., Evidence of different climatic adaptation strategies in humans and non-human primates. *Sci. Rep.* 9, 11025 (2019).
124. H. J. Grav, A. S. Blix, Brown adipose tissue-a factor in the survival of harp seal pups. *Can. J. Physiol. Pharmacol.* 54, 409–412 (1976).
125. A. A. J. J. van der Lans, et al., Cold acclimation recruits human brown fat and increases nonshivering thermogenesis. *J. Clin. Invest.* 123, 3395–3403 (2013).
126. J. Sanchez-Gurmaches, et al., Brown Fat AKT2 Is a Cold-Induced Kinase that Stimulates ChREBP-Mediated De Novo Lipogenesis to Optimize Fuel Storage and Thermogenesis. *Cell Metab.* 27, 195–209.e6 (2018).
127. Z. Yang, et al., Darwinian Positive Selection on the Pleiotropic Effects of KITLG Explain Skin Pigmentation and Winter Temperature Adaptation in Eurasians. *Mol. Biol. Evol.* 35, 2272–2283 (2018).
128. H. O. Koskela, Cold air-provoked respiratory symptoms: the mechanisms and management. *Int. J. Circumpolar Health* 66, 91–100 (2007).

129. T. M. Mäkinen, et al., Cold temperature and low humidity are associated with increased occurrence of respiratory tract infections. *Respir. Med.* 103, 456–462 (2009).
130. M. Fumagalli, et al., Greenlandic Inuit show genetic signatures of diet and climate adaptation. *Science* 349, 1343–1347 (2015).
131. A. Cardona, et al., Genome-wide analysis of cold adaptation in indigenous Siberian populations. *PLoS One* 9, e98076 (2014).
132. A. V. Khrunin, G. V. Khvorykh, A. N. Fedorov, S. A. Limborska, Genomic landscape of the signals of positive natural selection in populations of Northern Eurasia: A view from Northern Russia. *PLoS One* 15, e0228778 (2020).
133. S. Zhou, et al., Genetic architecture and adaptations of Nunavik Inuit. *Proc. Natl. Acad. Sci. U. S. A.* 116, 16012–16017 (2019).
134. A. W. Reynolds, et al., Comparing signals of natural selection between three Indigenous North American populations. *Proc. Natl. Acad. Sci. U. S. A.* 116, 9312–9317 (2019).
135. N. S. Yudin, D. M. Larkin, E. V. Ignatjeva, A compendium and functional characterization of mammalian genes involved in adaptation to Arctic or Antarctic environments. *BMC Genet.* 18, 111 (2017).
136. M. Mondal, J. Bertranpetti, O. Lao, Approximate Bayesian computation with deep learning supports a third archaic introgression in Asia and Oceania. *Nat. Commun.* 10, 246 (2019).
137. S. Sankararaman, S. Mallick, N. Patterson, D. Reich, The Combined Landscape of Denisovan and Neanderthal Ancestry in Present-Day Humans. *Curr. Biol.* 26, 1241–1247 (2016).
138. B. Vernot, et al., Excavating Neandertal and Denisovan DNA from the genomes of Melanesian individuals. *Science* 352, 235–239 (2016).
139. G. S. Jacobs, et al., Multiple Deeply Divergent Denisovan Ancestries in Papuans. *Cell* 177, 1010–1021.e32 (2019).
140. E. Huerta-Sánchez, et al., Altitude adaptation in Tibetans caused by introgression of Denisovan-like DNA. *Nature* 512, 194–197 (2014).
141. F. Racimo, et al., Archaic Adaptive Introgression in TBX15/WARS2. *Mol. Biol. Evol.* 34, 509–524 (2017).
142. G. Gower, P. I. Picazo, M. Fumagalli, F. Racimo, Detecting adaptive introgression in human evolution using convolutional neural networks. *eLife* (2021) <https://doi.org/10.7554/eLife.64669>.
143. R. M. Gittelman, et al., Archaic Hominin Admixture Facilitated Adaptation to Out-of-Africa Environments. *Curr. Biol.* 26, 3375–3382 (2016).
144. D. Setter, et al., VolcanoFinder: Genomic scans for adaptive introgression. *PLoS Genet.* 16, e1008867 (2020).
145. K. J. Karczewski, et al., The mutational constraint spectrum quantified from variation in 141,456 humans. *Nature* 581, 434–443 (2020).
146. C. Trimmer, et al., Genetic variation across the human olfactory receptor repertoire alters odor perception. *Proc. Natl. Acad. Sci. U. S. A.* 116, 9475–9480 (2019).
147. R. S. Dhindsa, B. R. Copeland, A. M. Mustoe, D. B. Goldstein, Natural Selection Shapes Codon Usage in the Human Genome. *Am. J. Hum. Genet.* 107, 83–95 (2020).
148. W. Zhou, W. Wei, Y. Sun, Genetically engineered mouse models for functional studies of SKP1-CUL1-F-box-protein (SCF) E3 ubiquitin ligases. *Cell Res.* 23, 599–619 (2013).
149. T. Cardozo, M. Pagano, The SCF ubiquitin ligase: insights into a molecular machine. *Nat. Rev. Mol. Cell Biol.* 5, 739–751 (2004).
150. J. C. Morales, et al., Role for the BRCA1 C-terminal repeats (BRCT) protein 53BP1 in maintaining genomic stability.

J. Biol. Chem. 278, 14971–14977 (2003).

151. I. M. Ward, K. Minn, J. van Deursen, J. Chen, p53 Binding protein 53BP1 is required for DNA damage responses and tumor suppression in mice. *Mol. Cell. Biol.* 23, 2556–2563 (2003).
152. M. Monte, et al., Cloning, chromosome mapping and functional characterization of a human homologue of murine *gtse-1* (B99) gene. *Gene* 254, 229–236 (2000).
153. Q. Yang, et al., Severe Fanconi Anemia phenotypes in Fancd2 depletion mice. *Biochem. Biophys. Res. Commun.* 514, 713–719 (2019).
154. M. Catinozzi, et al., The Drosophila FUS ortholog *cabeza* promotes adult founder myoblast selection by *Xrp1*-dependent regulation of FGF signaling. *PLoS Genet.* 16, e1008731 (2020).
155. M. Ballarino, et al., TAF15 is important for cellular proliferation and regulates the expression of a subset of cell cycle genes through miRNAs. *Oncogene* 32, 4646–4655 (2013).
156. R. Döffinger, et al., X-linked anhidrotic ectodermal dysplasia with immunodeficiency is caused by impaired NF-kappaB signaling. *Nat. Genet.* 27, 277–285 (2001).
157. K. M. Merath, B. Chang, R. Dubielzig, R. Jeannotte, D. J. Sidjanin, A spontaneous mutation in *Srebf2* leads to cataracts and persistent skin wounds in the lens opacity 13 (*lop13*) mouse. *Mamm. Genome* 22, 661–673 (2011).
158. I. Juranović, Z. Meić, I. Piantanida, L.-M. Tumir, M. Žinić, Interactions of phenanthridinium–nucleobase conjugates with polynucleotides in aqueous media. Recognition of poly UElectronic supplementary information (ESI) available: materials and methods and CD titrations. See <http://www.rsc.org/suppdata/cc/b2/b202615e/>. *Chem. Commun.*, 1432–1433 (2002).
159. M. J. Krashes, B. B. Lowell, A. S. Garfield, Melanocortin-4 receptor-regulated energy homeostasis. *Nat. Neurosci.* 19, 206–219 (2016).
160. B. L. Houghton, J. R. Meendering, B. J. Wong, C. T. Minson, Nitric oxide and noradrenaline contribute to the temperature threshold of the axon reflex response to gradual local heating in human skin. *J. Physiol.* 572, 811–820 (2006).
161. V. A. Pavlov, K. J. Tracey, Neural regulation of immunity: molecular mechanisms and clinical translation. *Nat. Neurosci.* 20, 156–166 (2017).
162. P. J. Brunton, J. A. Russell, The expectant brain: adapting for motherhood. *Nat. Rev. Neurosci.* 9, 11–25 (2008).
163. L. A. Palinkas, Mental and cognitive performance in the cold. *Int. J. Circumpolar Health* 60, 430–439 (2001).
164. T. M. Mäkinen, Human cold exposure, adaptation, and performance in high latitude environments. *Am. J. Hum. Biol.* 19, 155–164 (2007).
165. T. M. Mäkinen, et al., Effect of repeated exposures to cold on cognitive performance in humans. *Physiol. Behav.* 87, 166–176 (2006).
166. L. Taylor, S. L. Watkins, H. Marshall, B. J. Dascombe, J. Foster, The Impact of Different Environmental Conditions on Cognitive Function: A Focused Review. *Front. Physiol.* 6, 372 (2015).
167. J. C. Montgomery, J. A. Macdonald, Effects of temperature on nervous system: implications for behavioral performance. *Am. J. Physiol.* 259, R191–6 (1990).
168. C. Städele, S. Heigle, W. Stein, Neuromodulation to the Rescue: Compensation of Temperature-Induced Breakdown of Rhythmic Motor Patterns via Extrinsic Neuromodulatory Input. *PLoS Biol.* 13, e1002265 (2015).
169. E. de la Peña, et al., The Influence of Cold Temperature on Cellular Excitability of Hippocampal Networks. *PLoS One* 7, e52475 (2012).

170. M. J. Van Hook, Temperature effects on synaptic transmission and neuronal function in the visual thalamus. *PLoS One* 15, e0232451 (2020).
171. F. Viana, E. de la Peña, C. Belmonte, Specificity of cold thermotransduction is determined by differential ionic channel expression. *Nat. Neurosci.* 5, 254–260 (2002).
172. K. Zimmermann, et al., Sensory neuron sodium channel Nav1.8 is essential for pain at low temperatures. *Nature* 447, 855–858 (2007).
173. C.-H. Tan, P. A. McNaughton, The TRPM2 ion channel is required for sensitivity to warmth. *Nature* 536, 460–463 (2016).
174. W. M. Knowlton, A. Bifolck-Fisher, D. M. Bautista, D. D. McKemy, TRPM8, but not TRPA1, is required for neural and behavioral responses to acute noxious cold temperatures and cold-mimetics *in vivo*. *Pain* 150, 340–350 (2010).
175. D. M. Bautista, et al., The menthol receptor TRPM8 is the principal detector of environmental cold. *Nature* 448, 204–208 (2007).
176. T. J. Buijs, P. A. McNaughton, The Role of Cold-Sensitive Ion Channels in Peripheral Thermosensation. *Front. Cell. Neurosci.* 14, 262 (2020).
177. Z. A. K. Chan Lek Tan, Regulation of body temperature by the nervous system. *Neuron* 98, 31 (2018).
178. F. M. Key, et al., Human local adaptation of the TRPM8 cold receptor along a latitudinal cline. *PLoS Genet.* 14, e1007298 (2018).
179. Y. Saitoh, A. Kamijo, J. Yamauchi, T. Sakamoto, N. Terada, The membrane palmitoylated protein, MPP6, is involved in myelin formation in the mouse peripheral nervous system. *Histochem. Cell Biol.* 151, 385–394 (2019).
180. T. A. Forbes, V. Gallo, All Wrapped Up: Environmental Effects on Myelination. *Trends Neurosci.* 40, 572–587 (2017).
181. M. M. Saltykova, The Main Physiological Mechanisms of Cold Adaptation in Humans. *Neuroscience and Behavioral Physiology* 48, 543–550 (2018).
182. O. Keinan, et al., Glycogen metabolism links glucose homeostasis to thermogenesis in adipocytes. *Nature* 599, 296–301 (2021).
183. D. Szklarczyk, et al., The STRING database in 2021: customizable protein-protein networks, and functional characterization of user-uploaded gene/measurement sets. *Nucleic Acids Res.* 49, D605–D612 (2021).
184. P. Luisi, et al., Recent Positive Selection Has Acted on Genes Encoding Proteins with More Interactions within the Whole Human Interactome. *Genome Biol. Evol.* 7, 1141–1154 (2015).
185. D. Enard, L. Cai, C. Gwennap, D. A. Petrov, Viruses are a dominant driver of protein adaptation in mammals. *Elife* 5 (2016).
186. Y.-F. Huang, Dissecting Genomic Determinants of Positive Selection with an Evolution-Guided Regression Model. *Mol. Biol. Evol.* (2021) <https://doi.org/10.1093/molbev/msab291> (December 6, 2021).
187. B. S. Weir, C. C. Cockerham, ESTIMATING F-STATISTICS FOR THE ANALYSIS OF POPULATION STRUCTURE. *Evolution* 38, 1358–1370 (1984).
188. M. C. Whitlock, K. E. Lotterhos, Reliable Detection of Loci Responsible for Local Adaptation: Inference of a Null Model through Trimming the Distribution of F(ST). *Am. Nat.* 186 Suppl 1, S24–36 (2015).
189. L. Excoffier, N. Ray, Surfing during population expansions promotes genetic revolutions and structuration. *Trends Ecol. Evol.* 23, 347–351 (2008).
190. B. F. Voight, S. Kudaravalli, X. Wen, J. K. Pritchard, A map of recent positive selection in the human genome. *PLoS One* 15, e0232451 (2020).

- Biol. 4, e72 (2006).
191. P. C. Sabeti, et al., Genome-wide detection and characterization of positive selection in human populations. *Nature* 449, 913–918 (2007).
 192. X. Yi, et al., Sequencing of 50 human exomes reveals adaptation to high altitude. *Science* 329, 75–78 (2010).
 193. H. McColl, et al., The prehistoric peopling of Southeast Asia. *Science* 361, 88–92 (2018).
 194. M. A. Yang, et al., 40,000-Year-Old Individual from Asia Provides Insight into Early Population Structure in Eurasia. *Curr. Biol.* 27, 3202–3208.e9 (2017).
 195. F. Racimo, D. Marnetto, E. Huerta-Sánchez, Signatures of Archaic Adaptive Introgression in Present-Day Human Populations. *Mol. Biol. Evol.* 34, 296–317 (2017).
 196. B. M. Peter, 100,000 years of gene flow between Neandertals and Denisovans in the Altai mountains. *bioRxiv*, 2020.03.13.990523 (2020).
 197. K. Prüfer, et al., The complete genome sequence of a Neanderthal from the Altai Mountains. *Nature* 505, 43–49 (2014).
 198. K. Prüfer, et al., A high-coverage Neandertal genome from Vindija Cave in Croatia. *Science* 358, 655–658 (2017).
 199. F. Mafessoni, et al., A high-coverage Neandertal genome from Chagyrskaya Cave. *Proc. Natl. Acad. Sci. U. S. A.* 117, 15132–15136 (2020).